



Cite this: *Chem. Soc. Rev.*, 2025, 54, 4200

Practical issues toward high-voltage aqueous rechargeable batteries

Seongjae Ko, ^a Shin-ichi Nishimura, ^a Norio Takenaka, ^a Atsushi Kitada ^a and Atsuo Yamada ^{ab}

This review offers a critical and exhaustive examination of the current state and innovative advances in high-voltage Li, Na, K, and Zn aqueous rechargeable batteries, an area poised for significant technological breakthroughs in energy storage systems. The practical issues that have traditionally hampered the development of aqueous batteries, such as limited operating potential windows, challenges in stable solid–electrolyte interphase (SEI) formation, the need for active materials optimized for aqueous environments, the misunderstood intercalation chemistry, the unreliable assessment techniques, and the overestimated performance and underestimated physico-chemical and electrochemical drawbacks, are highlighted. We believe that this review not only brings together existing knowledge but also pushes the boundaries by providing a roadmap for future research and development efforts aimed at overcoming the longstanding challenges faced by the promising aqueous rechargeable batteries.

Received 6th August 2024

DOI: 10.1039/d4cs00779d

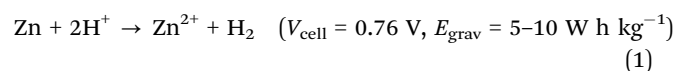
rsc.li/chem-soc-rev

1. Introduction

Chemical batteries are essential for clean and efficient energy conversion and storage, and have drawn significant attention for realizing a sustainable society. Notably, as recognized by the 2019 Nobel Prize,^{1–5} the development of Li-ion batteries has revolutionized the concept of “rechargeability,” potentially

aiding the realization of a zero carbon footprint. These batteries have profoundly impacted our lifestyle by facilitating the development of advanced, portable electronic devices for smart communications and healthcare, and also larger-scale applications such as electric vehicles, transportation systems, and grid storage for renewable energies.

Initially, battery systems utilized aqueous electrolytes (Fig. 1). The lineage of batteries dates back to the early 1800s, when the primary Voltaic pile (Cu|Zn)⁶ that employed an acidic H₂SO₄ solution as the electrolyte was used. The overall reaction is:



^a Department of Chemical System Engineering, The University of Tokyo, 7-3-1, Hongo, Bunkyo-ku, Tokyo 113-8656, Japan.

E-mail: yamada@chemsys.t.u-tokyo.ac.jp

^b Sungkyunkwan University Institute of Energy Science & Technology (SIEST), Sungkyunkwan University, Seobu-ro 2066, Jangan-gu, 16419 Suwon-si, Gyeonggi-do, Korea



Seongjae Ko

his research interests include electrolytes, battery design, and electrochemistry.

Seongjae Ko worked as a senior researcher at Samsung SDI in South Korea from 2012 to 2015. He joined Professor Atsuo Yamada's group as an academic support specialist in 2015. From 2017 to 2020, he worked as a research fellow at the Japan Society for the Promotion of Science (JSPS, DC1). He received his PhD in Engineering from the University of Tokyo in 2020. He is currently an assistant professor at the University of Tokyo, and



Shin-ichi Nishimura

Shin-ichi Nishimura received his PhD in Science from Tokyo Institute of Technology in 2009. Since 2009, he has worked as a research scientist with Professor Atsuo Yamada. His research has focused on solid electrode materials for secondary battery applications. The synthesis of the new electrode materials and their structural analysis with X-ray and neutron scattering/diffraction are the central interests of his research.

Here, V_{cell} and E_{grav} represent the output voltage and gravimetric energy density of the battery, respectively. Note that in this review, the cell configuration is represented as cathode|anode. In battery research, the electrode that undergoes oxidation during charging is often referred to as the cathode, while the electrode that undergoes reduction is referred to as the anode. This contrasts with the conventional electrochemical definition.

The evolution from the Voltaic pile to advanced batteries was driven by the need for a higher energy density, which can be defined as the product of the battery voltage (V) and capacity (A h kg⁻¹). The energy density of the Leclanché battery ($\text{MnO}_2|\text{Zn}$),⁷ which uses an acidic NH_4Cl or $\text{NH}_4\text{Cl} + \text{ZnCl}_2$ solution, was nearly five times higher than that of the Voltaic pile. The overall reaction is:



Norio Takenaka

Norio Takenaka received his PhD degree in information science from Nagoya University in 2010. From the same year to 2012, he worked as a postdoctoral fellow in Prof. Nagaoka's group in Nagoya University, from 2012 to 2019 at ESICB (Elements Strategy Initiatives on Catalysts and Batteries) in Kyoto University. In 2019, he joined Professor Atsuo Yamada's group at the University of Tokyo as an assistant professor and has been serving as a lecturer

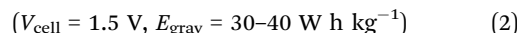
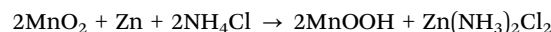
since 2022. His current research interests include theoretical calculations to elucidate the complex electrochemical reaction processes in rechargeable batteries.



Atsushi Kitada

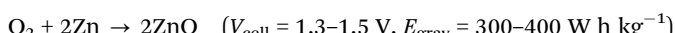
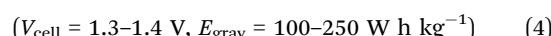
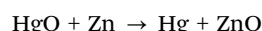
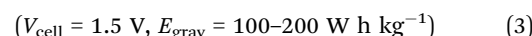
Atsushi Kitada received a PhD in Engineering from Kyoto University in 2012, and subsequently worked as an assistant professor. In 2022, he joined Professor Atsuo Yamada's group at the University of Tokyo as an associate professor. He has published over 90 peer-reviewed scientific papers on magnetic, electronic, and electrochemical materials of solid and liquid systems. He won the Young Scientist Award in 2019 in recognition of his outstanding research in the non-aqueous electrodeposition and the Paper Award in 2022 for highly-concentrated aqueous electrodeposition from the Surface Finishing Society of Japan.

aqueous electrodeposition and the Paper Award in 2022 for highly-concentrated aqueous electrodeposition from the Surface Finishing Society of Japan.



After one and half centuries of introducing the primary Voltaic pile, the transition from acidic to alkaline electrolytes significantly enhanced the energy density of the batteries. Under acidic and weakly alkaline conditions, the hydrogen evolution reaction (HER) is promoted, and/or a non-conductive $\text{Zn}(\text{OH})_2$ layer is formed on the Zn-metal surface, inhibiting the Zn/Zn^{2+} redox reaction. However, under highly alkaline conditions ($\text{pH} \geq 12$), Zn exists in the form of tetrahydrozincate ions ($\text{Zn}(\text{OH})_4^{2-}$) in the electrolyte, allowing for more efficient utilization of the Zn metal by thermodynamically inhibiting the HER and the formation of the $\text{Zn}(\text{OH})_2$ layer.

From the 1950s to 1970s, various aqueous primary alkaline batteries featuring diverse cathode active materials, Zn-metal anodes, and strongly alkaline KOH electrolytes were developed. Representative examples include alkaline–manganese ($\text{MnO}_2|\text{Zn}$),⁸ mercury ($\text{HgO}|\text{Zn}$),⁹ and Zn-air ($\text{O}_2|\text{Zn}$)¹⁰ batteries, which achieved energy densities up to 40 times higher than that of the Voltaic pile. Among these, alkaline–manganese and Zn-air batteries are widely used because they employ non-toxic materials, have low fire and explosion risk, are easy to recycle, and exhibit high energy densities and long usage times. The overall reactions for these batteries are as follows:



Atsuo Yamada

Atsuo Yamada has had a unique career in both academic and industrial research. After serving as the laboratory head of the Sony Research Center, he was immediately appointed as an associate professor at the Tokyo Institute of Technology in 2002, and he was then appointed as a full professor at the University of Tokyo in 2009. Among his numerous honors, he has been awarded the Spriggs Award (2010) and the Purdy Award

(2016) by the American Ceramic Society, the Scientific Achievement Award (2016) by the Electrochemical Society of Japan, the IBA Research Award (2016) by the International Battery Association, and the Battery Division Research Award (2022) by the Electrochemical Society.



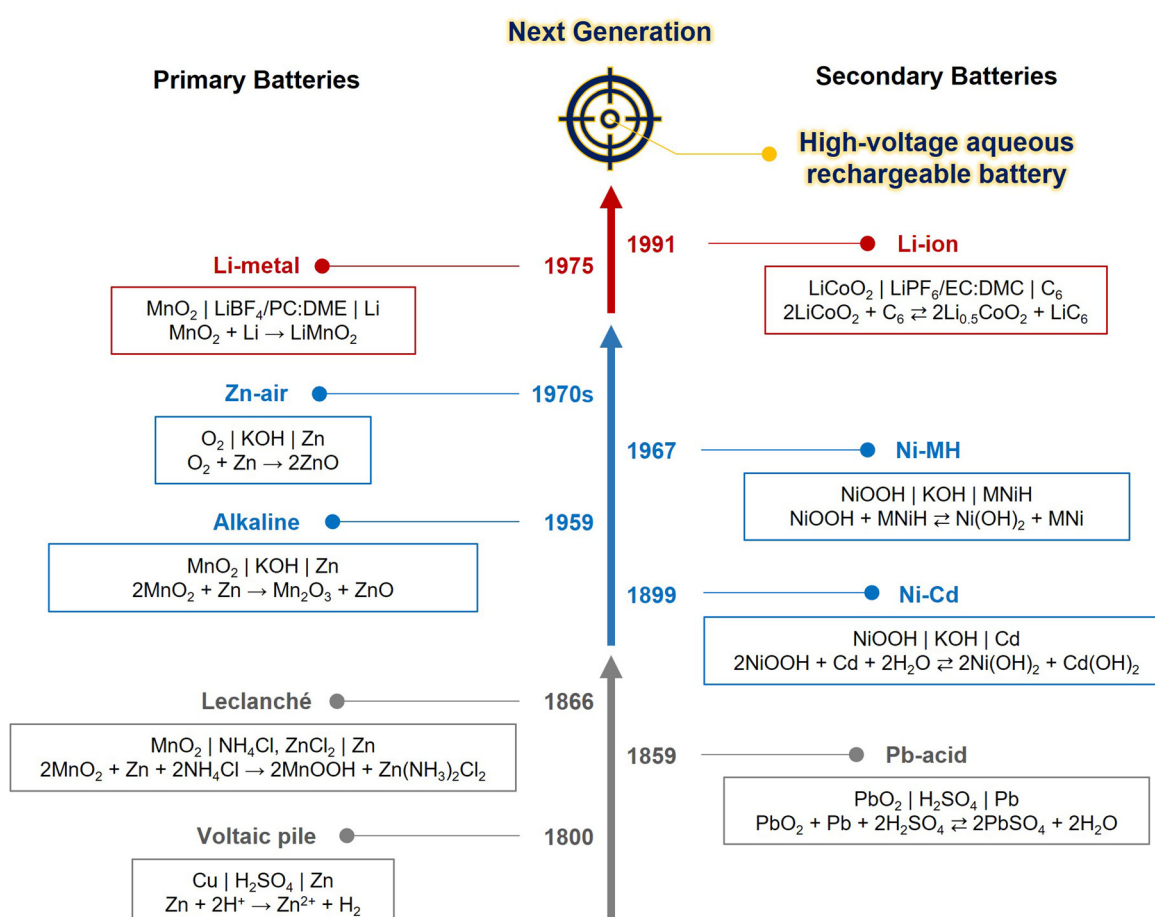
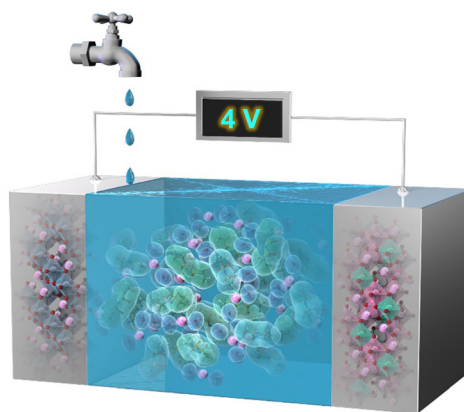
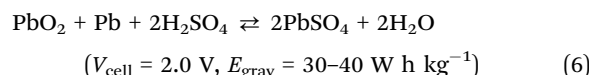


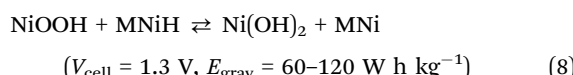
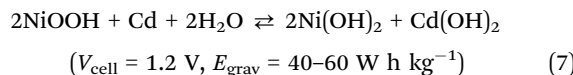
Fig. 1 History of practical batteries, listing the year of invention or commercialization, cell notations, and overall reactions. The transition of battery electrolytes is highlighted in gray (acidic aqueous electrolyte), blue (alkaline aqueous electrolyte), and red (nonaqueous electrolyte) arrows. One of the current technical targets is the development of aqueous rechargeable batteries with high voltage (high energy density), high safety, and high sustainability.

There has been considerable research and development since the 1800s to fabricate more efficient, practical, and environmentally friendly rechargeable (secondary) batteries. The lead-acid battery ($\text{PbO}_2|\text{Pb}$),¹¹ utilizing an acidic H_2SO_4 solution akin to that used in the Voltaic pile, was developed in the late 1850s. It is widely employed to power the starter motors of automobiles and is also used in uninterruptible power

supplies owing to its low cost, ease of large-scale production, and simple structure. The overall reaction for the lead-acid battery is:

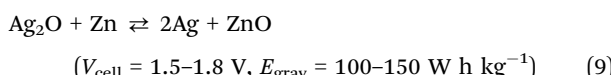


However, the cathode and anode of a lead-acid battery contain dense lead (Pb; 11.34 g cm⁻³), making the battery heavy. To address this, nickel-cadmium (Ni–Cd; Ni(OH)₂|Cd)¹² and nickel–metal hydride (Ni–MH; Ni(OH)₂|MnNiH)¹³ batteries were developed in the early and late 1900s, respectively. Their overall reactions are:



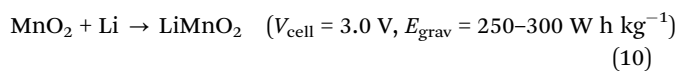
Ni–Cd batteries utilize a 6–7 mol L⁻¹ (M) KOH/H₂O electrolyte, which helps in suppressing the HER while providing a high ionic conductivity of over 500 mS cm⁻¹ and a low freezing point below –30 °C. These advantages have enabled their use in power tools, emergency medical equipment, and aerospace applications requiring high power density and a wide range of operating temperatures. However, Ni–Cd batteries suffer from the memory effect, necessitating periodic reconditioning (full charge and discharge cycles) and posing significant environmental risks owing to the high toxicity of cadmium, which can lead to severe environmental pollution if batteries rupture or are improperly discarded. These issues were addressed by replacing cadmium with metal hydride electrodes. The high hydrogen absorption and desorption capabilities of metal hydride electrodes, which are typically made from alloys of rare earth metals (e.g., La, Ce, and Nd) and transition metals (e.g., Ni, Co, Mn, Al, and Fe), enhance the battery capacity retention and efficiency, enabling over 1000 charge/discharge cycles.

Silver–zinc (Ag₂O|Zn)¹⁴ batteries, which can be configured for use as both primary and secondary batteries, was originally developed for space and military applications.



They boast the highest energy density among commercially available aqueous secondary batteries. However, their limitations, including a short cycle life and high production costs, have hampered their widespread utilization.

The demand for high-voltage batteries has significantly increased as electronic devices evolve to deliver higher power outputs. However, the narrow potential window of aqueous electrolytes, particularly their low reduction stability, which promotes the HER, has rendered the use of low-potential anode active materials challenging, thus limiting the battery output voltage. In the 1970s, a paradigm shift occurred from aqueous to nonaqueous electrolytes, leading to the commercialization of primary Li–metal batteries with voltages exceeding 3 V.¹⁵ The overall reaction is:



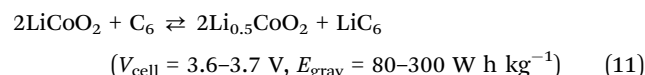
The redox potential of Li metal (Li/Li⁺: –3.04 V vs. standard hydrogen electrode (SHE)) is lower than the thermodynamic potential window of nonaqueous electrolytes, resulting in continuous electrolyte

decomposition on the Li–metal surface. To address this, the concept of a solid electrolyte interphase (SEI) was introduced, wherein protective layers/particles are formed to prevent direct contact between the Li metal and electrolyte, while facilitating Li⁺ transport. For instance, ethylene carbonate is reduced to form an SEI that is primarily composed of lithium ethylene dicarbonate ((CH₂OCO₂Li)₂) on the Li–metal surface.¹⁶ The developed nonaqueous electrolytes, which include highly dissociative and oxidation-resistant salts (such as LiPF₆ and LiBF₄) in a mixture of SEI-forming solvents (like ethylene carbonate) and low-viscosity solvents (such as linear carbonates and/or ethers), continue to remain fundamental for nonaqueous battery systems. Additionally, advancements in high-purity organic solvent purification technologies and the introduction of super-dry rooms with stringent humidity and impurity control measures in battery manufacturing environments have contributed significantly to the development of high-voltage nonaqueous batteries.

Nevertheless, the high reactivity of Li metal can lead to irreversible reactions with trace amounts of moisture, impurities, or gases (e.g., H₂, N₂) in the electrolyte and manufacturing environment, potentially rendering the Li metal inactive and posing significant fire and explosion risks. Moreover, the development of secondary batteries using Li metal has encountered challenges such as high volume changes during Li plating/stripping and the formation of dendrites and “dead” Li due to uneven electron distribution. These phenomena eventually led to SEI damage, continuous reduction and depletion of the electrolyte, and short circuits in the internal battery.

To realize a rechargeable system based on Li chemistry, the battery chemistry was changed by utilizing the “rocking chair” mechanism (*i.e.*, host–guest or intercalation chemistry). In this arrangement, the Li⁺ carrier ion initially resides in the cathode active material and shuttles between the anode and cathode through the electrolyte during the charging and discharging cycles.

This innovation allowed for the replacement of Li metal with a graphite anode, which acts as a reservoir for Li⁺. The overall reaction in modern Li–ion batteries (e.g., LiCoO₂|graphite) is described as follows:



This simple working principle significantly reduced the amount of electrolyte required, achieving an energy density of 80–100 W h kg⁻¹ in the 1990s. Over the years, energy densities in the range of 200–300 W h kg⁻¹, which significantly surpass that of secondary aqueous batteries, along with much better cycling performance exceeding 1000 cycles, have been achieved. However, the higher energy density of Li–ion batteries increases the risk of fire and explosions, particularly because of the use of flammable nonaqueous electrolytes. Moreover, the requirement for super-dry manufacturing conditions increases the production costs.

Fig. 2 illustrates the timeline of advancements and challenges in secondary batteries and their electrolytes, divided into periods before (left side) and after (right side) the advent of



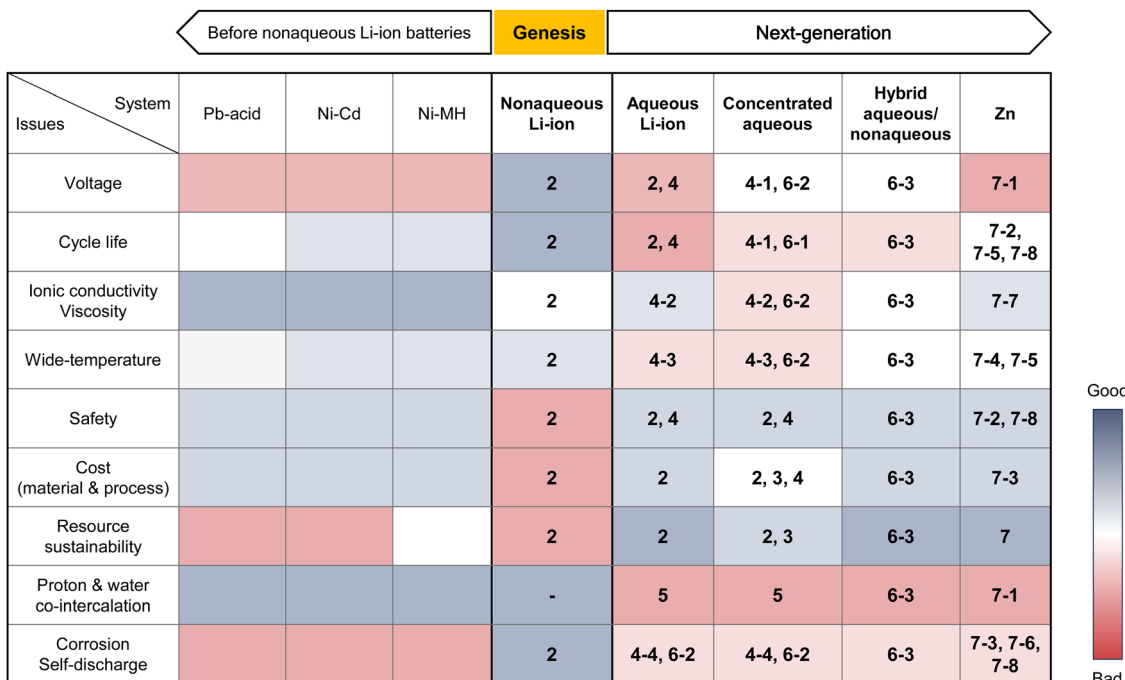


Fig. 2 Transitions in battery electrolyte issues. The issue of low output voltage in traditional aqueous rechargeable batteries was overcome with the development of nonaqueous Li-ion batteries, which offer both high output voltage (4 V-class) and high cycling stability. However, they introduced problems such as safety risks and increased manufacturing costs. Significant technical efforts have been devoted to exploring highly functional aqueous electrolytes and electrode materials based on diverse carrier ions (Li^+ , Na^+ , K^+ , and Zn^{2+}) toward the next generation of energy storage devices that ensure high voltage, ultimate safety, economic production, and high sustainability. This review article will focus on the research conducted after the "Genesis" on the right side of the table, providing chapter/section numbers that address the corresponding development approaches and their issues.

nonaqueous Li-ion batteries in 1991. Following this "Genesis," the major research trend shifted toward exploring various intercalation chemistries, including the pursuit of high-voltage aqueous batteries to ensure ultimate safety and low production costs.

The first prototype of an aqueous Li-ion battery was reported by Li, Dahn, and Wainwright in 1994, who achieved a reversible 1.5 V system with a LiMn_2O_4 cathode, a $\text{VO}_2(\text{B})$ anode, and a 5 M LiNO_3 + 0.001 M LiOH electrolyte.¹⁷ Twenty years later, the discovery of highly salt-concentrated aqueous electrolytes, which drastically widened the potential window above 3 V by significantly decreasing the water activity and forming an anion-derived SEI, revived the interest in aqueous Li-ion batteries.^{18–21} Similar strategies have been applied to other carrier ion-based batteries (Na^+ , K^+ , and Zn^{2+})^{22–27} and electroplating.²⁸ Despite these advancements, achieving high-voltage aqueous batteries remains a significant challenge.

In this review, the recent progress in high-voltage aqueous rechargeable batteries will be discussed in depth, along with the fundamental science of aqueous systems, the severity of the challenges faced, and the potential strategies for system optimization. The section index corresponding to each issue is marked in Fig. 2.

2. Challenges and prospects for aqueous Li-ion batteries

Aqueous rechargeable batteries are recognized as promising energy storage devices owing to their high safety, low product

cost, and high manufacturability and scalability, which facilitate the development of green technologies.^{29–32} However, despite their advantages, these batteries have struggled to match the energy density and cycling performance of nonaqueous rechargeable batteries over the past three decades, impeding their commercial viability.

Nonaqueous Li-ion batteries, which were first commercialized by Sony in 1991, are among the most well-developed and refined energy storage devices developed to date. The choice of Li^+ as the carrier ion in rechargeable batteries is primarily driven by the low atomic mass and redox potential of Li .^{34–39} The nature of the carrier ions, typically present in active materials and electrolytes, plays a crucial role in determining the overall electrochemical properties of batteries. For instance, the capacity per unit weight, expressed as the charge-to-mass ratio following Faraday's law, underscores the importance of high charge-to-mass ratios for achieving lightweight yet high-capacity batteries. Among the various ions, Li^+ possesses a higher charge-to-mass ratio (0.14; charge: 1, mass: 6.9) compared to Na^+ (0.04; charge: 1, mass: 23.0), K^+ (0.03; charge: 1, mass: 39.0), and Zn^{2+} (0.03; charge: 2, mass: 65.4). The operating voltage of the battery, reflecting the potential difference between the cathode and anode, is also crucial for efficient energy storage. An optimal battery configuration involves a high-potential cathode and a low-potential anode, where the minimum reaction potential of the anode is influenced by the standard redox potential of the carrier ion.



Therefore, it is widely acknowledged that Li-ion batteries, with the lowest standard redox potential of Li metal ($E_{\text{Li}/\text{Li}^+}^\circ = -3.04 \text{ V vs. SHE}$), offer the highest battery operating voltage and energy density (defined as the product of the battery operating voltage and capacity).

Sony's first-generation nonaqueous Li-ion batteries achieved an energy density of $\sim 80 \text{ W h kg}^{-1}$ and were capable of enduring hundreds of charge and discharge cycles.⁴⁰ Subsequent advancements and optimizations across all battery components, including active materials, electrolytes, carbon additives, separators, and overall electrode design, have resulted in significant performance enhancement compared to early models. The key attributes include high cathode loading ($\geq 20 \text{ mg cm}^{-2}$), limited electrolyte volume ($\leq 3 \text{ mg mA}^{-1}$), a controlled positive-to-negative (P/N) ratio approaching 1 based on the superior initial cycling efficiency ($\geq 90\%$), minimized electrolyte decomposition at electrode surfaces, and low electrolyte viscosity ($\leq 5 \text{ mPa s}$) paired with sufficient ion conductivity ($\geq 10 \text{ mS cm}^{-1}$).^{4,41-44} Owing to these positive attributes, modern nonaqueous Li-ion batteries can achieve a two- to three-fold increase in the energy density and cycling stability. For example, LiFePO₄|graphite batteries exhibit remarkable cycling stability, maintaining over 80% of their initial capacity even after several thousands of charge and discharge cycles. These batteries have a theoretical energy density of 340 W h kg^{-1} , calculated based on the capacities of LiFePO₄ (150 mA h g^{-1}) and graphite (360 mA h g^{-1}), with a P/N ratio of 0.9 and an average operating voltage of 3.3 V. Similarly, LiCoO₂|graphite batteries exhibit excellent cycling stability, enduring over 1000 cycles. These batteries offer a theoretical energy density of 380 W h kg^{-1} , utilizing LiCoO₂ (150 mA h g^{-1}) and graphite (360 mA h g^{-1}), with a P/N ratio of 0.9 and an average operating voltage of 3.7 V. LiNi_{0.8}Mn_{0.1}Co_{0.1}O₂|graphite/Si composite batteries also exhibit stable reversibility even after several hundred cycles, with a theoretical energy density of 525 W h kg^{-1} achieved through the integration of LiNi_{0.8}Mn_{0.1}Co_{0.1}O₂ (200 mA h g^{-1}) and graphite/Si composite (600 mA h g^{-1}), with a P/N ratio of 0.9 and an average operating voltage of 3.6 V. With a practical energy density ranging from 150 to 300 W h kg^{-1} , inclusive of the electrolyte, separator, cases, and other battery components, these batteries ensure reliable operation across a wide temperature range (-20 to 50°C). Furthermore, recent developments on a laboratory scale have demonstrated the stable cycling of high-energy-density nonaqueous Li-ion batteries with high-potential cathodes and/or high-capacity anodes (e.g., 4.8 V Li₂CoPO₄F|graphite and 4.4 V LiNi_{0.5}Mn_{1.5}O₄|SiO_x with SiO_x capacity $\geq 1600 \text{ mA h g}^{-1}$) for over 1000 cycles.⁴⁵⁻⁴⁸ Continuous research efforts are being devoted to the development of battery materials for ensuring stable operation under extreme conditions (e.g., $\leq -60^\circ\text{C}$ and/or $\geq 60^\circ\text{C}$).⁴⁹⁻⁵² Additionally, ongoing advancements in the cell-to-pack technology⁴¹ hold promise to further enhance the practical energy density of batteries for large-scale applications.

While the development history of aqueous Li-ion batteries parallels that of nonaqueous systems, their advancements in

energy density and cycling performance have been less impressive, characterized by a low output voltage and poor long-term cycling performance at low C-rates. Moreover, stable operation under extreme conditions remains uncertain. The performance of the developed aqueous Li-ion full cells is outlined in Table 1. Notably, during our literature survey, we found several papers where "M" and "m" were used interchangeably. Further, these expressions were quoted directly without any corrections, despite the fact that "M" (molarity, mol L⁻¹) specifies the amount of salt per unit volume of a solution (electrolyte), while "m" (molality, mol kg⁻¹) denotes the concentration of salt dissolved in 1 kg of a solvent.

In 1994, Li *et al.* reported a prototype aqueous Li-ion battery that exhibited a capacity of 10 mA h and operated at 1.5 V. Its composition included a LiMn₂O₄ cathode, a VO₂(B) anode, and an electrolyte comprising 5 M LiNO₃ and 0.001 M LiOH (Fig. 3).¹⁷ Despite being limited to only 20 continuous charge and discharge cycles, the theoretical energy density of this battery was 75 W h kg^{-1} based on the mass of the active materials, and the practical energy densities, including the electrolyte and other battery components, were predicted to be over $40-55 \text{ W h kg}^{-1}$, comparable to those of the aqueous Pb acid ($30-40 \text{ W h kg}^{-1}$) and aqueous Ni-Cd ($40-60 \text{ W h kg}^{-1}$) batteries.

There was no substantial improvement in the operating voltage and cycling stability of aqueous Li-ion batteries over the next 20 years, until their performance began to improve with the development of highly salt-concentrated aqueous electrolytes (Fig. 4 and 5).

In 2015, Wang and Xu groups achieved the successful cycling of a LiMn₂O₄|Mo₆S₈ full cell using a water-in-salt (21 mol kg⁻¹ (m) LiN(SO₂CF₃)₂ (LiTFSI)/H₂O) electrolyte at an operating voltage of 1.7 V (Fig. 6).¹⁸ However, notable enhancements were still necessary for achieving low C-rate cycling, as evidenced by a capacity retention less than 50% after 100 cycles at 0.15C; in contrast, stable reversibility was achieved at high C-rates, with 68% capacity retention after 1000 cycles at 4.5C. Furthermore, the cell design with high P/N ratios and a large amount of electrolyte rendered it challenging to improve the energy density of the batteries owing to the continuous loss of the electrolyte and Li⁺ sources at the electrode surface during charging and discharging. In 2016, Yamada *et al.* addressed these challenges by developing a 28 m dihydrate melt (Li(TFSI)_{0.7}(BETI)_{0.3}·2H₂O) by exploring the eutectic points of two Li salts, LiTFSI and LiN(SO₂C₂F₅)₂ (LiBETI), thereby demonstrating the reversible cycling of 3 V-class aqueous Li-ion batteries for the first time (Fig. 7).¹⁹ A 2.4 V LiCoO₂|Li₄Ti₅O₁₂ battery, engineered with a P/N ratio of 1.1–1.3, exhibited a satisfactory capacity retention of 84% after 500 cycles at 10C. However, it demonstrated poor capacity retention at lower C-rates, retaining only 67% and 79% of its initial capacity after 100 cycles at 0.2 and 0.5C, respectively. The 3.1 V LiNi_{0.5}Mn_{1.5}O₄|Li₄Ti₅O₁₂ battery, configured with a high P/N ratio of 2.5 and operated at a high C-rate of 10C, demonstrated a capacity retention of only 63% after 100 cycles. In 2019, further progress was achieved by successfully operating a 2.4 V





Table 1 Performance data of Li-ion full cells fabricated using aqueous electrolytes

Year	Electrolyte	Cathode	Anode	Anode L/L (mg cm ⁻²)	Full cell average (mg cm ⁻²)	Full cell cutoff (V/V)	P/N ratio	C-rate	Capacity (mA h g ⁻¹)	Capacity calculation based	Cycle number (-)	Retention ratio (%)
1994	5 M LiNO ₃ + LiOH/H ₂ O or 10 M LiOAc/H ₂ O or 10 M LiCl ₂ H ₂ O ¹⁷	LiMn ₂ O ₄	VO ₂ (B)	—	1.8/0.5	1.5	—	2 mA cm ⁻²	50	Cathode + anode	20	—
1998	6 M LiNO ₃ + 0.0015 M LiOH/H ₂ O ⁵³	LiMn ₂ O ₄	Li ₂ Mn ₄ O ₉ or Li ₄ Mn ₅ O ₁₂	—	1.6/0.5	1.1	—	1 mA cm ⁻²	100	Cathode + anode	5	98
2000	1 M Li ₂ SO ₄ /H ₂ O ⁵⁴	LiNi _{0.81} Co _{0.19} O ₂	LiV ₃ O ₈	—	1.3/0.6	1.0	1.0 (mass)	1 mA cm ⁻²	20	Cathode + anode	100	40
2006	5 M LiNO ₃ /H ₂ O ⁵⁵	LiMn ₂ O ₄	TiP ₂ O ₇ or LiTi ₂ (PO ₄) ₃	—	1.7/0.8 (TiP ₂ O ₇)	1.4	0.77 (mass)	0.1C	42	Cathode + anode	10	85
2007	5 M LiNO ₃ /H ₂ O + LiOH (pH 11) ⁵⁶	LiNi _{1/3} Mn _{1/3} Co _{1/3} O ₂	Li _x V ₂ O ₅ /polyaniline	—	1.8/0.5	1.1	—	0.2C (capacity)	45	Cathode + anode	10	75
2007	2 M Li ₂ SO ₄ /H ₂ O ⁵⁷	LiMn ₂ O ₄	LiV ₃ O ₈	—	1.5/0.5	1.0	—	0.2C	55	Cathode + anode	30	50
2007	Sat. LiNO ₃ /H ₂ O ⁵⁸	LiCoO ₂	LiV ₃ O ₈	—	1.5/0.5	1.1	—	0.2 mA cm ⁻²	55	Cathode + anode	400	18
2007	Sat. LiNO ₃ /H ₂ O ⁵⁹	LiCoO ₂	LiV ₃ O ₈	—	1.5/0.5	1.1	—	3.4 mA cm ⁻²	55	Cathode + anode	12	70
2007	1 M Li ₂ SO ₄ /H ₂ O ⁶⁰	LiMn ₂ O ₄	LiTi ₂ (PO ₄) ₃	10	1.85/0.0	1.5	1.0 (mass)	10 mA cm ⁻²	40	Cathode + anode	100	36
2007	5 M LiNO ₃ /H ₂ O ⁶¹	LiMn ₂ O ₄	Li _x V ₂ O ₅	—	1.7/0.5	1.2	0.75 (mass)	0.2C	43	Cathode + anode	200	80
2008	Sat. Li ₂ SO ₄ /H ₂ O ⁶²	LiMn ₂ O ₄	Polypyrrole	—	1.6/0.0	0.6	—	0.2 mA cm ⁻²	45	Cathode + anode	40	8
2008	2 M Li ₂ SO ₄ /H ₂ O ⁶³	LiNi _{1/3} Mn _{1/3} Co _{1/3} O ₂	LiV ₃ O ₈	—	1.5/0.3	0.8	—	0.2 mA cm ⁻²	55	Cathode + anode	22	85
2009	Sat. Li ₂ SO ₄ /H ₂ O ⁶⁴	LiMn _{0.05} Ni _{0.05} Fe _{0.9} PO ₄	LiTi ₂ (PO ₄) ₃	—	1.2/0.6	0.9	—	0.2 mA cm ⁻²	87	Cathode + anode	10	55
2010	1 M Li ₂ SO ₄ /H ₂ O (pH 13, O ₂ -free) ⁶⁵	LiFePO ₄	LiTi ₂ (PO ₄) ₃	10	1.4/0.0	0.9	1.0 (mass)	0.13C	55 (1C)	Cathode + anode	50	65
2010	10 mM Li ₂ SO ₄ /H ₂ O ⁶⁶	LiCoO ₂	Polypyrrole	—	1.5/0.1	0.9	—	0.1C	48	Cathode + anode	1000	90
2011	Sat. LiNO ₃ /H ₂ O ⁶⁷	LiMn ₂ O ₄	LiV ₃ O ₈	—	1.4/0.25	0.9	—	0.2C	120	Cathode + anode	130	63
2012	0.5 M Li ₂ SO ₄ /H ₂ O ⁶⁸	LiMn ₂ O ₄	Polypyrrole coated — MoO ₃	—	2.0/0.0	1.2	0.5 (mass)	500 mA g ⁻¹	88	Cathode + anode	150	90
2012	5 M LiNO ₃ /H ₂ O ⁶⁹	LiNi _{1/2} Mn _{1/3} Co _{1/3} O ₂ /polyppyrrole	LiV ₃ O ₈	—	1.4/0.1	0.9	—	0.2 mA cm ⁻²	70	Cathode + anode	50	70
2012	Sat. LiNO ₃ /H ₂ O ⁷⁰	LiMn ₂ O ₄	Polyaniline	—	1.5/0.5	1.1	—	75 mA g ⁻¹	110	Anode + anode	100	82
2013	1 M Li ₂ SO ₄ /H ₂ O ⁷¹	LiMn ₂ O ₄	TiP ₂ O ₇	9	1.7/0.0	1.5	1.0 (mass)	0.5C	77	Cathode + anode	100	85
2013	9 m LiNO ₃ /H ₂ O (O ₂ -free) ⁷²	LiFePO ₄	LiV ₃ O ₈	—	0.8/0.0	0.2	—	1,2, 5, 10C	113 (1C)	Cathode + anode	100	99-100
2013	Sat. LiNO ₃ /H ₂ O ⁷³	LiFePO ₄	VO ₂	—	1.4/0.0	0.3	—	0.33C	106	Cathode + anode	200	99-100
2014	5 M LiNO ₃ /H ₂ O ⁷⁴	LiCoO ₂	Polyimide	—	1.8/0.0	1.12	1.2 (mass)	500 mA g ⁻¹	71	Cathode + anode	200	94
2015	21 m LiTFSI/H ₂ O ¹⁸	LiMn ₂ O ₄	Mo ₆ S ₈	20	2.3/0.5	1.7	2.0 (mass)	0.15C	47 (0.15C)	Cathode + anode	100	48
2016	0.5 M Li ₂ SO ₄ /H ₂ O ⁷⁵	LiMn ₂ O ₄	Poly(naphthalene four formyl ethylenedi amine)	—	2.4/0.0	1.1	1.2 (mass)	10C	69	Cathode + anode	1000	66
2016	Li(TFSI) _{0.7} (BETI) _{0.3} ·2H ₂ O ¹⁹	LiCoO ₂ or LiNi _{1/2} O ₅ ·Mn _{1/2} O ₄	Li ₄ Ti ₅ O ₁₂	1.0 or 1.4 (LCO)	2.7/1.6 (LCO)	2.4	1.1-1.3 (capacity, LCO)	40-55 (LCO)	Cathode + anode	100	67	



Table 1 (continued)

Year	Electrolyte	Cathode	Cathode L/L (mg cm ⁻²)	Anode	Anode L/L (mg cm ⁻²)	Full cell cutoff (V/V)	Full cell average (V)	P/N ratio	C-rate	Capacity (mA h g ⁻¹)	Capacity calculation based	Cycle number (-)	Capacity retention ratio (%)
2016	21 m LiTFSI + 7 m LiOTf/H ₂ O ⁷⁶	LiMn ₂ O ₄	8	TiO ₂	4	2.5/0.8	3.1	2.5 (capacity city, LNMO)	10C (LCO) 6.8C (LNMO)	30 (LNMO)	500	84	
2017	2 M Li ₂ SO ₄ /H ₂ O ⁷⁷	LiMn ₂ O ₄	—	LiTi ₂ (PO ₄) ₃ /carbon	—	1.85/0.0	2.1	2.0 (mass)	0.5C (75 mA g ⁻¹)	48	Cathode + anode	100	78
2017	2 M Li ₂ SO ₄ /H ₂ O ⁷⁸	LiMn ₂ O ₄	—	LiTi ₂ (PO ₄) _{2.88} T _{0.12}	10-18	2.0/0.5	1.5	—	0.2C	108	—	200	88
2015	5 M LiNO ₃ /H ₂ O ⁷⁹	LiMn ₂ O ₄	6	Poly(1,4,5,8-naphthalene tetracarboxylic dianhydride)	7.2	1.75/0.0	1.4	1.5-2.0 (mass)	10C (1300 mA g ⁻¹)	43	Cathode + anode	200	95
2017	21 m LiTFSI/H ₂ O ⁸⁰	Polytriphenylamine	1.1	Naphthalenetetra carboxylic dianhydride	1	2.1/0.05	1.0	0.8 (mass)	2C	45	Cathode + anode	1000	95
2017	21 m LiTFSI/H ₂ O ⁸¹	LiMn ₂ O ₄	4.2	TiS ₂	2.1	2.3/0.7	1.4	2.0 (mass)	1C	58	Cathode + anode	700	86
2017	2.5 M Li ₂ SO ₄ /H ₂ O (pH 7 or pH 13) ⁸²	LiMn ₂ O ₄ or LiCoO ₂	—	Poly(pyrene-4,5,9,10-tetraone)	2.2	1.5/0.5 (LMO)	1.1	—	1C	81	Cathode + anode	50	74
2017	21 m LiTFSI/H ₂ O + HTFSI (pH 5) ⁸³	LiNi _{0.5} Mn _{1.5} O ₄	20	Mo ₆ S ₈	8	2.9/0.8	1.2	2.5 (mass)	0.5C	55	Cathode + anode	700	83
2018	21 m LiTFSI/H ₂ O ⁸⁴	Li ₃ V ₂ (PO ₄) ₃	14	LiTh ₂ (PO ₄) ₃	7	1.9/0.5	1.3	2.0 (mass)	0.1C	34 (0.5C)	Cathode + anode	50	90
2019	56 m Li ₂ O ⁸⁵	LiCoO ₂	2-10	Li ₄ Ti ₅ O ₁₂	—	2.7/1.7	2.4	0.7-1.0 (capacity)	1C (25 °C)	124 (0.1C)	Anode	400	75
2019	Li(PTFSI) _{0.6} (TFSI) _{0.4} ·1H ₂ O	LiCoO ₂	—	Li ₄ Ti ₅ O ₁₂	—	2.7/1.7	2.4	0.7-1.0 (capacity)	1C (45 °C)	103 (0.2C)	Cathode	100	83
2020	Li(PTFSI) _{0.6} (TFSI) _{0.4} ·1.15H ₂ O ⁸⁶	LiMn ₂ O ₄	—	Nb ₁₆ W ₅ O ₅₅ or Nb ₁₈ W ₁₆ O ₉₃	5-6	2.1/1.0	1.9	—	1C	92 (5C)	Cathode + anode	100	65
2020	21 m LiTFSI/H ₂ O ⁸⁷	LiMn ₂ O ₄	—	Nb ₁₆ W ₅ O ₅₅ or Nb ₁₈ W ₁₆ O ₉₃	—	—	—	—	1C	55	—	100	85
2022	Li(TFSI) _{0.7} (BETI) _{0.3} ·2H ₂ O ⁸⁸	Li _{1.2} Ni _{0.2} Mn _{0.6} O ₂	—	Li ₄ Ti ₅ O ₁₂	—	3.2/0.1	1.8	0.8 (capacity)	1C	75	Cathode + anode	100	88
2022	Li(TFSI) _{0.7} (BETI) _{0.3} ·2H ₂ O ⁸⁹	Li _{1.2} Ni _{0.2} Mn _{0.6} O ₂	—	Li ₄ Ti ₅ O ₁₂	—	3.2/0.1	1.8	0.5C (capacity)	1C	82	Cathode + anode	100	85

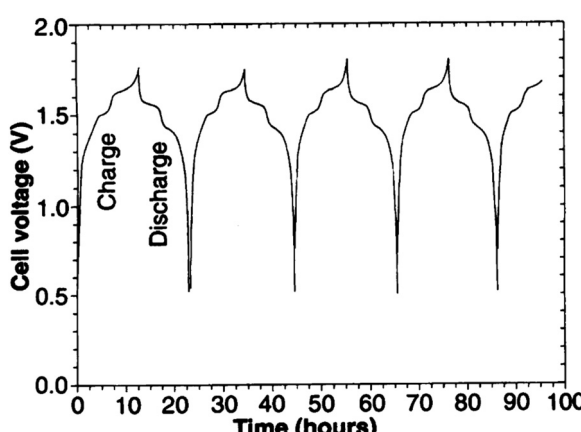


Fig. 3 Charge and discharge curves of a prototype aqueous LiMn_2O_4 - $\text{VO}_2(\text{B})$ battery.^{17,33} Reprinted with permission from *Journal of The Electrochemical Society*.

$\text{LiCoO}_2|\text{Li}_4\text{Ti}_5\text{O}_1_2$ battery with a P/N ratio close to 1 in an asymmetric imide salt (LiPTFSI ; $\text{LiN}(\text{SO}_2\text{CF}_3)(\text{SO}_2\text{C}_2\text{F}_5)$)-based 56 m monohydrate-melt ($\text{Li}(\text{PTFSI})_{0.6}(\text{TFSI})_{0.4}\cdot 1\text{H}_2\text{O}$) electrolyte (Fig. 7).⁸⁵ The asymmetric structure of LiPTFSI helped in preventing crystallization and enhanced the electrochemical stability of the aqueous electrolyte, while promoting Li-ion transport owing to its improved anion-exchange ability and high rotational mobility.⁸⁹⁻⁹¹ Consequently, 77%, 74%, and 67% of the initial capacity were retained after 100 cycles under various temperature and current conditions (25 °C/0.2C, 45 °C/1.0C, and 55 °C/1.0C, respectively). However, their reversibility still fell short of the typical standard defined in nonaqueous Li-ion batteries.

Overall, owing to the development of new electrolytes and the optimization of the cell design, aqueous Li-ion batteries have achieved higher operating voltages (2–3 V) and improved cycle life (approximately 100 cycles at low C ($\leq 0.5\text{C}$), with a Coulombic efficiency of 98–99%) compared to the initial prototypes developed in 1994 (1.5 V and 20 cycles). However, the substantial loss of the electrolyte and Li^+ sources at the electrode surfaces during continuous charge and discharge cycles, narrow operating temperature

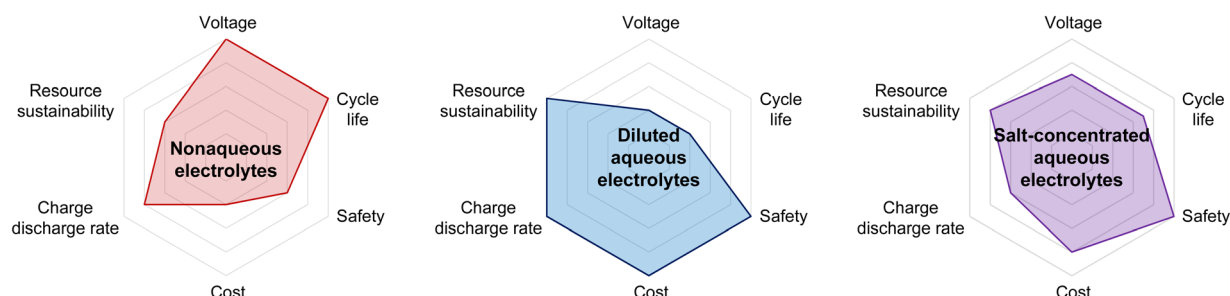


Fig. 4 Advantages and limitations of nonaqueous, diluted aqueous, and salt-concentrated aqueous electrolytes.

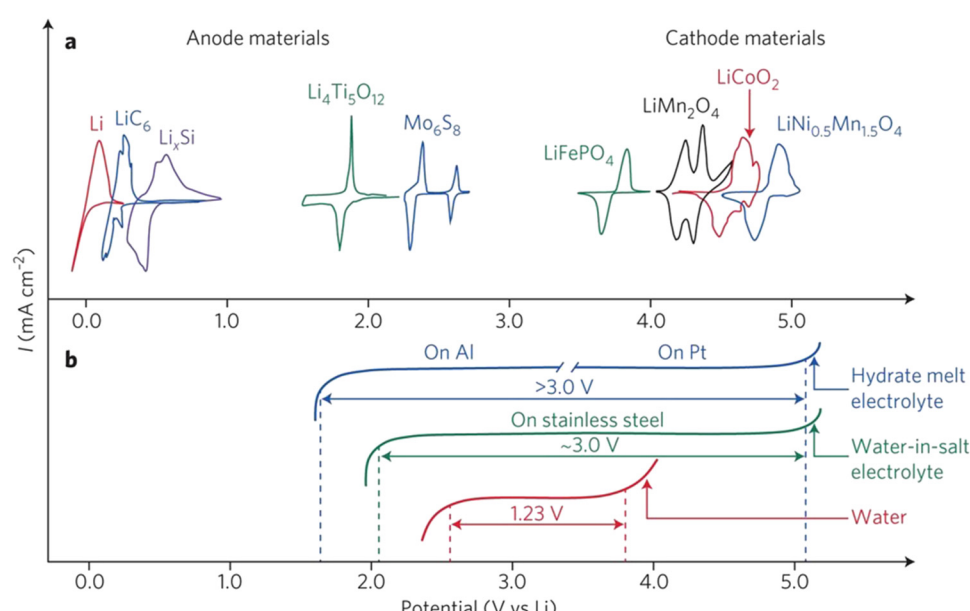


Fig. 5 (a) and (b) Broadened operating potential window in highly salt-concentrated aqueous electrolytes, such as water-in-salt (21 m $\text{LiTFSI}/\text{H}_2\text{O}$) and dihydrate melt (28 m $\text{Li}(\text{TFSI})_{0.7}(\text{BETI})_{0.3}\cdot 2\text{H}_2\text{O}$), contributing to an increase in output voltage of aqueous batteries.⁸⁸ Reprinted with permission from *Nature Energy*.



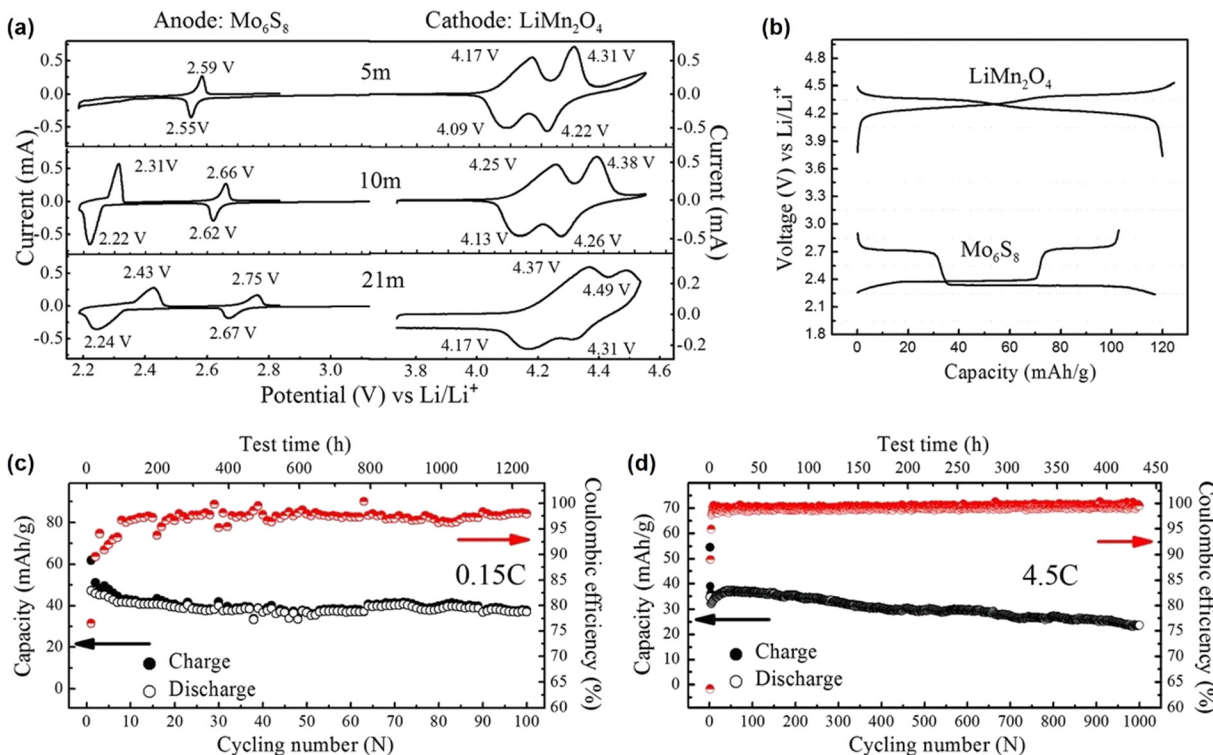


Fig. 6 (a) and (b) Cyclic voltammograms and galvanostatic charge and discharge curves of LiMn₂O₄ cathode and Mo₆S₈ anode in LiTFSI/H₂O with various concentrations. (c) and (d) Electrochemical performance of aqueous LiMn₂O₄|Mo₆S₈ full cells in water-in-salt 21 m LiTFSI/H₂O electrolyte.¹⁸ Reprinted with permission from *Science*.

ranges, and other issues such as high P/N ratios, high electrolyte amounts, and susceptibility to self-discharge, highlight the need for extensive improvements in various aspects. A significant gap still exists between the operating conditions of not only traditional aqueous NiMH batteries (with energy densities of 60–120 W h kg⁻¹ and 1000 cycles of reversibility), but also nonaqueous Li-ion batteries (operating voltage of ≥ 3.3 V and stable cycling under wide temperature ranges, with ≥ 1000 cycles at room temperature and several hundred cycles at low and high temperatures and Coulombic efficiencies $\geq 99.95\%$).

3. Sustainable alternatives to aqueous Na- and K-ion batteries: a greater challenge

Although rechargeable Li-ion batteries offer high energy density, their reliance on lithium—a resource primarily concentrated in a few geographic regions like South/North America, China, and Australia—raises concerns about global supply security, especially considering current geopolitical tensions.^{92–95} The widespread adoption of electric vehicles has increased the demand for Li, which, combined with the instability in the supply chain, has led to significant price fluctuations in Li, thereby aggravating concerns on the sustainability of Li-ion batteries (Fig. 8).^{92,93} Furthermore, the mining and extraction of Li can have adverse environmental impacts, including potential harm to groundwater resources and ecosystems.⁹⁵ Given these challenges, including

the limited availability and environmental concerns associated with Li resources, it becomes imperative to explore alternative battery technologies, such as aqueous Na- and K-ion batteries, which are potentially more sustainable and environmentally friendly.^{22–25}

Practically, the battery output voltage is not solely determined by the difference in the chemical potential of the carrier ions in the cathode and anode, but is also limited by the operating potential window of the electrolyte. Failure to maintain the reaction potential range of the cathode and anode within the operating potential window of the electrolyte can result in severe electrolyte decomposition on the electrode surfaces; this aspect is detailed in Section 4.1. It is also important to consider the fast charge and discharge capabilities of batteries, commonly quantified as the battery power density (product of the battery output voltage and the maximum current that the battery can provide per unit weight or volume). The physicochemical differences in carrier ions impact essential factors such as the diffusion of ions into the bulk structure of the cathode and anode active materials, ion movement within the electrolyte, and the desolvation process of ions at the electrode surface, all of which influence the battery power density significantly. Table 2 presents the physicochemical properties of alkali ions. Ion movement within the aqueous electrolyte largely depends on the Stokes radius, representing the hydrated-ion size. Generally, an ion with a smaller Stokes radius encounters less resistance during its movement through the electrolyte, as it has fewer interactions with ions and water molecules. The Stokes radii of Na⁺ (1.84 Å) and K⁺ (1.25 Å) are smaller than that of Li⁺ (2.38 Å), suggesting that Na⁺ and K⁺

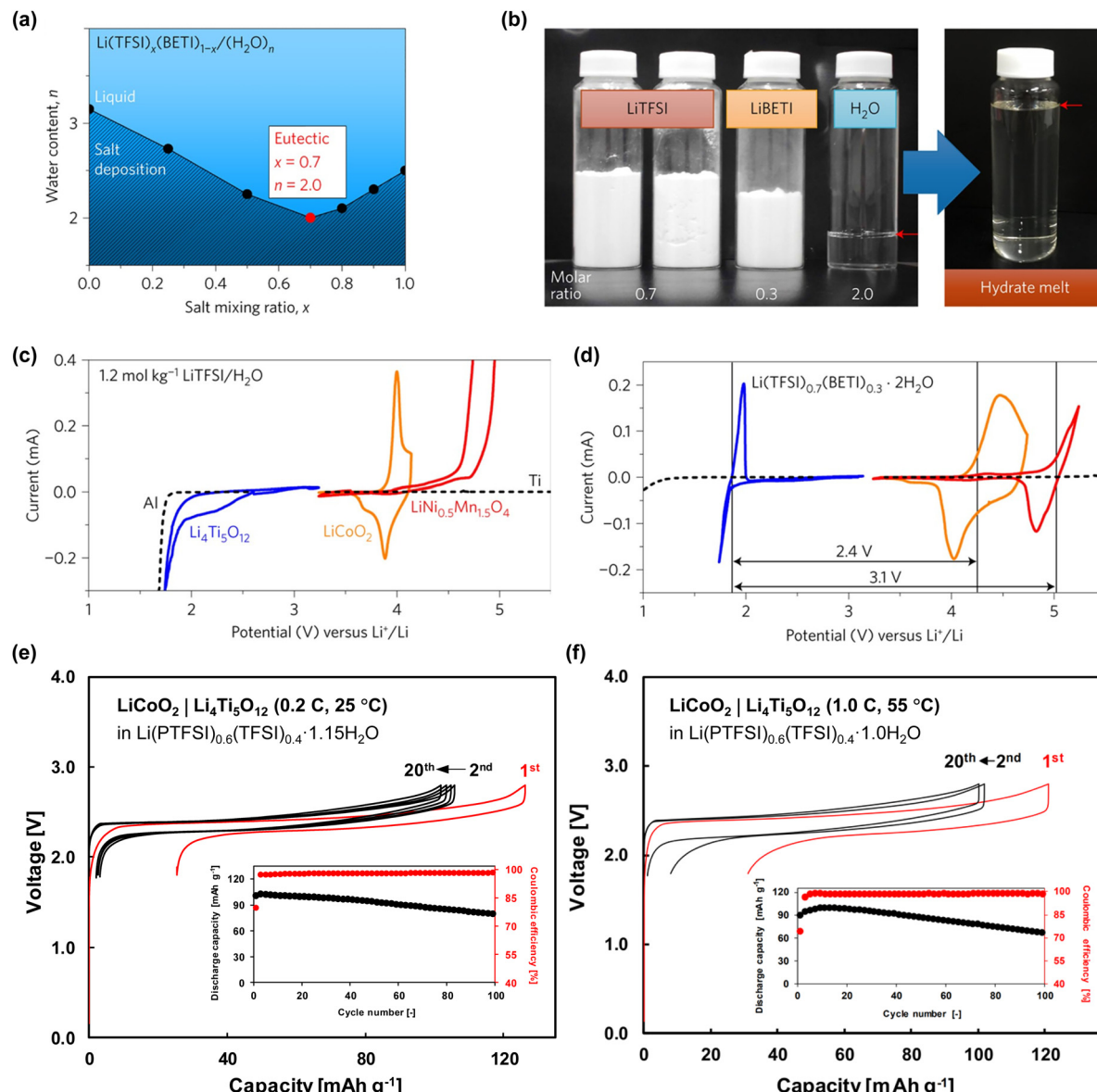


Fig. 7 (a) and (b) Preparation of dihydrate melt by exploring the eutectic point of $\text{Li}(\text{TFSI})_x(\text{BETI})_{1-x}/(\text{H}_2\text{O})_n$ salt/water mixtures. (c) and (d) Cyclic voltammograms of $\text{Li}_4\text{Ti}_5\text{O}_{12}$, LiCoO_2 , $\text{LiNi}_{0.5}\text{Mn}_{1.5}\text{O}_4$ electrodes in $\text{Li}(\text{TFSI})_{0.7}(\text{BETI})_{0.3}\cdot 2\text{H}_2\text{O}$.¹⁹ (e) and (f) Electrochemical performance of aqueous $\text{LiCoO}_2|\text{Li}_4\text{Ti}_5\text{O}_{12}$ full cells in the monohydrate-melt $\text{Li}(\text{PTFSI})_{0.6}(\text{TFSI})_{0.4}\cdot 1\text{H}_2\text{O}$ electrolyte.⁸⁵ Reprinted with permission from *Nature Energy* and *Electrochemistry Communications*.

experience lower resistance compared to Li^+ as they diffuse and migrate within the electrolyte.¹⁰⁰

Furthermore, because of the weaker Lewis acidity of Na^+ and K^+ compared to that of Li^+ , the interactions between the ions and coordinating water molecules are significantly weaker in aqueous Na and K electrolytes. Numerous experimental^{101,105–112} and computer simulation^{107,113–116} studies have demonstrated that the bond distance between water and a hydrated alkali ion is greater for Na^+ and K^+ , indicating that the solution viscosity and energy barrier for desolvation from the water molecules would be lower in aqueous Na and K electrolytes. All the physicochemical indicators related to hydrated ions, as discussed above, suggest that the ionic conductivity in aqueous electrolytes increases in the order $\text{K}^+ > \text{Na}^+ > \text{Li}^+$.^{25,117,118}

On the other hand, the ionic radii of Na^+ (1.02–1.07 Å) and K^+ (1.38–1.46 Å), determined by Shannon¹⁰² and in research using large angle X-ray scattering and double difference infrared spectroscopy,¹⁰¹ are larger than that of Li^+ (0.60–0.79 Å), suggesting that the diffusion of Na^+ and K^+ into the bulk structure of the cathode and anode active materials tends to be relatively challenging compared to that of Li^+ . Therefore, developing active materials that facilitate rapid ion diffusion into the bulk structures is essential for the advancement of aqueous Na- and K-ion batteries.

Consequently, leveraging the advantages of Na^+ and K^+ as battery carrier ions would offer a competitive edge for aqueous Na- and K-ion batteries, compared to aqueous Li-ion batteries,



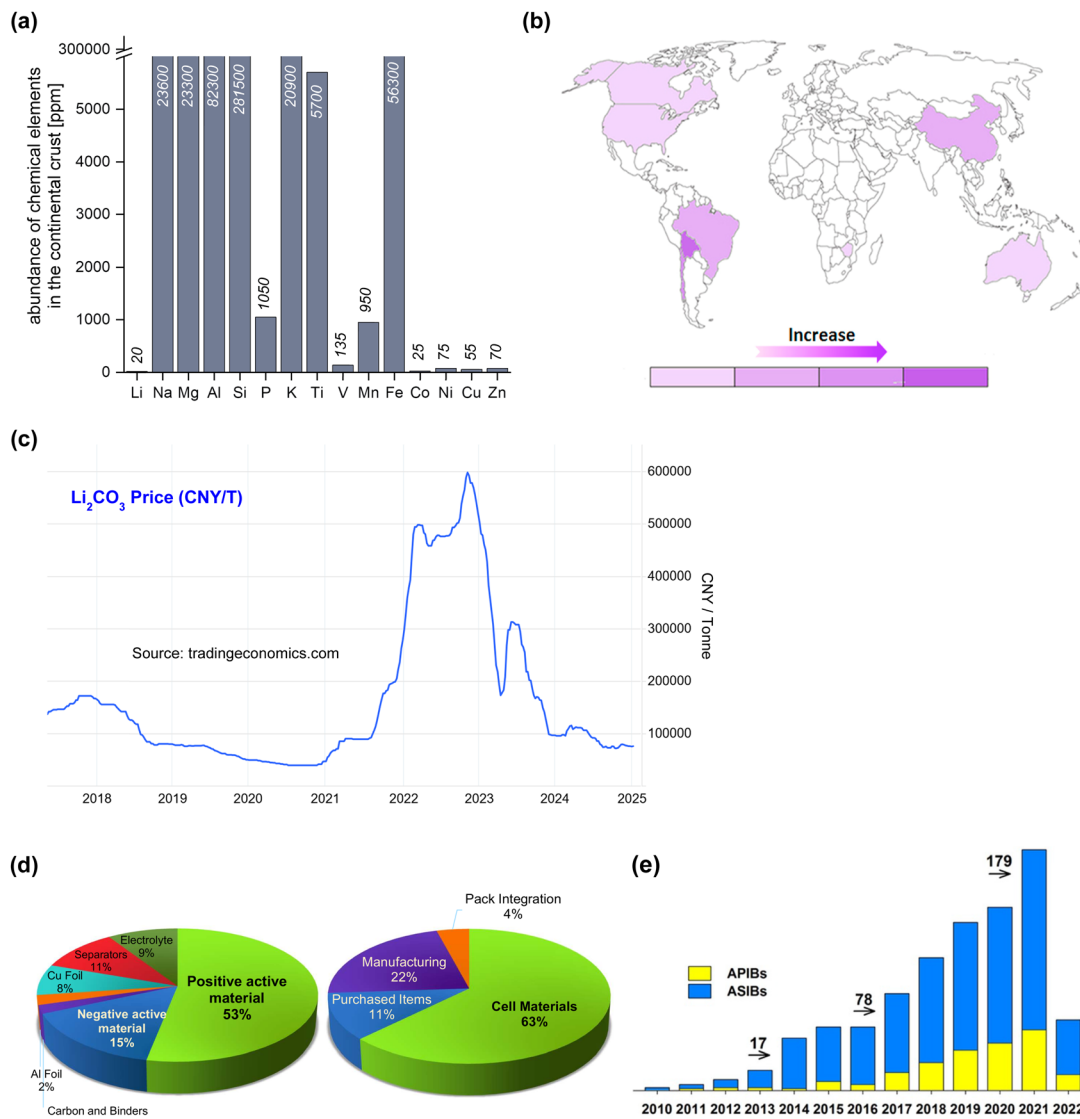


Fig. 8 (a) Elemental abundance in Earth's crust,⁹² (b) distribution of Li resources on Earth,⁹⁶ (c) evolution of the price of Li per metric ton of Li_2CO_3 equivalent units,⁹⁷ (d) the estimated cost percentage of Li-ion electric vehicle battery components,⁹⁸ (e) number of papers published on aqueous Na- and K-ion batteries.⁹⁹ Reprinted with permission from *Energy Storage Materials* (b) and *Journal of Physics: Energy* (e).

Table 2 Physicochemical properties of various carrier ions (Li^+ , Na^+ , and K^+)^{100–104}

	Li^+	Na^+	K^+
Stokes radius in water (Å)	2.38	1.84	1.25
Bond distance between $\text{H}_2\text{O}(\text{O})$ -hydrated M^+ ion (Å)	1.90–2.17 (four coordination)	2.34–2.50 (four–eight coordination)	2.65–2.97 (five–eight coordination)
Shannon's ionic radius (Å)	0.76	1.02	1.38
LAXS&DDIR-based ionic radius (Å)	0.60 (four coordination) 0.79 (six coordination)	1.02 (five coordination) 1.07 (six coordination)	1.38 (six coordination) 1.46 (seven coordination)

in terms of resource strategy, cost reduction, sustainability, and high-power-density applications.

The battery performance of various aqueous Na- and K-ion full cells fabricated using diverse electrolytes and electrodes is summarized in Tables 3 and 4. In 2013, Qian and Yang's groups tested a 1.3 V aqueous Na-ion full cell composed of a

$\text{Na}_2\text{Ni}[\text{Fe}(\text{CN})_6]$ cathode, $\text{NaTi}_2(\text{PO}_4)_3$ anode, and 1 M $\text{Na}_2\text{SO}_4/\text{H}_2\text{O}$ electrolyte.¹¹⁹ This battery maintained 88% of its initial capacity after 250 cycles at 5C, indicating its feasibility as an aqueous Na-ion battery (Fig. 9). Subsequently, in 2018 and 2019, the groups led by Okada and Hu successfully developed 1.7 V aqueous Na-ion batteries utilizing highly salt-concentrated aqueous sodium

Table 3 Performance data of Na-ion full cells fabricated using aqueous electrolytes

Year	Electrolyte	Cathode	Cathode			Full cell			Capacity (mA h g ⁻¹) calculation based on (—)			Cycle number Retention ratio (%)	
			L/L (mg cm ⁻²)	Anode	(mg cm ⁻²)	Anode	L/L cutoff (V/V)	average (V)	P/N ratio	C-rate	Anode		
2013	1 M Na ₂ SO ₄ /H ₂ O ¹²³	Na ₂ Ni[Fe(CN)] ₆	10	NaTi ₂ (PO ₄) ₃	5	1.6/0.2	1.2	2.0 (mass) 5C	90	Anode	250	88	
2014	1 M Na ₂ SO ₄ /H ₂ O ¹²⁴	Na _{0.44} Mn _{0.2}	—	Na ₂ V _{0.16} ·nH ₂ O	—	1.6/0.4	0.8	—	30	Cathode + anode	30	80	
2014	0.5 M Na ₂ SO ₄ /H ₂ O ¹²⁵	Na _{0.35} Mn _{0.2}	—	Polypprole coated MoO ₃	3	1.7/0.0	1.0	1.0 (mass) 550 mA g ⁻¹	24	Anode	1000	79	
2014	1 M Na ₂ SO ₄ /H ₂ O ¹²⁶	K _{0.27} MnO ₂	—	NaTi ₂ (PO ₄) ₃	—	1.8/0.0	0.8	—	200 mA g ⁻¹	62	—	—	
2014	5 M NaNO ₃ /H ₂ O ¹²⁷	NaVPO ₄ F	—	Polyimide	—	1.8/0.0	1.1	3.1 (mass) 50 mA g ⁻¹	40	Cathode + anode	20	75	
2014	10 m NaClO ₄ + Mn(ClO ₄) ₂ /H ₂ O ¹²⁷	KCu[Fe(CN)] ₆	10	KMn[Cr(CN) ₆]	10	1.3/0.5	0.9	—	10C	23	Cathode + anode	1000	100
2014	1 M Na ₂ SO ₄ /H ₂ O ¹²⁸	CoCuHCF	—	Disodium naphthalenediimide	—	1.5/0.5	1.1	—	20C charge	34	Cathode	100	88
2015	1 M Na ₂ SO ₄ /H ₂ O ¹²⁹	(K _{0.4} Na _{0.6})·δ-MnO ₂	—	NaTi ₂ (PO ₄) ₃	—	1.8/0.0	0.9	—	200 mA g ⁻¹	68	Cathode + anode	200	87
2015	1 M Na ₂ SO ₄ /H ₂ O ¹³⁰	Na _{0.66} Mn _{0.66} Ti _{0.34} O ₂	3.9	NaTi ₂ (PO ₄) ₃ /C	2.5	1.7/0.3	1.2	1.5 (mass)	2C	—	—	300	88
2015	1 M Na ₂ SO ₄ /H ₂ O ¹³¹	NaFePO ₄	—	NaTi ₂ (PO ₄) ₃	—	1.3/0.4	0.6	—	1C	70	Cathode	20	76
2015	1 M Na ₂ SO ₄ /H ₂ O ¹³²	Na ₂ Co[Fe(CN)] ₆	—	NaTi ₂ (PO ₄) ₃	—	2.0/0.5	1.3	0.8 (mass)	5C	95	Cathode + anode	100	98
2016	1 M Na ₂ SO ₄ /H ₂ O ¹³³	K _{0.27} MnO ₂	1.2	NaTi ₂ (PO ₄) ₃	1.2	1.6/0.0	0.7	—	200 mA g ⁻¹	81	—	100	83
2016	1 M Na ₂ SO ₄ /H ₂ O ¹³⁴	Na ₃ V ₂ (PO ₄) ₃	—	NaTi ₂ (PO ₄) ₃	—	1.6/0.5	1.2	0.9 (mass) 10 000 mA g ⁻¹	5.8	Cathode	50	50	
2016	1 M Na ₂ SO ₄ /H ₂ O ¹³⁵	Na ₃ MnTi(PO ₄) ₃	—	Na ₂ MnTi(PO ₄) ₃	—	1.8/0.4	1.4	1.0 (mass)	1C	57	—	100	98
2017	9.3 m NaOtf/H ₂ O ¹³⁶	Na _{0.66} Mn _{0.66} Ti _{0.34} O ₂	—	NaTi ₂ (PO ₄) ₃	—	1.7/0.2	1.0	2.0 (mass)	1C	25	Cathode + anode	1200	93
2017	17 m NaClO ₄ /H ₂ O ¹³⁷	Na ₂ Mn[Fe(CN)] ₆ ·2H ₂ O	—	NaTi ₂ (PO ₄) ₃	—	1.3/0.0	0.8	—	2 mA cm ⁻²	117	Cathode	50	81
2017	1 M NaNO ₃ /H ₂ O ¹³⁸	Fe[Fe(CN)] ₆	—	Fe[Fe(CN)] ₆	—	1.8/0.2	0.8	2.0 (mass)	2C	41	Cathode + anode	200	97
2018	1 M Na ₂ SO ₄ /H ₂ O ¹³⁹	Na _{0.44} MnO ₂	—	FePO ₄ ·2H ₂ O	—	1.2/0.0	0.6	2.4 (mass)	3C	70	Anode	300	87
2018	1 M Na ₂ SO ₄ /H ₂ O ¹⁴⁰	Na ₂ V ₁₁ PO ₄ ₃	—	Na ₂ V ₁₁ PO ₄ ₃	—	1.5/0.2	1.1	1.1 (mass)	10C	41	Cathode	1000	70
2018	1 M Na ₂ SO ₄ + Mn ₃ O ₄	Mn ₃ O ₄	—	NaTi ₂ (PO ₄) ₃	—	1.85/0.4	1.2	—	1C	103	Cathode	200	100
2018	8 m NaOAc + 2 M MgSO ₄ /H ₂ O ¹⁴¹	Na ₂ Mn[Fe(CN)] ₆	2.3	NaTi ₂ (PO ₄) ₃ /C	1.9	1.5/0.5	0.9	1.2 (mass) 100 mA g ⁻¹	57	Anode	85	65	
2018	32 m KOAc/H ₂ O ¹⁴²	Na ₂ Mn[Fe(CN)] ₆	—	Na ₂ V ₁₁ PO ₄ ₃ /C	—	1.5/0.5	1.1	1.0 (mass) 20C	25	Cathode + anode	1000	100	
2018	9.2 m NaOtf/H ₂ O ¹⁴³	Na ₂ V ₁₁ PO ₄ ₃	—	Na ₂ V ₁₁ PO ₄ ₃ /C	—	2.0/0.0	1.2	2.0 (mass)	1C	84	Anode	500	87
2018	1 M Na ₂ SO ₄ /H ₂ O ¹⁴⁴	Na ₄ [Fe(CN)] ₆	—	KMn[Cr(CN) ₆]	16	2.6/0.5	1.7	0.5 (mass)	5C	35	Cathode + anode	100	55
2018	17 m NaClO ₄ /H ₂ O ¹⁴⁵	Na ₂ Mn[Fe(CN)] ₆	8	Na _{0.27} MnO ₂	0.9	2.5/0.0	1.1	4.0 (mass)	23C	88	Cathode + anode	5000	100
2019	1 M Na ₂ SO ₄ /H ₂ O ¹⁴⁶	MnO ₂ /carbon nanotube ~5	—	NaTi ₂ (PO ₄) ₃	~5	1.8/0.4	1.0	0.9 (mass)	4C	83	Cathode	1000	72
2019	1 M Na ₂ SO ₄ + 2 M MgSO ₄ /H ₂ O ¹⁴⁷	Na _{0.66} Mn _{0.66} Ti _{0.34} O ₂	13	Na _{1.5} Ti _{1.5} Fe _{0.5} (PO ₄) ₃ /C	6.8	1.6/0.0	1.1	1.0 (mass) 2C	104	Anode	300	100	
2019	17 m NaClO ₄ /H ₂ O ¹⁴⁹	Na ₃ V ₂ (PO ₄) ₃ /carbon nanotube	—	NaTi ₂ (PO ₄) ₃ /carbon nanotube	—	2.1/0.6	1.5	—	1C	75	Cathode	20	74
2019	1.5 M Na ₂ SO ₄ /H ₂ O ¹⁵⁰	NaFePO ₄	2-3	Dissolved Na ₂ S ₂	—	1.0/0.0	0.6	—	1C	120	Cathode	200	38
2019	17 m NaClO ₄ /H ₂ O ¹⁵¹	Na ₂ FePO ₄ F	—	NaTi ₂ (PO ₄) ₃	—	1.8/0.0	0.7	1.0 (mass) 1 mA cm ⁻²	85	Cathode	100	64	
2019	2 M NaClO ₄ /H ₂ O ¹⁵²	Nano Ni(OH) ₂	—	NaTi ₂ (PO ₄) ₃ /C	1-3	1.4/0.2	1.3	1.2 (mass) 10C (50 °C)	100	Anode	500	83	
2019	17 m NaClO ₄ /H ₂ O ¹⁴⁹	Na ₃ V ₂ (PO ₄) ₃ /carbon nanotube	—	Na _{1.5} Ti _{1.5} Fe _{0.5} (PO ₄) ₃ /C	6.8	1.6/0.0	1.1	1.0 (mass) 2C	104	Anode	300	100	
2019	1.5 M Na ₂ SO ₄ /H ₂ O ¹⁵³	Na ₂ Mn[Fe(CN)] ₆	—	Na ₃ Fe ₂ (PO ₄) ₃	—	1.5/0.0	0.9	1.0 (mass) 5C	31	Cathode + anode	700	75	
2019	Sat. NaNO ₃ /H ₂ O ¹⁵⁴	FeHCF	2-3	CuHCF	—	1.5/0.0	0.7	0.8 (mass) 5C	50	Cathode + anode	250	96	
2019	15 m NaClO ₄ /H ₂ O ¹⁵⁵	TiS ₂	15	Na _x Mn _y [Fe(CN) ₆] _z	15	2.6/0.8	1.7	1.0 (mass) 1C (30 °C)	40	Cathode + anode	150	90	
2019	25 m NaFSI + 10 m NaFTFSI/H ₂ O ⁸⁹	Na ₃ (VOPO ₄) ₂ F	4-6	NaTi ₂ (PO ₄) ₃	—	2.2/0.3	1.4	1.1-1.2 (mass) 10C (25 °C)	80	Cathode	500	77	
2019	Na _{1.88} Mn-[Fe(CN) ₆] _{0.97} ·1.35H ₂ O	—	—	NaTiOPO ₄	—	2.6/0.6	1.7	0.5 (mass) 0.25C (2C)	41 (0.25C)	Cathode + anode	200	90	



Table 3 (continued)

Year	Electrolyte	Cathode	Cathode L/L (mg cm ⁻²)	Anode L/L (mg cm ⁻²)	Full cell			Capacity (mA h g ⁻¹) calculation based (-)	Cycle number Retention ratio (%)
					Full cell cutoff (V/V)	Full cell average (V)	P/N ratio		
2021	9 m NaOTf + 22 m tetraethylammonium- OTf/H ₂ O ¹²¹	Na ₃ V ₂ (PO ₄) ₃	3	Na ₃ V ₂ (PO ₄) ₃	5	1.9/0.8	1.7	1.2 (capacity)	40
2021	17 m NaClO ₄ + 2 m NaOTf/H ₂ O ¹⁵⁶	Na ₃ V ₂ (PO ₄) ₃	—	Na ₂ V ₂ (PO ₄) ₃	—	2.0/0.0	1.2	2.0 (mass) 0.8 (mass) 0.5 (mass)	32
2021	26 m NaTFA/H ₂ O ¹⁵⁷	Na ₂ V ₂ (PO ₄) ₃	—	NaTi ₂ (PO ₄) ₃	2–5	2.2/0.5	1.4	1C (P/N 0.8) 1C (P/N 0.5)	85
2021	25 m NaFSI + 10 m NaTFSI/H ₂ O ¹⁵⁸	Na ₃ (VPO ₄) ₂ F	—	—	—	—	—	1C (P/N 0.5)	250
2023	1 M Na ₂ SO ₄ /H ₂ O ¹⁵⁹	Na ₃ V _{1.3} Fe _{0.5} W _{0.2} (PO ₄) ₃	—	NaTi ₂ (PO ₄) ₃	—	1.6/0.0	1.2	0.7 (mass) 1000 mA g ⁻¹	64

electrolytes (Fig. 9).^{120,121} These included a Na₂Mn[Fe(CN)₆][KMn-Cr(CN)₆] battery with a 17 m NaClO₄/H₂O electrolyte, achieving 55% capacity retention after 100 cycles at 5C, and a Na_{1.88}Mn[Fe(CN)₆]_{0.97}·1.35H₂O|NaTiOPO₄ battery with 9 m NaOTf (NaSO₃CF₃) and 22 m tetraethylammonium-OTf/H₂O electrolytes, retaining 90% of its initial capacity after 200 cycles at 0.25C. In 2020, Li *et al.* reported a 1.3 V aqueous K-ion battery (Fig. 9).¹²² This battery was fabricated with a K_{1.85}Fe_{0.33}Mn_{0.67}[Fe(CN)₆]_{0.98}·0.77H₂O cathode, 3,4,9,10-perylenetetracarboxylic diimide (PTCDI) anode, and 22 m KOTf/H₂O electrolyte, and exhibited 73% capacity retention after 2000 cycles at 4C.

Nevertheless, the output voltage and cycling stability of aqueous Na- and K-ion batteries are even lower than those of the aqueous Li-ion systems. The weaker Lewis acidity and larger ionic radii of Na⁺ and K⁺ compared to those of Li⁺ pose challenges in widening the operating potential window of aqueous Na and K electrolytes and limit the development of suitable cathode and anode active materials (details are discussed in Sections 4.1, 5.2, and 5.3).

4. Outstanding challenges with advanced aqueous electrolytes

The critical issues with aqueous rechargeable batteries, such as the low output voltage, high P/N ratio, inferior cycling stability, and poor Coulombic efficiency even at room temperature, largely stem from the inherent limitations of aqueous electrolytes. To increase the battery output voltage and achieve stable cycling characteristics, it is imperative to suppress the continuous oxidation- and reduction-driven decomposition of the electrolyte at the cathode and anode surfaces. A conventional method to enhance the electrochemical stability of rechargeable aqueous batteries involves adjusting the pH of the electrolyte to optimize the operating potential window with the electrode reaction potentials (Fig. 10).

For instance, when aqueous Li-ion batteries were initially developed in 1994, an alkaline solution comprising 5 M LiNO₃ and 0.001 M LiOH/H₂O was employed to ensure the stable cycling of the VO₂(B) anode (Table 1 and Fig. 3).¹⁷ On the other hand, an acidic, highly salt-concentrated electrolyte was utilized to enhance the cycling performance of the high-potential LiNi_{0.5}Mn_{1.5}O₄ cathode (Table 1). However, this approach was not fundamentally effective for expanding the operating potential window of the electrolyte, as it was limited by the relatively low chemical stability of most candidate cathode and anode active materials and cell components in low- or high-pH environments.

When highly salt-concentrated aqueous electrolytes were introduced in 2015 and 2016, the elimination of free water molecules and water clusters was emphasized, which contributed to the widening of the operating potential window and thereby enhanced the battery energy density and cycling performance. The experimentally estimated operating potential windows of recently developed aqueous Li-, Na-, and K-ion electrolytes are summarized in Tables 5–7. For instance, compared to a 1.2 mol LiTFSI/H₂O electrolyte, a 21 m LiTFSI/H₂O



Table 4 Performance data of K-ion full cells fabricated using aqueous electrolytes

Year	Electrolyte	Cathode	Anode	Full cell average	P/N ratio	C-rate	Capacity (mA h g ⁻¹)	Capacity calculation based	Cycle number	Retention ratio (%)		
2016	3 M KCl/H ₂ O ¹⁶⁰	K _{0.22} V _{1.74} O _{4.37} ·0.82H ₂ O	1.6	K _{0.22} V _{1.74} O _{4.37} ·0.82H ₂ O	1.6	0.6/-0.6	0.0	1.0 (mass) 2000 mA g ⁻¹	62 (2000 mA g ⁻¹)	Cathode + anode	5000 96	
2019	22 m KOTf/H ₂ O ¹²²	K _{1.85} Fe _{0.33} Mn _{0.67} [Fe(CN) ₆] _{0.98} ·0.77H ₂ O	5.8	3,4,9,10-Perylene tetracarboxylic dimide	5.2	2.6/0.0	1.3	1.1-1.4 (mass)	20 000 mA g ⁻¹	42 (20000 mA g ⁻¹)	Cathode + anode	5000 100
2020	3 M KCl/H ₂ O ¹⁶¹	Fe ₄ [Fe(CN) ₆] ₃ ·3·4H ₂ O	—	Fe ₄ [Fe(CN) ₆] ₃ ·3·4H ₂ O	—	0.9/0.3	0.6	2.0 (mass)	—	Cathode + anode	2000 73	
2020	Sat. 3.75 m KNO ₃ /H ₂ O ¹⁶²	Fe[Fe(CN) ₆] ₁	8.5	1,4,5,8-Naphthalene tetracarboxylic dianhydride-derived polyimide	5.5	2.0/0.0	0.7	1.5 (mass) 2C	—	Cathode + anode	—	
2020	21 m KOTf/H ₂ O ¹⁶³	K _{1.93} Fe[Fe(CN) ₆] _{0.97} ·1.82H ₂ O	6.5	KTi ₂ (PO ₄) ₃ /C	6.5	2.3/0.0	1.5	1.0 (mass) 200 mA g ⁻¹	73 (200 mA g ⁻¹)	Cathode + anode	1000 99	
2020	21 m KFSI/H ₂ O ¹⁶⁴	Polytriphenylamine	—	3,4,9,10-Perylene tetracarboxylic dimide	—	1.6/0.0	0.7	1.0 (mass) 500 mA g ⁻¹	500 mA g ⁻¹	44 (5000 mA g ⁻¹)	Cathode + anode	30 000 100
2020	30 m KFSI/H ₂ O ¹⁶⁵	K ₂ Fe ₃ [Fe(CN) ₆] ₂	1	Perylene-3,4,9,10-tetracarboxylic dianhydride	1	2.0/0.0	1.0	1.0 (mass) 12.5C (2000 mA g ⁻¹)	48	Cathode + anode	900 95	
2021	22 m KOTf/H ₂ O ¹⁶⁶	δ-K _{0.5} V ₂ O ₅	—	3,4,9,10-Perylene tetracarboxylic dimide	—	1.75/0.0	0.9	1.0 (mass) 10C	85	Cathode + anode	1000 89	
2022	55 m K(FSI) _{0.6} ·(OTf) _{0.4} ·1.0H ₂ O ¹⁶⁷	K ₂ Fe _{0.5} Mn _{0.5} Fe(CN) ₆	0.5	3,4,9,10-Perylene tetracarboxylic dimide	0.65	2.3/0.0	1.4	0.8 (mass) 1C (156 mA g ⁻¹)	100	Cathode + anode	200 86	
2022	21 m KOTf + 0.01-0.2 m Fe(OTf) ₃ /H ₂ O ¹⁶⁸	K _{1.82} Mn[Fe(CN) ₆] _{0.96} ·0.47H ₂ O	3.5	3,4,9,10-Perylene tetracarboxylic dimide	3.5	2.2/0.0	1.3	—	1500 mA g ⁻¹	58	Cathode + anode	1500 82

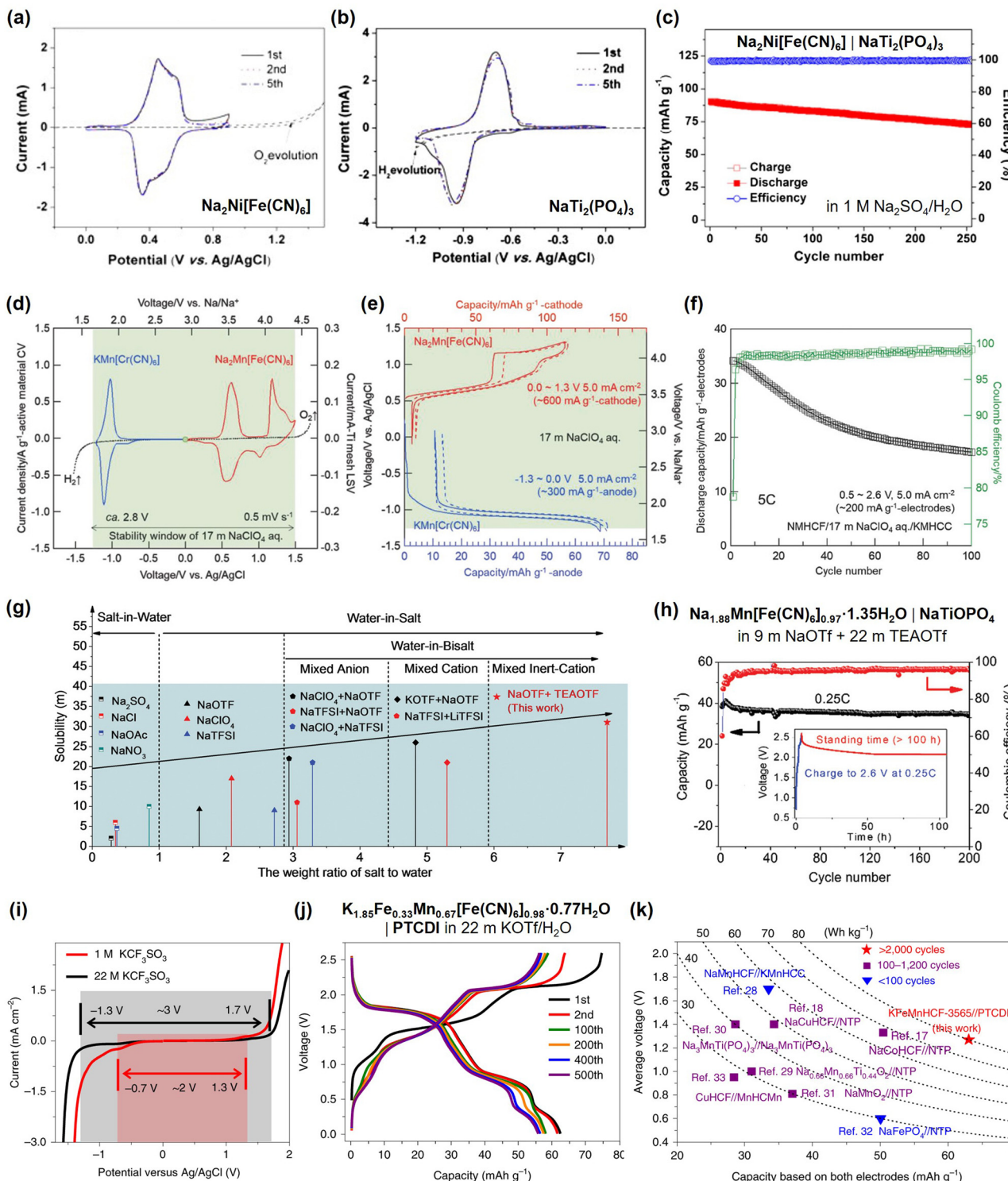


Fig. 9 (a)–(c) Reversible cycling of the $\text{Na}_2\text{Ni}[\text{Fe}(\text{CN})_6]$ cathode, $\text{NaTi}_2(\text{PO}_4)_3$ anode, and their full cell in 1 M $\text{Na}_2\text{SO}_4/\text{H}_2\text{O}$.¹¹⁹ (d)–(f) Electrochemical performance of aqueous $\text{Na}_2\text{Mn}[\text{Fe}(\text{CN})_6]||\text{KMn}[\text{Cr}(\text{CN})_6]$ full cell in 17 m $\text{NaClO}_4/\text{H}_2\text{O}$.¹²⁰ (g) and (h) Diagram representing a highly salt-concentrated aqueous electrolyte of 9 m NaOTf and 22 m tetraethylammonium-OTf/ H_2O , and the cycling stability of the aqueous $\text{Na}_{1.88}\text{Mn}[\text{Fe}(\text{CN})_6]_{0.97}\cdot1.35\text{H}_2\text{O}||\text{NaTiOPO}_4$ full cell in this electrolyte.¹²¹ (i)–(k) Broadened operating potential window in 22 m $\text{KOTf}/\text{H}_2\text{O}$, contributing to the stable cycling of a 1.3 V aqueous K-ion battery, $\text{K}_{1.85}\text{Fe}_{0.33}\text{Mn}_{0.67}[\text{Fe}(\text{CN})_6]_{0.98}\cdot0.77\text{H}_2\text{O}||\text{PTCDI}$.¹²² Reprinted with permission from *Electrochemistry Communications* (a)–(c), *Small Methods* (d)–(f), *Advanced Materials* (g) and (h), and *Nature Energy* (i)–(k).

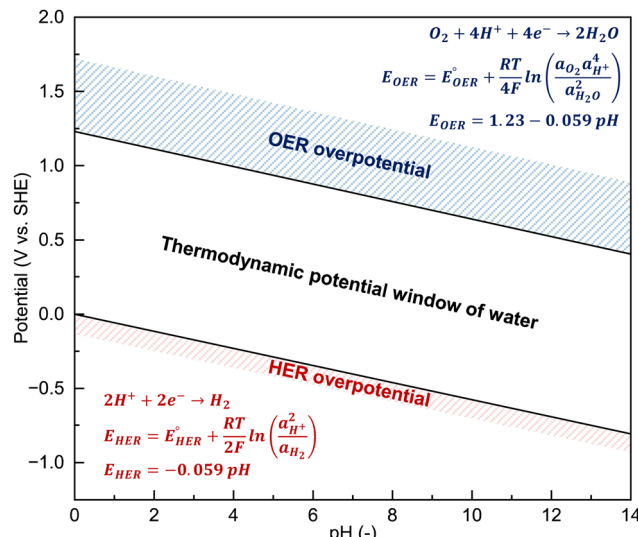


Fig. 10 pH dependency of the potential window of pure water. Thermodynamic potentials of the HER (E_{HER}) and OER (E_{OER}) can be estimated using the Nernst equation under ideal conditions, with standard redox potentials of the HER ($E_{\text{HER}}^{\circ} = 0 \text{ V vs. SHE}$) and OER ($E_{\text{OER}}^{\circ} = 1.23 \text{ V vs. SHE}$) and the activities of water ($a_{\text{H}_2\text{O}} = 1$), hydrogen gas ($a_{\text{H}_2} = 1 \text{ bar}$), and oxygen gas ($a_{\text{O}_2} = 1 \text{ bar}$).

electrolyte significantly improved the anodic and cathodic stabilities on stainless steel (SUS) by over 0.3 V each.¹⁸ In a 56 m Li(PTFSI)_{0.6}(TFSI)_{0.4}·1H₂O electrolyte, the anodic stability on Pt increased by 0.6 V, while the cathodic stability on Al increased by over 1.5 V, allowing the Al–Li alloy reaction to proceed at 0.2–0.6 V vs. Li/Li⁺ in the aqueous system.⁸⁵ Similar beneficial effects were observed in highly salt-concentrated aqueous Na- and K-ion electrolytes. The anodic and cathodic stabilities on Pt in 35 m NaFSI/H₂O improved by over 0.5 and 0.2 V, respectively, compared to those on 1.2 m NaTFSI/H₂O.¹⁶⁹ The use of a 62 m K(FSI)_{0.55}(OTf)_{0.45}·0.9H₂O electrolyte increased the anodic stability on Pt by 0.4–0.8 V compared to that of diluted aqueous electrolytes such as 1.0 m KOAc (KCH₃COO)/H₂O, 1.0 m KFSI (KN(SO₂F)₂)/H₂O, and 1.3 m KTFSI/H₂O, while the cathodic stability on Al increased by 0.3–1.3 V.^{167,170}

However, most studies have approximately estimated the operating potential window of aqueous electrolytes using potentiostatic methods such as linear sweep voltammetry (LSV). The stability of the electrolyte depends on various factors, including the type of electrodes and the test conditions (e.g., scan rate and cut-off current density). Kühnel *et al.* estimated the potential window of aqueous electrolytes using LSV at 0.1 mV s⁻¹ and noted significant variations depending on the types of substrates and cut-off current conditions (Fig. 11).¹⁷¹ For instance, the potential window of 21 m LiTFSI/H₂O exceeded 3.5 V when substrates like Al and Ti were combined, offering high overpotentials toward water hydrolysis and a high cut-off current density of 250 μA cm⁻². However, the potential window was less than 1.0 V with substrates like Pt, which has a low overpotential and a small cut-off current density of 2 μA cm⁻². Moreover, the surface areas of active materials and carbon additives are typically ten to thousand times larger than those of Al or Ti

electrodes, and such materials exhibit much stronger catalytic effects on water electrolysis.^{19,21,91,191} Generally, batteries operate in the galvanostatic mode and are often stored in a charged state for extended periods, subjecting them to harsher conditions compared to those in the potentiostatic mode. Consequently, despite the wide estimated operating potential window of highly salt-concentrated aqueous electrolytes, which ranges from 3 to 5 V as determined by LSV, aqueous rechargeable batteries exhibit significantly lower output voltages and poorer cycling stabilities.

This discrepancy indicates that the fundamental issues with aqueous electrolytes and battery systems must be carefully examined under appropriate experimental conditions.

4.1. Thermodynamic and kinetic limitations in expanding the operating potential window

A comprehensive understanding of the science behind the operating potential window is paramount. The thermodynamic potential window of pure water is only 1.23 V; surpassing this range typically leads to the oxygen evolution reaction (OER) at the cathode and the HER at the anode surfaces, disrupting the role of the electrolyte as a mediator for carrier ion transport. In dilute solutions, carrier ions and anions are surrounded by multiple water molecules, forming solvent-separated ion-pair structures. Concurrently, the water molecules tend to form clusters through hydrogen-bonded networks.

As the salt concentration increases, a distinct solution structure is generated. In this structure, the carrier ions intricately coordinate with anions and water molecules, altering the electron state of anions and water molecules and disrupting the formation of hydrogen bonds between the water molecules. Importantly, differences in the Lewis acidity of the carrier ions (Li⁺, Na⁺, and K⁺) significantly influence the thermodynamic and kinetic factors related to the operating potential windows of aqueous electrolytes, as discussed later.

In highly salt-concentrated electrolytes, the robust coordination between the strong Lewis acid Li⁺ and water molecules serves as a potent force in disrupting the hydrogen bonds among water molecules. For instance, in 56 m Li(PTFSI)_{0.6}(TFSI)_{0.4}·1H₂O, water clusters almost disappear, and only hydrated water molecules coordinated to Li⁺ remain.⁸⁵ This was evidenced by the disappearance of the O–H stretching vibration peaks of free water molecules (2900–3800 cm⁻¹), with only a sharp peak remaining at 3565 cm⁻¹ (Fig. 12). Density functional theory-based molecular dynamics (DFT-MD) calculations have further confirmed these observations in the solution structure (Fig. 12). These calculations indicated a decrease in the water activity and the existence of strong interactions between water molecules and Li⁺, contributing to an increased oxidation potential of water and thermodynamically improved anodic stability in the electrolyte.

However, while the anodic stability improves, the reduction potential of water also increases. The strong interaction between Li⁺ and H₂O facilitates the release of H⁺ from H₂O.^{192,193} Consequently, as the concentration of the Li salt in the solution increases, the activity of H⁺ increases (resulting in a decrease in pH), and the thermodynamic HER potential is upshifted (Fig. 13). The detailed implications of these shifts in the




Table 5 Physicochemical properties and electrochemical stabilities of aqueous Li electrolytes. The data were calibrated with an Ag/AgCl (sat. KCl) reference electrode

Year	Electrolyte	pH	Ionic viscosity (mPa s)	Ionic conductivity (mS cm ⁻¹)	Reduction stability				Oxidation stability						
					V vs. Ag/AgCl				V vs. Ag/AgCl						
					LSV scan rate, mV s ⁻¹		LSV cut-off condition, μm cm ⁻²		LSV scan rate, mV s ⁻¹		LSV cut-off condition, μm cm ⁻²				
Year	Electrolyte	pH	(mPa s)	(mS cm ⁻¹)	Pt	Al	Au	Ti	SUS	Pt	Al	Au	Ti	SUS	Carbon
2015	21 m LiTFSI/ H ₂ O ^{18,174}	6	51	10	-0.7 V 0.1 mV s ⁻¹ 20 μm cm ⁻²	-1.5 V 1 mV s ⁻¹ 15 μm cm ⁻²	-0.5 V 10 mV s ⁻¹ 50 μm cm ⁻²	1.35 V 0.1 mV s ⁻¹ 20 μm cm ⁻²	-1.34 V 10 mV s ⁻¹ 180 μm cm ⁻²	1.6 V 1 mV s ⁻¹ 15 μm cm ⁻²	2.1 V 10 mV s ⁻¹ 50 μm cm ⁻²	1.7 V 10 mV s ⁻¹ 50 μm cm ⁻²	>2.0 V 0.1 mV s ⁻¹ 20 μm cm ⁻²	1.66 V 10 mV s ⁻¹ 180 μm cm ⁻²	>2.0 V 0.1 mV s ⁻¹ 20 μm cm ⁻²
2016	1.2 m LiTFSI/ H ₂ O ^{19,174}	8	1.5	42	-0.89 V 0.1 mV s ⁻¹ 10 μm cm ⁻²	-1.46 V 0.1 mV s ⁻¹ 10 μm cm ⁻²	-0.89 V 0.1 mV s ⁻¹ 10 μm cm ⁻²	-1.19 V 0.1 mV s ⁻¹ 10 μm cm ⁻²	-1.0 V 0.1 mV s ⁻¹ 10 μm cm ⁻²	-1.21 V 0.1 mV s ⁻¹ 10 μm cm ⁻²	-1.0 V 0.1 mV s ⁻¹ 10 μm cm ⁻²	>2.5 V 0.1 mV s ⁻¹ 10 μm cm ⁻²	1.3 V 0.1 mV s ⁻¹ 10 μm cm ⁻²	>2.5 V 0.1 mV s ⁻¹ 10 μm cm ⁻²	
	Li(TFSI) _{0.7} (BETI) _{0.3} · 2H ₂ O ¹⁹	—	203	3	-0.89 V 0.1 mV s ⁻¹ 10 μm cm ⁻²	-2.0 V 0.1 mV s ⁻¹ 10 μm cm ⁻²	-0.89 V 0.1 mV s ⁻¹ 10 μm cm ⁻²	-1.3 V 0.1 mV s ⁻¹ 10 μm cm ⁻²	-1.2 V 0.1 mV s ⁻¹ 10 μm cm ⁻²	1.81 V 0.1 mV s ⁻¹ 10 μm cm ⁻²	1.81 V 0.1 mV s ⁻¹ 10 μm cm ⁻²	2.0 V 0.1 mV s ⁻¹ 20 μm cm ⁻²	>2.5 V 0.1 mV s ⁻¹ 20 μm cm ⁻²	1.81 V 0.1 mV s ⁻¹ 20 μm cm ⁻²	
2016	21 m LiTFSI + 7 m LiOH/H ₂ O ^{7,175}	—	—	6.5	—	—	-1.74 V 1 mV s ⁻¹ 2 μm cm ⁻²	—	-1.41 V 1 mV s ⁻¹ 4000 μm cm ⁻²	—	-1.41 V 10 mV s ⁻¹ 4000 μm cm ⁻²	—	1.66 V 10 mV s ⁻¹ 4000 μm cm ⁻²	0.86 V 1 mV s ⁻¹ 2 μm cm ⁻²	
2018	1 m LiNO ₃ / H ₂ O ^{17,177}	7	1	71	—	-0.89 V 10 mV s ⁻¹ 10 μm cm ⁻²	—	—	-0.89 V 10 mV s ⁻¹ 10 μm cm ⁻²	—	1.31 V 10 mV s ⁻¹ 10 μm cm ⁻²	—	1.75 V 0.1 mV s ⁻¹ 500 μm cm ⁻²		
25	m LiNO ₃ / H ₂ O ^{17,177}	3.6	—	0.74	—	—	—	—	—	—	—	—	—	1.75 V 0.1 mV s ⁻¹ 500 μm cm ⁻²	
	Sat. LiNO ₃ /H ₂ O (1/2.5, n/n) ^{17,177}	—	—	—	—	-0.89 V 10 mV s ⁻¹ 10 μm cm ⁻²	—	—	-0.85 V 0.1 mV s ⁻¹ 500 μm cm ⁻²	—	—	—	—	1.66 V 10 mV s ⁻¹ 10 μm cm ⁻²	
2018	21 m LiTFSI/H ₂ O + 3 mol% Mg(TFSI) ₂ ¹⁷⁸	82	9	—	—	—	—	—	—	—	—	—	—	1.66 V 10 mV s ⁻¹ 10 μm cm ⁻²	
	21 m LiTFSI/H ₂ O + 5 mol% Ca(TFSI) ₂ ¹⁷⁸	90	6	—	—	—	—	—	—	—	—	—	—	1.66 V 10 mV s ⁻¹ 15 μm cm ⁻²	
2018	8 m LiOAc + 32 m KOAc/H ₂ O ¹⁷⁹	—	374	5	—	-1.3 V 0.2 mV s ⁻¹ 100 μm cm ⁻²	—	—	-1.3 V 0.2 mV s ⁻¹ 100 μm cm ⁻²	—	—	—	—	1.4 V 0.2 mV s ⁻¹ 100 μm cm ⁻²	
2019	Li(PTFSI) _{0.6} (TFSI) _{0.4} · H ₂ O ⁹¹	—	8555	0.1	—	-0.89 V 0.1 mV s ⁻¹ 10 μm cm ⁻²	—	-0.89 V 0.1 mV s ⁻¹ 10 μm cm ⁻²	-3.0 V 0.1 mV s ⁻¹ 10 μm cm ⁻²	—	—	—	—	>2.8 V 0.1 mV s ⁻¹ 10 μm cm ⁻²	

Table 6 Physicochemical properties and electrochemical stabilities of aqueous Na electrolytes. The data were calibrated with an Ag/AgCl (sat. KCl) reference electrode

Year	Electrolyte	pH (mPa s)	Ionic viscosity conductivity (mS cm ⁻¹)	Reduction stability			Oxidation stability		
				LSV scan rate, mV s ⁻¹		LSV cut-off condition, μm cm ⁻²		LSV scan rate, mV s ⁻¹	
				V vs. Ag/AgCl	V vs. Ag/AgCl	LSV cut-off condition, μm cm ⁻²	LSV cut-off condition, μm cm ⁻²	V vs. Ag/AgCl	V vs. Ag/AgCl
2017	8 m NaTFSI/H ₂ O ¹⁸⁰	—	80	48	—	—	—	—	—
2017	9 m NaOTf/H ₂ O ^{121,136}	—	—	50	-1.4 V 10 mV s ⁻¹ 100 μm cm ⁻²	-1.3 V 10 mV s ⁻¹ 100 μm cm ⁻²	-1.2 V 10 mV s ⁻¹ 100 μm cm ⁻²	1.3 V 10 mV s ⁻¹ 100 μm cm ⁻²	1.3 V 10 mV s ⁻¹ 100 μm cm ⁻²
2017	17 m NaClO ₄ / 2019 H ₂ O ^{137,181-183}	6	5	108	-0.9 V 0.1 mV s ⁻¹ 10 μm cm ⁻²	-1.1 V 1 mV s ⁻¹ 50 μm cm ⁻²	-1.21 V 10 mV s ⁻¹ 100 μm cm ⁻²	1.6 V 0.1 mV s ⁻¹ 50 μm cm ⁻²	1.59 V 10 mV s ⁻¹ 100 μm cm ⁻²
2018	8 m NaOAc + 32 m KOAc/H ₂ O ¹⁴²	11	—	12	-2.0 V 10 mV s ⁻¹ 50 μm cm ⁻²	-2.0 V 10 mV s ⁻¹ 50 μm cm ⁻²	-1.7 V 10 mV s ⁻¹ 50 μm cm ⁻²	>2.5 V 10 mV s ⁻¹ 50 μm cm ⁻²	>2.5 V 10 mV s ⁻¹ 50 μm cm ⁻²
2019	1.2 m (1 M) NaTFSI/H ₂ O ⁹⁰	6	1.5	43	-0.85 V 0.5 mV s ⁻¹ 20 μm cm ⁻²	-1.35 V 0.5 mV s ⁻¹ 20 μm cm ⁻²	-1.21 V 10 mV s ⁻¹ 20 μm cm ⁻²	1.15 V 0.5 mV s ⁻¹ 20 μm cm ⁻²	1.15 V 0.5 mV s ⁻¹ 20 μm cm ⁻²
18	m Na(PTFSI) _{0.65} ⁻ (TFSI) _{0.14} ^{0.21} (OTf) _{0.21} ⁺ 3H ₂ O ⁹⁰	6	47	14	-1.0 V 0.5 mV s ⁻¹ 20 μm cm ⁻²	-1.65 V 0.5 mV s ⁻¹ 20 μm cm ⁻²	-1.65 V 0.5 mV s ⁻¹ 20 μm cm ⁻²	1.7 V 0.5 mV s ⁻¹ 20 μm cm ⁻²	1.7 V 0.5 mV s ⁻¹ 20 μm cm ⁻²
2019	35 m NaTFSI/H ₂ O ^{89,169,184}	4	8	95	-1.1 V 0.1 mV s ⁻¹ 5 μm cm ⁻²	-0.9 V 0.1 mV s ⁻¹ 10 μm cm ⁻²	-0.9 V 0.1 mV s ⁻¹ 10 μm cm ⁻²	1.6 V 0.1 mV s ⁻¹ 5 μm cm ⁻²	1.8 V 0.1 mV s ⁻¹ 10 μm cm ⁻²
2019	30 m NaTFSI + 5 m NaFTFSI/H ₂ O ⁺ hydroxide solution ⁸⁹	5	83	13	-1.1 V 0.1 mV s ⁻¹	—	-1.3 V 0.1 mV s ⁻¹	—	1.7-1.8 V 0.1 mV s ⁻¹
2019	25 m NaTFSI + 10 m NaTFSI/H ₂ O ⁺ hydroxide solution	5	94	12	0.1 mV s ⁻¹	—	0.1 mV s ⁻¹	—	0.1 mV s ⁻¹
2020	9 m NaOTf + 22 m tetraethylammonium- OTf/H ₂ O ¹²¹	—	30	11	5 μm cm ⁻²	-1.7 V 10 mV s ⁻¹ 100 μm cm ⁻²	-1.4 V 10 mV s ⁻¹ 100 μm cm ⁻²	10 μm cm ⁻² 10 mV s ⁻¹ 100 μm cm ⁻²	1.6 V 10 mV s ⁻¹ 100 μm cm ⁻²
2021	26 m NaTFA/H ₂ O ⁻ (1/2,1, n/n) ₁₅₇	7	—	22	—	-1.8 V 0.5 mV s ⁻¹ 50 μm cm ⁻²	-1.15 V 0.5 mV s ⁻¹ 50 μm cm ⁻²	>2.0 V 0.5 mV s ⁻¹ 50 μm cm ⁻²	1.65 V 0.5 mV s ⁻¹ 50 μm cm ⁻²
2023	28 m Na(PTFSI) _{0.55} ⁻ (HTFSI) _{0.45} ⁺ 2H ₂ O ⁸⁵	6	293	3	-1.1 V 0.5 mV s ⁻¹ 20 μm cm ⁻²	-1.65 V 0.5 mV s ⁻¹ 20 μm cm ⁻²	-1.65 V 0.5 mV s ⁻¹ 20 μm cm ⁻²	1.7 V 0.5 mV s ⁻¹ 20 μm cm ⁻²	>2.0 V 0.5 mV s ⁻¹ 20 μm cm ⁻²


Table 7 Physicochemical properties and electrochemical stabilities of aqueous K electrolytes. The data were calibrated with an Ag/AgCl (sat. KCl) reference electrode

Year	Electrolyte	pH (mPa s)	Ionic viscosity conductivity (mS cm ⁻¹)	Reduction stability				Oxidation stability			
				V vs. Ag/AgCl (sat. KCl)		V vs. Ag/AgCl (sat. KCl)		LSV scan rate, mV s ⁻¹		LSV scan rate, mV s ⁻¹	
				LSV cut-off condition, $\mu\text{m cm}^{-2}$	LSV cut-off condition, $\mu\text{m cm}^{-2}$	LSV cut-off condition, $\mu\text{m cm}^{-2}$	LSV cut-off condition, $\mu\text{m cm}^{-2}$	LSV cut-off condition, $\mu\text{m cm}^{-2}$	LSV cut-off condition, $\mu\text{m cm}^{-2}$	LSV cut-off condition, $\mu\text{m cm}^{-2}$	LSV cut-off condition, $\mu\text{m cm}^{-2}$
2018	1 m (0.9 M) KOAc	7.8–1	48–61	-0.75 V 0.2 mV s ⁻¹ 100 $\mu\text{m cm}^{-2}$	-0.5 V 0.2 mV s ⁻¹ 100 $\mu\text{m cm}^{-2}$	-0.59 V 1 mV s ⁻¹ 100 $\mu\text{m cm}^{-2}$	0.8 V 0.2 mV s ⁻¹ 100 $\mu\text{m cm}^{-2}$	0.9 V 0.2 mV s ⁻¹ 100 $\mu\text{m cm}^{-2}$	0.64 V 1 mV s ⁻¹ 100 $\mu\text{m cm}^{-2}$	0.64 V 1 mV s ⁻¹ 100 $\mu\text{m cm}^{-2}$	0.64 V 1 mV s ⁻¹ 100 $\mu\text{m cm}^{-2}$
2020	$\text{H}_2\text{O}^{122,179,186,187}$	9.8	—	—	—	—	—	—	—	—	—
25 m (10 M) KOAc/ $\text{H}_2\text{O}^{187-189}$	—	25	31	—	—	—	—	—	—	—	—
30 m KOAc/ $\text{H}_2\text{O}^{124,179,186,187,189}$	—	36	32	-1.25 V 0.5 mV s ⁻¹ 10 $\mu\text{m cm}^{-2}$	-1.7 V 1 mV s ⁻¹ 10 $\mu\text{m cm}^{-2}$	-1.2 V 10 mV s ⁻¹ 200 $\mu\text{m cm}^{-2}$	-1.2 V 10 mV s ⁻¹ 940 $\mu\text{m cm}^{-2}$	-1.2 V 10 mV s ⁻¹ 200 $\mu\text{m cm}^{-2}$			
2019	40 m KOAc/ H_2O + 10 m LiOAc.	—	185	11	-1.2 V 10 mV s ⁻¹ 200 $\mu\text{m cm}^{-2}$	-1.2 V 10 mV s ⁻¹ 200 $\mu\text{m cm}^{-2}$	-1.2 V 10 mV s ⁻¹ 940 $\mu\text{m cm}^{-2}$	-1.2 V 10 mV s ⁻¹ 200 $\mu\text{m cm}^{-2}$			
2019	40 m KCOOH (potassium formate)/ H_2O [K:H ₂ O = 1:1.38, <i>n</i> : <i>n</i>] ¹⁸⁹	—	—	—	—	—	—	—	—	—	—
2019	21–22 m KOrf/ $\text{H}_2\text{O}^{122,167}$	—	76	6.5	-0.78 V 5 mV s ⁻¹ 5 $\mu\text{m cm}^{-2}$	-1.3 V 10 mV s ⁻¹ 200 $\mu\text{m cm}^{-2}$	-0.78 V 5 mV s ⁻¹ 5 $\mu\text{m cm}^{-2}$	-0.78 V 5 mV s ⁻¹ 5 $\mu\text{m cm}^{-2}$	-0.78 V 5 mV s ⁻¹ 5 $\mu\text{m cm}^{-2}$	-0.78 V 5 mV s ⁻¹ 5 $\mu\text{m cm}^{-2}$	-0.78 V 5 mV s ⁻¹ 5 $\mu\text{m cm}^{-2}$
2019	1.3 m (1 M) KTFSI/ H_2O^{90}	6	1	58	-0.85 V 0.5 mV s ⁻¹ 20 $\mu\text{m cm}^{-2}$	-1.45 V 0.5 mV s ⁻¹ 20 $\mu\text{m cm}^{-2}$	-0.85 V 0.5 mV s ⁻¹ 20 $\mu\text{m cm}^{-2}$				
28 m K(PTFSI) _{0.12} ²⁷ (TFSI) _{0.08} (OTf) _{0.8} ²⁸	6	26	35	-0.9 V 0.5 mV s ⁻¹ 20 $\mu\text{m cm}^{-2}$	-1.65 V 0.5 mV s ⁻¹ 20 $\mu\text{m cm}^{-2}$	-0.9 V 0.5 mV s ⁻¹ 20 $\mu\text{m cm}^{-2}$	-1.65 V 0.5 mV s ⁻¹ 20 $\mu\text{m cm}^{-2}$	-1.65 V 0.5 mV s ⁻¹ 20 $\mu\text{m cm}^{-2}$	-1.65 V 0.5 mV s ⁻¹ 20 $\mu\text{m cm}^{-2}$	-1.65 V 0.5 mV s ⁻¹ 20 $\mu\text{m cm}^{-2}$	-1.65 V 0.5 mV s ⁻¹ 20 $\mu\text{m cm}^{-2}$
2020	1 m KFSI/ H_2O^{170}	5	0.9	61	-0.75 V 0.5 mV s ⁻¹ 20 $\mu\text{m cm}^{-2}$	-1.4 V 0.5 mV s ⁻¹ 20 $\mu\text{m cm}^{-2}$	-0.75 V 0.5 mV s ⁻¹ 20 $\mu\text{m cm}^{-2}$	-0.75 V 0.5 mV s ⁻¹ 20 $\mu\text{m cm}^{-2}$	-0.75 V 0.5 mV s ⁻¹ 20 $\mu\text{m cm}^{-2}$	-0.75 V 0.5 mV s ⁻¹ 20 $\mu\text{m cm}^{-2}$	-0.75 V 0.5 mV s ⁻¹ 20 $\mu\text{m cm}^{-2}$
30–31 m KFSI/ $\text{H}_2\text{O}^{16,167,170}$	—	17	40	-1.5 V 5 mV s ⁻¹ 5 $\mu\text{m cm}^{-2}$	-1.5 V 5 mV s ⁻¹ 5 $\mu\text{m cm}^{-2}$	-1.5 V 5 mV s ⁻¹ 5 $\mu\text{m cm}^{-2}$	-1.5 V 5 mV s ⁻¹ 5 $\mu\text{m cm}^{-2}$	-1.5 V 5 mV s ⁻¹ 5 $\mu\text{m cm}^{-2}$	-1.5 V 5 mV s ⁻¹ 5 $\mu\text{m cm}^{-2}$	-1.5 V 5 mV s ⁻¹ 5 $\mu\text{m cm}^{-2}$	-1.5 V 5 mV s ⁻¹ 5 $\mu\text{m cm}^{-2}$
62 m K(FSI) _{0.55} ²⁵ (OTf) _{0.45} ²⁹ H_2O^{170}	5	98	12	-1.05 V 0.5 mV s ⁻¹ 20 $\mu\text{m cm}^{-2}$	-1.8 V 0.5 mV s ⁻¹ 20 $\mu\text{m cm}^{-2}$	-1.05 V 0.5 mV s ⁻¹ 20 $\mu\text{m cm}^{-2}$	-1.05 V 0.5 mV s ⁻¹ 20 $\mu\text{m cm}^{-2}$	-1.05 V 0.5 mV s ⁻¹ 20 $\mu\text{m cm}^{-2}$	-1.05 V 0.5 mV s ⁻¹ 20 $\mu\text{m cm}^{-2}$	-1.05 V 0.5 mV s ⁻¹ 20 $\mu\text{m cm}^{-2}$	-1.05 V 0.5 mV s ⁻¹ 20 $\mu\text{m cm}^{-2}$

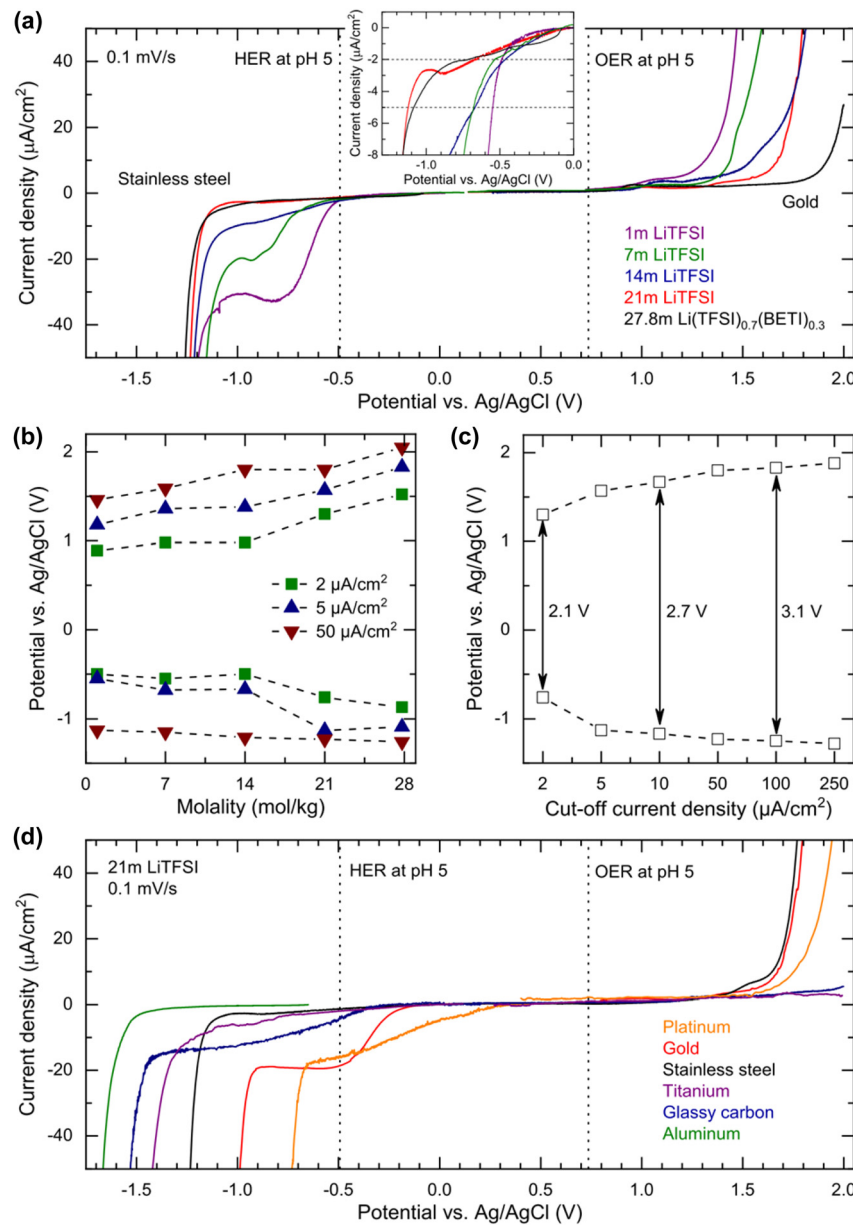


Fig. 11 (a)–(d) Results of LSV conducted at 0.1 mV s^{-1} in $\text{LiTFSI}/\text{H}_2\text{O}$ with various salt concentrations, using SUS for the anode and gold for the cathode substrates. (b)–(d) Estimated potential window of 21 m $\text{LiTFSI}/\text{H}_2\text{O}$ (pH 5) with different cut-off current densities and substrates.¹⁷¹ Reprinted with permission from *Journal of The Electrochemical Society*.

electrode potentials related to the variation in the activity of carrier ions in the electrolyte are discussed in Section 6.1.

The development of aqueous Li electrolytes, particularly with an emphasis on enhancing the kinetic hindrance of the HER through the formation of a protective surface film, known as the SEI, on the anode surface, is of utmost importance. Initial studies involving aqueous electrolytes with concentrated LiNO_3 or Li_2SO_4 showed no evidence of the formation of a functional SEI, leading to the operating potential window of such solutions being largely dependent on the thermodynamic potential of water reduction.^{194–196} The significance of the SEI in aqueous electrolytes has been increasingly recognized with the introduction of highly salt-concentrated electrolytes containing imide salts.¹⁸

However, the formation and stable maintenance of the SEI pose significant challenges in aqueous electrolytes. The competitive reduction of water, leading to the generation of hydrogen gas bubbles, can impede the stable growth of the SEI from anion reduction on the anode surface.^{21,197} Additionally, most components of an anion-derived SEI are susceptible to water. For example, NO_3^- anions are reduced to NH_xO_y and N_2 , while SO_4^{2-} anions are reduced to SO_x and H_2S , all of which readily dissolve in or react with water, thus impeding the stable maintenance of the SEI.^{195,196} In conventional dilute solutions, which contain many water clusters with high water activity, the formation of a stable SEI is exceedingly challenging.^{21,197}

In contrast, in highly salt-concentrated aqueous Li electrolytes based on imide salts, the stability of the SEI is significantly



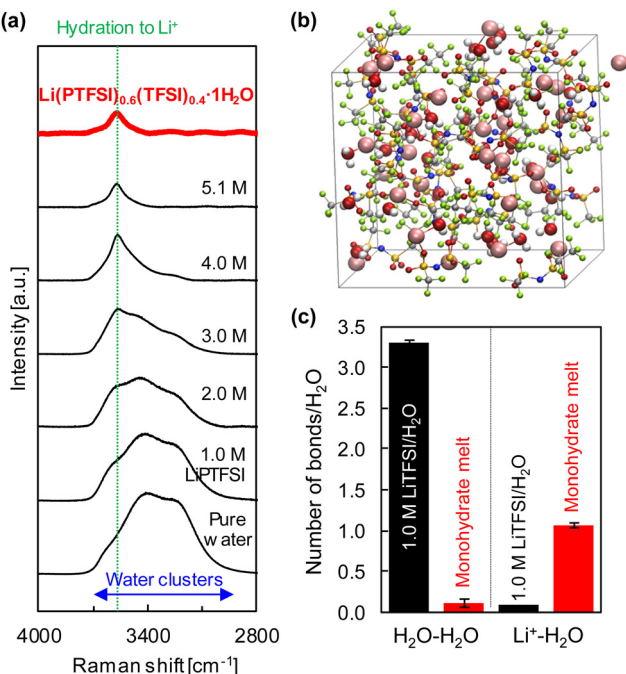


Fig. 12 (a) Raman spectra of LiPTFSI solutions and the monohydrate melt, Li⁺(PTFSI)_{0.6}(TFSI)_{0.4}·1H₂O. (b) Solution structure of the monohydrate melt obtained through DFT-MD simulations. (c) Number of hydrogen bonds and coordination to cations around a water molecule in the given electrolytes.⁸⁵ Reprinted with permission from *Electrochemistry Communications*.

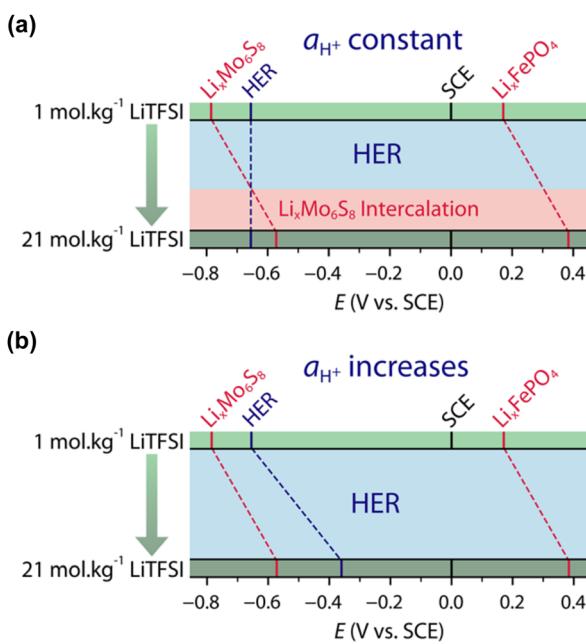


Fig. 13 Electrode potential shifts (a) without and (b) with consideration of the H⁺ activity in LiTFSI/H₂O electrolytes.^{192,193} Reprinted with permission from *The Journal of Chemical Physics*.

enhanced. In these electrolytes, two critical changes occur. The lowest unoccupied molecular orbital levels of the anions become lower than those of the water molecules, allowing the

rapid formation of an SEI with the reduction of the anions at a higher potential than that of the HER (Fig. 14).^{198–202}

The maintenance of the SEI is also improved because the reduction products of the imide salts, such as LiF and Li_xH_yN-SO₂CF₃, exhibit low solubility or low reactivity with water.^{203–205} Moreover, the unique solution structure of these electrolytes, with minimal formation of water clusters owing to the strong Lewis acidity of Li⁺, substantially stabilizes the SEI (Fig. 14).^{198,199} Consequently, highly salt-concentrated aqueous Li electrolytes based on imide salts offer an expanded operating potential window that is more than twice as wide as that of diluted solutions, with thermodynamically and kinetically improved oxidation and reduction stabilities, respectively (Fig. 14).

On the other hand, the weaker Lewis acidity of Na⁺ and K⁺ presents challenges in expanding the operating potential window of aqueous electrolytes. The interactions among carrier ions (Na⁺ and K⁺), anions, and water molecules are relatively weak, resulting in several limitations: (1) the degree of variation in the electronic states of water molecules and anions is limited, leading to lower oxidation stability of the electrolyte.^{198–202} (2) It is difficult to achieve an anion reduction potential that is higher than the HER potential, thereby hindering the formation of an anion-derived SEI on the anode surface (Fig. 15).^{198–202} (3) Owing to the weak coordination of Na⁺ or K⁺ with water molecules, a relatively large number of free water molecules (large water clusters) are present, as evident from computational simulations wherein larger sizes of water clusters were observed in Na and K hydrate melts than in Li hydrate melts (Fig. 14).¹⁹⁸ The presence of many free water molecules (large water clusters) in aqueous electrolytes hinders the growth and maintenance of the SEI, posing significant challenges in expanding the operating potential window at the anode. This issue persists even if the increase in the H⁺ activity, which is typically seen with high salt concentrations, is relatively suppressed in highly salt-concentrated aqueous Na and K electrolytes compared to that in Li⁺-based systems. Consequently, while highly salt-concentrated aqueous Na and K electrolytes provide improved electrochemical stability, the degree of extension of their operating potential window is still lower than that of Li-based electrolytes (Fig. 15).

Despite efforts to enhance the kinetic hindrance of the HER by forming stable SEI layers at the anode, highly salt-concentrated electrolytes still exhibit a significantly narrower potential window compared to nonaqueous systems. Specifically, electrolyte decomposition and hydrogen gas evolution at the anode necessitate the use of anode active materials with relatively high reaction potentials, resulting in a decreased output voltage of aqueous batteries. For instance, while nonaqueous rechargeable batteries typically use carbon materials such as graphite and hard carbon, which have average reaction potentials ranging from 0.1 to 0.3 V (vs. M/M⁺, where M = Li, Na, and K), aqueous batteries have been limited to testing with 1.5 V-class active materials like Li₄Ti₅O₁₂, NaTiOPO₄, and KTi₂(PO₄)₃, even in highly salt-concentrated aqueous electrolytes like the 56 m Li electrolyte (Li(PTFSI)_{0.6}(TFSI)_{0.4}·1H₂O),⁸⁵ 28 m Na electrolyte (Na(PTFSI)_{0.55}(HTFSI)_{0.45}·2H₂O (HTFSI is N(SO₂C₃F₇)(SO₂CF₃)),¹⁸⁵ and 62 m K electrolyte (62 m K(FSI)_{0.55}(OTf)_{0.45}·0.9H₂O)¹⁷⁰ (Tables 1, 3 and 4).

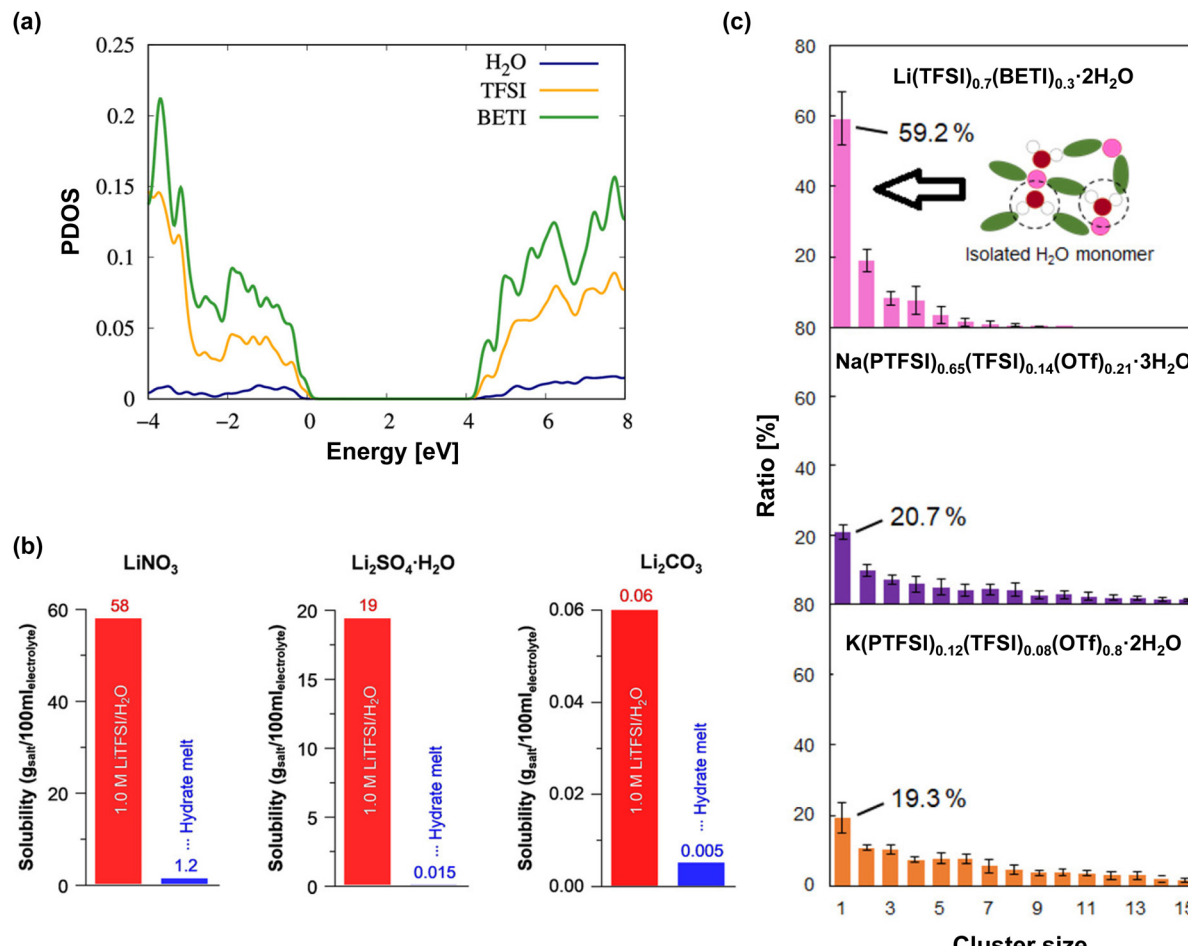


Fig. 14 (a) Normalized partial density of states (PDOS, per ion and/or molecule) of the dihydrate melt, $\text{Li}(\text{TFSI})_{0.7}(\text{BETI})_{0.3} \cdot 2\text{H}_2\text{O}$.^{198,199} (b) Suppressed solubility of model components in the SEI within the dihydrate melt.²¹ (c) Histograms showing water cluster distribution in hydrate melts with various carrier ions.¹⁹⁸ Reprinted with permission from *The Journal of Chemical Physics Letters* (a), *ACS Applied Materials & Interfaces* (b) and (c).

These limitations are particularly pronounced in tests conducted at elevated temperatures, where electrolyte decomposition is accelerated, and there are few reports on full-cell tests in such conditions. These factors indicate the limitation of SEI functionalities in aqueous electrolytes. Additionally, consuming large amounts of carrier ion sources for SEI formation and maintenance hinders the achievement of an ideal P/N ratio (close to 1), thereby limiting the maximization of the battery energy density. This underscores the necessity for developing new strategies, beyond simply increasing salt concentrations, to enhance the stability of aqueous electrolytes.

4.2. Increase in viscosity and decrease in ionic conductivity

While increasing the salt concentration in aqueous electrolytes can enhance interactions among carrier ions, anions, and water molecules, thereby contributing to expanding the operating potential windows both thermodynamically and kinetically, it also leads to the formation of bulky ion-solvent aggregates. These aggregates critically increase the viscosity of the electrolyte, as reflected in Tables 5–7. This increase in viscosity poses significant challenges, not only for the mass production of

batteries, but also for the transport of carrier ions within the electrolyte itself.

In state-of-the-art nonaqueous Li-ion batteries, the electrode loading level exceeds 20 mg cm^{-2} . Even for electrolytes with viscosities lower than 5 mPa s , the electrode-wetting process is slow, necessitating an additional long-period aging process. This aging process, which includes wetting and formation steps, is one of the longest production processes in battery manufacturing, typically requiring 1 to 2 weeks. Such lengthy processes significantly impede the reduction of battery production costs.^{206–208} Considering these factors, the use of highly salt-concentrated aqueous electrolytes with viscosities ranging from tens to thousands of mPa s is impractical.

Recent research on highly salt-concentrated aqueous electrolytes has revealed a distinct ion transport mechanism that involves a disproportionation of cation solvation, leading to the formation of water-rich and anion-rich nanodomains, and switching between a vehicle-type and hopping-type ion transport mechanism in the respective regions (Fig. 16).^{209–213}

As more salt and less water are used to prepare the highly salt-concentrated aqueous electrolytes to increase their operating

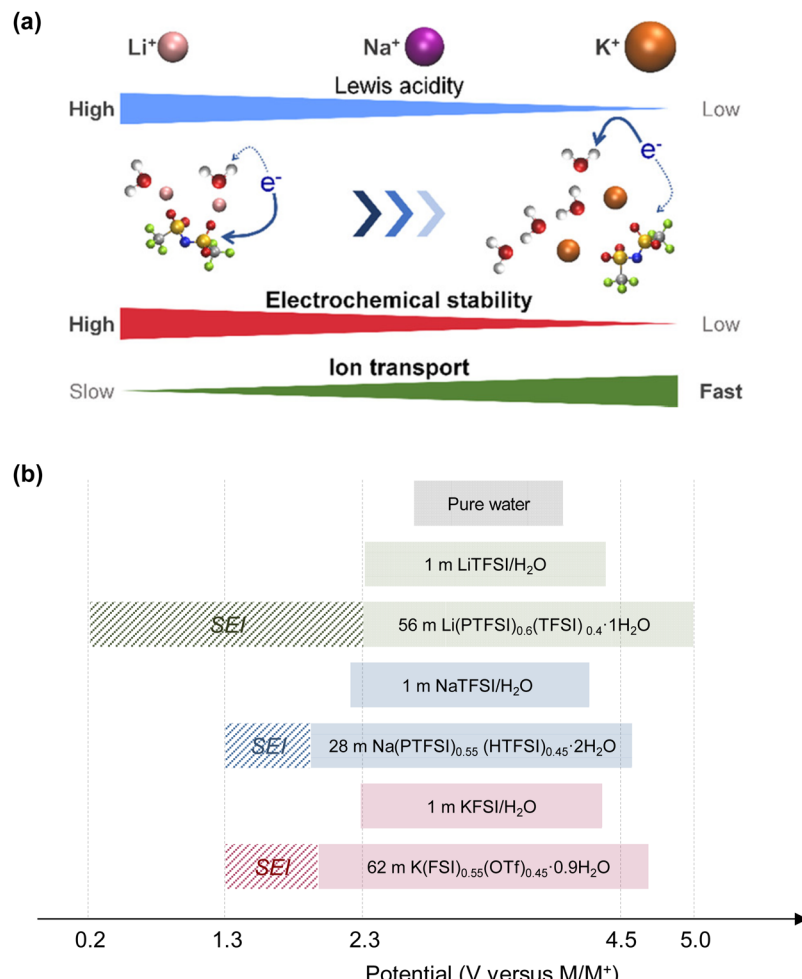


Fig. 15 (a) Carrier ion-dependent electrochemical and physicochemical properties of hydrate melts.¹⁹⁸ Reprinted with permission from ACS *Applied Materials & Interfaces*. (b) Comparison of aqueous electrolytes based on salt concentration and carrier ion types. The plot was created based on the LSV results obtained using Al and Pt as working electrodes. The areas marked with bold colors and diagonal lines represent the operating potential window of each electrolyte and the kinetic (SEI) contributions within it, respectively.^{91,170,185}

potential windows, the decrease in the water-rich domain reduces ion movement in the vehicle mode and the hopping speed (Fig. 16).^{214–222}

The reduced mobility of carrier ions in highly salt-concentrated aqueous electrolytes can also be understood through the classical Stokes–Einstein–Sutherland equation.^{223–225}

$$\text{Diffusion coefficient } (D) = \frac{kT}{6\pi r\mu} \quad (12)$$

Here, k is Boltzmann's constant, T is the absolute temperature, r is the effective radius of the diffusing species, and μ is the viscosity of the solution. The ion mobility is represented by the diffusion coefficient D . Therefore, the formation of large-size aggregates and the increase in viscosity cause a significant decrease in the carrier ion mobility. Indeed, the ion conductivity decreases ten-fold with an increase in the salt concentration from 1 to 30 m. Moreover, in the ultra-high concentration range (value over 50 m), the ion conductivity can decrease 100-fold or even lower (Tables 5–7 and Fig. 17). Note that the ionic conductivity of electrolytes reflects the

mobility of both cations and anions. The transference number (proportion of the total electric current carried by a specific ion in an electrolyte; t_+ in eqn (13)) must be considered to estimate the conductivity of the carrier ions (Li^+ , Na^+ , and K^+), which are specifically involved in energy storage and release. For instance, if an electrolyte exhibits an ionic conductivity of 1 mS cm^{-1} and the carrier ion transference number is 0.4, the conductivity attributable to the carrier ions would be 0.4 mS cm^{-1} .

$$\text{Transference number of carrier ions } (t_+) = \frac{I_+}{I_{\text{total}}} = \frac{\sigma_+}{\sigma_{\text{total}}} \quad (13)$$

Here, I_{total} , I_+ , σ_{total} , and σ_+ are the total current in the electrolyte, current carried by the carrier ions, total ionic conductivity of the electrolyte, and ionic conductivity of the carrier ions, respectively.

4.3. Poor wide-temperature-range performance

As shown in Tables 1, 3 and 4, highly salt-concentrated electrolytes exhibit poor performance in wide-temperature-range battery applications. Primarily, they tend to undergo partial crystallization below room temperature because they utilize

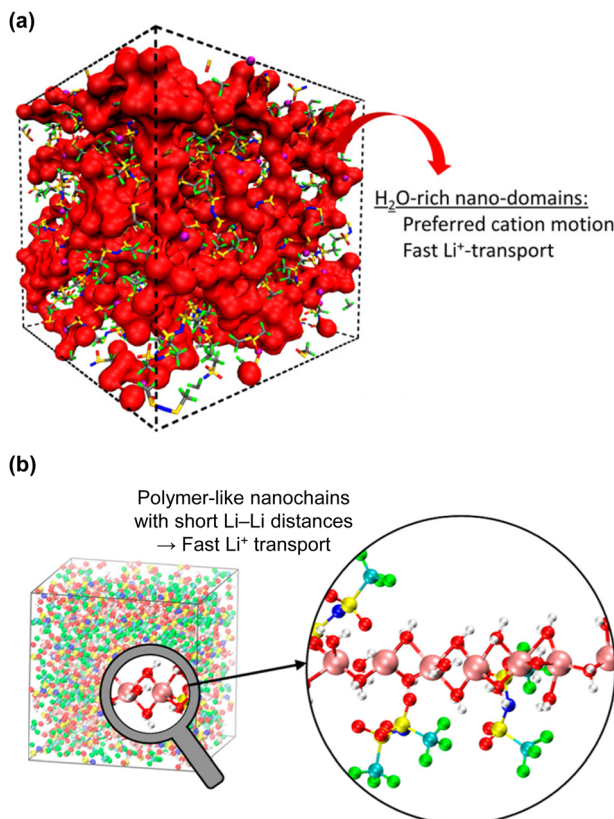


Fig. 16 (a) and (b) Carrier ion transport via vehicle-type and/or hopping-type mechanism in highly salt-concentrated aqueous electrolytes.^{213,214} Reprinted with permission from ACS Nano (a) and Journal of the American Chemical Society (b).

the maximum salt-to-solvent solubility achievable at room temperature. Lu *et al.* analyzed the theoretical relationship between the phase-transition temperature (T_p ; below this temperature, aqueous electrolytes undergo crystallization and ice/hydrated-salt precipitation, ultimately leading to degradation in the battery performance) of aqueous electrolytes and their salt concentration.²²⁷ Fig. 18 illustrates the equilibrium and non-equilibrium phase diagrams of a typical salt/H₂O binary solution.

In the equilibrium binary system, the lowest phase-transition temperature (T_p) of aqueous electrolytes is obtained at the eutectic point (E in Fig. 18a), which can be understood based on the competitive relationship between the enthalpy and entropy, as described in eqn (14).

Phase-transition temperature (T_p)

$$= \frac{\Delta H}{\Delta S} \quad (14)$$

$$= \frac{H_{\text{solution}} - H_{\text{ice}} - H_{\text{hydrated salt}}}{S_{\text{solution}} - S_{\text{ice}} - S_{\text{hydrated salt}}}$$

Here, H_{solution} , H_{ice} , $H_{\text{hydrated salt}}$, S_{solution} , S_{ice} , $S_{\text{hydrated salt}}$ are the enthalpies and entropies of the solution, ice, and hydrated salt ($S \cdot n\text{H}_2\text{O}$ and $S \cdot b\text{H}_2\text{O}$ in Fig. 18a), respectively. As the salt concentration increases, the phase-transition temperature (T_p)

of the solution initially decreases owing to an increase in the entropy change (ΔS), and then increases owing to a large increase in the enthalpy change (ΔH).

A non-equilibrium system achieves a supercooling zone and a glass-state zone, where crystallization and precipitation of the electrolyte components barely occur even at extremely low temperatures (Fig. 18b). Theoretically, a solution with a longer crystallization time (τ) provides a stronger liquid supercooling ability.^{228–230} The crystallization time (τ) is proportional to the reciprocal of the nucleation rate (I), as demonstrated in eqn (15).²²⁹

$$\text{Nucleation rate } (I) = AD \exp\left(-\frac{16\pi\sigma^3}{3kT\Delta G^2}\right) \propto \frac{1}{\tau} \quad (15)$$

Here, A , D , k , T , σ , and ΔG are the constant, effective diffusivity, Boltzmann constant, absolute temperature, interfacial energy between the nuclei and liquid phase, and the Gibbs free energy difference between the crystalline and liquid states, respectively. The nucleation rate (I) is generally maximized in aqueous electrolytes with a mild salt concentration, considering the thermodynamic (e.g., enthalpy and entropy changes described in eqn (14)) and kinetic (e.g., diffusivity related to solution viscosity) factors. For instance, in a LiTFSI/H₂O binary system (Fig. 19)⁸⁵ at a concentration of 1.0 M, the melting point is close to 0 °C owing to the presence of numerous free water molecules. At slightly higher concentrations (~3.0 M), the solution exhibits a supercooling phenomenon, indicating an amorphous state with a complex coordination of cations and water molecules, thus hindering the phase transition by virtue of a low nucleation rate (I). As the salt concentration exceeds 3.0 M, the phase-transition temperature (T_p) gradually increases and eventually reaches 25 °C at 5.1 M (representing a highly salt-concentrated 21 M LiTFSI/H₂O electrolyte). Similar trends are observed in various carrier ion-based solutions (Fig. 19). These situations, wherein lowering the salt concentration is necessary to address low-temperature cycling, while increasing the salt concentration is essential to broaden the battery output voltage window, present a critical dilemma and are a bottleneck in maximizing the battery performance.

The cycling performance of aqueous batteries at high temperatures is even worse than at low temperatures (Tables 1, 3 and 4). The side reactions, such as the HER and OER, are strongly dependent on the temperature according to the Arrhenius equation:^{232,233}

$$\text{Reaction constant} = A \exp\left(-\frac{E_a}{RT}\right) \quad (16)$$

Here, A , E_a , R , and T correspond to the frequency factor (a constant), molar activation energy of the reaction, universal gas constant, and absolute temperature, respectively. Additionally, as the temperature increases, most of the SEI components are more prone to dissolution in the bulk electrolyte, thereby further increasing the reaction constant of the side reactions. Consequently, the electrolyte decomposition is significantly pronounced at the cathode and anode surfaces at high temperatures. While increasing the salt concentration to reduce the water activity can partially inhibit the side reactions at high temperatures, it is insufficient to fully address this issue. This is



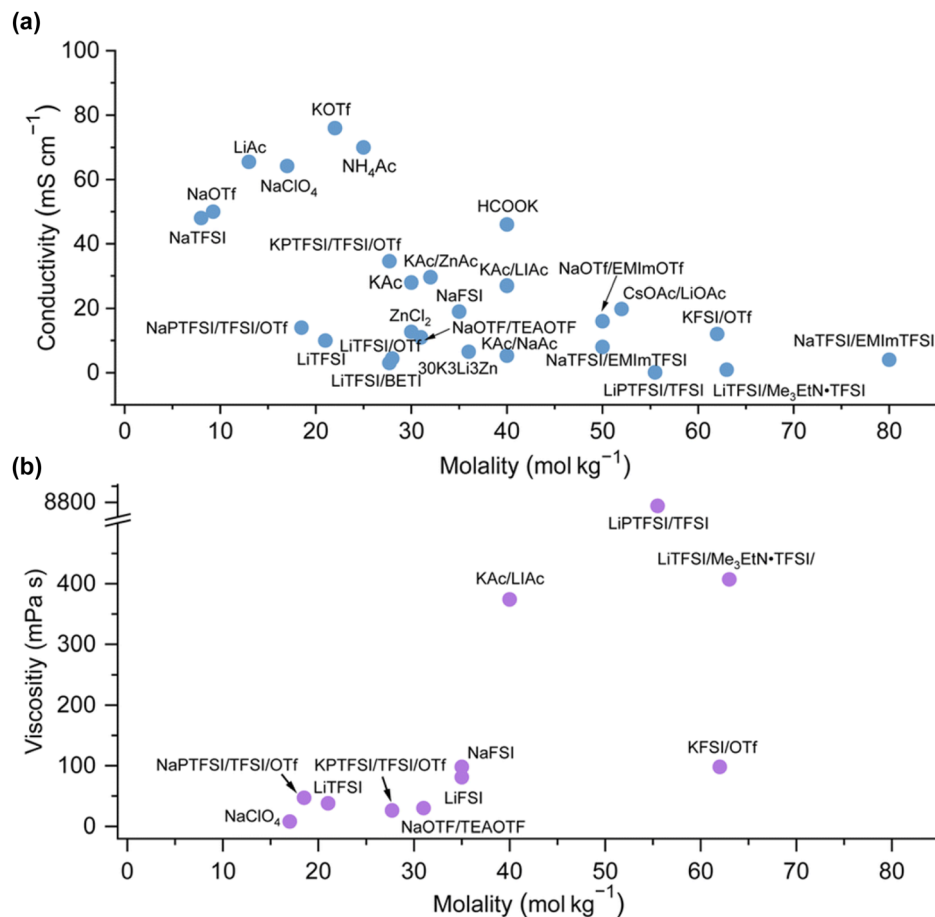


Fig. 17 (a) Ionic conductivity and (b) viscosity of various aqueous electrolytes.²²⁶ Reprinted with permission from *Energy & Environmental Science*.

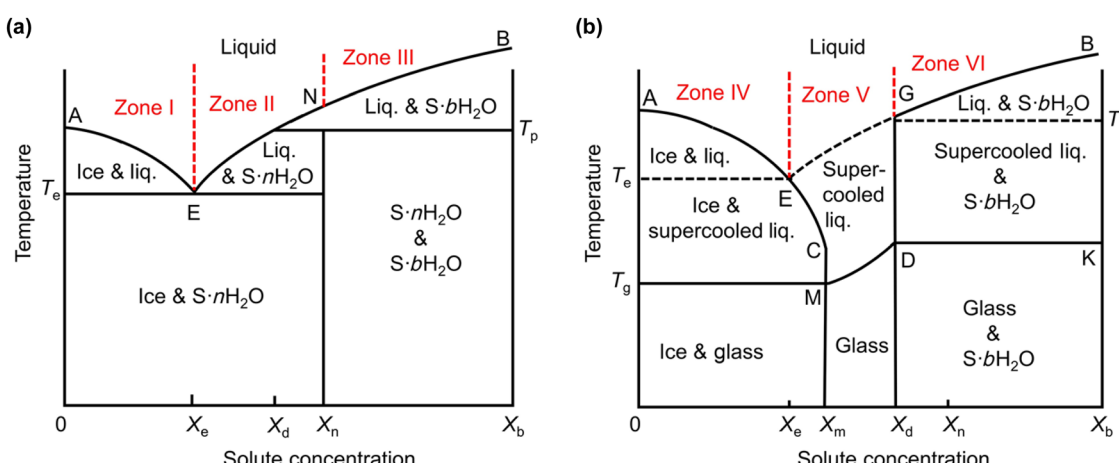


Fig. 18 (a) Equilibrium binary H₂O-salt and (b) non-equilibrium binary H₂O-salt phase diagrams of aqueous solutions.²²⁷ Reprinted with permission from *Nano Research Energy*.

evident from the performance of LiCoO₂|Li₄Ti₅O₁₂ aqueous full cells, which retain only 70% of their initial capacities after 100 cycles at 1C and 55 °C in a 56 m Li(PTFSI)_{0.6}(TFSI)_{0.4}·1H₂O electrolyte.⁸⁵ Therefore, achieving high-temperature stability in aqueous batteries solely through high-salt-concentration strategies is challenging.

4.4. Constraints of material selection

Salts containing PF₆⁻ and BF₄⁻ anions are known for their high oxidation stability, low cost, and high passivation capabilities for the Al cathode current collector. However, they cannot be used in aqueous electrolytes because these salts tend to hydrolyze, rendering the electrolyte solution acidic and forming

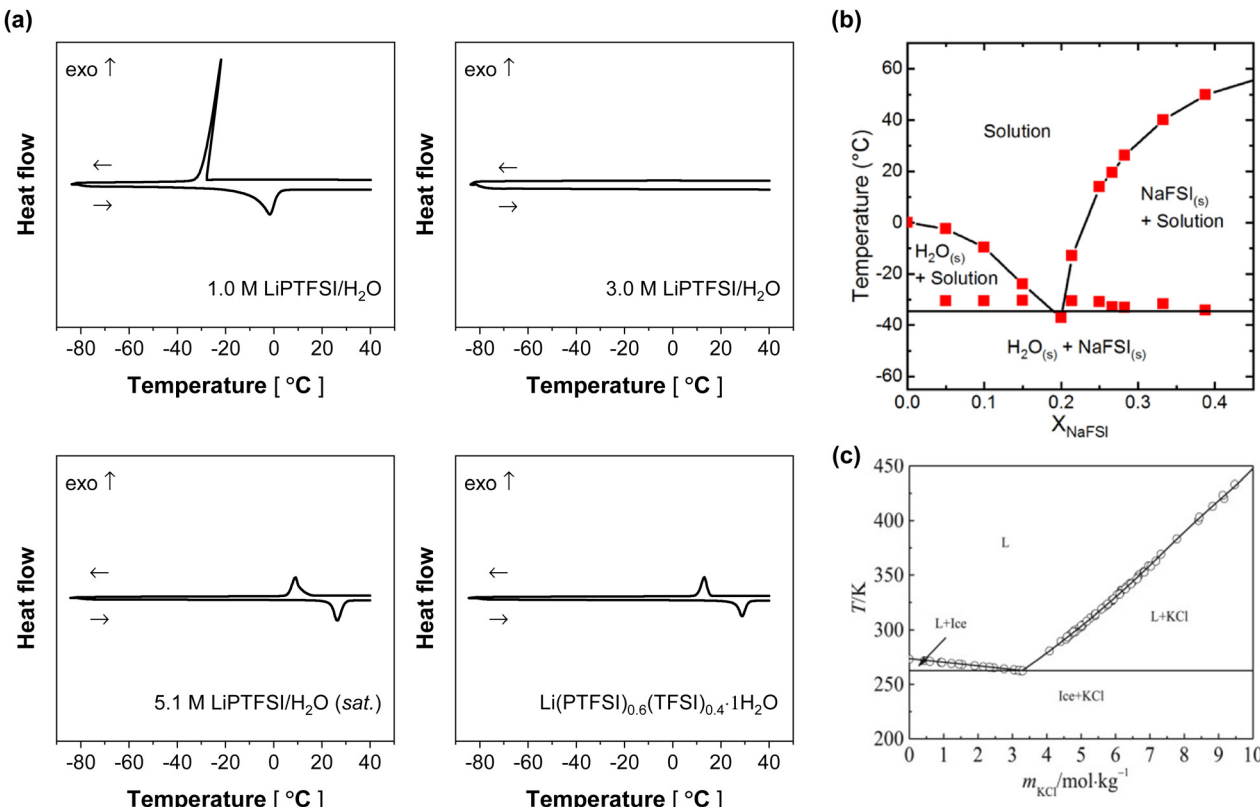


Fig. 19 (a) Thermal stability of LiPTFSI-based aqueous electrolytes evaluated by differential scanning calorimetry at a rate of 5 °C min⁻¹.⁸⁵ Phase diagrams of (b) NaFSI–H₂O⁸⁹ and (c) KCl–H₂O binary systems.²³¹ Reprinted with permission from *Electrochemistry Communications* (a), *ACS Materials Letters* (b), and *Calphad* (c).

harmful compounds like hydrogen fluoride.^{169,234–239} This limitation necessitates the use of imide salts, which are resistant to hydrolysis but significantly more expensive than PF₆⁻ and BF₄⁻ anion-based salts. Moreover, the pronounced dissolution of Al at relatively low potentials (≤ 4 V vs. Li/Li⁺) in imide-based aqueous electrolytes renders Ti the only viable choice as a cathode current collector.^{240–243} Ti is preferred because it forms a stable passivating oxide layer of TiO₂ on its surface, protecting itself from corrosion and oxidative dissolution.^{244–246} Notably, the oxidation stabilities of Al measured by LSV are often overestimated, as discussed in Section 4.1. This is also apparent from the rarity of full cells using Al as a cathode current collector in aqueous electrolytes.²⁴⁷ However, Ti is not an ideal choice for a battery current collector. Currently, batteries are commonly assembled in cylindrical, prismatic, and pouch formats. The performance of these batteries largely depends on the type of current collector used.^{248–252} For instance, the production process of most modern batteries involves several key steps. Initially, a slurry is coated onto the current collector and the prepared electrode is dried. This is followed by a calendering process to press the electrodes and reduce their porosity, thereby enhancing the energy density of the battery. After an additional vacuum drying process to remove any remaining solvents from the electrodes, a winding process is conducted to tightly roll the electrodes and separators into a jelly-roll configuration suitable for each battery type. During these processes, the

current collector must remain undamaged and intact. Additionally, thin and flexible current collectors enhance the battery energy density and enable the fabrication of batteries with various sizes and shapes. However, using Ti is challenging because of its high deformation resistance and limited ductility, which endow low flexibility and pose substantial difficulties in refining and processing compared to those for Al and Cu, which are commonly used as cathode and anode current collectors, respectively, in nonaqueous systems.²⁵³ This not only limits the available battery form factors (*i.e.*, rendering it difficult to achieve the jelly-roll configuration), but also leads to an increased production cost of thin Ti foils (several hundred times higher than those of Al and Cu foils).^{254–256} Additionally, the electrical conductivity of Ti foils is approximately one-tenth that of Al and Cu foils, potentially reducing the power density of the battery.²⁵⁷ These limitations affect not only the current collectors but all battery components, resulting in increased overall costs and poor battery performance.

Aqueous batteries also encounter an obstacle in terms of separator compatibility, owing to the limited wettability of aqueous electrolytes with traditional separators. Separators made of polypropylene or polyethylene, which are widely used in nonaqueous batteries and are often thinner than 20 µm, cannot be adequately wetted by aqueous electrolytes. This limitation led researchers to use glass fiber-based separators, which typically have a thickness of several hundred micrometers. The increased thickness not only requires more space within the battery but



also necessitates a greater volume of electrolyte to ensure that the separator is fully saturated, thereby leading to a decrease in the energy density of the battery. As an alternative, cellulose-based separators, which are thin and environmentally friendly as well as offer better wettability with aqueous electrolytes, can be used. However, they face challenges such as low strength, high flammability, and susceptibility to dissolution or degradation, especially when exposed to electrolytes with extreme pH levels.^{258,259}

Consequently, aqueous electrolytes with high salt concentrations face issues such as limited expansion of the potential window, increased viscosity, decreased ion conductivity, compromised performance at low temperatures, restrictions on battery materials, and higher production costs. These factors collectively raise doubts about their viability for practical use. Without innovative solutions to these significant challenges, the commercialization of advanced aqueous rechargeable batteries remains uncertain.

5. Issues with active materials for aqueous batteries

In the development of cathode and anode active materials for aqueous rechargeable batteries, careful consideration of their

reaction potential and chemical stability is essential. Fig. 20 illustrates the thermodynamic potential window of pure water and the electrode reaction potentials. For instance, if the reaction potential of the cathode surpasses the oxidation potential of the electrolyte, oxygen is likely to be produced on the cathode surface, potentially hindering the deintercalation reaction. Similarly, if the reaction potential of the anode is below the reduction potential of the electrolyte, hydrogen is likely to be generated on the anode surface, disrupting the intercalation process. These factors lead to a rapid decline in the battery capacity, often accompanied by significant electrolyte depletion. Therefore, it is imperative to select active materials with optimized reaction potentials that are within the operating potential window of the aqueous electrolyte.

Moreover, the active materials must exhibit high chemical stability across a wide pH range. This would enable pH adjustments in the electrolyte for enhancing the battery performance by fine-tuning the overall potential diagram. Additionally, the catalytic effect of electrode materials, particularly transition metals, on water electrolysis should be considered. The overpotential of water electrolysis typically depends on the relative activity of water-splitting catalysts. To maximize the overpotential for the OER and HER, materials with relatively low catalytic activity should be used.

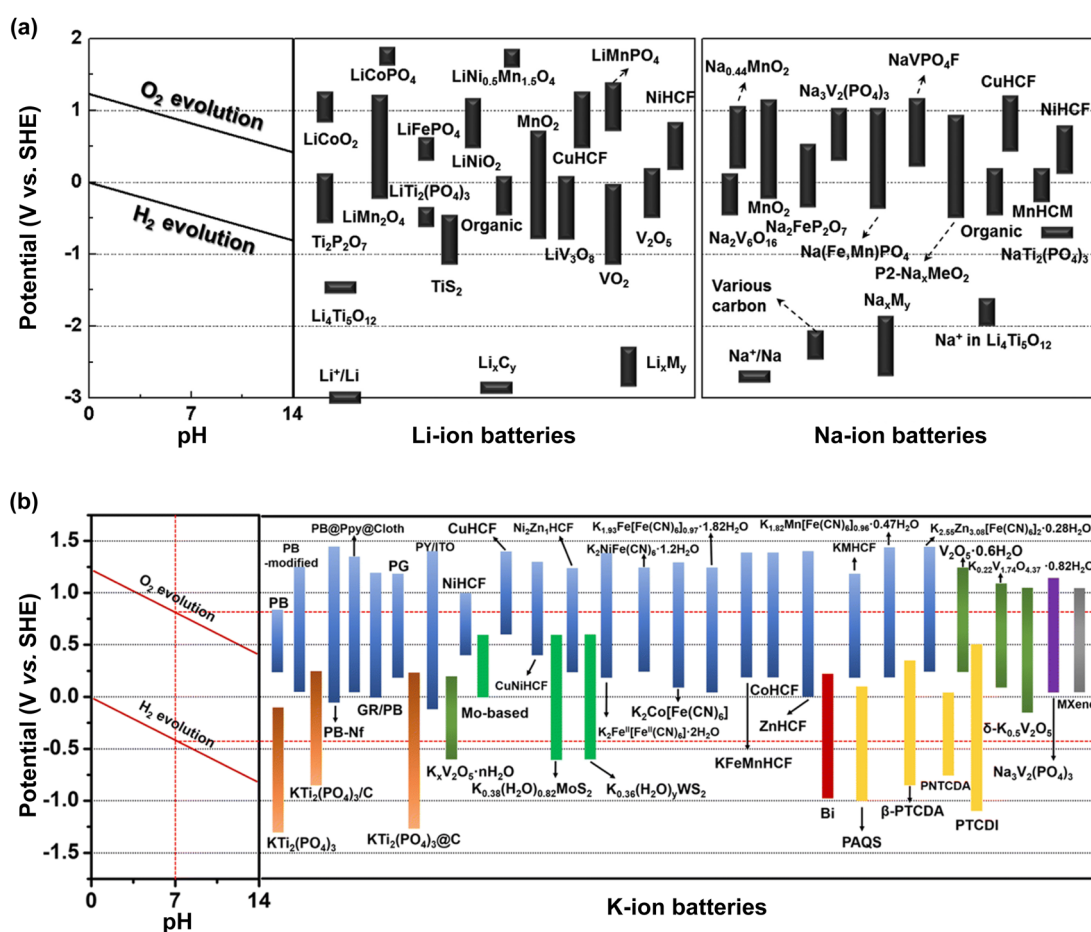


Fig. 20 Thermodynamic potential window of water and redox potentials of cathode and anode active materials for (a) Li-, Na-, and (b) K-ion batteries.^{260,261} Reprinted with permission from *Chemical Reviews* (a) and *Energy & Environmental Science* (b).

Another critical consideration is the co-intercalation of proton and/or water into the active materials. In addition to the insertion of carrier ions (such as Li^+ , Na^+ , or K^+), which are responsible for energy storage and release, co-intercalation of proton and/or water is observed, especially in materials with layered structures.²⁶² The presence of substituted proton and/or water within the bulk structure of active materials, even those with high chemical stability across a wide pH range, can obstruct the insertion pathways of carrier ions, leading to reduced cycling stability and battery energy density.²⁶³ While proton insertion can be mitigated by increasing the electrolyte pH, this approach is only viable when active materials and battery components provide high chemical stability at high pH levels. Therefore, the development of active materials with minimal proton insertion is paramount to the advancement of aqueous rechargeable battery technology.

Additional attention should be paid to the dissolution of transition metals from the active materials. During the charge and discharge processes, transition metal ions in the active material serve as centers for oxidation and reduction reactions, counterbalancing the charge changes associated with the insertion and extraction of carrier ions. The transition metal ions

must remain stably anchored within the structure of the active material throughout the repeated cycles of insertion and extraction of carrier ions. However, the high permittivity and ion conductivity of aqueous electrolytes accelerate the rapid diffusion of transition metal ions into the bulk electrolyte and the reduction of dissolved transition metal ions on the anode surface, leading to critical issues such as bulk structural damage of the active material, increased resistance on the electrode surfaces, and overall degradation of the battery performance.

5.1. Active materials for aqueous Li-ion batteries

One of the most extensively studied cathode materials in aqueous Li-ion batteries is lithium manganese oxide, LiMn_2O_4 . Since the prototype battery demonstrating the stable reversibility of LiMn_2O_4 in a 5 M LiNO_3 + 0.001 M LiOH solution was reported in 1994,¹⁷ LiMn_2O_4 has been widely utilized in aqueous Li-ion batteries. LiMn_2O_4 features a spinel structure, with oxygen ions forming a face-centered cubic lattice.^{264,265} Within this lattice, lithium occupies one-eighth of the tetrahedral sites between oxygen ions, while manganese occupies half of the octahedral sites (Fig. 21).^{264,265} LiMn_2O_4 exhibits a theoretical

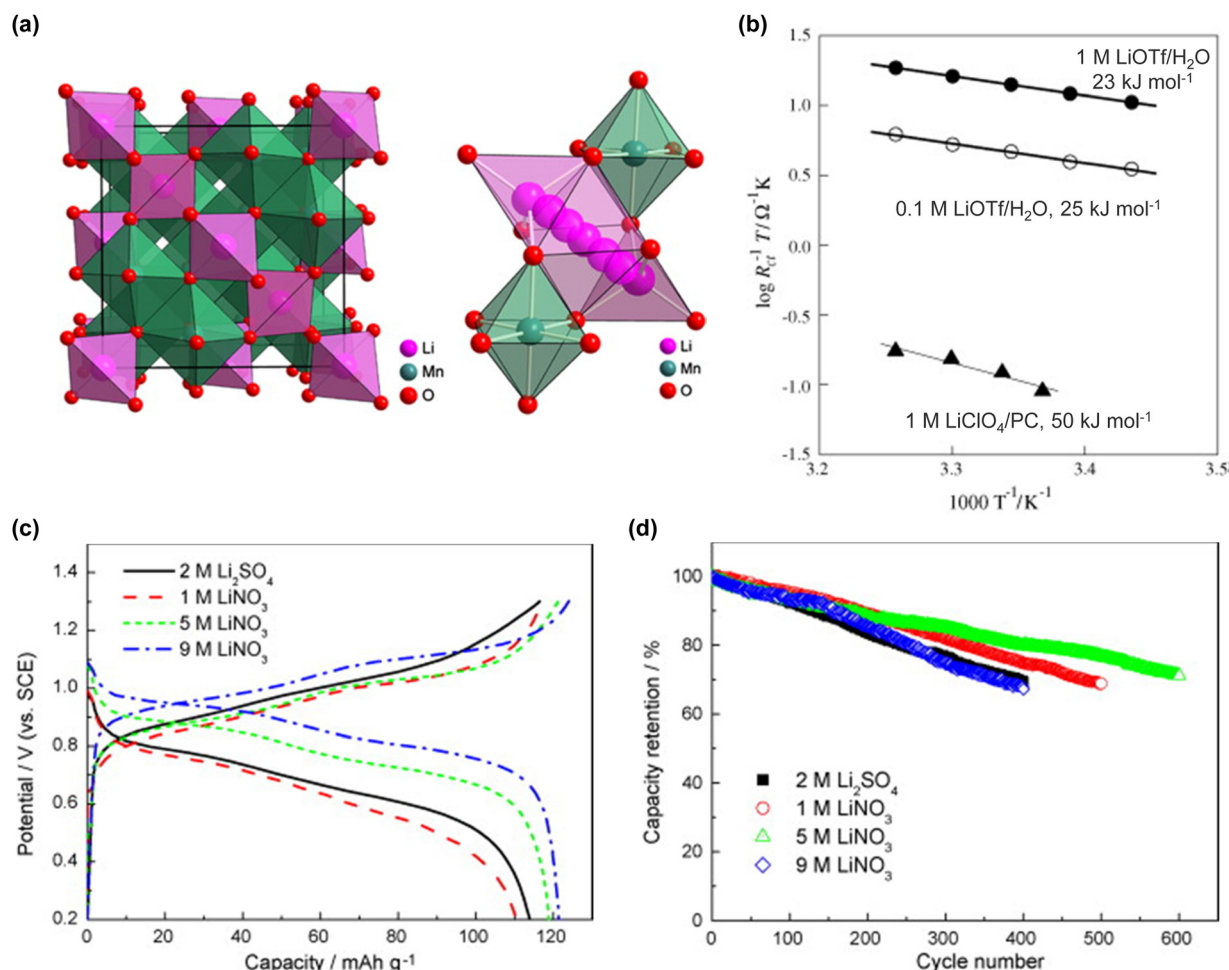


Fig. 21 Crystal structure and Li^+ diffusion pathway in spinel LiMn_2O_4 .²⁶⁸ (b) Activation energies for interfacial Li^+ ion transfer reactions.²⁶⁶ (c) charge/discharge curves, and (d) cycling stability of LiMn_2O_4 in the given electrolytes.²⁶⁷ Reprinted with permission from *Progress in Natural Science: Materials International* (a) and *Journal of Power Sources* (b)–(d).



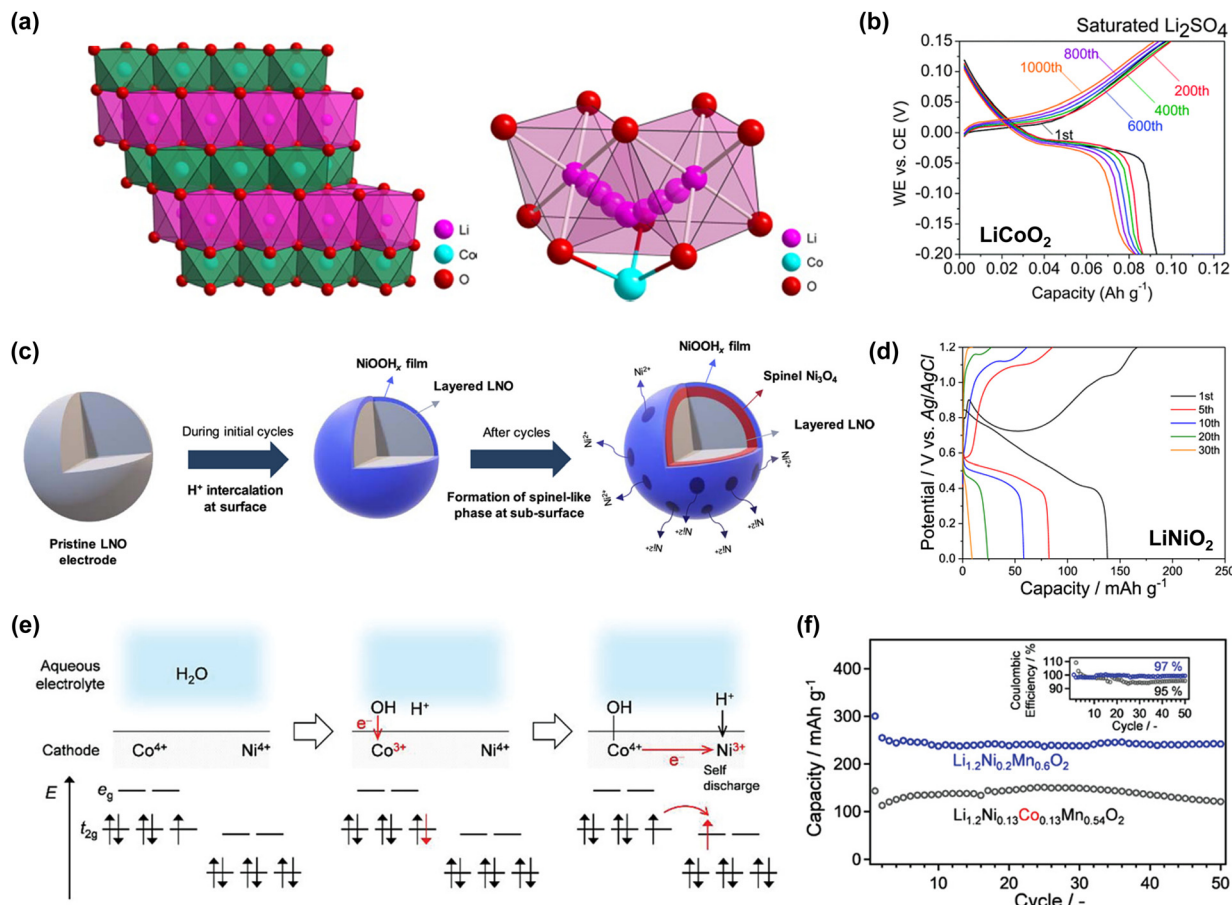


Fig. 22 (a) Crystal structure and Li^+ diffusion pathway in layered LiCoO_2 .²⁶⁸ (b) Long-term cycling of LiCoO_2 in a sat. Li_2SO_4 solution.²⁷³ (c) Degradation mechanism of LiNiO_2 in the aqueous electrolyte.²⁷⁴ (d) Charge/discharge curves of LiNiO_2 in 1.0 M $\text{LiNO}_3/\text{H}_2\text{O}$.²⁷⁴ (e) Schematic of the self-discharge process in the Co-doped layered oxide, $\text{Li}_{1.2}\text{Ni}_{0.13}\text{Co}_{0.13}\text{Mn}_{0.54}\text{O}_2$.²⁷⁵ (f) Cycling stability of $\text{Li}_{1.2}\text{Ni}_{0.2}\text{Mn}_{0.6}\text{O}_2$ and $\text{Li}_{1.2}\text{Ni}_{0.13}\text{Co}_{0.13}\text{Mn}_{0.54}\text{O}_2$ in the dihydrate melt, $\text{Li}(\text{TSFI})_{0.7}(\text{BETI})_{0.3}2\text{H}_2\text{O}$.²⁷⁵ Reprinted with permission from *Progress in Natural Science: Materials International* (a), *Energy & Environmental Science* (b), *ACS Applied Materials & Interfaces* (c), and *Advanced Science* (d).

capacity of 148 mA h g⁻¹ with a redox potential of 3.9 V vs. Li/Li^+ based on the $\text{Mn}^{3+}/\text{Mn}^{4+}$ redox reaction, which is within the operating potential window of most aqueous electrolytes.^{264,265} Moreover, its catalytic effect on water electrolysis is relatively low, and it exhibits low activation energies (23–25 kJ mol⁻¹) for interfacial Li^+ transfer reactions in aqueous solutions (Fig. 21).²⁶⁶ The dissolution of the transition metal from LiMn_2O_4 into the electrolyte can be sufficiently suppressed even in a mildly concentrated 5 M LiNO_3 solution (Fig. 21).²⁶⁷ Owing to these advantages, LiMn_2O_4 remains a mainstream cathode material for aqueous Li-ion batteries to date.

Lithium nickel manganese oxide, $\text{LiNi}_{0.5}\text{Mn}_{1.5}\text{O}_4$, with the same spinel structure, offers a theoretical capacity of 147 mA h g⁻¹, which is comparable to that of LiMn_2O_4 . Additionally, its high redox potential of 4.7 V vs. Li/Li^+ based on the $\text{Ni}^{2+}/\text{Ni}^{4+}$ redox reaction contributes to an increased battery output voltage.²⁶⁹ However, achieving stable cycling with it is challenging because its reaction potential does not lie within the operating potential window, even in highly salt-concentrated aqueous Li electrolytes (Table 1).

In 2009, Ruffo *et al.* introduced lithium cobalt oxide (LiCoO_2) in aqueous systems, a material long used in nonaqueous Li-ion

batteries.²⁷⁰ LiCoO_2 possesses an $\alpha\text{-NaFeO}_2$ -type structure, characterized by layered cationic ordering within a NaCl -type prototype (Fig. 22).^{271,272} It offers a theoretical capacity of 137 mA h g⁻¹ based on the $\text{Co}^{3+}/\text{Co}^{3.5+}$ redox couple [*i.e.*, Li_xCoO_2 ($0.5 \leq x \leq 1$)], with a reaction potential of 3.7 V vs. Li/Li^+ .^{271,272} In 2016, Yushin and co-workers reported that LiCoO_2 could achieve high reversibility in a saturated $\text{Li}_2\text{SO}_4/\text{H}_2\text{O}$ solution, with over 90% capacity retention after 1500 cycles at 1C (Fig. 22),²⁷³ highlighting its potential as a cathode material in aqueous Li-ion batteries.

In contrast, experiments on the aqueous full cell utilizing lithium nickel oxide, LiNiO_2 , whose structure is similar to that of LiCoO_2 , have not been as successful. Lee *et al.* demonstrated that LiNiO_2 undergoes consecutive H^+ intercalation and transition metal dissolution in aqueous electrolytes, forming a thick NiOOH_x film on the LiNiO_2 surface. This film impedes the insertion and extraction of Li^+ (Fig. 22).^{274,276–280}

On the other hand, recent reports have highlighted high-capacity aqueous batteries utilizing the oxygen redox of Li-rich layered oxides.²⁷⁵ A full cell comprising $\text{Li}_{1.2}\text{Ni}_{0.2}\text{Mn}_{0.6}\text{O}_2$ | $\text{Li}_4\text{Ti}_5\text{O}_{12}$ exhibited reversible cycling for over 100 cycles in a 28 m $\text{Li}(\text{TSFI})_{0.7}(\text{BETI})_{0.3}2\text{H}_2\text{O}$ dihydrate melt, with an initial

capacity close to 250–300 mA h g⁻¹ based on the cathode mass, surpassing the performance in nonaqueous electrolytes (Fig. 22). The study also emphasized the significance of transition metal types in active materials. For example, doping a small amount of Co into $\text{Li}_{1.2}\text{Ni}_{0.2}\text{Mn}_{0.6}\text{O}_2$ (forming $\text{Li}_{1.2}\text{Ni}_{0.13}\text{Co}_{0.13}\text{Mn}_{0.54}\text{O}_2$) led to a notable decrease in the capacity, to less than half that of $\text{Li}_{1.2}\text{Ni}_{0.2}\text{Mn}_{0.6}\text{O}_2$. It was suggested that the coexistence of Co^{4+} and Ni^{4+} in the Li-rich layered oxide triggered a rapid self-discharge process ($\text{Co}^{4+} + \text{Ni}^{4+} + \text{H}_2\text{O} \rightarrow \text{Co}^{3+}\text{--OH} + \text{Ni}^{4+} + \text{H}^+ \rightarrow \text{Co}^{4+}\text{--OH} + \text{Ni}^{3+} + \text{H}^+$), thereby resulting in significant degradation of the reversible capacity. Notably, the stable cycling of LiCoO_2 in an aqueous electrolyte can be achieved despite the high catalytic effect of Co^{n+} toward water electrolysis. This suggests that the catalytic effect of transition metals can vary significantly depending on the bulk and surface structures of the active material, the oxidation state of oxygen, the type of electrolyte, and other relevant factors.

Lithium iron phosphate, LiFePO_4 , has emerged as a useful cathode active material in aqueous electrolytes. LiFePO_4 comprises PO_4 tetrahedra and FeO_6 octahedra, with lithium atoms aligned in a one-dimensional [010] direction within the octahedral interstitial spaces. Since 1997, when Goodenough *et al.* first reported the $\text{Fe}^{2+}/\text{Fe}^{3+}$ redox reaction generating 3.4 V vs. Li/Li^+ ,^{281,282} LiFePO_4 has remained one of the prominent

cathode materials for nonaqueous Li-ion batteries because of its high theoretical capacity (170 mA h g⁻¹), substantial cycling stability without bulk structure degradation, and excellent thermal stability (limited oxygen generation even at temperatures above 700 °C).^{283,284} In 2010, Xia *et al.* introduced carbon-coated LiFePO_4 and an O_2 -free alkali 1 M Li_2SO_4 electrolyte to suppress side reactions such as proton insertion and Fe_2O_3 formation. This enabled the stable charge and discharge of an aqueous $\text{LiFePO}_4|\text{LiTi}_2(\text{PO}_4)_3$ full cell for over 1000 cycles (800 h) (Fig. 23).^{65,285,286}

Additionally, lithium manganese phosphate, LiMnPO_4 , was evaluated in aqueous systems and was expected to exhibit a low catalytic effect owing to manganese, as well as offer high cycling stability because of a robust polyanion structure similar to that of LiFePO_4 . However, the use of this material resulted in high battery resistance, low capacity, and poor cyclability, which could be attributed to the Jahn-Teller distortion. This distortion caused stronger local deformations and higher Li^+ migration barriers than LiFePO_4 , highlighting the complex interplay between the material structure and battery performance.^{288,289}

A crucial factor in selecting anode active materials for aqueous Li-ion batteries is their compatibility with the operating potential window of the electrolyte, as HER typically has lower overpotential than OER (Fig. 10). Early research explored layered vanadium oxide, $\text{VO}_2(\text{B})$, which features a monoclinic

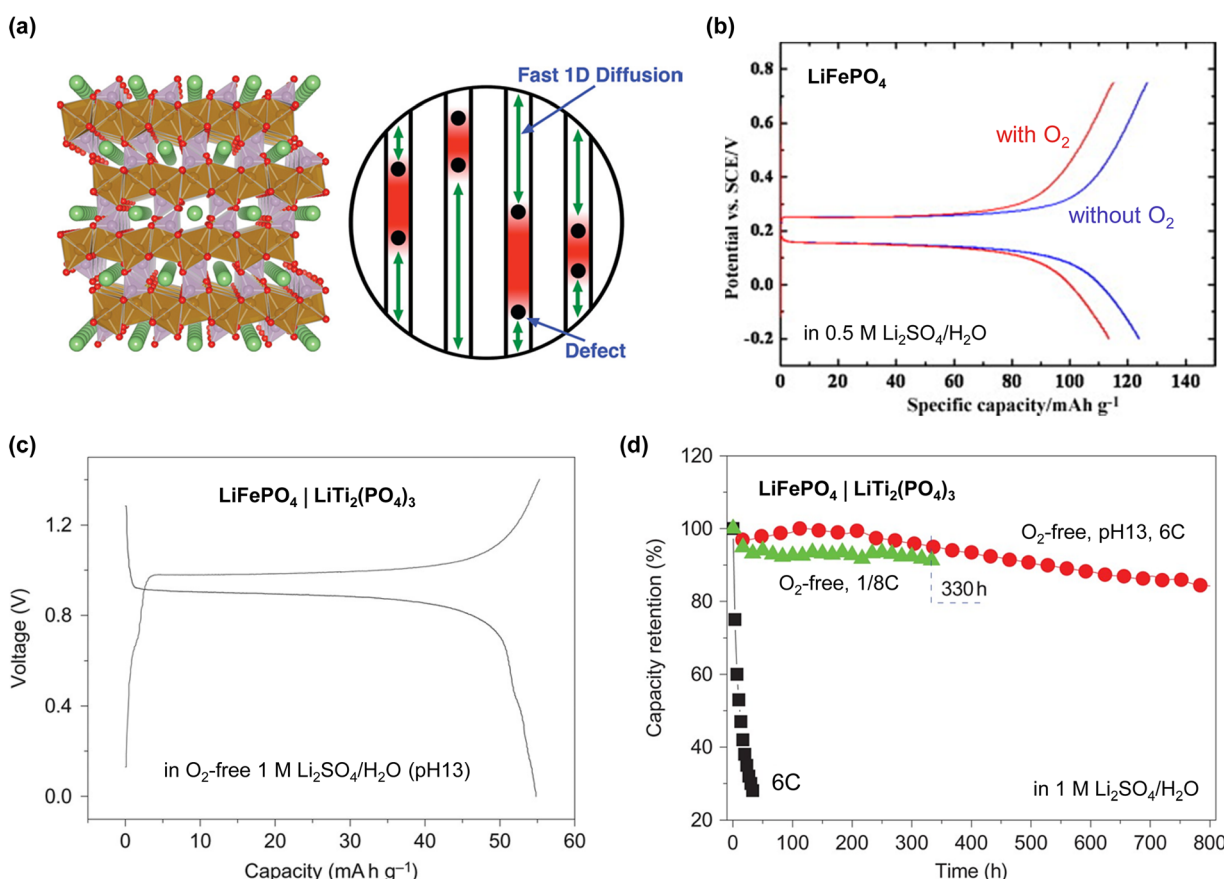


Fig. 23 (a) Crystal structure and Li^+ diffusion pathway in olivine LiFePO_4 .²⁸⁷ (b) Increased reversible capacity of LiFePO_4 in an O_2 -free aqueous electrolyte.²⁸⁶ (c) Charge/discharge curves and (d) long-term cycling of aqueous $\text{LiFePO}_4|\text{LiTi}_2(\text{PO}_4)_3$ full cells under the given conditions.⁶⁵ Reprinted with permission from *Nano Letters* (a), *Electrochimica Acta* (b) and *Nature Chemistry* (c) and (d).



structure with tunnels that facilitate fast Li^+ insertion and deintercalation. $\text{VO}_2(\text{B})$ offers a high theoretical capacity exceeding 320 mA h g^{-1} and a reaction potential (2.5 V vs. Li/Li^+) close to the HER potential at neutral pH (Fig. 24).^{290–292} Zhang and Dahn demonstrated that the reversibility of $\text{VO}_2(\text{B})$ was strongly dependent on the electrolyte pH.²⁹³ Using 4 M LiNO_3 solutions across a wide pH range, they revealed that electrolyte reduction at the anode surface occurred under nearly neutral conditions (pH 6), while strong alkaline environments (pH > 11) promoted V dissolution, resulting in rapid capacity fading. Although mildly alkaline solutions (pH 8–10) improved the capacity retention, significant electrode dissolution occurred, with over 20% of the $\text{VO}_2(\text{B})$ material dissolving in the electrolyte after just 10 cycles in a pH 8 solution. This led to a substantially low practical capacity of $80\text{--}160 \text{ mA h g}^{-1}$ and a low Coulombic efficiency (Fig. 24). The vulnerability to air oxidation and the complex synthesis of $\text{VO}_2(\text{B})$ further hindered its practical application in aqueous batteries.

To address the limitations of $\text{VO}_2(\text{B})$, Kohler *et al.* explored layered lithium vanadium oxide, LiV_3O_8 , as a potential alternative.⁵⁴ LiV_3O_8 offers a higher reaction potential (2.8 V vs. Li/Li^+) than $\text{VO}_2(\text{B})$, ensuring improved capacity retention in aqueous electrolytes, while reducing electrolyte decomposition at the anode surface. To evaluate the feasibility of LiV_3O_8 in practical battery configurations, researchers assembled aqueous Li-ion full cells with various cathode active materials, including common materials like $\text{LiNi}_{0.81}\text{Co}_{0.19}\text{O}_2$, $\text{LiNi}_{1/3}\text{Mn}_{1/3}\text{Co}_{1/3}\text{O}_2$, LiCoO_2 , LiMn_2O_4 , and LiFePO_4 . For example, an aqueous full cell utilizing $\text{LiNi}_{0.81}\text{Co}_{0.19}\text{O}_2$ cathodes and LiV_3O_8 anodes exhibited a capacity retention of 20% after 100 cycles at a constant current rate of 1 mA cm^{-2} , with a specific capacity of

20 mA h g^{-1} based on the total mass of the cathode and anode materials (Fig. 24).⁵⁴ In 2013, Zhao *et al.* reported significant advancements in the development of a highly reversible aqueous $\text{LiFePO}_4|\text{LiV}_3\text{O}_8$ full cell, achieving a remarkable capacity retention of over 99% after 100 cycles at a current density of 1C in an oxygen-free 9 M $\text{LiNO}_3/\text{H}_2\text{O}$ electrolyte (Fig. 24).²⁹⁶ However, the average discharge voltage of LiV_3O_8 -based full cells is inherently low (0.2–1.0 V) because of the high reaction potential of LiV_3O_8 , which limits the increase in the battery energy density.

The range of viable anode active materials has broadened significantly with the advent of highly salt-concentrated aqueous electrolytes. In 2015, the research group led by Wang and Xu demonstrated the feasibility of using Chevrel phase consisting of molybdenum sulfide clusters, Mo_6S_8 , as an anode active material in these electrolytes, despite the previously assumed non-reversibility of this compound in typical aqueous electrolytes due to lower reaction potentials.¹⁸ Mo_6S_8 exhibits a practical capacity of over 100 mA h g^{-1} in $\text{Li}_x\text{Mo}_6\text{S}_8$ ($0 < x < 3.6$) between 2.5 and 2.1 V vs. Li/Li^+ (Fig. 25).^{297,298} However, the high catalytic effect of Mo^{n+} poses challenges in maintaining high cycling stability, even in highly salt-concentrated aqueous electrolytes.

Anode active materials based on Ti are favored for aqueous batteries owing to their weak catalytic effect toward the HER. For instance, in the study by Wang *et al.* in 2006, lithium titanium phosphate, $\text{LiTi}_2(\text{PO}_4)_3$, featuring a Na super-ionic conductor (NASICON)-type structure, exhibited reversible Li^+ intercalation and deintercalation in aqueous electrolytes, despite a slightly lower reaction potential of 2.5 V vs. Li/Li^+ compared to the theoretical HER potential (Fig. 26).³⁰⁰ In 2007, Luo and Xia

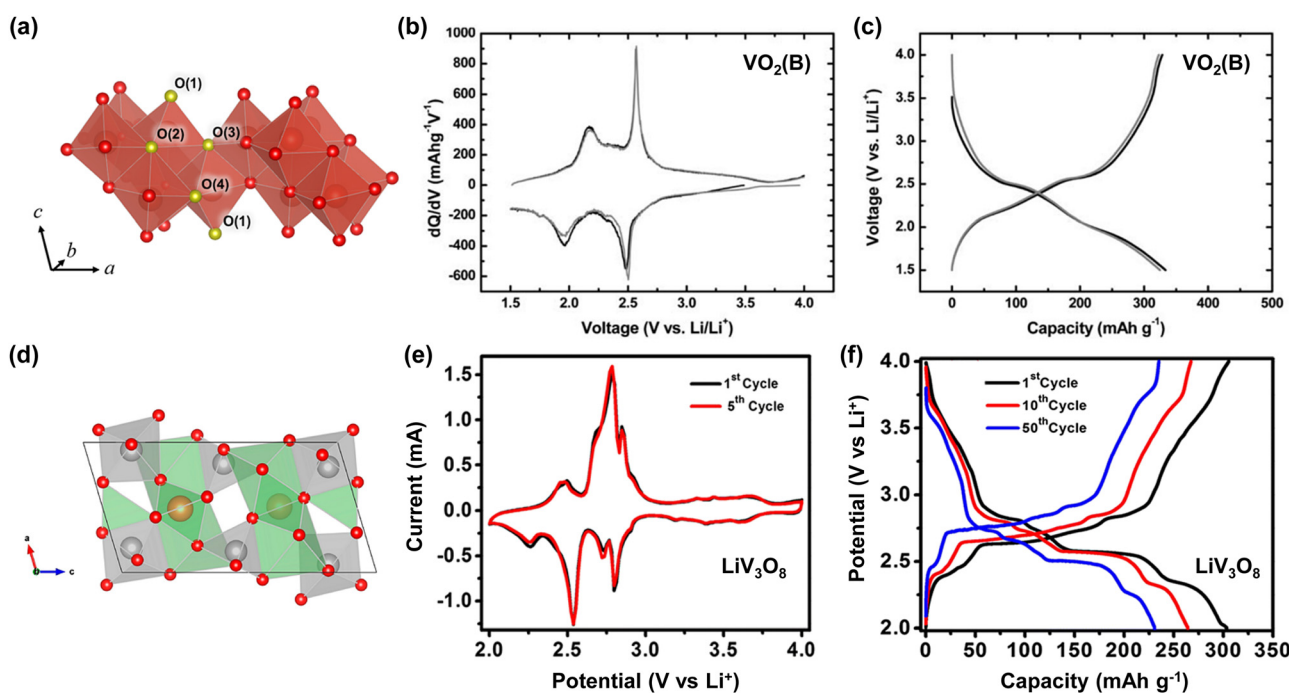


Fig. 24 Crystal structures and electrochemical properties of (a)–(c) $\text{VO}_2(\text{B})$,^{292,294} and (d)–(f) LiV_3O_8 .^{294,295} The lithiation/delithiation curves of $\text{VO}_2(\text{B})$ and LiV_3O_8 were obtained in 1 M LiClO_4 /ethylene carbonate : diethyl carbonate (1 : 1, v : v) and 1.0 M LiPF_6 /ethylene carbonate : dimethyl carbonate (1 : 1, v : v), respectively. Reprinted with permission from ACS Applied Energy Materials (a), Journal of Materials Chemistry (b) and (c), ACS Energy Letters (d), and Journal of Materials Science (e) and (f).



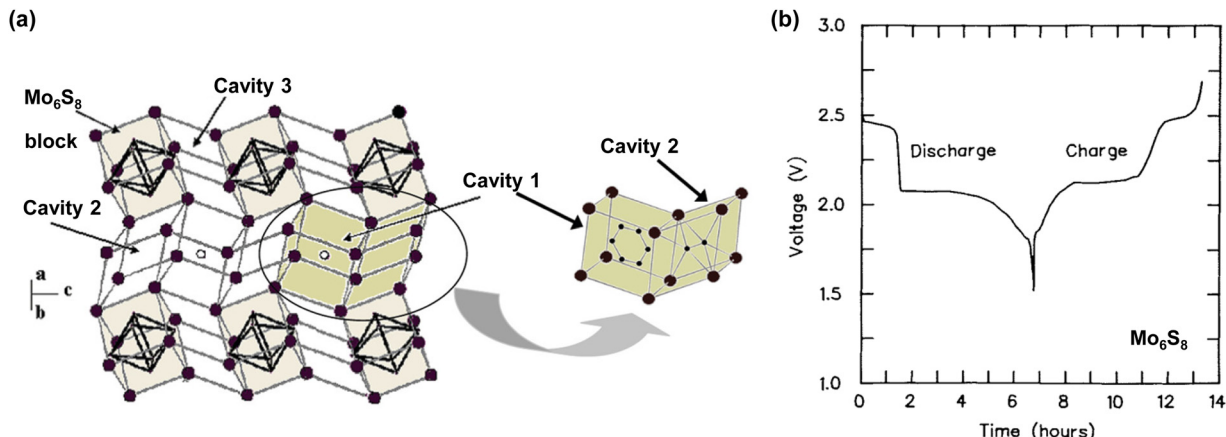


Fig. 25 (a) and (b) Crystal structure and electrochemical properties of Mo_6S_8 .^{297–299} Reprinted with permission from *Inorganic Chemistry* (a) and *Canadian Journal of Physics* (b).

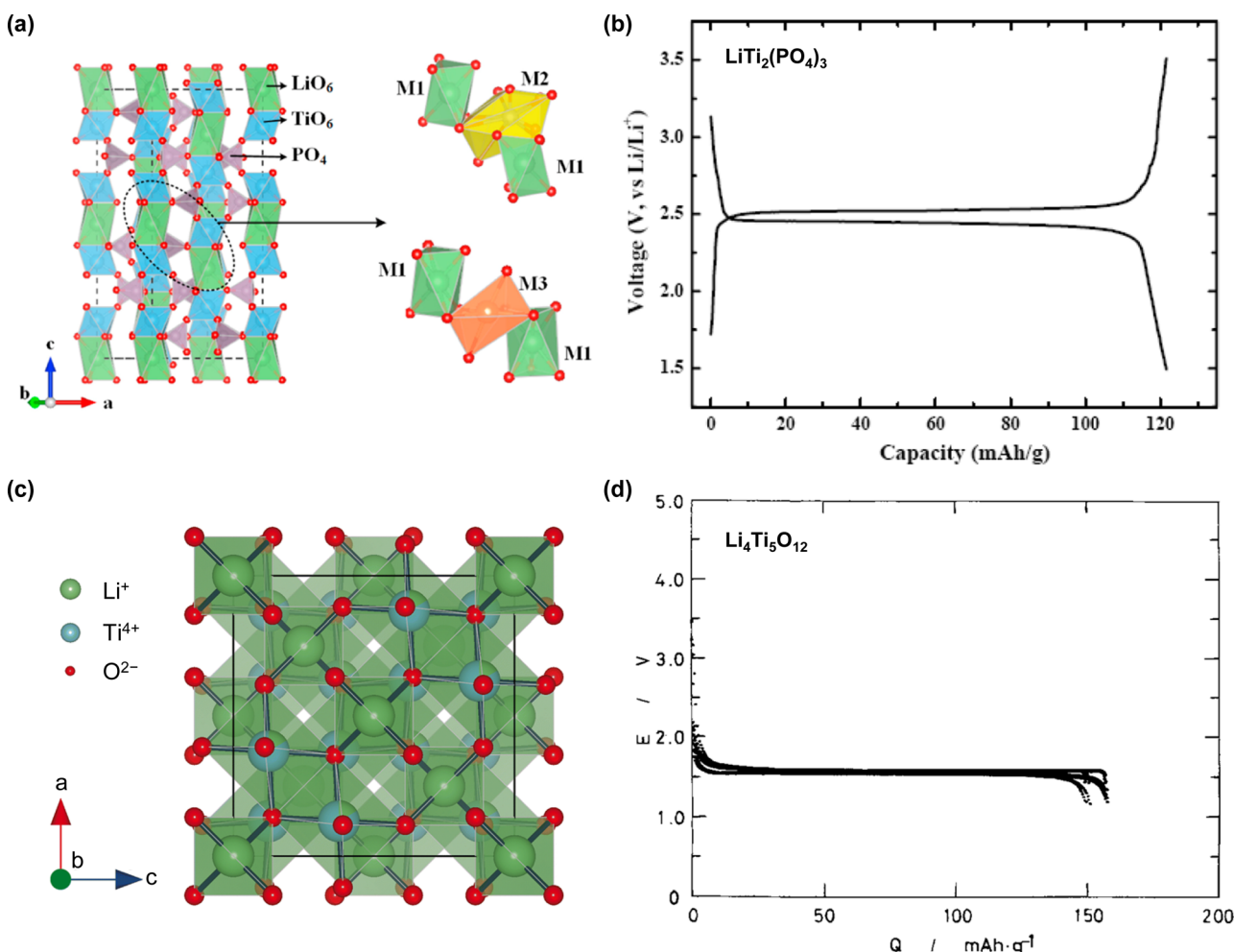


Fig. 26 Crystal structures and electrochemical properties of (a) and (b) $\text{LiTi}_2(\text{PO}_4)_3$ ^{60,301} and (c) and (d) $\text{Li}_4\text{Ti}_5\text{O}_{12}$.^{302,303} Lithiation/delithiation curves of $\text{LiTi}_2(\text{PO}_4)_3$ and $\text{Li}_4\text{Ti}_5\text{O}_{12}$ were obtained in 1 M LiPF_6 /ethylene carbonate : dimethyl carbonate : ethyl methyl carbonate (1:1:1, v:v:v) and 1 M LiClO_4 /ethylene carbonate : 1,2-dimethoxyethane (1:1, v:v), respectively. Reprinted with permission from *Energy Storage Materials* (a), *Advanced Functional Materials* (b), *Advanced Composites and Hybrid Materials* (c), and *Journal of The Electrochemical Society* (d).



successfully operated a 1.5 V aqueous $\text{LiMn}_2\text{O}_4\text{||LiTi}_2(\text{PO}_4)_3$ full cell, achieving a capacity retention of 80% after 200 cycles at 10 mA cm^{-2} in 1 M $\text{Li}_2\text{SO}_4/\text{H}_2\text{O}$ (Fig. 26).⁶⁰

In 2016, Yamada *et al.* introduced spinel lithium titanium oxide, $\text{Li}_4\text{Ti}_5\text{O}_{12}$, into the aqueous system,¹⁹ a material previously tested as an anode in nonaqueous Li-ion batteries by Ohzuku and Thackeray in 1994.^{304,305} $\text{Li}_4\text{Ti}_5\text{O}_{12}$ has a face-centered cubic structure in which the 32e site of space group $Fd\bar{3}m$ is occupied by oxygen anions, the tetrahedral 8a sites are occupied by Li^+ , and the octahedral 16d sites are occupied by Ti^{4+} . The remaining Li^+ are randomly distributed into the 16d sites at a Li/Ti weight ratio of 1/5 (Fig. 26).^{302,306–308} $\text{Li}_4\text{Ti}_5\text{O}_{12}$ exhibits a flat charge and discharge potential around 1.5–1.6 V vs. Li/Li^+ and possesses a theoretical capacity of 175 mA h g^{-1} . Ohzuku *et al.* reported that the overall variation in the lattice parameter of $\text{Li}_4\text{Ti}_5\text{O}_{12}$ was less than 0.1% before and after Li^+ intercalation (Fig. 26),^{303,308,309} exemplifying its “zero strain” characteristic, which is advantageous for maintaining SEI stability during battery cycling in aqueous electrolytes.³¹⁰ Although the reaction potential of $\text{Li}_4\text{Ti}_5\text{O}_{12}$ is lower than the HER potential in typical aqueous electrolytes, reversible Li^+ intercalation and deintercalation over hundreds of cycles are achievable in the highly-salt concentrated aqueous electrolytes due to its weak catalytic effect and upshifted reaction potentials (Fig. 7) (details of electrode potential shift will be further discussed in Section 6.1). However, the cycling stability of $\text{Li}_4\text{Ti}_5\text{O}_{12}$ rapidly decreases under harsh operating conditions such as low C-rates and elevated temperatures, which accelerate electrolyte decomposition on the anode surface. Moreover, its low ionic conductivity necessitates nano-size engineering and carbon coating, which ultimately increase the reaction area, thus making it challenging to inhibit the reduction decomposition of aqueous electrolytes.

5.2. Active materials for aqueous Na-ion batteries

Mn-based oxides and V-based phosphates have emerged as promising candidates for cathode active materials in aqueous Na-ion batteries, primarily because of their favorable reaction potential (Table 3). The electrochemical behavior of sodium manganese oxide, $\text{Na}_{0.44}\text{MnO}_2$, was first explored by Sauvage *et al.* in 2007.³¹¹ This material features an orthorhombic crystal structure with Na^+ tunnels that facilitate rapid Na^+ diffusion within the material (Fig. 27). However, its limited capacity, which ranges from 35 to 55 mA h g^{-1} in aqueous electrolytes, has restricted its practical application.

To address this limitation, researchers incorporated delithiated spinel manganese oxide, $\lambda\text{-MnO}_2$, which offers a capacity of 80 mA h g^{-1} in 1 M $\text{Na}_2\text{SO}_4/\text{H}_2\text{O}$.³¹² This capacity enhancement is attributed to an irreversible structural change upon initial Na^+ insertion, and is thought to result in the formation of a layered structure, followed by subsequent reversible cycling involving 0.6 Na atoms per formula unit (Fig. 27). Nevertheless, the absence of Na sources within $\lambda\text{-MnO}_2$ necessitates a pre-sodiation process before its practical utilization. Moreover, the high catalytic activity of $\lambda\text{-MnO}_2$ in water splitting leads to oxygen generation at its surface. This reaction consumes the electrolyte and Na sources and significantly degrades the battery performance.

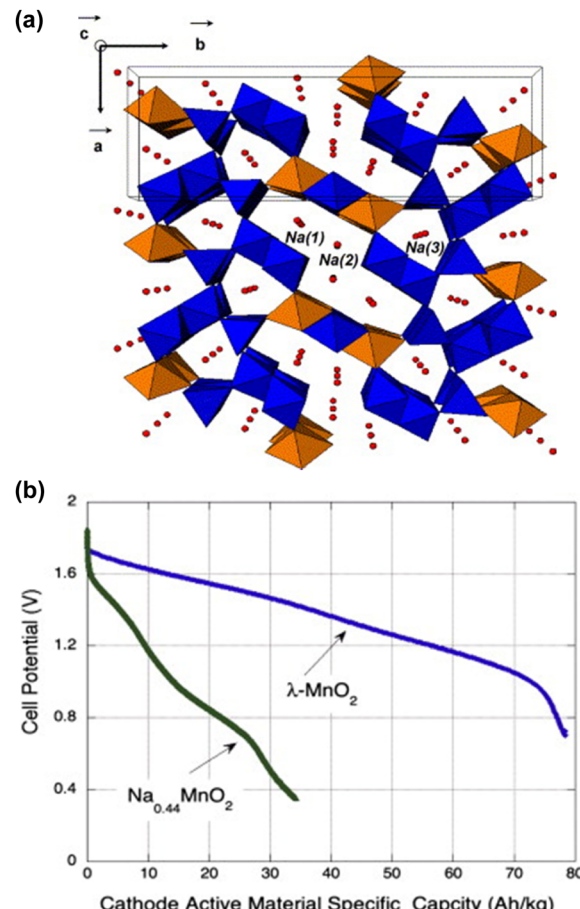


Fig. 27 Crystal structure of $\text{Na}_{0.44}\text{MnO}_2$.³¹¹ (b) Galvanostatic discharge curves of $\text{Na}_{0.44}\text{MnO}_2$ and $\lambda\text{-MnO}_2$ in 1 M $\text{Na}_2\text{SO}_4/\text{H}_2\text{O}$.³¹² Reprinted with permission from *Sensors and Actuators B* (a) and *Journal of Power Sources* (b).

Since 2014, when Song *et al.* initiated the study on the reversible reaction of sodium vanadium phosphate, $\text{Na}_3\text{V}_2(\text{PO}_4)_3$, various V-based phosphates in aqueous Na electrolytes have been extensively explored (Fig. 28).³¹³ Carbon-coated $\text{Na}_3\text{V}_2(\text{PO}_4)_3$ exhibits a capacity exceeding 110 mA h g^{-1} , with a redox potential of 3.4 V vs. Na/Na^+ based on the $\text{V}^{3+}/\text{V}^{4+}$ redox couple. Jin *et al.* achieved the stable cycling of $\text{Na}_3\text{V}_2(\text{PO}_4)_3$ ($\text{V}^{3+}/\text{V}^{4+}$ redox)– $\text{Na}_3\text{V}_2(\text{PO}_4)_3$ ($\text{V}^{3+}/\text{V}^{2+}$ redox) symmetric batteries, which retained 88% of the initial capacity after 100 cycles at 1C, with a reversible capacity of 40 mA h g^{-1} (based on the cathode and anode masses) and an output voltage of 1.7 V in a highly salt-concentrated aqueous Na electrolyte (17 M NaClO_4 + 2 M $\text{NaOTf}/\text{H}_2\text{O}$).¹⁵⁶ However, its overcharge stability, linked to the partial utilization of the $\text{V}^{4+}/\text{V}^{5+}$ redox couple, was inferior, leading to the substantial dissolution of V^{5+} into the electrolyte. This impeded the utilization of thick cathode electrodes, fast charge protocols, and wide-temperature-window operation in the aqueous system.^{314,315}

The research group led by Croguennec investigated the water stability and overcharge resistance of $\text{Na}_3(\text{VPO}_4)_2\text{F}_3$ – $\text{Na}_3(\text{VOPO}_4)_2\text{F}$ solid solutions, which achieved a high redox potential of 3.8 V vs. Na/Na^+ and a high theoretical capacity of ~ 130 mA h g^{-1} with two Na^+ per formula unit during

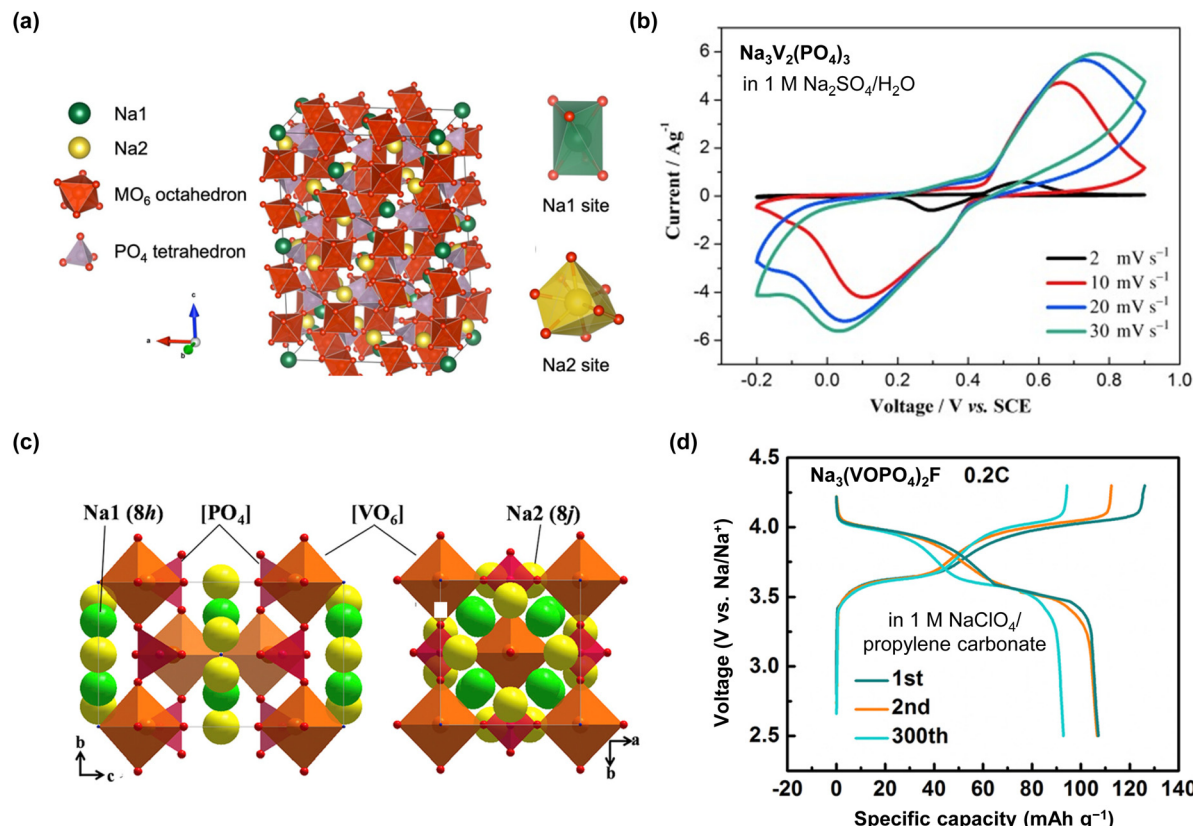


Fig. 28 Crystal structures and electrochemical properties of (a) and (b) $\text{Na}_3\text{V}_2(\text{PO}_4)_3$ ^{313,316} and (c) and (d) $\text{Na}_3(\text{VOPO}_4)_2\text{F}$.³¹⁷ Reprinted with permission from *Electrochemistry* (a), *ChemElectroChem* (b), and *Joule* (c) and (d).

reversible charge and discharge processes.³¹⁴ Their investigations revealed that a series of solid solution compounds, denoted as $\text{Na}_3\text{V}_{2-x}\text{V}_x^{4+}(\text{PO}_4)_2\text{F}_{3-x}\text{O}_x$ (where $0 \leq x \leq 2$), demonstrated complete water stability. Even a water wash could effectively remove the soluble and undesirable impurities formed during synthesis, without compromising their electrochemical performance in batteries. This indicated the potential use of this solid solution as a cathode active material in aqueous Na-ion batteries. Moreover, it was found that oxygen-rich compositions, such as $\text{Na}_3(\text{VOPO}_4)_2\text{F}$, remained stable during overcharging, with neither the local environment of V nor its oxidation state being altered. Indeed, a test on the $\text{Na}_3(\text{VOPO}_4)_2\text{F}|\text{NaTi}_2(\text{PO}_4)_3$ full cell conducted by Rebel *et al.* demonstrated long-term cycling over 500 cycles at both, a low temperature (-10°C) and room temperature (30°C), in a 25 m NaFSI + 10 m NaFTFSI ($\text{NaN}(\text{SO}_2\text{F})(\text{SO}_2\text{CF}_3)$)/ H_2O electrolyte.⁸⁹

Sodium titanium phosphate, $\text{NaTi}_2(\text{PO}_4)_3$, has been extensively studied as an anode active material for aqueous Na-ion batteries, showing significant promise owing to its efficient electrochemical performance and good chemical stability (Table 3 and Fig. 29).³¹⁸ This material features a three-dimensional framework that allows the reversible intercalation of two Na^+ at potentials close to 2.1 and 2.2 V vs. Na/Na^+ (corresponding to the $\text{Ti}^{4+}/\text{Ti}^{3+}$ redox reaction), aligning closely with the HER potential in aqueous Na electrolytes. The use of carbon coating and nanoparticle engineering has further enhanced its capacity to an impressive

value of $\sim 130 \text{ mA h g}^{-1}$, which approaches its theoretical limit while ensuring rapid charge and discharge performance.

Suo *et al.* demonstrated the remarkable stability of the $\text{NaTi}_2(\text{PO}_4)_3$ anode in an aqueous Na full cell paired with a $\text{Na}_{0.66}\text{Mn}_{0.66}\text{Ti}_{0.34}\text{O}_2$ cathode in a 9.3 m NaOTf/ H_2O solution. Their findings showed that 93% of the initial capacity was retained after 1200 cycles at 1C.¹³⁶ However, challenges remain, primarily owing to the increased surface area associated with nanosizing, which exacerbates electrolyte decomposition on the anode surface.

Layered vanadium oxides, $\text{V}_x\text{O}_y \cdot n\text{H}_2\text{O}$, have been evaluated as potential anode materials in aqueous Na-ion batteries.^{124,320} Wu *et al.* conducted the galvanostatic cycling of $\text{V}_2\text{O}_5 \cdot 0.6\text{H}_2\text{O}$ within a potential range of 0–1.0 V vs. the saturated calomel electrode (SCE) at a constant current of 100 mA g^{-1} .³²⁰ They observed reversible capacities of 37, 43, and 50 mA h g^{-1} in Li_2SO_4 , Na_2SO_4 , and K_2SO_4 solutions, respectively. Furthermore, Deng *et al.* demonstrated that $\text{Na}_2\text{V}_6\text{O}_{16} \cdot n\text{H}_2\text{O}$ provided a reversible capacity of 40 mA h g^{-1} in 1 M $\text{Na}_2\text{SO}_4/\text{H}_2\text{O}$ under operating potentials in the range from -0.05 to -0.65 V vs. SCE at a constant current of 40 mA g^{-1} .¹²⁴ However, layered vanadium oxides generally exhibit poor capacity retention and Coulombic efficiency owing to irreversible structural changes upon Na^+ insertion and the dissolution of vanadium ions into the bulk electrolyte. Additionally, as noted in Table 3, most aqueous Na-ion batteries exhibit output voltages below 1.7 V, which is considerably lower than



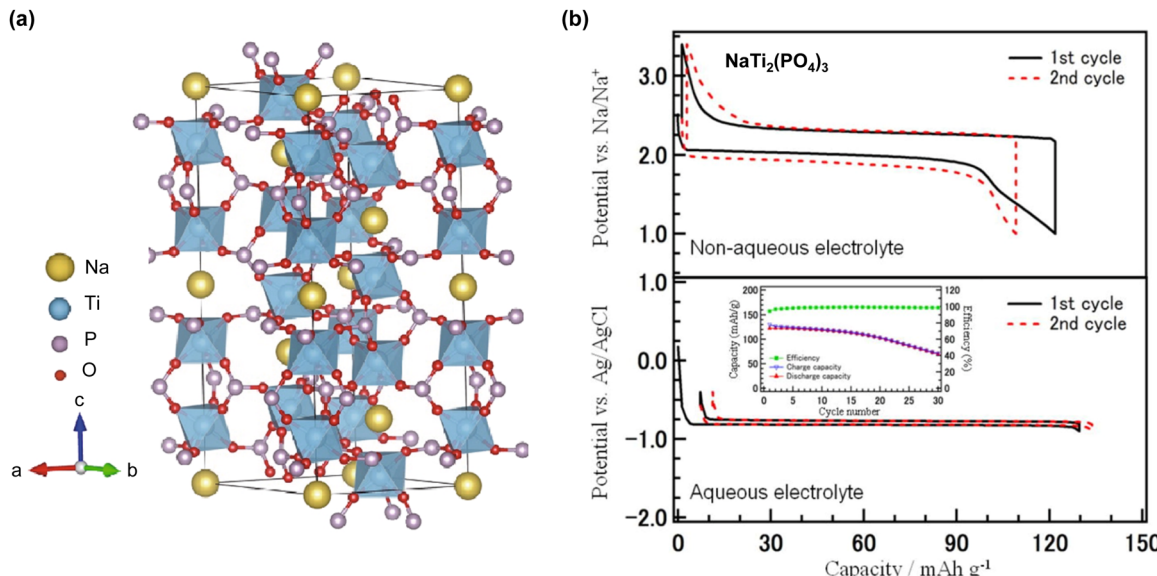


Fig. 29 (a) and (b) Crystal structure and electrochemical properties of $\text{NaTi}_2(\text{PO}_4)_3$.^{318,319} The sodiation/desodiation curves of $\text{NaTi}_2(\text{PO}_4)_3$ were obtained in 1 M NaClO_4 /ethylene carbonate : dimethyl carbonate (1:1, v:v) and 2 M Na_2SO_4 /H₂O. Reprinted with permission from *Nano-micro Letters* (a) and *Journal of The Electrochemical Society* (b).

those of their nonaqueous counterparts (which typically exceed 3 V). This discrepancy is largely attributed to the narrow operating potential window of aqueous Na electrolytes (Table 3), necessitating the use of anode active materials like $\text{NaTi}_2(\text{PO}_4)_3$ and $\text{V}_x\text{O}_y \cdot n\text{H}_2\text{O}$, which offer a substantially higher reaction potential compared to those used in nonaqueous systems, such as hard carbons (0.3 V vs. Na/Na^+).

5.3. Active materials for aqueous K-ion batteries

For aqueous K-ion batteries, Prussian blue, $\text{Fe}_4[\text{Fe}(\text{CN})_6]_3$, and its analogs, $\text{A}_x\text{Tm}_1\text{Tm}_2(\text{CN})_6(\text{H}_2\text{O})_n$, where A represents alkali metal ions (Li, Na, or K) and Tm_1 , Tm_2 represent transition metal ions (e.g., Fe, Mn, Ni, Co),³²¹ have been primarily employed as cathode active materials. This choice is influenced by the considerably larger ionic radius of K^+ (1.38–1.46 Å) compared to those of Li^+ (0.60–0.79 Å) and Na^+ (1.02–1.07 Å) (Table 2).^{322–324} Their open and flexible frameworks provide ample void sites for the rapid transport and storage of large metal ions like K^+ .^{322–324}

Neff *et al.* first reported the electrochemical activity of Prussian blue in aqueous electrolytes in 1978 (Fig. 30).³²⁵ Subsequent developments of its analogs have aimed to achieve higher capacity, redox potential, and faster charge/discharge properties. For instance, $\text{K}_{1.85}\text{Fe}_{0.33}\text{Mn}_{0.67}[\text{Fe}(\text{CN})_6]_{0.98} \cdot 0.77\text{H}_2\text{O}$ demonstrated a high capacity of 130 mA h g⁻¹ with a redox potential exceeding 4 V (vs. K/K^+). It retained 70% of its initial capacity at 100C in a 22 m KOTf aqueous solution (Fig. 30).¹²² However, challenges persist during synthesis, particularly in achieving uniform control over the contents and distribution of structural water, alkali metal, and transition metal ions, often leading to defect formation in the framework and deteriorating the electrochemical performance. Furthermore, most organic materials exhibit high solubility in water, and the dissolution of transition metals during charge and discharge processes can occur. Notably, the

calendar life of Prussian blue and most of its analogs is less than 30 days, suggesting that their impressive cycling numbers may have been overestimated under high-rate cycling conditions, masking issues of dissolution and parasitic reactions.³²⁶

To address the stability issue in aqueous K-ion batteries, Hosaka *et al.* explored the use of highly salt-concentrated aqueous electrolytes. They tested the electrochemical stability of a $\text{K}_2\text{Fe}_{0.5}\text{Mn}_{0.5}[\text{Fe}(\text{CN})_6]$ electrode in 20 m KOTf-2.8H₂O, 31 m KFSI-1.8H₂O, and 55 m K(FSI)_{0.6}(OTf)_{0.4}·1.0H₂O electrolytes.¹⁶⁷ The results demonstrated that a higher salt concentration in the electrolyte provides better stability. For instance, a capacity retention of 72% after 200 cycles at 1C was achieved in the 55 m K(FSI)_{0.6}(OTf)_{0.4}·1.0H₂O electrolyte, significantly surpassing the results achieved with 20 m KOTf-2.8H₂O (21%) and 31 m KFSI-1.8H₂O (36%). Scanning electron microscopy (SEM) observations and inductively coupled plasma-atomic emission spectroscopy tests indicated that the highly salt-concentrated K(FSI)_{0.6}(OTf)_{0.4}·1.0H₂O electrolyte helped prevent the dissolution of both, transition metals from the cathode active material and the cathode active material itself (Fig. 30).

However, despite these advancements, achieving perfect control over dissolution remains a significant challenge, as evidenced by the relatively poor cycling stability compared to those of metal oxide-based cathode active materials in Li and Na aqueous electrolytes (Tables 1, 3 and 4). Furthermore, the presence of large void volumes in Prussian blue and its analogs decreases the battery energy density per unit volume (W h L⁻¹), necessitating the further development of cathode active materials for aqueous K-ion batteries.

In the realm of anode active materials for aqueous K-ion batteries, PTCDI, a dark red pigment with a monoclinic lattice structure characterized by the $P2_1/n$ space group, has been the primary focus of studies.^{328,329} In 2019, the team led by Hu

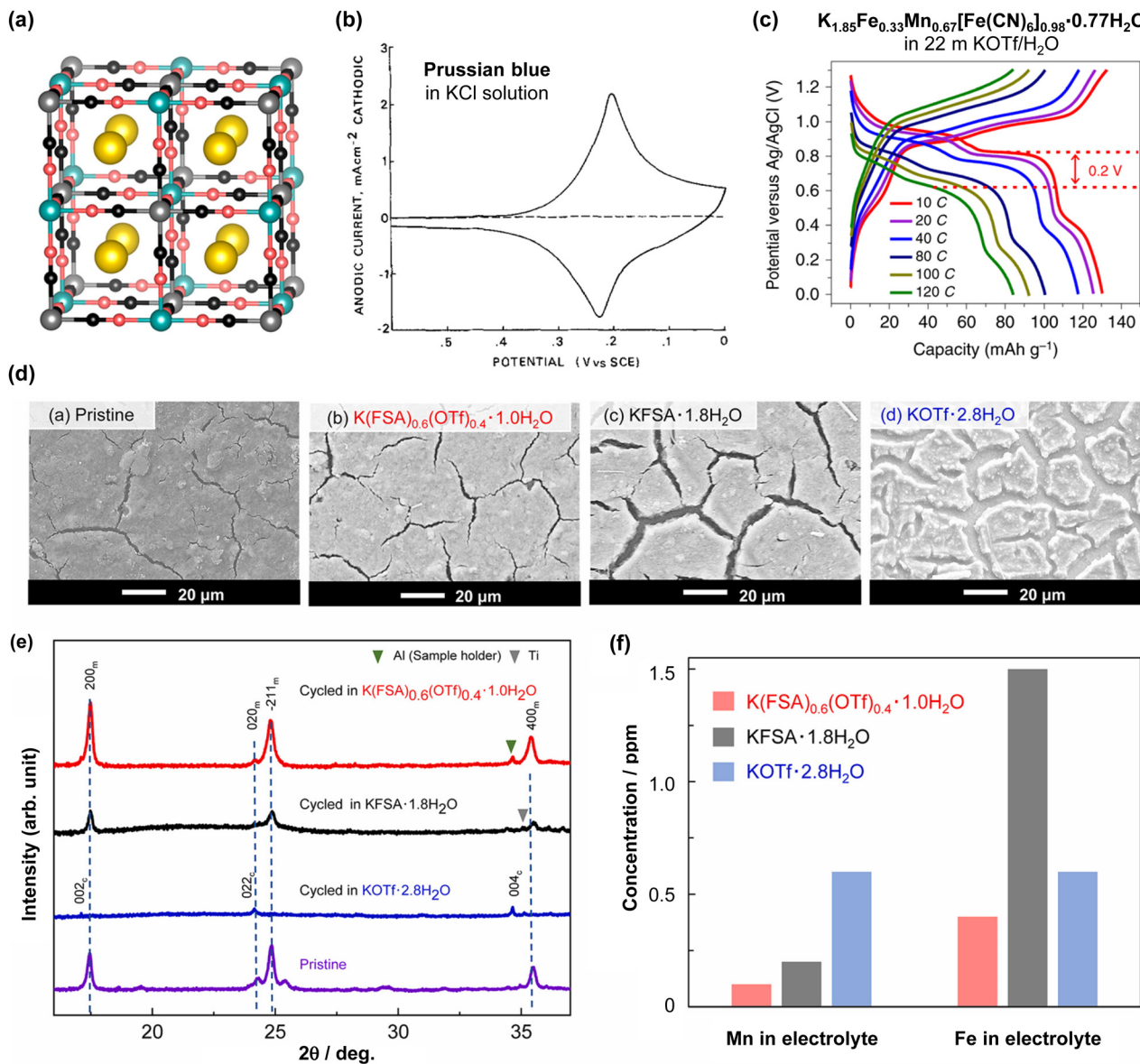


Fig. 30 (a) Crystal structure of Prussian blue and its analogues.³²⁷ Electrochemical properties of (b) Prussian blue in 0.1 M KCl/H₂O³²⁵ and (c) K_{1.85}Fe_{0.33}Mn_{0.67}[Fe(CN)₆]_{0.98}·0.77H₂O in 22 m KOTf/H₂O.¹²² (d) SEM images and (e) X-ray diffraction (XRD) patterns of K₂Fe_{0.5}Mn_{0.5}[Fe(CN)₆] electrodes before and after 200 cycles in diverse aqueous K electrolytes.¹⁶⁷ (f) Inductively coupled plasma-atomic emission spectrometry results for the electrolytes used in the K₂Fe_{0.5}Mn_{0.5}[Fe(CN)₆] cell test.¹⁶⁷ KFSA and KFSI refer to the same chemical compound, KN(SO₂F)₂. Reprinted with permission from ACS Applied Materials & Interfaces (a), Journal of The Electrochemical Society (b), Nature Energy (c), and Journal of Power Sources (d)–(f).

showcased its electrochemical activation in an aqueous K electrolyte, highlighting several advantageous features, including a high reversible capacity exceeding 120 mA h g⁻¹ within a reaction potential range of 1.7–3.0 V vs. K/K⁺, limited solubility in water, and high ionic conductivity, which enabled rapid K⁺ insertion and extraction over a broad temperature range.¹²² An aqueous K-ion full cell coupled with a K_{1.85}Fe_{0.33}Mn_{0.67}[Fe(CN)₆]_{0.98}·0.77H₂O cathode and a PTCDI anode delivered a high capacity of 65 mA h g⁻¹ based on the total mass of the cathode and anode, with an output voltage of 1.3 V, and demonstrated high cycling stability, retaining 77% of the initial capacity after 2000 cycles at 4C (Fig. 31).¹²²

Another noteworthy candidate is potassium titanium phosphate, KTi₂(PO₄)₃, which features a three-dimensional framework composed of PO₄ tetrahedra and TiO₆ octahedra, offering ample interstitial sites for K⁺ insertion.^{330,331} This material exhibits lower potential hysteresis in aqueous electrolytes compared to nonaqueous systems and offers a low reaction potential of 1.6–2.0 V vs. K/K⁺ with the Ti⁴⁺/Ti³⁺ redox couple (Fig. 31).¹⁸⁸ However, the notably low ionic and electronic conductivities of KTi₂(PO₄)₃ necessitate enhancements such as carbon coating and nanoparticle engineering. These modifications, while beneficial for the conductivity, reduce the battery energy density and increase surface reaction areas, leading to severe electrolyte decomposition.



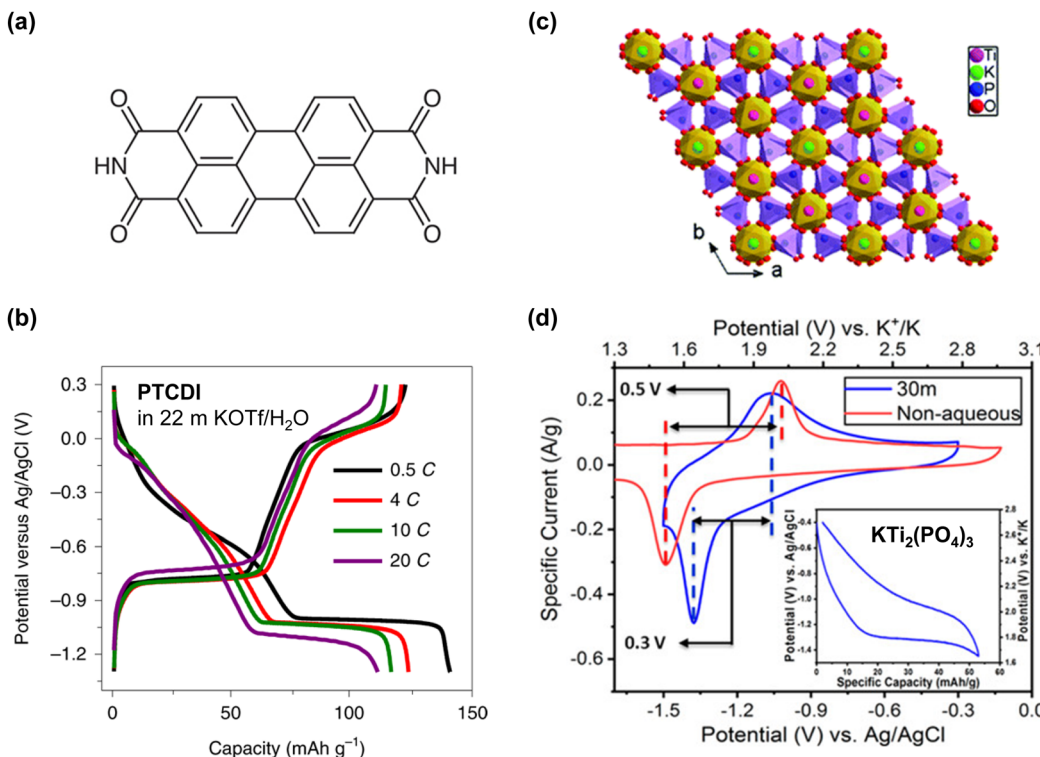


Fig. 31 (a) and (b) Molecular structure and electrochemical properties of PTCI,¹²² (c) and (d) Crystal structure and electrochemical properties of $\text{KTi}_2(\text{PO}_4)_3$ in 30 m KOAc/H₂O.^{188,330} Reprinted with permission from *Nature Energy* (a) and (b), *Chemical Communications* (c) and *ACS Energy Letters* (d).

Furthermore, the reaction potential of both PTCDI and $\text{KTi}_2(\text{PO}_4)_3$ is still significantly higher than those of the anode active materials used in nonaqueous K-ion batteries (e.g., graphite; ~ 0.1 V vs. K/K^+) owing to the narrow operating potential window of aqueous K electrolytes (Table 7).³³² This limits the output voltage of the aqueous K-ion full cell under 1.5 V, which is not comparable with that of nonaqueous batteries providing an output of over 3 V.

Indeed, the cathode and anode active materials currently demonstrated in aqueous batteries are primarily borrowed from those employed in nonaqueous batteries. The practical utilization and performance improvement of aqueous batteries may remain largely limited unless distinct design strategies for active materials are developed. Effective methods must be developed to enhance ionic and electronic conductivities, without increasing the surface reaction areas, and to mitigate issues such as water solubility, transition metal dissolution, catalytic effects on water electrolysis, carrier ion-blocking oxide film formation, and proton intercalation under various operating conditions like extreme temperatures, low C-rates, and long-term storage in a charged state.

6. Strategies for overcoming challenges with aqueous batteries

The challenges of enhancing the narrow operating potential window, low output voltage, and cycling performance of aqueous rechargeable batteries have led to the development of various

strategies, each with its own challenges and potential benefits. Initial efforts focused on manipulating the thermodynamic potential of the HER and OER by adjusting the pH of the electrolyte. Subsequent strategies involved the *ex situ* coating of electrodes with inorganic materials such as Al_2O_3 , TiO_2 , SiO_2 , or organic compounds like carbons and polymers. These coating layers are intended to prevent direct contact between the electrode and the aqueous electrolyte, thereby helping to reduce electrolyte decomposition, kinetically. However, the approach faces several challenges, including non-uniformity in the coatings, inadequate ion conductivity of the coating layer, and reduced electrical conductivity of the electrode. Additionally, the continuous expansion and contraction of active materials during charging and discharging can damage the coating. The risk of dissolution or breakdown of the coating materials in aqueous electrolytes also remains, thereby questioning the universal applicability of coating techniques across various carrier ions.

For instance, Droguet *et al.* tested the chemical stability of a LiF coating in a standard nonaqueous electrolyte (1 M LiPF₆ in ethylene carbonate:dimethyl carbonate) and in highly salt-concentrated aqueous electrolytes (20 m LiTFSI/H₂O and 28 m Li(TFSI)_{0.7}(BETI)_{0.3}·2H₂O) (Fig. 32).³³³ The result indicated minimal gas release when the LiF-coated Li metal encountered the nonaqueous electrolyte (approximately $0.5 \times 10^{-2}\%$), nearing the detection limit of a gas chromatography-flame ionization detector. In contrast, when the LiF-coated Li metal was exposed to a 20 m LiTFSI solution, significant amounts of hydrogen gas (4–8%) were detected, accompanied by nearly 80% depletion of

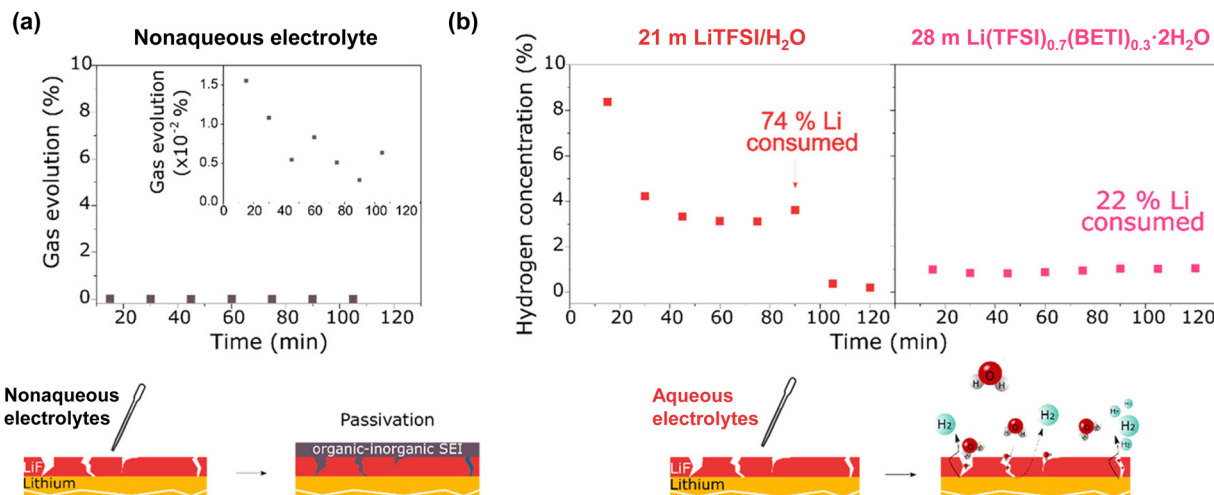


Fig. 32 Estimated gas evolution during exposure of LiF-protected Li metal to (a) nonaqueous and (b) highly salt-concentrated aqueous electrolytes.³³³ Reprinted with permission from ACS Energy Letters.

the Li metal. Similarly, ~1% of hydrogen gas was continuously detected with 28 m Li(TFSI)_{0.7}(BETI)_{0.3}·2H₂O, resulting in ~22% of the Li metal being consumed after 2 h.

These findings suggest that while highly salt-concentrated aqueous electrolytes lower the solubility of inorganic (LiF) coatings, such coatings remain stable only in nonaqueous systems and are fundamentally unstable in aqueous solutions.

Strategies to completely separate the electrode and electrolyte have also been introduced. In 2005, Visco *et al.* demonstrated aqueous Li-ion batteries based on a glass-protected Li metal.^{334,335} In 2013, Holze *et al.* inserted a lithium super-ionic conductor (LISICON, Li₂O-Al₂O₃-SiO₂-P₂O₅-TiO₂-GeO₂) between the cathode and Li metal anode, through which aqueous electrolytes could not pass.³³⁶ They constructed a full cell with a LiMn₂O₄|0.5 M Li₂SO₄ aqueous solution|LISICON|Li configuration and cycled it between 3.7 and 4.25 V at a constant current of 100 mA g⁻¹. This setup demonstrated high initial Coulombic efficiency (88.5%) and negligible capacity degradation over 30 cycles, showcasing performance levels similar to those of nonaqueous systems (Fig. 33).

In a similar vein, in 2017, Wang and Xu groups devised a Li⁺-conducting hydrophobic layer by mixing 0.5 M LiTFSI/highly fluorinated ether (1,1,2,2-tetrafluoroethyl-2,2,2-trifluoroethyl ether, HFE) with 10 wt% polyethylene oxide at 70 °C. This layer was then applied over anodes made of Li metal or graphite (Fig. 33).³³⁷ Fifty cycles in various 4 V-class full cells, including LiVPO₄F|HFE-based layer|Li, LiVPO₄F|HFE-based layer|graphite and LiMn₂O₄|HFE-based layer|Li configurations, were achieved using a constant current of 0.3C in a 21 m LiTFSI + 7 m LiOTf/H₂O + 10 wt% polyvinyl alcohol electrolyte. Despite achieving multiple cycles, the systems showed low Coulombic efficiency (98–99.5%) and continuous capacity degradation.

Although employing a Li⁺-conducting layer to fully isolate the electrode from the electrolyte offers the potential to achieve higher output voltages in aqueous battery systems, its effectiveness is significantly constrained. Challenges include the existence of a thick coating layer that drastically reduces ion conductivity, chemical instability under extreme pH conditions, and the

complexity and high cost of manufacturing processes. These issues echo the difficulties encountered with previously discussed *ex situ* coating methods, motivating researchers to develop functional electrolytes and optimize the battery potential diagram to address the limitations effectively.

6.1. Optimization of potential diagram

To maximize the battery performance, the potential diagram between the electrode reaction potential and the electrolyte potential window must be considered carefully. For example, the reaction potential of the Li₄Ti₅O₁₂ anode (1.5–1.6 V *vs.* Li/Li⁺) is lower than the HER potential in most aqueous electrolytes. Nevertheless, Yamada *et al.* demonstrated in 2016 and 2019 that reversible lithiation and delithiation of the Li₄Ti₅O₁₂ anodes are achievable using highly salt-concentrated aqueous electrolytes, specifically 28 m Li(TFSI)_{0.7}(BETI)_{0.3}·2H₂O and 56 m Li(PTFSI)_{0.6}(TFSI)_{0.4}·1H₂O electrolytes.^{19,91} This is attributed to not only a significant decrease in the water activity, facilitating the rapid growth and maintenance of the SEI, but also an upward shift in the reaction potential of the Li₄Ti₅O₁₂ anode within these electrolytes (Fig. 34). Importantly, this upshifted electrode potential reduces the thermodynamic driving force for the electrolyte reduction and alleviates the burden on the kinetic support provided by the SEI, thereby largely suppressing electrolyte degradation on the anode surface.⁴⁸

The equilibrium potential (*E*) of an electrode reaction (*i.e.*, the intercalation and deintercalation of carrier ions into active materials) is influenced by the activity (*a*) of carrier ions in the electrolyte.^{338–340} For instance, according to the Nernst equation (eqn (17)), the value of *E* in a highly salt-concentrated aqueous electrolyte, 56 m Li(PTFSI)_{0.6}(TFSI)_{0.4}·1H₂O, is expected to be higher than that in a 1 m solution, 1 m LiTFSI/H₂O.⁸⁵

$$E = E^0 + \frac{RT}{nF} \ln a_{\text{Li}^+} \quad (17)$$

Here, *E*⁰, *R*, *T*, *n*, and *F* represent the standard potential, gas constant, absolute temperature, number of transferred



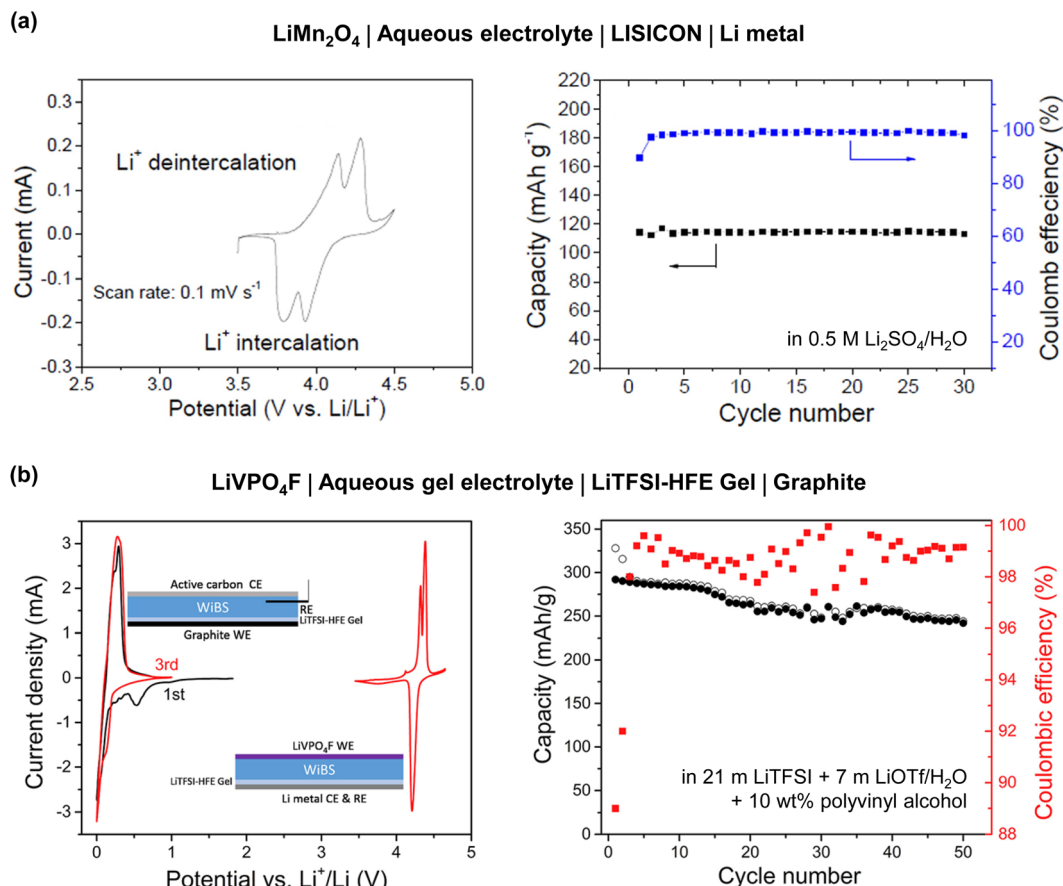


Fig. 33 Electrochemical properties of the (a) LiMn_2O_4 | LISICON | Li full cell in $0.5 \text{ M Li}_2\text{SO}_4/\text{H}_2\text{O}$ ³³⁶ and (b) LiVPO_4F | LiTFSI-HFE Gel | Graphite full cell in $21 \text{ M LiTFSI} + 7 \text{ M LiOTf}/\text{H}_2\text{O} + 10 \text{ wt\% polyvinyl alcohol}$ electrolyte.³³⁷ Reprinted with permission from *Scientific Reports* (a) and *Joule* (b).

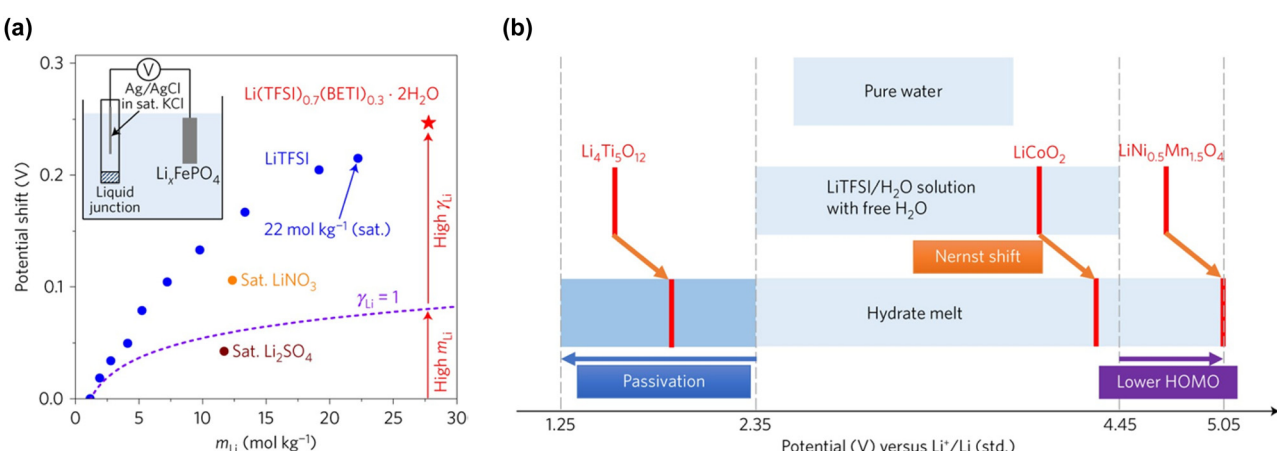


Fig. 34 (a) Electrode potential shift depending on the electrolyte concentration. (b) Relationship between the operating potential windows of aqueous electrolytes and the reaction potentials of electrodes. The upshifted electrode potential in the hydrate melt contributes to mitigating electrolyte reduction on the $\text{Li}_4\text{Ti}_5\text{O}_{12}$ surface.¹⁹ Reprinted with permission from *Nature Energy*.

electrons, and Faraday constant, respectively. The activity is the product of the concentration (c) and activity coefficient (r). Thus, assuming that the measurement was conducted at 25°C , the potential shift ($\Delta E = E_{56\text{m}} - E_{1\text{m}}$) can be estimated as follows:

$$\begin{aligned} \Delta E &= E_{56\text{m}} - E_{1\text{m}} = \frac{RT}{nF} \ln \frac{a_{\text{Li}^+}(56\text{m})}{a_{\text{Li}^+}(1\text{m})} \\ &= 0.059 \times \log \frac{c_{\text{Li}^+}(56\text{m})r_{\text{Li}^+}(56\text{m})}{c_{\text{Li}^+}(1\text{m})r_{\text{Li}^+}(1\text{m})} \end{aligned} \quad (18)$$

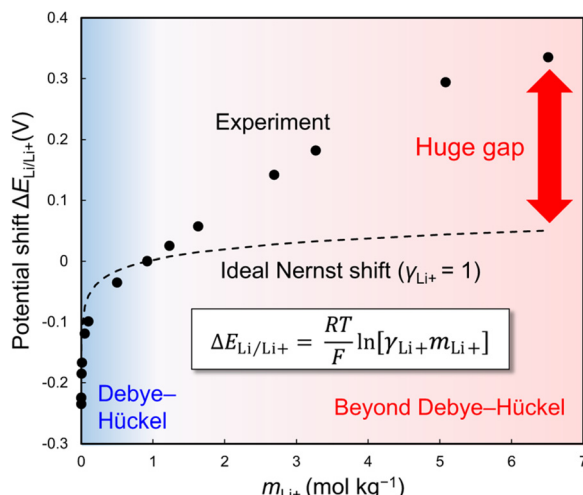


Fig. 35 Anomalous shift in the Li/Li^+ redox potential. The large gap between the experimentally obtained and calculated potential shifts cannot be explained by either the classical Debye–Hückel theory or its phenomenological extensions.^{342,343} Reprinted with permission from *Nature Communications*.

The measured electrode reaction potential of the $\text{Li}_4\text{Ti}_5\text{O}_{12}$ anode in 56 m $\text{Li}(\text{PTFSI})_{0.6}(\text{TFSI})_{0.4}\cdot\text{H}_2\text{O}$ exhibited a 300 mV upshift compared to that in 1 m $\text{LiTFSI}/\text{H}_2\text{O}$. According to eqn (18), the activity (a) and activity coefficient (r) of Li^+ in 56 m $\text{Li}(\text{PTFSI})_{0.6}(\text{TFSI})_{0.4}\cdot\text{H}_2\text{O}$ should be 1.2×10^5 and 1.8×10^3 times higher, respectively, than those in 1 m $\text{LiTFSI}/\text{H}_2\text{O}$. This significant deviation from the ideal Nernstian response (where $r = 1$) suggests that the classical Nernst equation and the related Debye–Hückel theory,³⁴¹ formulated a century ago, which assume Coulombic interactions in electrolytes under infinitely dilute conditions, cannot be applied in a straightforward manner to the concentration range typical in modern and next-generation battery electrolytes (Fig. 35).^{342,343} Although attempts to extend the Debye–Hückel theory phenomenologically to higher concentrations by incorporating intricate empirical calibration terms with adjustable parameters may result in partial alignment with experimental data, the fundamental physical mechanisms driving the potential shift remain uncertain.^{341,344,345}

Recently, Yamada *et al.*, proposed the concept of the “liquid Madelung potential” to quantitatively correlate the local coordination structure and thermodynamics within the system.³⁴³ This liquid Madelung potential for carrier ions, such as Li^+ , is derived by summing all the electrostatic interactions of the surrounding solvents and ions for each atom individually (Fig. 36 and eqn (19)):

$$\text{Liquid Madelung potential} = \frac{1}{N_{\text{Li}^+}} \left\langle \sum_i \frac{q_i}{4\pi\epsilon_0 r_i} \right\rangle \quad (19)$$

Here, N_{Li^+} , ϵ_0 , q_i , and r_i represent the number of Li^+ , vacuum permittivity, atomic charge of the molecules and ions, and the distance of the atoms of the surrounding solvents and ions from the central Li^+ , respectively. The brackets $\langle \rangle$ denote time-averaging in MD simulations. This concept parallels the classical Madelung

potential for inorganic crystals, where the sum of electrostatic interactions of ions is estimated by fixed point charges within a crystal lattice, leading to discrete alterations in the Coulombic energy based on the distance from the central Li^+ . For calculating the “liquid Madelung potential,” all atoms of the solvents and ions are approximated by point charges determined using the restrained electrostatic potential method. Given the high mobility and random distribution of ions and solvent molecules within electrolyte solutions, the “liquid Madelung potential” needs to be estimated through spatial averaging across all Li^+ within a calculation cell and subsequent time-averaging across all snapshots.

The variation in the “liquid Madelung potential” is attributed to the coordination environment of the carrier ion within the electrolyte. Therefore, three factors are worth considering in this regard. First, as the salt concentration increases, the carrier ion tends to be predominantly coordinated by anions to form contact ion pairs and/or ion-pair aggregates, rather than by solvents to form solvent-separated ion pairs. Second, the electrostatic stability of the carrier ion is enhanced when it is strongly solvated by electron-localized species, whereas it decreases when coordinated by electron-delocalized species within the electrolyte. This is primarily because the higher electron density largely influences the Coulombic energy in the first-coordination sphere, although the “liquid Madelung potential” is a converged value obtained by considering the Coulombic interactions of all constituent atoms up to infinite distances. Third, electrons, in general, are strongly localized on oxygen atoms in the solvent, whereas they are delocalized in bulky and weak Lewis basic anions such as TFSI^- . With increasing salt concentration, the dominant first-coordination species shifts from electron-localized solvents to the electron-delocalized anions. This transition destabilizes the “liquid Madelung potential” of the carrier ion, resulting in a substantial upshift in the electrode potential (Fig. 36). Another critical consideration is the electrode potential shift, which simultaneously alters the redox potentials of both the cathode and anode by equal magnitudes (Fig. 37). Since these parallel shifts offer a constant battery voltage, they are challenging to detect in typical two-electrode batteries, leading to frequent oversights.

Consequently, in addition to conventional strategies such as expanding the operating potential window of electrolytes using highly oxidation- and reduction-tolerant co-solvents and salts and addressing kinetic limitations induced by the formation of surface passivation films, it is crucial to consider the electrode potential shift depending on the electrolyte solution structure. Without a comprehensive understanding of the overall potential diagram of full cells (including the parallel shift of the reaction potentials of cathode and anode) and the operating potential window of electrolytes, stable battery performance cannot be ensured, as demonstrated by recent studies.^{48,342,343}

6.2. Utilization of functional anions

The electrochemical stability of aqueous electrolytes largely depends on the choice of anions (Fig. 38).^{226,346} The selection criteria for anions in aqueous electrolytes encompass several aspects:¹⁹

- (1) A high hydrolysis resistance is required to maintain the pH and a stable electrolyte composition.



(a) Classical Madelung potential for inorganic crystals

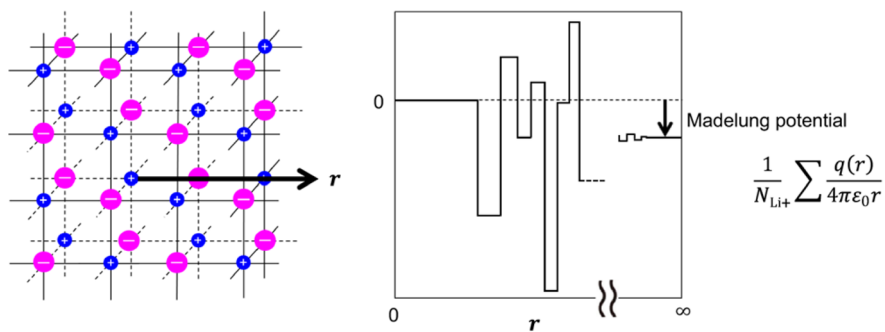
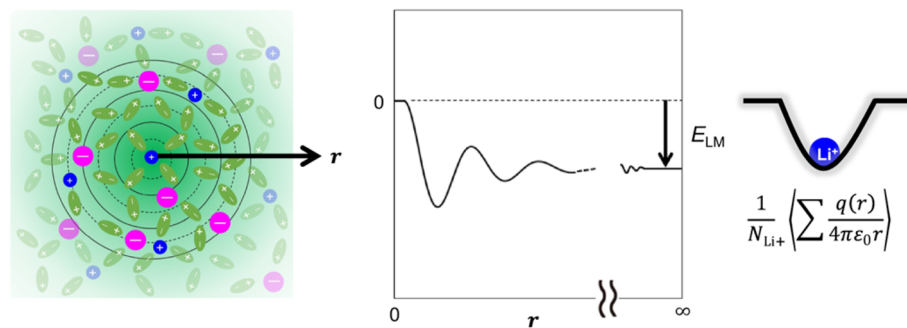
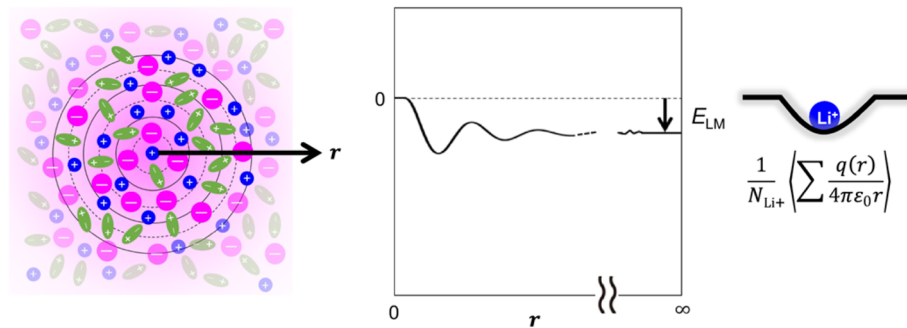
(b) Liquid Madelung potential (E_{LM}) for low concentration electrolyte solutions(c) E_{LM} for high concentration electrolyte solutions

Fig. 36 Concept of the (a) classical Madelung potential for inorganic crystals, (b) and (c) liquid Madelung (Ewald) potential, represented by the sum of overall electrostatic interactions between the surrounding ions and/or solvents and the central Li^+ in the electrolyte.³⁴³ Reprinted with permission from *Nature Communications*.

(2) In aqueous batteries, the SEI is primarily formed by anion reduction. Therefore, the ability to form a functional SEI with low solubility and reactivity toward water while providing high carrier ion conductivity is essential.^{20,21,85,333} This helps broaden the reduction stability of the electrolyte by preventing direct contact between the electrolyte and electrode, thereby suppressing electrolyte decomposition at the anode kinetically.

(3) A high salt solubility is necessary to create a unique solution structure that stabilizes the SEI and prevents transition metal and electrode dissolution.

(4) A plasticizing effect that prevents electrolyte crystallization and maintains an amorphous liquid state with minimal water content broadens the operating temperature range of the battery.³⁴⁷

(5) Bulky organic anions are preferred over small-size inorganic anions because they occupy a larger volume, thereby improving the electrochemical stability of the electrolyte by reducing water concentration on the electrode surface.^{90,346,348,349}

(6) A high oxidation stability is crucial to broaden the operating potential window of the electrolyte.

For example, commonly used salts in nonaqueous batteries, such as LiPF_6 , LiBF_4 , LiBOB ($\text{Li}(\text{C}_2\text{O}_4)_2$), and LiDFOB ($\text{Li}(\text{C}_2\text{O}_4)\text{F}_2$), are susceptible to hydrolysis, and are hence unsuitable for use in aqueous systems.^{169,234–239,350} Inorganic salts such as LiCl , LiNO_3 , and Li_2SO_4 typically offer low salt solubility and/or poor SEI formation ability.^{21,194} Using perchlorate complexes (*e.g.*, LiClO_4) at high concentrations poses safety risks as they are prone to explosion.^{351,352} As an alternative, lithium acetate (LiOAc) exhibits poor oxidation stability and SEI-forming

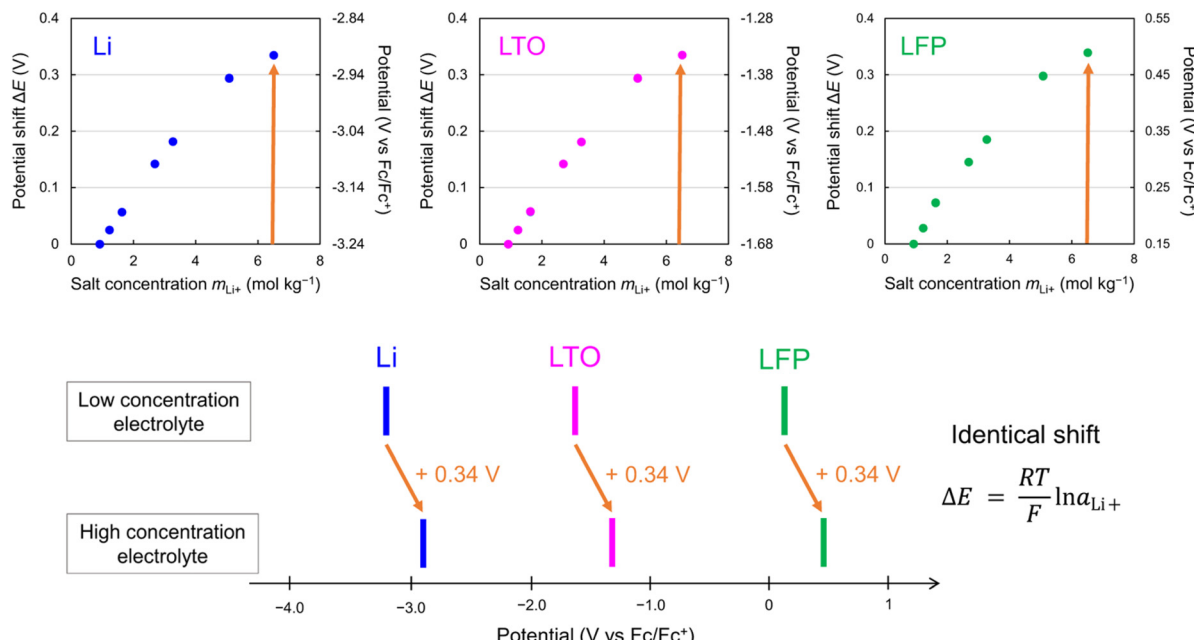


Fig. 37 Simultaneous shift in the redox/reaction potentials³⁴³ To maximize the battery performance, the overall potential diagram of full cells and the operating potential window of electrolytes should be optimized.^{48,342,343} Reprinted with permission from *Nature Communications*.

ability, making it challenging to expand the operating potential window of the electrolyte.³⁵³

As a result, the preparation of aqueous electrolytes predominantly relies on imide salts, which offer high resistance to hydrolysis and exhibit high salt solubility, good SEI-forming ability, a plasticizing effect, and high oxidation stability. The introduction of multiple imide salts with symmetric (e.g., LiTFSI, LiBETI) and asymmetric structures (e.g., LiPTFSI, LiHTFSI) helps suppress crystallization and improve the electrochemical stability of the aqueous electrolyte, while also allowing a high ionic conductivity with enhanced anion exchange and rotational mobility (Fig. 38).^{42–44}

However, as noted previously, imide salts, especially those with asymmetric structures, are significantly more expensive than the typical PF_6^- and BF_4^- -based salts. Additionally, they can only provide a particle-type SEI including inorganic compounds like LiF and Li_2CO_3 , which is unfavorable for the complete coverage of the anode surface compared to that in a film (polymer)-type or particle-film-mixed-type SEI obtained in nonaqueous electrolytes.^{354–356} This restricts the improvement of the reduction stability in aqueous electrolytes.

The selection of anions can vary based on the Lewis acidity of carrier ions. For instance, the FSI^- anion is more susceptible to hydrolysis than the TFSI^- anion because the S–F bond in the former is weaker than the C–F bond in the latter. However, as illustrated in Fig. 39, minimal pH reduction with suppressed hydrolysis of the FSI^- anion was demonstrated in aqueous Na and K electrolytes.^{169,170} This stable condition was maintained for extended periods exceeding 3000 h in a 62 m $\text{K}(\text{FSI})_{0.55}(\text{OTf})_{0.45} \cdot 0.9\text{H}_2\text{O}$ hydrate melt with extremely low water concentration. The strong interaction between the strong Lewis acid Li^+ and the Lewis basic sulfonyl oxygen of the FSI^- anion reduced the electron

density around the sulfonyl group, thereby weakening the S–F bond. This catalytic effect of Li^+ increased the susceptibility of the S–F bond to cleavage when in contact with water molecules. In contrast, in electrolytes containing the weak Lewis acidic K^+ , which exhibits a weaker catalytic effect, the stability of the FSI^- anions was improved. Nevertheless, the use of FSI^- as an anion in aqueous electrolytes is only feasible below room temperature, as interactions between carrier ions and anions become more pronounced at elevated temperatures, leading to a severe reduction in the electrolyte pH with accelerated FSI^- hydrolysis (Fig. 39).

6.3. Hybrid aqueous/nonaqueous systems

This review underscores the critical role of SEI design on the anode surface in enhancing the output voltage of aqueous batteries. The SEI must completely envelop the anode surface before the HER and remain stable throughout battery cycling. The use of highly salt-concentrated aqueous electrolytes increases the SEI formation potential and aids in stabilizing the SEI with their distinctive solution structure, which significantly reduces the water activity. However, employing such electrolytes, which necessitates dissolving a large amount of salts, increases the electrolyte viscosity and decreases the ion conductivity. These factors present challenges in battery manufacturing, elevate production costs, diminish the battery power density, and impair performance across a wide temperature range. Additionally, the SEI formed in aqueous electrolytes primarily consists of inorganic particles such as LiF and Li_2CO_3 , derived from anions, leading to only partial coverage of the surface (Fig. 40).^{20,21,201,357} This is in contrast to the SEI obtained in nonaqueous electrolytes, which contains a mix of film-type species, such as alkylcarbonate and



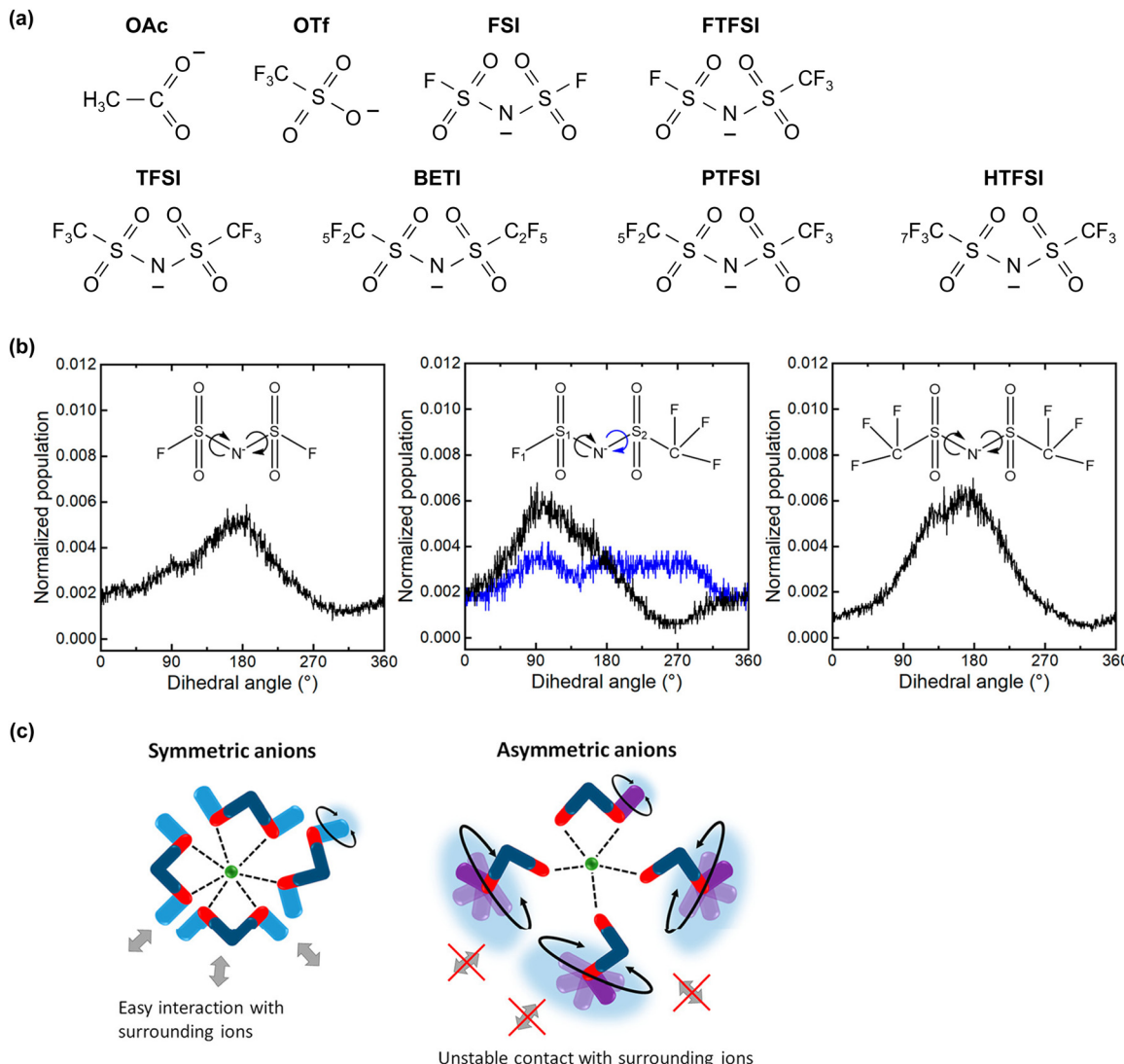


Fig. 38 (a) Chemical structures of anions introduced into aqueous electrolytes. (b) Normalized distribution of dihedral angles in 35 m LiFSI (symmetric), LiFTFSI (asymmetric), and LiTFSI (symmetric) solutions.⁹¹ The homogeneous distribution of the dihedral angle in the SO_2CF_3 group of the FTSI anion, highlighted in blue, indicates high anion exchange and rotational mobility, which facilitate fast ion hopping and suppress electrolyte crystallization at low temperatures.^{89–92,185} (c) Schematic showing the differences in local coordination between symmetric TFSI and asymmetric FTSI anions.⁹¹ Reprinted with permission from *The Journal of Physical Chemistry Letters* (b) and (c).

alkoxide-based organic polymers, along with inorganic particles.^{358–361} This composition significantly limits the access of the electrolyte to the anode surface, providing high battery cycling stability and high Coulombic efficiency (Fig. 40).

To address the aforementioned issues, the introduction of organic solvents into aqueous electrolytes has been explored, as detailed in Tables 8–10.³⁶² In 2009, Mentus *et al.* developed an electrolyte by incorporating 1 wt% of vinylene carbonate, a known electrolyte additive for promoting robust SEI formation in nonaqueous Li-ion batteries, into a saturated $\text{LiNO}_3/\text{H}_2\text{O}$ solution.³⁶³ They assessed the reversibility of a V_2O_5 anode using an excess LiMn_2O_4 cathode as a counter electrode in this additive-containing electrolyte and confirmed no capacity degradation over 25 cycles at a current density of 50 mA cm^{-2} . In 2018, Xu and Wang groups introduced dimethyl carbonate as

a co-solvent.³⁶⁴ They prepared a hybrid aqueous/nonaqueous electrolyte by mixing 9.25 m of nonaqueous LiTFSI/dimethyl carbonate electrolyte into a highly salt-concentrated 21 m LiTFSI/ H_2O aqueous electrolyte. This blending of organic solvents with aqueous electrolytes can modify solvation structures by introducing competitive interactions between H_2O and nonaqueous species, including organic solvents, carrier ions, and anions. In this hybrid electrolyte, the organic solvent substituted some of the Li^+ ligands. As a result, a robust SEI was formed on the anode surface through the continuous reduction of $\text{Li}^+(\text{TFSI}^-)_n$ and $\text{Li}^+(\text{dimethyl carbonate})_n$ complexes. Furthermore, as the carrier ion (Li^+) was surrounded by a limited number of water molecules, the approach of the water molecules to the electrode surface was restricted, which enhanced both, the anodic and cathodic stabilities. They successfully

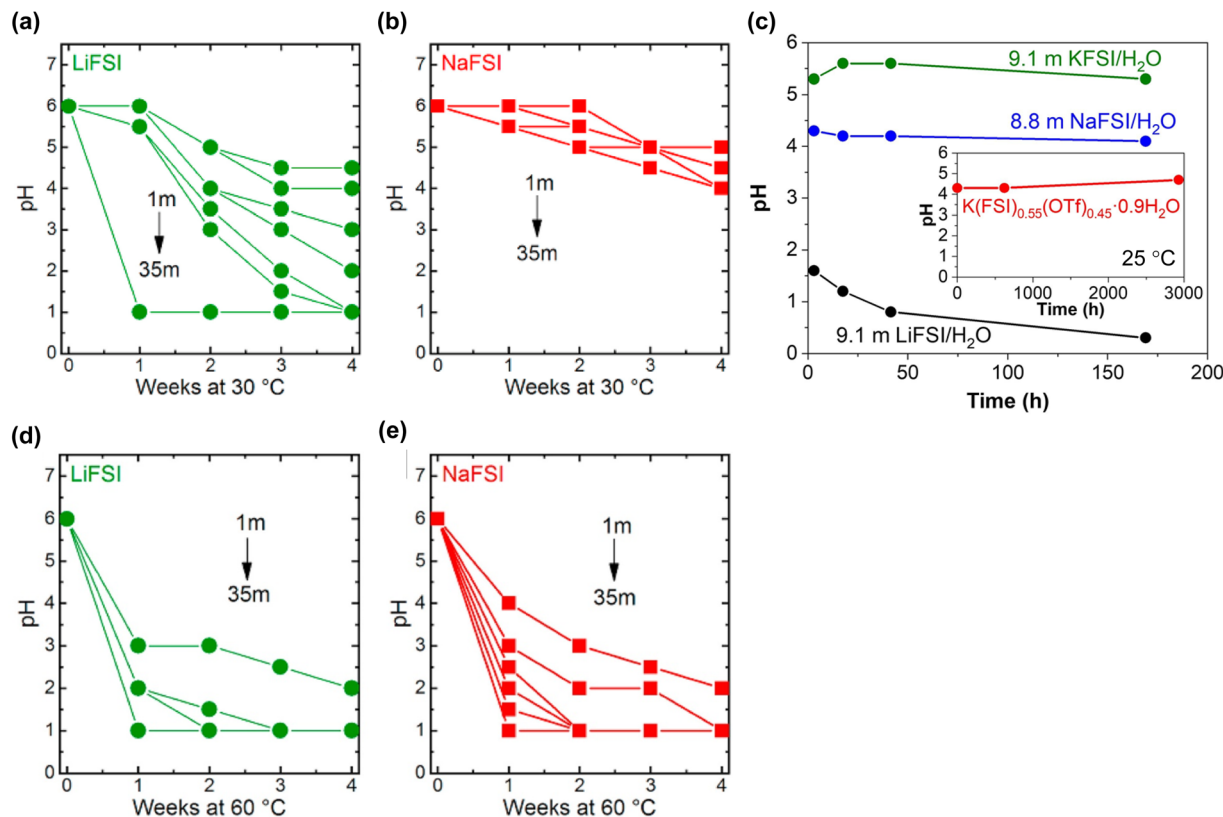


Fig. 39 pH levels of FSI⁻ anion-based aqueous electrolytes under various salt concentrations and temperature conditions.^{169,170} Reprinted with permission from *Electrochimica Acta* (a), (b), (d) and (e) and *Electrochemistry Communications* (c).

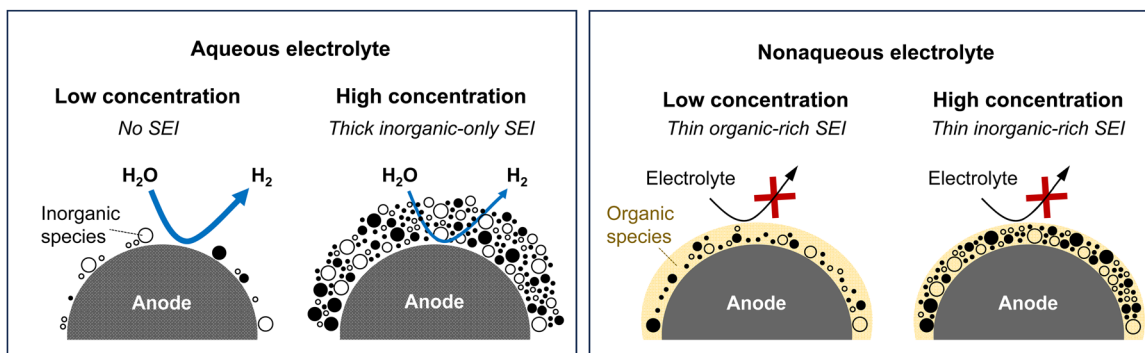


Fig. 40 Schematic comparison of SEI components in aqueous and nonaqueous electrolytes across various salt concentrations.

cycled a LiNi_{0.5}Mn_{1.5}O₄|Li₄Ti₅O₁₂ full cell, achieving a high output voltage of 3.2 V, which was comparable to those of nonaqueous batteries, and maintaining stable cycling (90% capacity retention after 100 cycles) at a low constant current of 0.5C.

Since 2018, various developments in hybrid aqueous/nonaqueous electrolytes have been achieved from diverse perspectives (Fig. 41). For example, (i) solvents that strongly solvate carrier ions (e.g., dimethyl carbonate,³⁶⁴ tetraethylene glycol dimethyl ether,³⁷⁰ glymes,³⁹³⁻³⁹⁵ acetonitrile,³⁷² dimethyl sulfoxide,³⁹⁶⁻³⁹⁹ 1,3-dioxolane³⁷⁹) have been integrated to limit the approach of water to the electrode surface. Moreover, to lower the water activity in the electrolyte, (ii) weakly solvating solvents

(e.g., 1,5-pentanediol,¹⁷⁶ 1,4-dioxane^{376,400}), modifying the solution structure similar to that of locally salt-concentrated nonaqueous electrolytes; (iii) hydrogen-bond-anchoring solvents (e.g., propylene carbonate,⁴⁰¹ sulfolane,^{374,402} organic phosphates,^{391,403-408} dimethylacetamide⁴⁰⁹⁻⁴¹²), disrupting hydrogen bonds between water molecules; (iv) deep eutectic solvents (e.g., methylsulfonylmethane,^{367,413} urea,^{373,380,381,414-416} methylurea³⁸²), providing a lower melting point compared to that of each electrolyte component and possessing functional groups that can serve as both donors and acceptors, thus breaking hydrogen bonds between water molecules; (v) molecular crowding agents (e.g., polyethylene glycol,^{368,417,418} polyethylene glycol dimethyl





Table 8 Performance data for Li-ion full cells fabricated using hybrid aqueous/nonaqueous electrolytes

Year	Electrolyte	Cathode	Anode	Full cell average	Capacity based	Cycle number	Retention
		L/L (mg cm ⁻²)	I/L (mg cm ⁻²)	cutoff (V/V)	(mA h g ⁻¹)	(-)	ratio (%)
2011	Sat. LiNO ₃ /H ₂ O + 1 wt% vinylene carbonate ³⁶³	LiMn ₂ O ₄ or Li _{1.05} Cr _{0.10} Mn _{1.85} O ₄	V ₂ O ₅	—	1.0/0.0	0.9	—
2016	21 m LiTFSI/H ₂ O + 0.1 wt% Li[tris(trimethylsilyl)borate] ³⁶⁵	—	Mo ₆ S ₈	—	2.5/1.0	1.8	1.0 (mass) 0.5C 2.5C
2017	21 m LiTFSI + 7 m LiOTf/ H ₂ O + 10 wt% polyvinyl alcohol ³⁶⁶	LiMn ₂ O ₄ or LiCoO ₂	Sulfur-Ketichen black	8	2.2/0.5 (LMO) (LMO) 1.6 (LCO) 1.6 (LCO)	0.2C (LMO) (capacity) 1C (LMO)	84 (LMO, 0.2C) 119 (LCO, 0.2C)
2018	21 m LiTFSI/H ₂ O + 9.25 m LiTFSI/dimethylcarbonate ³⁶⁴	LiNi _{0.5} Mn _{1.5} O ₄	—	—	3.5/2.0	3.2	2.0 (mass) 0.5C 6.5C
2019	56 m LiClO ₄ : methylsulfonylmethane: H ₂ O (1:1.8:1, n:n:n) ³⁶⁷	LiMn ₂ O ₄	Li ₄ Ti ₅ O ₁₂	1.2	2.7/0.8	2.4	3.0 (mass) 4.5C
2020	2 m LiTFSI/polyethylene glycol:H ₂ O (94:6, w:w) ³⁶⁸	LiMn ₂ O ₄	Li _{1.3} Al _{0.3} Ti _{1.7} (PO ₄) ₃ coated	3	3.2/1.0	2.3	1.2 (mass) 1C 49
2020	42 m LiTFSI/H ₂ O + 21 m trimethyllethylammonium-TFSI ³⁶⁹	LiMn ₂ O ₄	Li ₄ Ti ₅ O ₁₂	0.55 mA h cm ⁻²	2.8/1.8	2.5	1.1 (capacity) 1C
2020	LiTFSI: tetraethylene glycol LiMn ₂ O ₄ (4:1:7, n:n:n) ³⁷⁰	2-4	Li ₄ Ti ₅ O ₁₂	1-2	2.8/1.0	2.5	2 (mass) 3C 10C
2020	21 m LiTFSI/H ₂ O + 9.25 m LiTFSI/dimethylcarbonate ³⁷¹	Graphite	Li ₄ Ti ₂ (PO ₄) ₃ or 2.4	4.3	2.05/0.0	1.5 (LTP) 2.5 (LTO)	1.8 (mass) 200 mA g ⁻¹ 36
2020	15.3 m LiTFSI/acetonitrile: LiMn ₂ O ₄ or LiNi _{0.8} Co _{0.15} Al _{0.05} O ₂ (1:1, n:n) ³⁷²	—	Li ₄ Ti ₅ O ₁₂	5	2.8/1.5 (LMO) (LMO)	2.5 (mass, 1C (LMO, 25 °C) 5C (LMO, 25 °C) 1C (LMO, 0 °C))	49 (3C) 27
2020	LiClO ₄ :urea:H ₂ O (1:2:3, n:n:n) ³⁷³	LiMn ₂ O ₄	—	—	—/— (NCA)	2.1 (NCA) 1.0 (mass, NCA) 1C (NCA, 25 °C)	46 (LMO/LTO) 81 (NCA/LTO)
2021	12.5 m LiNO ₃ /1,5-pentanediol:H ₂ O (1:1, w:w) + 6 wt% tetraethylene glycol dimethyl ether + 0.5 wt% 2-hydroxy-2-methylpropiophenone (polymerization) ¹⁷⁶	LiMn ₂ O ₄	Mo ₆ S ₈	—	2.3/0.8	2.0	1.0 (mass) 0.1C 10C
2021	3.6 m LiTFSI/sulfolane: H ₂ O (1:1, n:n) ³⁷⁴	LiMn ₂ O ₄	LiAlO ₂ coated 2.3	2.3	3.0/1.5	2.5	1.0 (mass) 1C 5C
2021	33 m LiNO ₃ /H ₂ O + 10 wt% polyvinyl alcohol (ps. H ₂ O) ³⁷⁵	LiNi _{0.5} Mn _{1.5} O ₄ or LiMn ₂ O ₄	Li ₄ Ti ₅ O ₁₂ VO ₂	3.5	2.5/1.1 (LNMO) (mass) 2.0/0.8 (LMO) 1.3 (NMC/TiO ₂) 1.8 (NMC/TiO ₂)	72 (LNMO, 25 °C) 3C (LMO, 60 °C) 74 0.5C (NMC/TiO ₂) 67 (capacity)	
2021	—	—	TiO ₂ or Li ₄ Ti ₅ O ₁₂	—	1.7 (TiO ₂)	—	—



Table 8 (continued)

Year	Electrolyte	Cathode	Anode	Full cell average	P/N ratio	C-rate	Capacity (mA h g ⁻¹)	Capacity calculation based	Cycle number	Retention ratio (%)
2019	40 m LiTFSI/H ₂ O + 20 m 1-ethyl-3-ethylimidazolium·Co _{0.1} O ₂ or LiMn ₂ O ₄	LiNi _{0.8} Mn _{0.1}	2.75/0.5 (NMC/LTO)	2.1	0.5C (NMC/LTO)	72	200	6.5		
2020	40 m LiTFSI/H ₂ O + 20 m 1-ethyl-3-methylimidazolium·OTf	LiMn ₂ O ₄	1.8–3.2 (LTO)	3.0/0.8 (LMO/ 2.3 LTO)	1C (NMC/LTO)	66	300	68		
2021	1.9 m LiTFSI/H ₂ O; 1,4-dioxane LiTFSI; H ₂ O; 1,4-dioxane (1:2.6:5.2, n:n:n) ³⁷⁶	LiMn ₂ O ₄	5	2.6/1.0	2.5	2.0 (mass) 0.57C (100 mA g ⁻¹)	165	Anode	300	65
2022	2 m LiTFSI/polyethylene glycol dimethyl ether: H ₂ O (94:6, w:w) ³⁷⁷	LiMn ₂ O ₄	—	Li _{1.3} Al _{0.3} Ti _{1.7} (PO ₄) ₃ coated TiO ₂	3.2/1.0	2.4	—	1C 5C	50 32	Cathode + anode
2022	21 m LiTFSI/H ₂ O + 5 mol% LiMn ₂ O ₄ acrylamide or polyacrylamide ³⁷⁸	4	Li ₄ Ti ₅ O ₁₂	2	2.5/0.8	2.2	2.0 (mass) 1C 5C	157	Anode	300 800
2022	LiTFSI; 1,3-dioxolane; H ₂ O LiMn ₂ O ₄ (1:1.08:1.08, n:n:n) ³⁷⁹	Li ₄ Ti ₅ O ₁₂	2 or 1	2.8/1.5	2.4	2.5 (mass) 1C (25 °C) 5C (25 °C) 0.5C (–20 °C)	164 110 105	Anode	200 2000 100	
2022	LiClO ₄ ; urea: H ₂ O (1:2:3, LiMn ₂ O ₄ n:n:n) ³⁸⁰	20 or 60	Li ₄ Ti ₅ O ₁₂	14 or 42	2.5/1.0	2.2	1.4 (mass) 0.5C 10C	105 (0.5C)	Cathode	100 100 100
2022	4.5 m LiTFSI + 0.1 m KOH/ LiMn ₂ O ₄ or [urea H ₂ O (8.6:1, v:v)] ³⁸¹ LiVPO ₄ F	14 or 24	Li ₄ Ti ₅ O ₁₂	9 or 16	3.0/1.8 (LMO) 2.4 (LVPF)	1.14 (mass)	0.25C (12 A h pouch)	400	Cathode + anode	1000 500
2022	LiTFSI/methylurea: H ₂ O (1:2.7, n:n) ³⁸²	LiMn ₂ O ₄	7–10	NbO ₂	4–5	3.3/1.5	0.9–1.0 (capacity) 0.7C 3.5C	225 (0.35C)	Anode	100 300
2022	LiTFSI; 1-methyl-1-propylpiperidinium·FSI: H ₂ O (1:4:1, n:n:n) ³⁸³	LiMn ₂ O ₄	4	LiAlO ₂ coated 2 Li ₄ Ti ₅ O ₁₂	2.8/1.6	2.5	2.0 (mass) 2C	160	Anode	1500 1000



Table 9 Performance data for Na- and K-ion full cells fabricated using aqueous/nonaqueous hybrid electrolytes

Year	Electrolyte	Cathode	Anode	Full cell cutoff (V/V)	Full cell average (V)	P/N ratio	C-rate	Capacity (mA h g ⁻¹)	Capacity calculation based	Cycle calculation based (–)	Capacity retention ratio (%)	
2016	10 M NaClO ₄ /H ₂ O + 2 vol% Na ₃ V ₂ O ₅ (PO ₄) ₂ F/VC ³⁸⁴	Cathode I/L (mg cm ⁻²)	Anode I/L (mg cm ⁻²)	1.8/1.0	1.5	—	1C	53	—	—	100 80	
2019	10 M NaClO ₄ /H ₂ O + 2 vol% Na ₃ MnV(PO ₄) ₃ /VC ³⁸⁵	nanotube	NaTi ₂ (PO ₄) ₃ /carbon nanotube	—	1.65/0.8	1.3	0.5 (mass)	10C	97	Cathode	100 52	
2020	NaClO ₄ ·H ₂ O:urea:N ₂ N-dimethylformamide (1:2:2:1, <i>n</i> : <i>n</i> : <i>n</i> : <i>n</i>) ³⁸⁶	Na ₃ V ₂ (PO ₄) ₂ F ₃	4–6	NaTi ₂ (PO ₄) ₃ /C	4–6	1.6/0.6	1.2	1.1 (mass)	10C	68	Cathode + anode	100 86
2021	80 m NaOTf/H ₂ O + 1-ethyl- Na ₂ Mn[Fe(CN) ₆] ₂ ·OTf ³⁸⁷	—	NaTi ₂ (PO ₄) ₃	2–5	2.2/0.5	1.2–1.3	0.5 (mass)	1C (OTf-based)	88	Cathode	300 68	
2021	80 m NaTFSI/H ₂ O + 1-ethyl-3-methylimidazolium-TFSI	—	—	—	—	—	1C (TFSI-based)	98	—	—	300 78	
2021	2 m NaClO ₄ /H ₂ O + dimethyl sulfoxide (H ₂ O:dimethyl sulfoxide = 1:1, <i>n</i> : <i>n</i>) ³⁸⁷	Na ₃ V ₂ (PO ₄) ₃	1.2–2.4	Na ₃ V ₂ (PO ₄) ₃	1.2–2.4	2.1/0.0	1.7	0.8 (capacity)	5C	90	Cathode	300 90
2023	18 m NaClO ₄ /H ₂ O + Na ₄ Fe(CN) ₆ ³⁸⁸	Na _{1.58} Fe _{0.07} Mn _{0.97} —Fe(CN) ₆ ·2.65H ₂ O	—	3,4,9,10-Perylene tetracarboxylic diimide	—	2.2/0.0	1.3	0.8 (mass)	500 mA g ⁻¹	157	Cathode	300 100
2021	20 m KOTf + 30 m KFSI/H ₂ O + acrylamide ³⁸⁹	KMnFe(CN) ₆	—	—	2.8/0.0	1.5	1.5 (mass)	100 mA g ⁻¹	135 (100 mA g ⁻¹)	Anode	100 98	
2021	2 m KFSI/N ₂ N-dimethylformamide·H ₂ O (1:1, <i>n</i> : <i>n</i>) ³⁹⁰	K ₂ Zn ₃ [Fe(CN) ₆] ₂	—	—	2.2/0.01	1.2	2.0 (mass)	200 mA g ⁻¹	70 (1000 mA g ⁻¹)	Cathode	3000 88	
2023	KOTf: trimethyl phosphate: H ₂ O (12:56:32, <i>n</i> : <i>n</i> : <i>n</i>) ³⁹¹	K _{1.1} Mn _{0.61} Fe _{0.39} [Fe(CN) ₆] _{0.77} ·H ₂ O	—	3,4,9,10-Perylene tetracarboxylic diimide	—	2.5/0.0	1.6	—	0.8C (pouch)	40	Cathode + anode	200 67
2024	5.6 m KFSI/succinonitrile: H ₂ O (2:1, <i>n</i> : <i>n</i>) ³⁹²	Preycled KVPO ₄ F	—	Preycled 3,4,9,10-Perylene tetracarboxylic diimide	—	3.2/0.0	2.0	1.5 (mass)	500 mA g ⁻¹ (25 °C)	50 (25 °C)	Cathode + anode	10 000 78
									100 mA g ⁻¹ (0 °C)	46 (0 °C)		500 74
									50 mA g ⁻¹ (–20 °C)	40 (–20 °C)		500 70
									1.7 (mass, pouch)	150 mA g ⁻¹ (pouch, 25 °C)		300 80



Table 10 Physicochemical and electrochemical properties of hybrid aqueous/nonaqueous electrolytes. The data were calibrated with an Ag/AgCl (sat. KCl) reference electrode

Year	Electrolyte	Reduction stability				Oxidation stability			
		V vs. Ag/AgCl		V vs. Ag/AgCl		V vs. Ag/AgCl		V vs. Ag/AgCl	
		LSV scan rate, mV s ⁻¹	LSV cut-off condition, μm cm ⁻²	LSV scan rate, mV s ⁻¹	LSV cut-off condition, μm cm ⁻²	LSV scan rate, mV s ⁻¹	LSV cut-off condition, μm cm ⁻²	LSV scan rate, mV s ⁻¹	LSV cut-off condition, μm cm ⁻²
2018	21 m LiTFSI/H ₂ O + 9.25 m LiTFSI/ dimethylcarbonate ³⁶⁴	—	1	—	—	—	—	1.86 V 5 mV s ⁻¹ 10 μm cm ⁻²	1.86 V 5 mV s ⁻¹ 10 μm cm ⁻²
2019	56 m LiClO ₄ : methysulfonylmethane: H ₂ O (1:1.8:1, <i>n</i> : <i>n</i> : <i>n</i>) ³⁶⁷	—	148	3.7	—	—1.4 V 0.2 mV s ⁻¹ 30 μm cm ⁻²	—	2.1 V 0.2 mV s ⁻¹ 30 μm cm ⁻²	2.1 V 0.2 mV s ⁻¹ 30 μm cm ⁻²
2020	2 m LiTFSI/polyethylene glycol:H ₂ O (94:6, w:w) ³⁶⁸	—	—	0.8	—	—	—	—	—
						(Carbon coated)	(Carbon coated)	(Carbon coated)	(Carbon coated)
2020	42 m LiTFSI/H ₂ O + 21 m trimethylethylammonium- TFSI ³⁶⁹	—	407	0.9	—	—	—	—	—
2020	15 m LiTFSI: tetraethylene glycol dimethyl ether: H ₂ O (4:7:1, <i>n</i> : <i>n</i> : <i>n</i>) ³⁷⁰	—	—	0.6	—	—2.64 V 5 mV s ⁻¹ 10 μm cm ⁻²	—	—2.64 V 5 mV s ⁻¹ 10 μm cm ⁻²	—
2020	15.3 m LiTFSI/acetonitrile: — H ₂ O (1:1, <i>n</i> : <i>n</i>) ³⁷²	—	—	3	—	—2.54 V 5 mV s ⁻¹ 50 μm cm ⁻²	—	—2.54 V 5 mV s ⁻¹ 50 μm cm ⁻²	—
2020	LiClO ₄ : urea:H ₂ O (1:2:3, — <i>n</i> : <i>n</i> : <i>n</i>) ^{373,380}	—	35	26	—	—1.24 V 0.05 mV s ⁻¹ 500 μm cm ⁻²	—	—1.24 V 0.05 mV s ⁻¹ 500 μm cm ⁻²	—
2021	3.6 m LiTFSI/sulfolane: H ₂ O (1:1, <i>n</i> : <i>n</i>) ³⁷⁴	—	—	2.5	—	—	—	—	—
						(Carbon coated)	(Carbon coated)	(Carbon coated)	(Carbon coated)
2021	33 m LiNO ₃ /H ₂ O + 10 wt% — polyvinyl alcohol (vs. H ₂ O) ³⁷⁵	—	12 000	0.25	—	—	—	—	—
2021	1.9 m LiTFSI/H ₂ O:1,4- dioxane LiTFSI: H ₂ O:1,4- dioxane (1:2.6:5.2, <i>n</i> : <i>n</i>) ³⁷⁶	—	17	8	—	—1.5 V 0.1 mV s ⁻¹ 50 μm cm ⁻²	—	—1.5 V 0.1 mV s ⁻¹ 50 μm cm ⁻²	—
2021	12.5 m LiNO ₃ /1,5- pentanediol:H ₂ O (1:1, w:w) + 6 wt% tetraethylene glycol dimethyl ether + 0.5 wt% 2-hydroxy-2- methylpropiophenone (polymerization) ³⁷⁶	—	52	0.16	—	—	—	—	—
						(Carbon coated)	(Carbon coated)	(Carbon coated)	(Carbon coated)
12.5 m LiNO ₃ /1,5- pentanediol:H ₂ O (1:1, w:w) ³⁷⁶	3.4 22	0.23	—	—	—	—1.0 V 0.1 mV s ⁻¹ 500 μm cm ⁻²	—	—1.0 V 0.1 mV s ⁻¹ 500 μm cm ⁻²	—
10.5 m LiTFSI/ethylene carbonate:H ₂ O (1:1, w:w) ³⁷⁶	3.9 —	—	—	—	—	2.0 V 0.1 mV s ⁻¹ 500 μm cm ⁻²	2.0 V 0.1 mV s ⁻¹ 500 μm cm ⁻²	2.0 V 0.1 mV s ⁻¹ 500 μm cm ⁻²	2.0 V 0.1 mV s ⁻¹ 500 μm cm ⁻²



Table 10 (continued)

Year	Electrolyte	Reduction stability				Oxidation stability			
		V vs. Ag/AgCl		V vs. Ag/AgCl		V vs. Ag/AgCl		V vs. Ag/AgCl	
		LSV scan rate, mV s ⁻¹	LSV cut-off condition, μm cm ⁻²	LSV scan rate, mV s ⁻¹	LSV cut-off condition, μm cm ⁻²	LSV scan rate, mV s ⁻¹	LSV cut-off condition, μm cm ⁻²	LSV scan rate, mV s ⁻¹	LSV cut-off condition, μm cm ⁻²
2011	12.5 m LiNO ₃ /ethylene carboxylate :H ₂ O (1:1, w:w) ¹⁷⁶	—	—	—0.8 V	—0.1 mV s ⁻¹	—1.9 V	—0.1 mV s ⁻¹	—1.46 V	—500 μm cm ⁻²
2021	40 m LiTFSI/H ₂ O + 20 m 1-ethyl-3-methylimidazolium-TFSI ¹⁷⁵	293	1.2	—1.94 V	—1 mV s ⁻¹	—1.66 V	—1 mV s ⁻¹	—1.46 V	—2 μm cm ⁻²
2022	40 m LiTFSI/H ₂ O + 20 m 1-ethyl-3-methylimidazolium·OTf ¹⁷⁵	302	1.4	—2.44 V	—1 mV s ⁻¹	—1.34 V	—1 mV s ⁻¹	—1.66 V	—2 μm cm ⁻²
2022	21 m LiTFSI/H ₂ O + 5 mol% acrylamide ³⁷⁸	45	10	—2.44 V	—2 μm cm ⁻²	—1.34 V	—10 mV s ⁻¹	—1.66 V	—10 μm cm ⁻²
2022	4.5 m LiTFSI + 0.1 m KOH/—[urea H ₂ O (8.6:1, v:v)] ³⁸¹	320	1	—1.74 V	—0.2 mV s ⁻¹	—1.56 V	—0.2 mV s ⁻¹	—1.0–1.6 V	—200 μm cm ⁻²
2022	LiTFSI/methylurea: H ₂ O (1:2.7, n:n) ³⁸²	646	3.2	—2.44 V	—200 μm cm ⁻²	—2.74 V	—5 mV s ⁻¹	—1.76 V	—50 μm cm ⁻²
2022	LiFSI: 1-methyl-1-propylpiperidinium bis(fluorosulfonyl)imide: H ₂ O (1:4:1, n:n:n) ³⁸³	—	—	—2.44 V	—5 mV s ⁻¹	—2.46 V	—5 mV s ⁻¹	—2.46 V	—50 μm cm ⁻²
Reduction stability									
Year	Electrolyte	V vs. Ag/AgCl				Oxidation stability			
		LSV scan rate, mV s ⁻¹	LSV cut-off condition, μm cm ⁻²	LSV scan rate, mV s ⁻¹	LSV cut-off condition, μm cm ⁻²	LSV scan rate, mV s ⁻¹	LSV cut-off condition, μm cm ⁻²	LSV scan rate, mV s ⁻¹	LSV cut-off condition, μm cm ⁻²
		Pt	Al	Au	Ti	SUS	Pt	Al	Au
2020	NaClO ₄ :H ₂ O:urea:N ₂ N-dimethylformamide (1:2:2:1, n:n:n:n) ³⁸⁶	—	—	—	—	—	—1.4 V	—1.4 V	—1.4 V
							1 mV s ⁻¹	1 mV s ⁻¹	1 mV s ⁻¹
							150 μm cm ⁻²	150 μm cm ⁻²	150 μm cm ⁻²



Table 10 (continued)

Year	Electrolyte	Reduction stability						Oxidation stability						
		V vs. Ag/AgCl			V vs. Ag/AgCl			LSV scan rate, mV s ⁻¹			LSV scan rate, mV s ⁻¹			
		LSV cut-off condition, $\mu\text{m cm}^{-2}$			LSV cut-off condition, $\mu\text{m cm}^{-2}$			LSV cut-off condition, $\mu\text{m cm}^{-2}$			LSV cut-off condition, $\mu\text{m cm}^{-2}$			
Year	Electrolyte	pH	Viscosity (mPa s)	Ionic conductivity (mS cm ⁻¹)	Pt	Al	Au	Ti	SUS	Pt	Al	Au	Ti	SUS
2021	2 m NaClO ₄ /H ₂ O + dimethyl sulfoxide (H ₂ O:dimethyl sulfide = 1:1, $n:n$) ³⁸⁷	—	—	—	—	—	—	—	—	—	—	—	—	—
2020	20 m KOAc/H ₂ O + 2 wt% Na-carboxymethyl cellulose ¹⁸⁷	9.5	3275	4.3	—	—	—	—	—	—	—	—	—	—
2021	2 m KFSI/ <i>N,N</i> -dimethylformamide: H ₂ O (1:1, $n:n$) ³⁹⁰	—	25	3	—	—	—	—	—	—	—	—	—	—
2023	KOTf: trimethyl phosphate: H ₂ O (12: 56: 32, $n:n:n$) ³⁹¹	—	45	8	—	—	—	—	—	—	—	—	—	—
2024	5.6 m KFSI/sucinonitrile: H ₂ O (2:1, $n:n$) ³⁹²	—	10	22	—	—	—	—	—	—	—	—	—	—

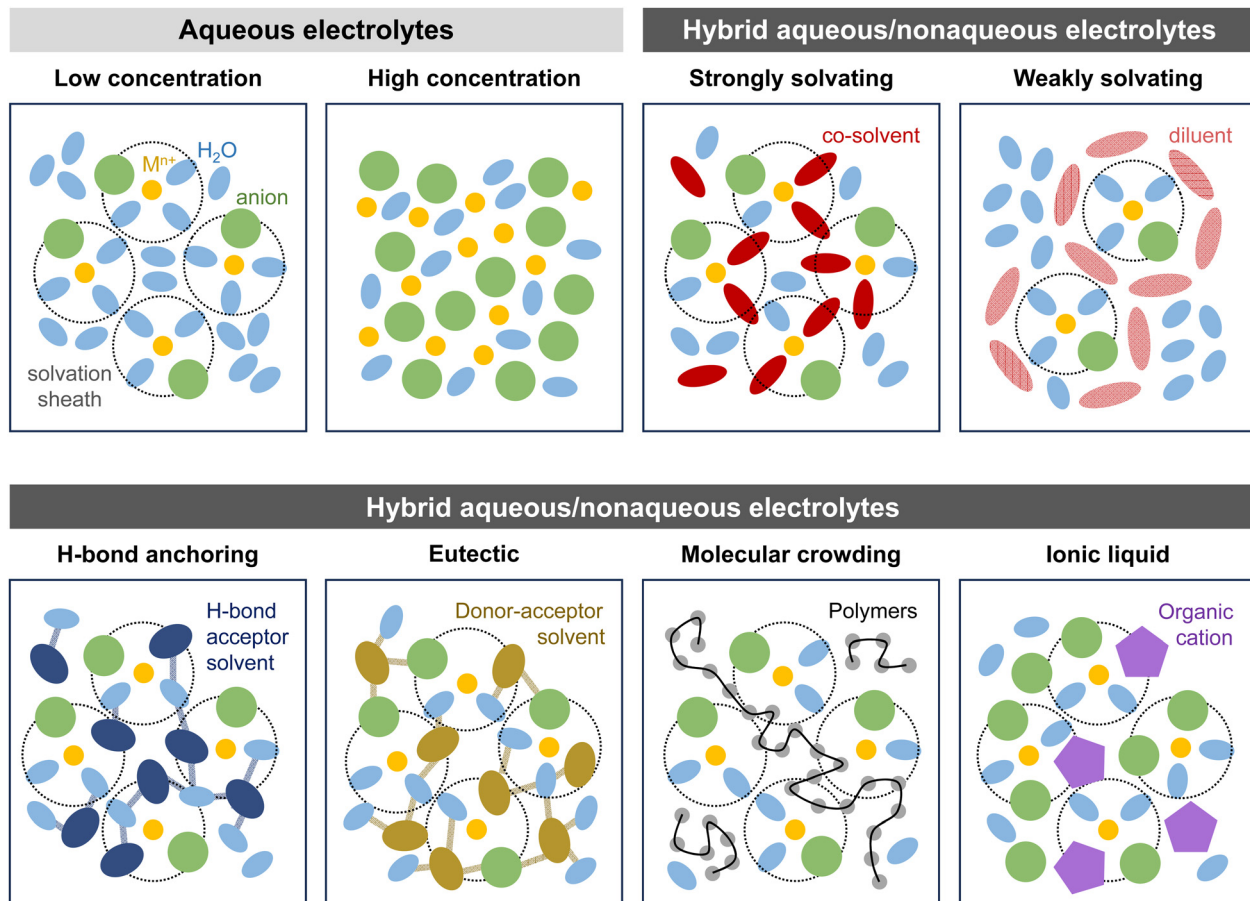


Fig. 41 Schematic comparison of the solution structures of aqueous and hybrid aqueous/nonaqueous electrolytes using diverse strategies.

ether³⁷⁷); and (vi) ionic liquids (e.g., trimethylethylammonium-TFSI,³⁶⁹ 1-ethyl-3-ethylimidazolium-TFSI,¹⁷⁵ 1-ethyl-3-ethylimidazolium-OTf,¹⁷⁵ 1-methyl-1-propylpiperidinium-FSI³⁸³), offering nonflammability, high-temperature stability, and low vapor pressure, have been introduced. These hybrid aqueous/nonaqueous electrolytes have enabled the reversible cycling of 2 V-class batteries such as $\text{LiMn}_2\text{O}_4\text{||Li}_4\text{Ti}_5\text{O}_{12}$ and $\text{LiMn}_2\text{O}_4\text{||Mo}_6\text{S}_8$ for hundreds of cycles (Table 8). These examples include cases where the carrier ion is an alkali ion (Li^+ , Na^+ , and K^+) and Zn^{2+} .^{362,419}

Hybrid aqueous/nonaqueous electrolytes also help improve the wide-temperature-range performance of aqueous batteries. In 2019, Xing *et al.* developed a 15.3 m LiTFSI/acetonitrile : H_2O (1 : 1, n) electrolyte by incorporating acetonitrile, which has a low freezing point ($-48\text{ }^\circ\text{C}$) and low viscosity.¹⁸⁸ This electrolyte remained non-crystallized even at $-20\text{ }^\circ\text{C}$, providing an ion conductivity of 0.6 mS cm^{-1} . Moreover, the robust SEI, which included nitrile ($\text{C}\equiv\text{N}$) and sulfamide ($\text{R}-\text{S}-\text{N}-\text{S}$) species resulting from the reduction of acetonitrile, enhanced the reduction stability of the electrolyte. Consequently, the stable operation of 2 V-class full cells consisting of LiMn_2O_4 or $\text{LiNi}_{0.8}\text{Co}_{0.15}\text{Al}_{0.05}\text{O}_2$ cathodes and $\text{Li}_4\text{Ti}_5\text{O}_{12}$ anodes for hundreds of cycles was achieved at 25 and $0\text{ }^\circ\text{C}$. In 2022, Ma *et al.* introduced 1,3-dioxolane, which has an even lower freezing point ($-95\text{ }^\circ\text{C}$) than acetonitrile, into an aqueous electrolyte.³⁷⁹ By employing the

developed LiTFSI : 1,3-dioxolane : H_2O (1 : 1.08 : 1.08, $n : n : n$) electrolyte, high cycling performance of the 2 V-class $\text{LiMn}_2\text{O}_4\text{||Li}_4\text{Ti}_5\text{O}_{12}$ full cells was achieved, with a capacity retention of 94% after 100 cycles at a low C-rate (0.5C) and low temperature ($-20\text{ }^\circ\text{C}$). However, these hybrid aqueous/nonaqueous electrolytes still exhibited higher viscosity compared to nonaqueous electrolytes.

Gas-assisted SEI formation technology was developed to tackle this challenge, as depicted in Fig. 42. In 2022, Suo and Xu's group prepared 5.0 m LiTFSI/ H_2O electrolytes saturated with air, O_2 , Ar, and CO_2 gases.⁴²⁰ They observed that Li_2CO_3 formation was accelerated in the electrolyte saturated with CO_2 gas, effectively passivating the anode surface. By utilizing this electrolyte (5 m LiTFSI/ H_2O + sat. CO_2 gas), stable $\text{LiMn}_2\text{O}_4\text{||Mo}_6\text{S}_8$ full cells were achieved, offering a capacity retention of over 90% after 100 cycles at both 25 and $-40\text{ }^\circ\text{C}$ at a low constant current of 0.5C.

While there has been some progress in overcoming low-temperature limitations, the issue of electrolyte decomposition at high temperatures remains a significant challenge. Most organic solvents are prone to hydrolysis, a vulnerability that is exacerbated under non-neutral pH conditions and elevated temperatures. Moreover, it is important to recognize that although the development of hybrid aqueous/nonaqueous electrolytes with various types of organic solvents and salts has improved the

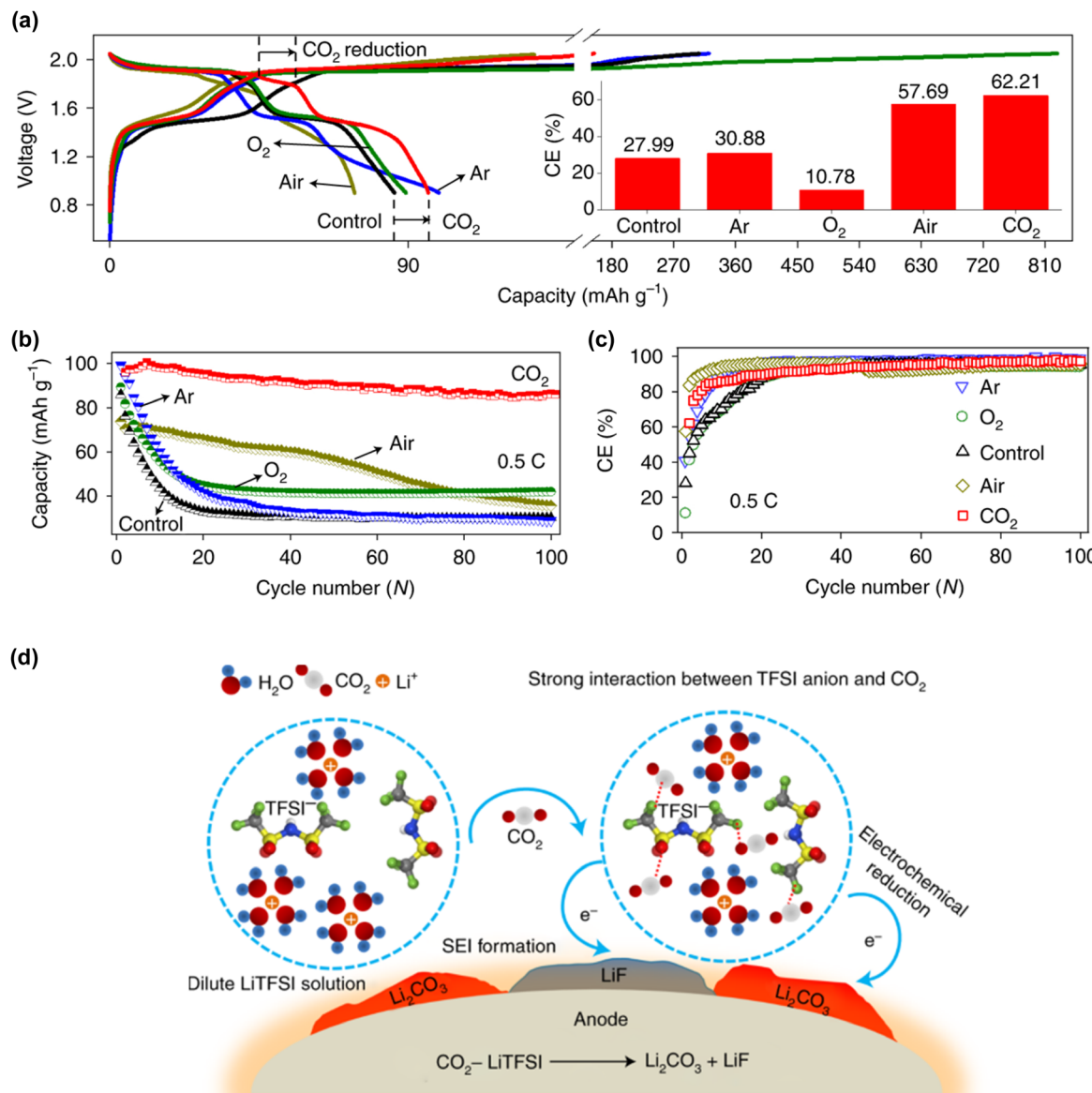


Fig. 42 (a)–(c) Electrochemical performance of an aqueous $\text{LiMn}_2\text{O}_4\text{||Mo}_6\text{S}_8$ full cell in 5 m LiTFSI/ H_2O saturated by various gases, and (d) the schematic of the SEI formation mechanism in a 5 m LiTFSI/ H_2O + sat. CO_2 electrolyte.⁴²⁰ Reprinted with permission from *Nature Chemistry*.

cycling performance of batteries, this enhancement has not sufficed to increase the battery energy density, particularly in terms of the output voltage. The batteries tested with these hybrid electrolytes mostly operated within the 2 V-class range, significantly lagging behind the 4 V-class typical of nonaqueous batteries. This notable difference is primarily due to the poor reduction stability of the electrolyte, which necessitates the selection of anode active materials with higher reaction potentials. Indeed, since 2016, when $\text{Li}_4\text{Ti}_5\text{O}_{12}$ was first introduced as an anode material in aqueous batteries, there has been negligible progress in employing anode materials that offer lower potentials than the reaction potentials of 1.5–1.6 V vs. Li/Li^+ (Tables 1 and 8).

Addressing these challenges requires a deeper understanding of the solution structure of electrolytes at a molecular level, which is particularly challenging in aqueous and hybrid aqueous/nonaqueous electrolytes. Techniques such as Raman and

Fourier transform infrared spectroscopy are frequently utilized to estimate the solution structure of nonaqueous electrolytes, as demonstrated in Fig. 43.^{421,422} For example, when the FSI^- anion forms a solvent-separated ion pair with aprotic solvents—indicating weak interactions—the corresponding Raman peak for the S–N–S vibration appears at $\sim 720 \text{ cm}^{-1}$. As the interaction between the Lewis acidic carrier ion and the FSI^- anion strengthens, leading to ion pairing, the Raman peak shifts to higher wavenumbers: $725\text{--}735 \text{ cm}^{-1}$ for a contact ion pair and further to $745\text{--}760 \text{ cm}^{-1}$ for an ion-pair aggregate. This technique helps trace the interactions between the anion and the molecules in the electrolyte, indirectly determining the ligands of the carrier ion based on the assumption that the anion interacts weakly with the aprotic solvent.

However, these spectroscopic techniques are less effective for aqueous and hybrid aqueous/nonaqueous electrolytes. For the FSI^- anion, the Raman shift corresponding to the transformation



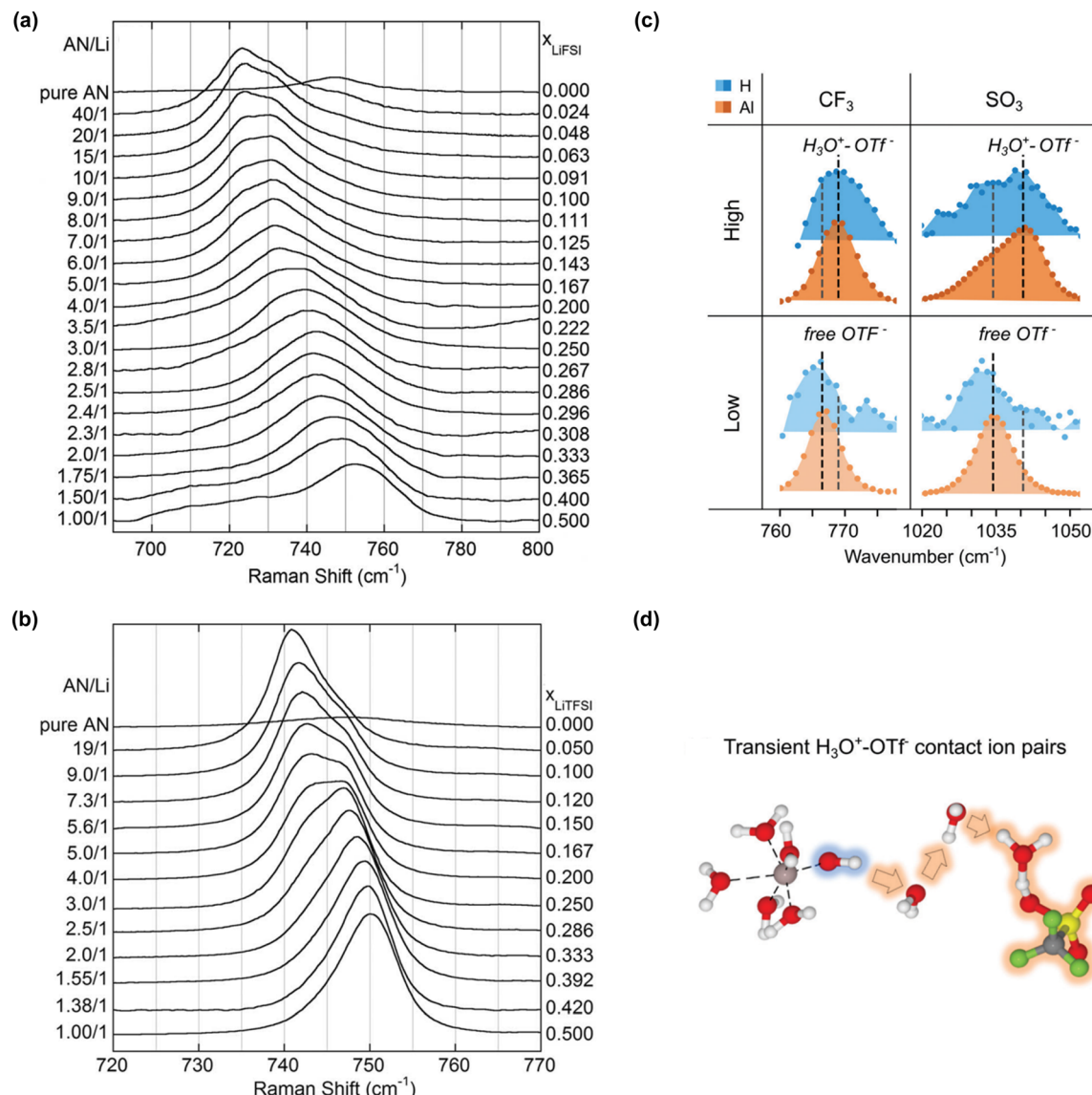


Fig. 43 Representative Raman spectra of (a) FSI⁻⁴²¹ and (b) TFSI⁻ anions⁴²³ in nonaqueous electrolytes, illustrating variational bands of the anion in LiFSI/acetonitrile and LiTFSI/acetonitrile electrolytes. (c) Raman spectra of CF₃ and SO₃ vibrational bands in Al(OTf)₃ and H₃O⁺-OTf⁻ solutions at different salt concentrations, labelled “low” and “high” in the figure.⁴²⁴ (d) Schematic of H₃O⁺-OTf⁻ ion pairing.⁴²⁴ Reprinted with permission from *Journal of The Electrochemical Society* (a) and (b) and *Energy & Environmental Science* (c) and (d).

of the solvent-separated ion pair to ion-pair aggregate was only ~ 10 cm⁻¹, ranging from 740 to 750 cm⁻¹, thus requiring high-resolution spectroscopy measurements, as illustrated in Fig. 43.^{423,425} Additionally, water, being a highly protic solvent with a high dielectric constant (78 at 25 °C)⁴²⁶ and a high acceptor number (AN = 55),^{427,428} strongly coordinates with the anion. This implies that even when the anion is surrounded by water molecules (*i.e.*, solvent-separated ion pair), their interactions are sufficiently strong to cause a shift in the Raman spectra. Considering that the Lewis acidic carrier ion and protic water compete to coordinate with the anion and that the electrolyte pH influences the Raman spectra, identifying the ligands of the carrier ion becomes significantly more complex (Fig. 43).⁴²⁴ Moreover, highly salt-concentrated aqueous electrolytes and

hybrid aqueous/nonaqueous electrolytes typically contain only a small amount of water—less than 10 wt% relative to the salts and co-solvents—making it difficult to detect the O-H vibrational changes in water. This poses additional challenges in understanding the hydrogen bonding and clustering of water molecules in these electrolytes.

7. Substantial challenges with aqueous Zn-metal batteries

Aqueous rechargeable Zn-metal batteries, employing Zn-metal anodes, are emerging as promising candidates for next-generation energy storage systems, offering cost efficiency, environmental

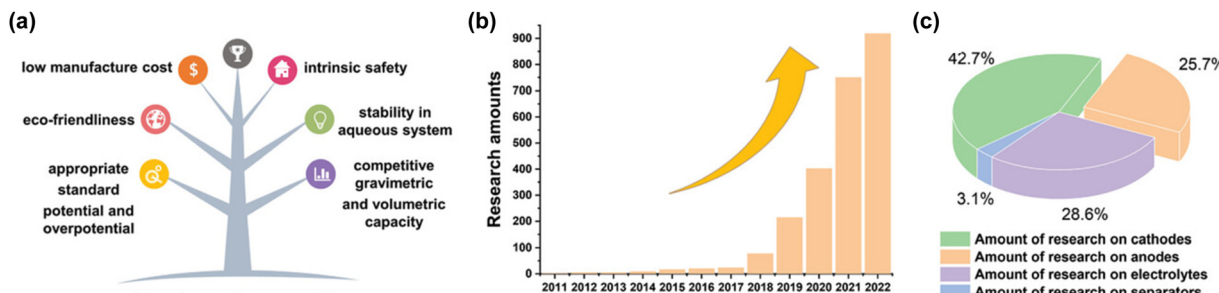


Fig. 44 (a) Advantages of aqueous Zn-metal batteries. (b) and (c) Number and proportion of research publications on aqueous Zn-metal batteries from 2011 to 2022.⁴³² Reprinted with permission from *Advanced Functional Materials*.

advantages, and safety, as shown in Fig. 44. Zn metal offers a high theoretical capacity (820 mA h g^{-1} , $5855 \text{ mA h cm}^{-3}$), has abundant availability, and is almost non-reactive with water. The mild reduction potential of Zn/Zn^{2+} (-0.76 V vs. SHE), closely aligned with the HER potential, further underscores its suitability for aqueous rechargeable batteries. Research on aqueous Zn-metal batteries is primarily driven by the hope that such batteries can overcome the constraints associated with Li^+ and other carrier ion-based batteries. However, recent studies have revealed critical misunderstandings in the intercalation chemistry of Zn cathode active materials in aqueous electrolytes.^{429–431} Moreover, the thermodynamic and kinetic limitations in suppressing electrochemical and chemical side reactions during Zn plating and stripping, which lead to significant consumption of the electrolyte and Zn resources and is accompanied by the irreversible formation of byproducts, present substantial challenges for the development of high-performance aqueous Zn-metal batteries. The following sections will delve into common misunderstandings and overlooked aspects of aqueous Zn-metal batteries.

7.1. Complex intercalation chemistry of Zn cathode active materials

The type of cathode active material significantly influences the energy density of aqueous Zn-metal batteries. Extensive research has been conducted to explore high-capacity and high-potential Zn^{2+} -intercalation cathode active materials, as outlined in Table 11. However, a misunderstanding of the intercalation chemistry and unreasonable design concepts have misdirected research efforts and material development. While initial assumptions based on the small radius of Zn^{2+} ($\sim 0.9 \text{ \AA}$) suggested that it should facilitate solid-state transport and storage,⁴³³ its high charge density results in strong interactions with lattice oxide ions in the active materials. This makes solid-state transport much more challenging than for monovalent ions, as depicted in Fig. 45.^{434–437} Moreover, most proposed Zn cathode active materials have been evaluated under extremely high C-rates, and their electrochemical properties, as detailed in Table 11, are considered to be primarily derived from the intercalation of protons and/or water-coordinated Zn^{2+} rather than pure (desolvated) Zn^{2+} .^{430,438–443} The issue is that proton and water co-intercalation increase the complexity of active material and cell design, leading to unexpected electrochemical reactions. For

instance, the increased electrolyte pH due to proton intercalation, which occurs even under nearly neutral conditions, damages the cathode active materials and leads to the formation/precipitation of byproducts (e.g., $\text{Zn}(\text{OH})_2$ and $\text{Zn}(\text{anion})_x(\text{OH})_y$) on the Zn-metal anode surface.⁴⁴⁴ Additionally, water co-intercalation causes significant volume changes in the cathode active materials during charge and discharge processes, thereby reducing their structural integrity. This section will introduce the representative cathode active materials tested in aqueous Zn-metal batteries, highlighting their structural features, intercalation chemistry, and practical feasibility. As we demonstrated in Section 1, ‘M’ and ‘m’ were used interchangeably in several papers. Further, these expressions were quoted directly without any corrections, despite the fact that ‘M’ (molarity, mol L^{-1}) specifies the amount of salt per unit volume of a solution (electrolyte), while ‘m’ (molality, mol kg^{-1}) denotes the concentration of salt dissolved in 1 kg of a solvent.

Manganese oxide (MnO_2) was first utilized in primary Zn alkaline batteries (Fig. 46).⁵³⁹ Among its various polymorphs, α - and δ - MnO_2 facilitate water co-intercalation owing to their large tunnels, interlayer spaces, and flexible structural interstitials, which provide sufficient tolerance for large guest ions.^{445,560,561} Conversely, γ - MnO_2 , with its limited structural interstitials and tunnel sizes, tends to prevent water co-intercalation. However, in acidic and neutral electrolytes, the intercalation of protons into all MnO_2 polymorphs occurs kinetically much faster than that of Zn^{2+} . Additionally, MnO_2 dissolves easily into the bulk electrolyte, a degradation mode that is accelerated in alkaline conditions by forming OH-ranked complex ions, $[\text{Mn}(\text{OH})_{n+2}]^{n-}$.⁵⁶² Although aqueous Zn electrolytes containing Mn^{2+} salts such as MnSO_4 mitigate the issue of MnO_2 dissolution,⁴⁵¹ the presence of Mn^{2+} in the electrolyte can cause anodic electrolysis of Mn^{2+} , producing additional γ - MnO_2 deposits while consuming water, which would alter the initial electrolyte formulation. As another degradation mechanism, Laberty-Robert, Balland, and Limoges *et al.* demonstrated that weak acid proton donors (e.g. $[\text{Zn}(\text{H}_2\text{O})_6]^{2+}$), which readily form in aqueous Zn solutions, facilitate the electrodissolution of various MnO_x .^{563,564}

Based on the rich chemistry of V, diverse types of vanadium oxides (V_xO_y) have been explored and tested for aqueous Zn-metal batteries. V_xO_y provides a large capacity owing to its multiple electron reactions ($\text{V}^{3+}/\text{V}^{5+}$). A layered structure of $\text{Zn}_{0.25}\text{V}_2\text{O}_5 \cdot n\text{H}_2\text{O}$, consisting of V_2O_5 bilayers with interlayer



Table 11 Performance data for Zn-metal full cells with various cathode active materials

Year	Electrolyte	Cathode	Cathode I/L (mg cm ⁻²)	Anode	Anode I/L (mg cm ⁻²)	Full cell cutoff (V/V)	Full cell average (V)	N/P ratio	C-rate	Capacity (mA h g ⁻¹)	Capacity calculation based	Cycle number (-)	Retention ratio (%)
2012	0.1 M Zn([NO ₃] ₂ /H ₂ O (pH 5.2) ⁴⁴⁵	α-MnO ₂	—	Zn foil	—	1.9/1.0	1.3	—	6C	132	Cathode	100	74
2013	1 M ZnSO ₄ /H ₂ O ⁴⁴⁶	Todorokite-type- MnO ₂ or α-MnO ₂	50	Zn foil	10 μm	2.0/0.7	1.4 or 1.3	—	50 mA g ⁻¹	108 (todorokite-type-MnO ₂) ²²⁷ (α-MnO ₂)	Cathode	50	83
2014	1 M ZnSO ₄ /H ₂ O ⁴⁴⁷	α-MnO ₂	5	Zn foil	—	2.0/0.7	1.3	—	0.2C	205	Cathode	50	56
2014	0.5 M Zn(OAc) ₂ + 0.5 M NaOAc/H ₂ O ⁴⁴⁸	Na _{0.95} MnO ₂	—	Zn foil	—	2.0/1.0	1.4	—	4C	40	Cathode	30	63
2014	2 M ZnSO ₄ /H ₂ O ⁴⁴⁹	Mn ₃ O ₄	—	Zn foil	—	1.9/0.8	1.3	—	500 mA g ⁻¹	147	Cathode	300	72
2015	1 M ZnSO ₄ /H ₂ O (pH 4) ⁴⁵⁰	γ-MnO ₂	—	Zn foil	—	1.8/0.8	1.3	—	0.5 mA cm ⁻²	250	Cathode	40	63
2016	2 M ZnSO ₄ + 0.1 M MnSO ₄ / H ₂ O ⁴⁵¹	α-MnO ₂	1–5	Zn foil	—	1.8/1.0	1.4	—	5C	161	Cathode	5000	92
2016	1–4 M Zn(OTf) ₂ /H ₂ O ⁴⁵²	ZnMn ₂ O ₄	2	Zn foil	—	1.9/0.8	1.4	—	500 mA g ⁻¹	90	Cathode	500	94
2017	2 M ZnSO ₄ + 0.1 M MnSO ₄ / Mn ₂ O ₃	—	—	Zn foil	—	1.9/1.0	1.4	—	2000 mA g ⁻¹	89	Cathode	2000	49
2017	3 M LiCl + 2 M ZnCl ₂ + 0.4 M MnSO ₄ /H ₂ O + lignocellulose + poly(vinyl alcohol) ⁴⁵⁴	Poly(3,4-ethylenedioxy thiophene) coated MnO ₂	—	Zn foil	—	1.8/1.0	1.3	—	1860 mA g ⁻¹	150	Cathode	300	78
2017	2 M ZnSO ₄ + 0.2 M MnSO ₄ / α-MnO ₂ /carbon fiber	—	—	Zn foil	—	1.8/1.0	1.3	—	1.3C	260	Cathode	300	58
2017	3 M Zn(OTf) ₂ + 0.1 M Mn(OTf) ₂ /H ₂ O ⁴⁵⁶	β-MnO ₂	2	Zn foil	—	1.9/0.8	1.2	—	0.65C	70	Cathode	10000	71
2018	Polyacrylamide polymer soaked in 2 M ZnSO ₄ + 0.1 M MnSO ₄ /H ₂ O ⁴⁵⁷	α-MnO ₂	2.5–5	Zn/carbon nanotube	7–10	1.85/0.8	1.3	—	6.5C	258	Cathode	100	87
2018	2 M ZnSO ₄ + 0.2 M MnSO ₄ / Graphene coated H ₂ O ⁴⁵⁸	Graphene coated —	—	Zn foil	—	1.85/1.0	1.4	—	2000 mA g ⁻¹	151	Cathode	2000	94
2018	1 M ZnSO ₄ + 0.1 M MnSO ₄ / MgMn ₂ O ₄	—	3–3.5	Zn foil	—	1.9/0.5	1.5	—	50 mA g ⁻¹	103	Cathode	500	98.5
2018	2 M ZnSO ₄ + 0.1 M MnSO ₄ / Mn ₃ O ₄	—	H ₂ O ⁴⁵⁹	Zn foil	—	1.8/1.0	1.4	—	500 mA g ⁻¹	239	Cathode	500	82
2017	1 M ZnSO ₄ /H ₂ O (pH 4) ⁴⁶¹	LiV ₃ O ₈	—	Zn foil	—	1.2/0.6	0.8	—	300 mA g ⁻¹	382 (300 mA g ⁻¹)	Cathode	100	95
2017	1 M Zn(OTf) ₂ + 21 m LiTFSI/H ₂ O ⁴⁶²	α-MnO ₂	—	Zn foil	—	1.6/0.2	1.0	—	1000 mA g ⁻¹	166 (3000 mA g ⁻¹)	Cathode	100	100
2018	3 M Zn(OTf) ₂ /H ₂ O ⁴⁴³	V ₂ O ₅ ·nH ₂ O/ graphene	2.5	Zn foil	—	1.5/0.3	0.8	—	3000 mA g ⁻¹	120	Cathode	300	80
2018	3 M Zn(OTf) ₂ /H ₂ O ⁴⁶³	V ₂ O ₅ /H ₂ O ₅	2–10	Zn foil	—	1.6/0.2	0.7	—	6000 mA g ⁻¹	~290	Cathode	500	82
2018	3 M ZnSO ₄ /H ₂ O ⁴⁶⁴	LiV ₃ O ₈	—	Zn foil	—	1.4/0.4	0.7	—	200 mA g ⁻¹	470	Cathode	100	100
2018	3 M Zn(OTf) ₂ or 3 M ZnCl ₂ or V ₂ O ₅	—	—	Zn foil	—	1.4/0.4	0.7	—	500 mA g ⁻¹	465	Cathode	100	100
2018	3 M ZnOAc ₂ or 3 M Zn(NO ₃) ₂ /H ₂ O ⁴⁶⁴	—	—	Zn foil	—	1.7/0.7	1.0	—	1000 mA g ⁻¹	455	Cathode	4000	91
2018	3 M Zn(OTf) ₂ /H ₂ O ⁴⁶⁵	V ₁₀ O ₂₄ ·12H ₂ O	—	Zn foil	—	—	—	—	5000 mA g ⁻¹	408	Cathode	30	81
2018	3 M ZnSO ₄ or 3 M ZnCl ₂ or V ₂ O ₅	—	—	Zn foil	—	—	—	—	100 mA g ⁻¹	224	Cathode	400	99
2018	3 M ZnOAc ₂ or 3 M Zn(NO ₃) ₂ /H ₂ O ⁴⁶⁴	—	—	Zn foil	—	—	—	—	2000 mA g ⁻¹	121	Cathode	400	100
2018	3 M Zn(OTf) ₂ /H ₂ O ⁴⁶⁵	V ₁₀ O ₂₄ ·12H ₂ O	—	Zn foil	—	—	—	—	500 mA g ⁻¹	113	Cathode	200	83
2018	3 M ZnSO ₄ /H ₂ O ⁴⁶³	—	—	Zn foil	—	—	—	—	5000 mA g ⁻¹	135 (500 mA g ⁻¹)	Cathode	1000	81
2018	3 M Zn(OTf) ₂ /H ₂ O ⁴⁶⁵	—	—	Zn foil	—	—	—	—	10 000 mA g ⁻¹	10 000	Cathode	3000	80



Table 11 (continued)

Year	Electrolyte	Cathode	Anode	Anode L/L (mg cm ⁻²)	Full cell L/L (mg cm ⁻²)	Full cell cutoff (V/V)	Full cell average (V)	N/P ratio	C-rate	Capacity (mA h g ⁻¹)	Capacity calculation based	Cycle number (–)	Cycle retention ratio (%)	
2018	2 M ZnSO ₄ /H ₂ O ⁴⁶⁶	Li _x V ₂ O ₅ ·nH ₂ O	~2.8	Zn foil	—	1.4/0.4	0.7	—	1000 mA g ⁻¹	408 (1000 mA g ⁻¹)	Cathode	50	68	
2018	3 M Zn(OTf) ₂ /H ₂ O ⁴⁶⁷	Na _{0.33} V ₂ O ₅	—	Zn foil	—	1.6/0.2	0.6	—	5000 mA g ⁻¹	304 (5000 mA g ⁻¹)	Cathode	500	76	
2018	1 M ZnSO ₄ /H ₂ O ⁴⁶⁸	Na ₂ V ₆ O ₁₆ ·3H ₂ O	3–3.5	Zn foil	—	1.4/0.4	0.8	—	200 mA g ⁻¹	277	Cathode	1000	62	
2018	3 M Zn(OTf) ₂ /H ₂ O ⁴⁶⁹	Mg _{0.34} V ₂ O ₅ ·0.84H ₂ O	5–7	Zn foil	—	1.8/0.1	0.8	—	1000 mA g ⁻¹	235	Cathode	100	91	
2018	3 M Zn(OTf) ₂ /H ₂ O (pH 4) ⁴⁷⁰	NH ₄ V ₄ O ₁₀	2	Zn foil	—	1.7/0.8	1.0	—	2000 mA g ⁻¹	81	Cathode	1000	93	
2018	2 M ZnSO ₄ /H ₂ O ⁴⁷¹	(NH ₄) ₂ V ₁₀ O ₂₅ ·8H ₂ O	—	Zn foil	—	1.7/0.7	1.0	—	2000 mA g ⁻¹	126	Cathode	400	80	
2019	1 M ZnSO ₄ /H ₂ O ⁴⁷²	VO ₂	—	Zn foil	—	1.2/0.2	0.6	—	100 mA g ⁻¹	72	Cathode	300	94	
2019	1 M ZnSO ₄ /H ₂ O ⁴⁷³	VO ₂	—	Zn foil	—	1.3/0.2	0.6	—	500 mA g ⁻¹	196	Cathode	1000	70	
2019	3 M ZnSO ₄ /H ₂ O ⁴⁷⁴	VO ₂ (D)	1.2–1.5	Zn foil	—	1.5/0.2	0.8	—	5000 mA g ⁻¹	124	Cathode	100	95	
2019	3 M Zn(OTf) ₂ /H ₂ O ⁴⁷⁵	V ₂ O ₃	—	Zn foil	—	1.5/0.3	0.7	—	10000 mA g ⁻¹	326	Cathode	5000	97	
2019	2 M ZnSO ₄ /H ₂ O ⁴⁷⁶	V ₂ O ₅	3	Zn foil	—	1.6/0.2	0.7	—	10000 mA g ⁻¹	272	Cathode	200	98	
2019	3 M Zn(OTf) ₂ /H ₂ O ⁴⁷⁷	V ₂ O ₅	2	Zn foil	—	1.5/0.5	0.9	—	10000 mA g ⁻¹	228	Cathode	5000	70	
2019	3 M Zn(OTf) ₂ /H ₂ O ⁴⁷⁸	V ₆ O ₁₃ ·nH ₂ O	7.2	Zn foil	—	1.4/0.2	0.7	—	10000 mA g ⁻¹	341	Cathode	1000	94	
2019	2 M ZnSO ₄ /H ₂ O ⁴⁷⁹	V ₁₀ O ₂₄ ·12H ₂ O	—	Zn foil	—	1.5/0.5	0.9	—	10000 mA g ⁻¹	219	Cathode	500	90	
2019	3 M Zn(OTf) ₂ /H ₂ O ⁴⁷⁹	Al doped V ₁₀ O ₂₄ ·1.8 12H ₂ O	1.8	Zn foil	—	1.6/0.3	0.9	—	2C	205	Cathode	500	85	
2019	3 M Zn(OTf) ₂ /H ₂ O ⁴⁸⁰	V ₃ O ₇ ·nH ₂ O	1–2	Zn foil	—	1.7/0.05	0.7	—	5000 mA g ⁻¹	300	Cathode	3000	98	
2019	1 M Zn(OTf) ₂ + 21 m LiFSI/H ₂ O ⁴⁸¹	V ₂ O ₅ ·nH ₂ O/V ₃ O ₇ — nH ₂ O	—	Zn foil	—	1.6/0.4	0.7	—	10000 mA g ⁻¹	355	Cathode	300	89	
2019	3 M Zn(OTf) ₂ /H ₂ O ⁴⁸²	V ₅ O ₁₂ ·6H ₂ O	4.5	Zn foil	—	1.6/0.2	0.7	—	5000 mA g ⁻¹	307	Cathode	3000	80	
2019	3 M Zn(OTf) ₂ /H ₂ O ⁴⁸³	V ₅ O ₁₂ ·6H ₂ O/gra-phen oxide	1.1	Zn foil	—	1.6/0.2	0.7	—	10000 mA g ⁻¹	365	Cathode	300	82	
2019	3 M Zn(OTf) ₂ /H ₂ O ⁴⁸⁴	V ₆ O ₁₃	1.0–1.5	Zn foil	—	1.5/0.2	0.7	—	4000 mA g ⁻¹	172	Cathode	1000	85	
2019	3 M Zn(OTf) ₂ /H ₂ O ⁴⁸⁵	V ₆ O ₁₃	—	Zn foil	—	1.4/0.3	0.7	—	5000 mA g ⁻¹	250	Cathode	1200	80	
2019	1 M ZnSO ₄ /7H ₂ O + 0.2 M Na ₂ SO ₄ /H ₂ O ⁴⁸⁶	Na ₂ V ₆ O ₁₂ ·2.14H ₂ O	1.5	Zn foil	—	1.6/0.2	0.8	—	10000 mA g ⁻¹	250	Cathode	500	84	
2019	3 M Zn(OTf) ₂ /H ₂ O ⁴⁸⁷	Ca _{0.67} V ₂ O ₃ ·3.5H ₂ O	0.8	Zn foil	—	1.5/0.4	0.7	—	20000 mA g ⁻¹	145	Cathode	2000	90	
										5000 mA g ⁻¹	291	Cathode	2000	74



Table 11 (continued)

Year	Electrolyte	Cathode	Anode	Anode L/L (mg cm ⁻²)	Anode L/L (mg cm ⁻²)	Full cell cutoff (V/V)	Full cell average (V)	N/P ratio	C-rate	Capacity (mA h g ⁻¹)	Capacity calculation based	Cycle number (–)	Retention ratio (%)
2019	3 M ZnSO ₄ /H ₂ O ⁴⁸⁸	Ag _{0.4} V ₂ O ₅	—	Zn foil	—	1.4/0.4	0.7	—	5000 mA g ⁻¹	283	Cathode	1000	76
2019	1 M Zn(OTf) ₂ + 20 m LiTFSI/H ₂ O ⁴⁸⁹	Co _{0.25} V ₂ O ₅ ·0.94H ₂ O	1–3	Zn foil	—	2.2/0.6	1.0	—	10 000 mA g ⁻¹	155	Cathode	4000	93
2019	1 M ZnSO ₄ /H ₂ O ⁴⁹⁰	K ₂ V ₂ O ₅	3	Zn foil	—	1.4/0.4	0.7	—	4000 mA g ⁻¹	215	Cathode	7500	90
2019	3 M Zn(OTf) ₂ /H ₂ O ⁴⁹¹	CuV ₂ O ₆ ·(NH ₄) ₂ V ₆ O ₁₆ ·1.5H ₂ O	1–2	Zn foil	—	1.6/0.2	0.8	—	3000 mA g ⁻¹	91	Cathode	500	91
2019	2 M ZnSO ₄ /H ₂ O ⁴⁹²	(NH ₄) ₂ V ₆ O ₁₆ ·1.5H ₂ O	—	Zn foil	—	1.6/0.2	0.8	—	8000 mA g ⁻¹	156	Cathode	1500	96
2019	3 M Zn(OTf) ₂ /H ₂ O ⁴⁹³	(NH ₄) ₂ V ₆ O ₁₆ ·1.5H ₂ O	—	Zn foil	—	1.6/0.4	0.8	—	5000 mA g ⁻¹	300	Cathode	3000	100
2019	3 M Zn(OTf) ₂ /H ₂ O ⁴⁹⁴	NaCa _{0.6} V ₆ O ₁₆ ·3H ₂ O	1.1	Zn foil	—	1.5/0.4	0.8	—	2000 mA g ⁻¹	221 (3000 mA g ⁻¹)	Cathode	1000	95
2020	3 M Zn(OTf) ₂ /H ₂ O ⁴⁹⁵	Polypyrrole coated VO ₂ (A)	1.2	Zn foil	—	1.4/0.2	0.8	—	2000 mA g ⁻¹	231	Cathode	3000	60
2020	3 M Zn(OTf) ₂ /H ₂ O ⁴⁹⁶	VO ₂ (B)/graphene oxide	1	Zn foil	—	1.4/0.2	0.7	—	5000 mA g ⁻¹	189	Cathode	5000	90
2020	2 M Zn(OTf) ₂ /H ₂ O ⁴⁹⁷	V ₂ O ₃	2	Zn foil	—	1.6/0.2	0.7	—	100 mA g ⁻¹	213	Cathode	100 000	75
2020	2 M ZnSO ₄ /H ₂ O ⁴⁹⁸	V ₆ O ₁₃	1.5	Zn/carbon cloth	2.5	1.4/0.2	1.0	1.7 (mass)	300 mA g ⁻¹	139	Cathode	300	85
2020	3 M Zn(TFSI) ₂ /H ₂ O ⁴⁹⁹	Oxygen deficient 2 V ₆ O ₁₃	—	Zn foil	—	1.5/0.2	0.8	—	2000 mA g ⁻¹	231	Cathode	2000	94
2020	2 M Zn(OTf) ₂ /H ₂ O (pH 4) ⁵⁰⁰	K _{0.23} V ₂ O ₅	—	Zn foil	—	1.7/0.1	0.7	—	2000 mA g ⁻¹	~305	Cathode	2000	86
2020	2 M Zn(TFSI) ₂ /H ₂ O ⁵⁰¹	MbV ₂ O ₄	1–1.5	Zn foil	—	1.4/0.2	0.8	—	100 mA g ⁻¹	~245	Cathode	50	85
2020	3 M Zn(OTf) ₂ /H ₂ O ⁵⁰²	PEDOT/NH ₄ V ₃ O ₈ 2	—	Zn foil	—	1.6/0.4	0.7	—	2000 mA g ⁻¹	111	Cathode	500	93
2020	3 M Zn(OTf) ₂ /H ₂ O ⁵⁰³	(NH ₄) ₂ V ₃ O ₈	—	Zn foil	—	1.6/0.4	0.8	—	200 mA g ⁻¹	293	Cathode	50	93
2020	3 M ZnSO ₄ /H ₂ O ⁵⁰⁴	δ-Ni _{0.25} V ₂ O ₅ ·nH ₂ O	2.5–3.5	Zn foil	—	1.7/0.3	0.7	—	4000 mA g ⁻¹	192	Cathode	500	67
2021	3 M Zn(OTf) ₂ /H ₂ O ⁵⁰⁵	Nanotube-type VO ₂ 1–2	—	Zn foil	—	1.4/0.2	0.8	—	200 mA g ⁻¹	346	Cathode	100	95
2021	2 M ZnSO ₄ /H ₂ O ⁵⁰⁶	Polypyrrole coated oxygen deficient VO ₂ nH ₂ O	1–3	Zn foil	—	1.6/0.2	0.8	—	10 000 mA g ⁻¹	171	Cathode	5000	94
2021	3 M ZnSO ₄ /H ₂ O ⁵⁰⁷	N doped carbon coated V ₂ O ₃	1.8	Zn foil	—	1.6/0.3	—	—	100 mA g ⁻¹	310	Cathode	50	69
2021	3 M Zn(OTf) ₂ /H ₂ O ⁵⁰⁸	Oxygen deficient 1 V ₂ O ₅	—	Zn foil	—	1.6/0.1	0.8	—	200 mA g ⁻¹	290	Cathode	100	74
2021	2 M Zn(OTf) ₂ /H ₂ O ⁵⁰⁹	Oxygen deficient V ₂ O ₅	—	Zn foil	—	1.5/0.4	0.8	—	1000 mA g ⁻¹	266	Cathode	2000	51
2021	2.5 M Zn(OTf) ₂ /H ₂ O ⁵¹⁰	V ₂ O ₅	—	Zn foil	—	1.6/0.2	0.8	—	5000 mA g ⁻¹	385	Cathode	50	90
2021	3 M Zn(OTf) ₂ /H ₂ O ⁵¹¹	V ₂ O ₅ /graphene oxide	2	Zn foil	—	1.6/0.3	0.8	—	1000 mA g ⁻¹	152	Cathode	1200	98
2021	3 M ZnSO ₄ /H ₂ O ⁵¹²	—	—	Zn foil	—	1.6/0.3	0.8	—	5000 mA g ⁻¹	318	Cathode	1000	99
2021	3 M ZnSO ₄ /H ₂ O ⁵¹³	—	—	Zn foil	—	1.6/0.2	0.8	—	200 mA g ⁻¹	195	Cathode	5000	84
2021	3 M ZnSO ₄ /H ₂ O ⁵¹⁴	—	—	Zn foil	—	1.6/0.3	0.8	—	10 000 mA g ⁻¹	337	Cathode	500	87
2021	3 M ZnSO ₄ /H ₂ O ⁵¹⁵	—	—	Zn foil	—	1.6/0.3	—	—	10 000 mA g ⁻¹	206	Cathode	1000	76
2021	3 M ZnSO ₄ /H ₂ O ⁵¹⁶	—	—	Zn foil	—	1.6/0.3	—	—	100 mA g ⁻¹	428	Cathode	152	93
2021	3 M Zn(OTf) ₂ /H ₂ O ⁵¹⁷	—	—	Zn foil	—	1.6/0.1	0.8	—	10 000 mA g ⁻¹	351	Cathode	4000	92
2021	2 M Zn(OTf) ₂ /H ₂ O ⁵¹⁸	—	—	Zn foil	—	1.5/0.4	0.8	—	200 mA g ⁻¹	361	Cathode	200	82
2021	2.5 M Zn(OTf) ₂ /H ₂ O ⁵¹⁹	—	—	Zn foil	—	1.6/0.2	0.8	—	2000 mA g ⁻¹	251	Cathode	1000	85
2021	2.5 M Zn(OTf) ₂ /H ₂ O ⁵²⁰	—	—	Zn foil	—	1.6/0.3	0.8	—	20 000 mA g ⁻¹	108	Cathode	2000	87
2021	2.5 M Zn(OTf) ₂ /H ₂ O ⁵²¹	—	—	Zn foil	—	1.6/0.3	0.8	—	500 mA g ⁻¹	361	Cathode	5000	95
2021	2.5 M Zn(OTf) ₂ /H ₂ O ⁵²²	—	—	Zn foil	—	1.6/0.3	0.8	—	100 mA g ⁻¹	528	Cathode	2000	71
2021	2.5 M Zn(OTf) ₂ /H ₂ O ⁵²³	—	—	Zn foil	—	1.6/0.3	0.8	—	20 000 mA g ⁻¹	212	Cathode	50	79
2021	3 M ZnSO ₄ /H ₂ O ⁵²⁴	—	—	Zn foil	—	1.6/0.3	—	—	40 000 mA g ⁻¹	114	Cathode	1000	91

Table 11 (continued)

Year	Electrolyte	Cathode	Anode	Anode L/L (mg cm ⁻²)	Full cell L/L (mg cm ⁻²)	Full cell cutoff (V/V)	Full cell average (V)	N/P ratio	C-rate	Capacity (mA h g ⁻¹)	Capacity calculation based	Cycle number (→)	Retention ratio (%)
2021	3 M Zn(OTf) ₂ /H ₂ O ⁵¹²	V ₂ O ₅ ·nH ₂ O V ₃ O ₇ ·H ₂ O	—	Zn foil Zn foil	— —	1.6/0.3 1.1/0.4	0.7 0.8	—	5000 mA g ⁻¹ 100 mA g ⁻¹ 2000 mA g ⁻¹	342 323 (100 mA g ⁻¹)	Cathode Cathode	1000 50 800	97 92 83
2021	3 M Zn(OTf) ₂ /H ₂ O ⁵¹³	V ₆ O ₁₃ /carbon nanotubes	1	Zn foil	—	1.5/0.3	0.8	—	500 mA g ⁻¹ 5000 mA g ⁻¹ 2000 mA g ⁻¹	~325 165 305	Cathode Cathode	500 5000 4000	95 91 80
2021	3 M Zn(OTf) ₂ /H ₂ O ⁵¹⁴	CO ₂ modified V ₆ O ₁₃	1–2	Zn foil	—	1.5/0.3	0.7	—	500 mA g ⁻¹ 5000 mA g ⁻¹ 2000 mA g ⁻¹	165 305	Cathode	5000	91
2021	3 M Zn(OTf) ₂ /H ₂ O ⁵¹⁵	Na ₃ V ₂ O ₅ /NaOAc/H ₂ O ⁵¹⁶	1	Zn foil	—	1.4/0.4	0.8	—	500 mA g ⁻¹ 5000 mA g ⁻¹ 100 mA g ⁻¹	350 288 170	Cathode Cathode	1000 800 500	86 94 88
2023	3 M ZnSO ₄ /H ₂ O + 1-ethyl-3-methylimidazolium·FSI ⁵¹⁷	K ₂ V ₆ O ₁₆ ·1.5H ₂ O Zn _{0.25} V ₂ O ₅ ·nH ₂ O	3 or 13	Zn foil or 10 μm	Excess 10 μm	1.4/0.5 1.4/0.5	0.7 0.7	Zn excess (3 mg cm ⁻² , 30 °C)	5000 mA g ⁻¹ 100 mA g ⁻¹ (3 mg cm ⁻² , 30 °C)	350 288 149	Cathode Cathode	1000 800 500	86 94 88
2023	2 m Zn(OTf) ₂ /H ₂ O + ether [pH 4] [ether; 15-crown-5 or 12-crown-4 or triglyme] ⁵¹⁸	Zn _{0.25} V ₂ O ₅ ·nH ₂ O	3.2	Zn foil	—	1.6/0.2	0.7	2.0 (capacity) 2C 2.2 (capacity) 0.16C	1000 mA g ⁻¹ (3 mg cm ⁻² , 60 °C)	275 (2C)	Cathode	400	85
2016	0.5 M Zn(OAc) ₂ /H ₂ O ⁵¹⁹	Na ₃ V ₂ (PO ₄) ₃	—	Zn foil	—	1.7/0.8	1.2	—	0.5C 0.5C	97 93	Cathode Cathode	1000 200	74 77
2016	1 M Zn(OAc) ₂ + 0.5 M NaOAc/H ₂ O ⁵²⁰	Na ₃ V ₂ (PO ₄) ₃	—	Zn foil	—	1.7/0.8	1.4	—	0.5C 0.5C	93	Cathode	200	77
2016	2 M ZnSO ₄ + 1 M Li ₂ SO ₄ /H ₂ O (pH 4) ⁵²¹	Li ₃ V ₂ (PO ₄) ₃ or Na ₃ V ₂ (PO ₄) ₃	6	Zn foil	—	2.1/0.7	1.2	—	0.2C (LVP) (NVP)	114 0.2C 0.2C	Cathode	200	85
2016	0.5 M ZnSO ₄ + 21 m LiTFSI/ LiMn _{0.8} Fe _{0.2} PO ₄ _{H₂O} ⁵²²	—	Zn foil	—	2.35/1.0	1.8	50 wt% Zn excess	50 wt% Zn 0.3C 0.1 (mass)	96 112 200 mA g ⁻¹ 1000 mA g ⁻¹	Cathode	200	84	
2018	2 M Zn(OTf) ₂ /H ₂ O ⁵²³	Na ₃ V ₂ (PO ₄) ₂ F ₃	10	Zn powder/ carbon/ PTFE	1.9/0.8	1.6	0.1 (mass)	200 mA g ⁻¹ 1000 mA g ⁻¹	64 48	Cathode	3200	80	
2019	1 M Zn(OTf) ₂ _{H₂O} ⁵²⁴ + 21 m LiTFSI/H ₂ O ⁵²⁵	VOPO ₄ /carbon nanotube	2	Zn foil	—	2.1/0.8	1.6	—	1000 mA g ⁻¹	82	Cathode	1000	93
2019	13 m ZnCl ₂ + 0.8 m H ₃ PO ₄ /V ₂ O ₅ /H ₂ O ⁵²⁶	—	Zn foil	—	1.9/0.7	1.4	—	2000 mA g ⁻¹	98	Cathode	500	92	
2019	1 M Zn(OTf) ₂ /H ₂ O: acetonitrile (90:10, v:v) ⁵²⁶	Polypyrrole intercalated VOPO ₄	0.7–1.5	Zn foil	—	1.7/0.6	1.4	—	100 mA g ⁻¹	86	Cathode	350	91
2019	2 M Zn(OTf) ₂ /H ₂ O ⁵²⁷	Na ₃ V ₂ (PO ₄) ₃ /graphene oxide	—	Zn foil	—	1.8/0.6	1.2	—	50 mA g ⁻¹ 500 mA g ⁻¹ 100 mA g ⁻¹	114 101 161	Cathode	500	83
2020	2 M Zn(OTf) ₂ /H ₂ O ⁵²⁸	Zn _{0.4} VOPO ₄ _{0.8H₂O}	2	Zn foil	—	1.9/0.2	1.5	—	100 mA g ⁻¹	90	Cathode	2000	75
2020	0.5 M Zn(OAc) ₂ /H ₂ O ⁵²⁹	Na ₃ V ₂ (PO ₄) ₃	—	Zn foil	—	1.6/0.6	1.2	—	1C	90	Cathode	1000	71
2020	25 m ZnCl ₂ + 5 m NH ₄ Cl/H ₂ O _{H₂O} ⁵³⁰	Na ₃ V ₂ (PO ₄) ₂ O _{1.6} F _{1.4}	2.9	Zn foil	—	2.1/0.4	1.5	500 mA g ⁻¹	139	Cathode	2000	83	
								2000 mA g ⁻¹	83			7000	74



Table 11 (continued)

Year	Electrolyte	Cathode	Anode	Anode L/L (mg cm ⁻²)	Anode L/L (mg cm ⁻²)	Full cell cutoff (V/V)	Full cell average (V)	N/P ratio	C-rate	Capacity (mA h g ⁻¹)	Capacity calculation based	Cycle number (–)	Retention ratio (%)
2021	2 M ZnSO ₄ /H ₂ O ⁵³¹	VOPO ₄ ·2H ₂ O	Zn foil	—	1.9/0.2	1.1	—	100 mA g ⁻¹	313	Cathode	500	95	
2021	2 M Zn(OTf) ₂ /H ₂ O ⁵³²	Phenylamine intercalated VOPO ₄ ·2H ₂ O	Zn foil	—	1.9/0.2	1.2	—	5000 mA g ⁻¹	206	Cathode	2000	77	
2021	1 M Zn(ClO ₄) ₂ /H ₂ O: acetonitrile (89:11, v:v) ⁵³³	Li ₃ V ₂ (PO ₄) ₃	Zn foil	—	2.2/0.7	1.5	—	2C	125	Cathode	200	95	
2021	1 M Zn(OTf) ₂ +15 m LiTFSI/H ₂ O ⁵³⁴	Li ₃ V ₂ (PO ₄) ₃	Zn foil	—	2.1/0.6	1.8	—	5C	106	Cathode	1000	89	
2022	2 M Zn(OTf) ₂ /H ₂ O + 70 wt% polyethylene glycol ⁵³⁵	LiV ₂ (PO ₄) ₃	Zn foil	—	1.9/0.2	1.4	—	200 mA g ⁻¹	127	Cathode	2000	100	
2022	2 M Zn(OTf) ₂ +1 M NaOTf/ Na ₃ V ₂ (PO ₄) ₃ H ₂ O + polyethylene glycol ⁵³⁶	Zn foil	—	1.6/0.6	1.4	—	1000 mA g ⁻¹	109	Cathode	100	84		
2023	30 m ZnCl ₂ + 5 m LiCl + 10 m trimethylammonium Cl/H ₂ O ⁵³⁷	VOPO ₄ ·2H ₂ O	Zn foil	—	1.9/0.2	1.1	2.0–2.3 (capacity)	50 mA g ⁻¹	102 (0.5C)	Cathode	300	75	
2023	30 m ZnCl ₂ /H ₂ O + vanillin VOPO ₄ ·2H ₂ O (5 mg v.s. 1 mL H ₂ O) ⁵³⁸	Zn foil	—	1.9/0.2	1.3	2.0 (capacity)	2000 mA g ⁻¹ (swagelok, 3 mg cm ⁻²)	90	Cathode	300	67		
2015	30 mM ZnSO ₄ /H ₂ O (pH 6) ⁵³⁹	Cu[Fe(CN) ₆] ₃	Zn foil	—	—	1.7	—	300 mA g ⁻¹ (swagelok, 25 mg cm ⁻²)	85 (swagelok, 3 mg cm ⁻²)	Cathode + anode	4000	85	
2015	1 M ZnSO ₄ /H ₂ O ⁵⁴⁰	Zn ₃ [Fe(CN) ₆] ₂	Zn powder/ carbon/ PVDF	0.7	2.0/0.8	1.7	0.1 (mass)	1C (60 mA g ⁻¹)	55	Cathode	1600	79	
2016	1 M Zn(OAc) ₂ in [CH ₃]OAc + K _{0.05} Fe[Fe(CN) ₆] ₃ + 30 wt% H ₂ O ⁵⁴¹	Zn foil	—	2.0/1.0	1.1	—	5C (300 mA g ⁻¹)	65	Cathode	100	76		
2016	1 M ZnSO ₄ + 0.01 M H ₂ SO ₄ / H ₂ O ⁵⁴²	Cu[Fe(CN) ₆] ₃	Hyper dendritic Zn	—	2.1/1.4	1.7	—	10 mA g ⁻¹	53	Cathode	81	82	
2017	1 M ZnSO ₄ /H ₂ O + additives Na ₂ Mn[Fe(CN) ₆] ₁₀ sodium dodecyl sulfate sodium carboxymethylcellulose sodium dodecylbenzenesulfonate dodecyl trimethylammonium bromide ⁵⁴³	Zn foil	—	2.0/1.0	1.6	—	5C (80 mA g ⁻¹)	121	Cathode	10	95		
2023	0.3 M ZnSO ₄ /H ₂ O ⁵⁴⁴	Fe ₄ [Fe(CN) ₆] ₃	Zn foil	80 μm (56 mg cm ⁻²)	2.3/1.4	1.9	—	0.5C (80 mA g ⁻¹)	125 (0.5C)	Cathode	500	82	
2016	1 M ZnSO ₄ /H ₂ O ⁵⁴⁵	Mo ₆ S ₈	Zn foil	—	1.0/0.25	0.5	—	180 mA g ⁻¹	63	Cathode	2000	75	
2016	1 M ZnSO ₄ /H ₂ O ⁵⁴⁵	Mo ₆ S ₈	Zn foil	—	—	—	2000 mA g ⁻¹	30	Cathode	200	60		
2016	1 M ZnSO ₄ /H ₂ O ⁵⁴⁵	Mo ₆ S ₈	Zn foil	—	—	—	180 mA g ⁻¹	63	Cathode	150	94		



Table 11 (continued)

Year	Electrolyte	Cathode	Cathode I/L (mg cm ⁻²)	Anode	Anode I/L (mg cm ⁻²)	Full cell cutoff (V/V)	Full cell average (V)	N/P ratio	C-rate	Capacity (mA h g ⁻¹)	Capacity calculation based	Cycle number (–)	Retention ratio (%)
2009	0.1 M ZnCl ₂ + 0.1 M NH ₄ Cl / Poly(2,2,6,6-tetramethylpiperidinyloxy-4-vinyl ether)	—	Zn foil	—	2.0/1.4	1.7	—	60C	131	Cathode	500	65	
2011	1 M ZnCl ₂ /H ₂ O ⁵⁴⁷	—	Zn foil	—	2.0/1.0	1.5	—	(60% dis-charge) 5000 mA cm ⁻²	70	Cathode	200	98	
2015	1 M ZnCl ₂ /H ₂ O (pH 6) ⁵⁴⁸	Poly(5-cyanoindole)	—	Zn foil	—	2.2/1.0	1.8	—	(60% dis-charge) 0.2C	100	Cathode	800	75
2016	1 M Zn(BF ₄) ₂ ·nH ₂ O (pH 6) ⁵⁴⁹	9,10-Di(1,3-dithiol-2-ylidene)-9,10-dihydro-anthracene	1.5	Zn foil	—	1.7/0.6	1.1	—	1C	91	Cathode	800	68
									2C	82	Cathode	800	63
									10C	100	Cathode	9400	86
									120C	111	Cathode	1000	95
2018	1 M Zn(OTf) ₂ /H ₂ O or 1 M Zn(OTf) ₂ /H ₂ O + poly(vinyl alcohol) ⁵⁵⁰	Polyaniline/carbon nanofiber	1.5	Zn foil	11-2500 mg	1.5/0.5	1.1	—	500 mA g ⁻¹	109	Cathode	200	93
2018	1 M ZnCl ₂ /H ₂ O ⁵⁵¹	Polyaniline/carbon fiber	—	Zn foil	—	1.7/0.7	1.1	—	5000 mA g ⁻¹	89	Cathode	3000	92
2018	1 M ZnSO ₄ /H ₂ O ⁵⁵²	Sulfo-doped-polyaniline	—	Zn foil	—	1.6/0.5	1.1	—	1C	162	Cathode	65	85
2018	3 M Zn(OTf) ₂ /H ₂ O ⁵⁵³	Calix[4]quinone	10	Zn foil	13	1.8/0.2	1.0	1.2 (mass)	10 000 mA g ⁻¹	130	Cathode	2000	85
2018	3 M Zn(OTf) ₂ /H ₂ O ⁵⁵⁴	Poly(benzoquinonyl sulfide)	1	Zn foil	—	1.8/0.2	1.0	—	100 mA g ⁻¹	250	Cathode	50	93
2018	2 M ZnSO ₄ /H ₂ O ⁵⁵⁵	Pyrene-4,5,9,10-tetraone	—	Zn foil	—	1.5/0.4	0.8	—	500 mA g ⁻¹	160	Cathode	1000	87
2018	1 M Zn(OTf) ₂ /H ₂ O (pH 4) ⁵⁵⁶	Tetrachloro-1,4-benzoquinone/mesoporous carbon	3-5	Zn foil	—	1.4/0.8	1.1	—	0.2C	166	Cathode	50	86
									1C	210	Cathode	1000	70
2020	2 M ZnSO ₄ /H ₂ O ⁵⁵⁷	Sulfur heterocyclic quinone dibenzof[<i>h</i>]thianthren-5,7,12,14-tetraone	5	Zn foil	—	1.3/0.3	0.8	—	0.2C	118 (1C)	Cathode	100	53
									1C	190	Cathode	200	70
									2000 mA g ⁻¹	105	Cathode	150	99
2023	10 m Zn(OAc) ₂ + 15 m KOAc/H ₂ O ⁵⁵⁸	Pyrene-4,5,9,10-tetraone	2	Zn foil	—	1.6/0.2	0.9	1.2 (mass)	10C	200	Cathode	4000	70
	10 m Zn(OAc) ₂ /H ₂ O + 24 m CO(NH ₂) ₂											23 000	0
	10 m Zn(OAc) ₂ /H ₂ O + 30 m C ₂ H ₅ NO												
2023	0.3 M ZnSO ₄ /H ₂ O ⁵⁴⁴	Polyaniline	11	Zn foil	80 μm (56 mg cm ⁻²)	1.5/0.5	1.1	—	1000 mA g ⁻¹	62	Cathode	200	68

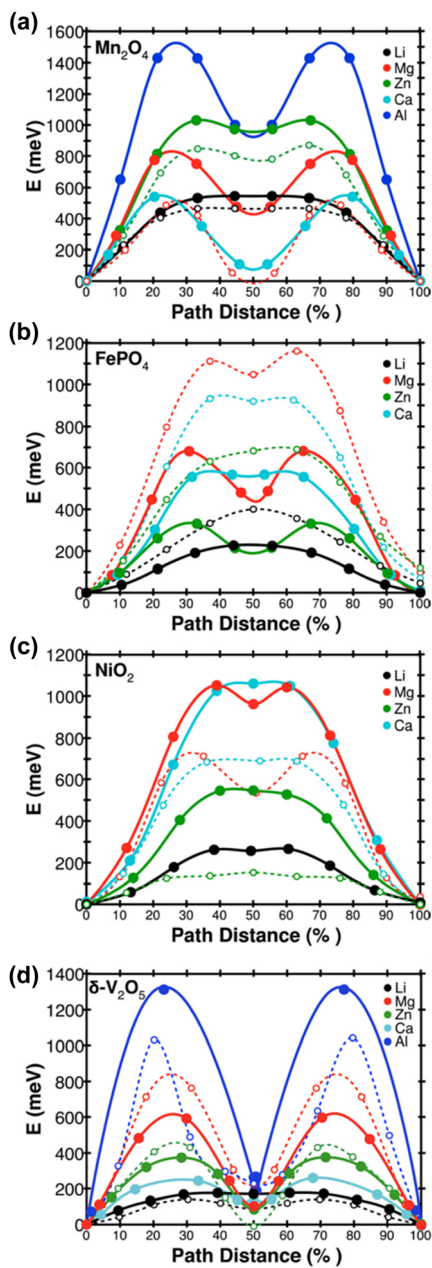


Fig. 45 Computational calculation results for the migration energies of monovalent and multivalent ions in (a) spinel Mn_2O_4 , (b) olivine FePO_4 , (c) layered NiO_2 , and (d) orthorhombic $\delta\text{-V}_2\text{O}_5$ structures.⁴³⁵ Reprinted with permission from *Chemistry of Materials*.

Zn^{2+} and water molecules, allows for water co-intercalation.⁴³⁸ In contrast, bronze-type VO_2 is expected to restrict water co-intercalation due to geometrical limitations arising from its bridged interlayer gap.⁵⁶⁵ However, bronze-type VO_2 undergoes hydrolysis in aqueous electrolytes and transforms into a water-inserted layered structure.⁵⁶⁶ Similar to MnO_2 , proton intercalation into V_xO_y is much faster than Zn^{2+} intercalation.^{473,567} These observations indicate that the reported electrochemical properties of V_xO_y largely originate from proton and water co-intercalation rather than Zn^{2+} intercalation.

The strong interactions between Zn^{2+} and lattice oxide ions create a significant diffusion barrier, fundamentally limiting the use of oxide materials as Zn cathode active materials.⁴³⁵ In contrast, sulfides and selenides, such as MS_2 ($\text{M} = \text{Ti, V, Mo}$), $\text{Zn}_x\text{Mo}_6\text{S}_8$, and their sulfur–selenium substitutions,^{568–573} have weaker interactions with hard cations, including divalent Zn^{2+} , Mg^{2+} , and Al^{3+} , and possess robust, flexible frameworks, thus presenting viable alternatives.^{545,570,574,575} Notably, $\text{Zn}_x\text{Mo}_6\text{S}_8$ exhibits identical charge and discharge curves in aprotic nonaqueous and protic aqueous Zn electrolytes, as shown in Fig. 46.^{545,570} Crystallographic analysis with *ex situ* powder X-ray diffraction (XRD) confirmed Zn^{2+} insertion, and Fourier synthesis revealed the presence of electron density in interstitial voids, further validating the Zn^{2+} insertion.⁵⁷⁰

Prussian blue analogs, $\text{A}_x\text{M}_y[\text{Fe}(\text{CN})_6]\cdot n\text{H}_2\text{O}$, have also been studied as Zn^{2+} host materials.⁵⁷⁶ The octahedrally coordinated M and Fe are interconnected by linear CN^- , forming an expanded ReO_3 -like structure (Fig. 30). The A cations occupy the interstitials corresponding to the A-site of the perovskite structure. This expanded ReO_3 framework provides three-dimensional open channels that allow the diffusion of Zn^{2+} . The rich chemistry of Prussian blue analogs, along with their intrinsic structural flexibility and high redox potentials (*e.g.*, 1.7 V vs. Zn/Zn^{2+} in $\text{Zn}_3[\text{Fe}(\text{CN})_6]_2$),⁵⁴⁰ render Zn^{2+} promising as host materials. However, the large but sparse open channel structure allows water co-intercalation and limits the battery energy density per unit weight and unit volume.

Beyond adapting known materials from monovalent-ion systems, unique designs to accommodate Zn^{2+} are necessary to develop Zn cathode active materials. The first step involves gaining a deeper understanding of the topochemical interactions and the deconvolution of Zn^{2+} and other intercalants (proton and water co-intercalation) through direct analysis to validate Zn^{2+} intercalation in active materials. This can be achieved using methods like electrochemical quartz crystal micro-balance measurements and by quantitative evaluations of the atomistic structure, structure factors, and elemental composition. Additionally, electrochemical tests with aprotic nonaqueous electrolytes, which exclude proton and water co-intercalation, will help understand Zn^{2+} intercalation/deintercalation reactions in the material.

7.2. Dilemma in pH selection

The pH of the electrolyte significantly impacts the thermodynamic HER potential and the kinetics of byproduct formation during the Zn plating and stripping processes. Therefore, thoroughly understanding the influence of the electrolyte pH on these electrochemical and chemical side reactions is crucial for enhancing the performance and safety of aqueous Zn–metal batteries. Elevated pH levels help reduce hydrogen gas evolution by lowering the thermodynamic HER potential, as illustrated in Fig. 10. However, according to the Pourbaix diagram for Zn (Fig. 47),⁵⁷⁷ undesirable byproducts such as zinc oxide (ZnO) and zinc hydroxide ($\text{Zn}(\text{OH})_2$) can form at pH 8–11. This problem is often exacerbated by precipitates of Zn-anion complexes, such as $\text{Zn}_4(\text{OH})_6\text{SO}_4\cdot n\text{H}_2\text{O}$, $\text{Zn}_5(\text{OH})_8\text{Cl}_2\cdot n\text{H}_2\text{O}$, and $\text{Zn}_4(\text{OH})_7\text{ClO}_4\cdot n\text{H}_2\text{O}$.^{483,578,579} These byproducts exhibit poor electrical and Zn^{2+} ionic conductivities, which

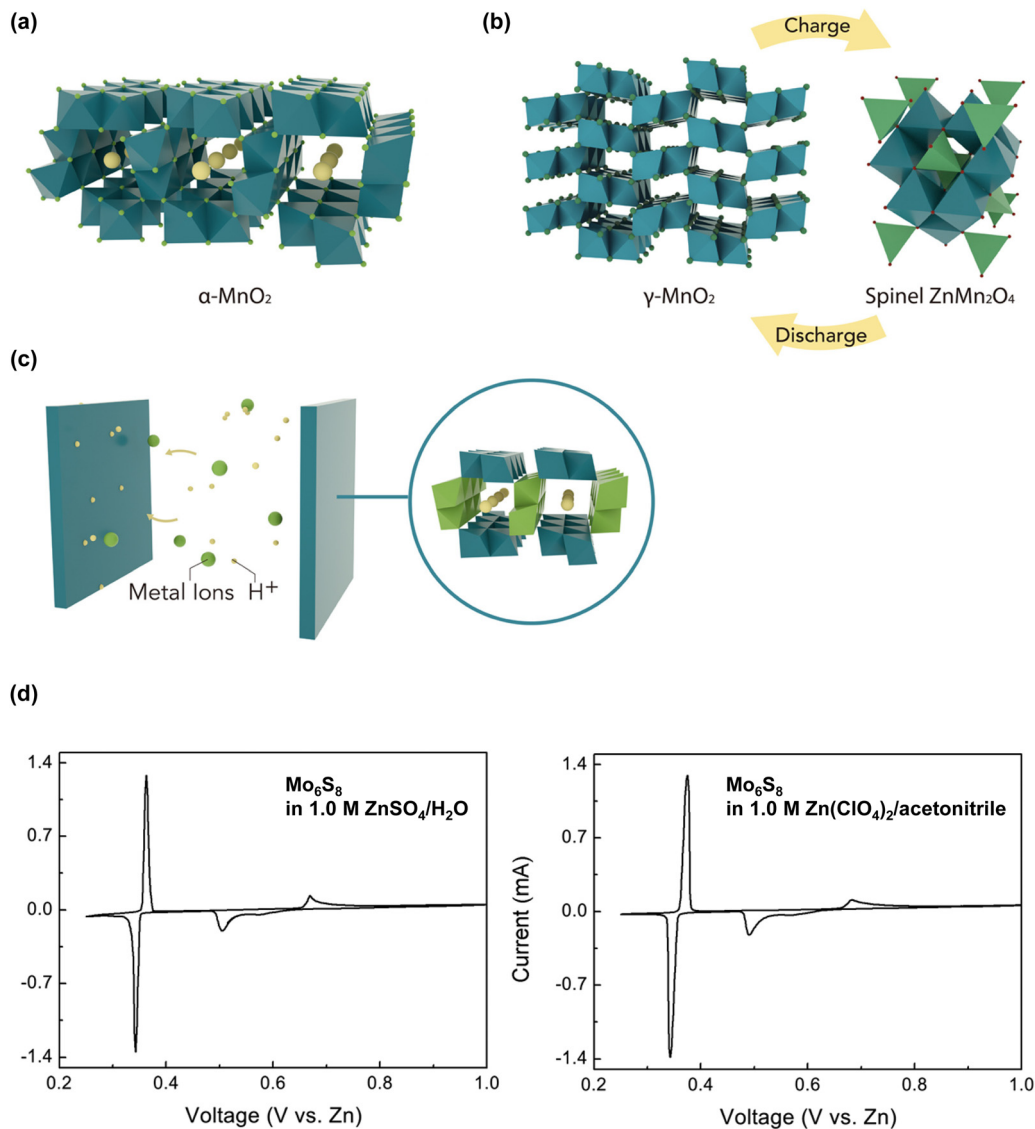


Fig. 46 Schematics of proposed energy storage mechanisms in Zn cathode active materials;³¹ (a) pure (desolvated) Zn²⁺ intercalation, (b) conversion reaction, and (c) Zn²⁺/H⁺ co-intercalation in MnO₂. (d) Cyclic voltammograms of Mo₆S₈ for Zn²⁺ intercalation/deintercalation in protic aqueous and aprotic nonaqueous electrolytes.⁵⁴⁵ Reprinted with permission from Joule (a)–(c) and ACS Applied Materials & Interfaces (d).

result in poor Coulombic efficiency during Zn plating and stripping. At high pH levels (pH > 11), the formation of soluble zincate ions (Zn(OH)₃⁻ and Zn(OH)₄²⁻) is promoted, which can lead to severe chemical self-corrosion and create uneven electrode surfaces. This not only poses risks of short-circuiting but can also severely undermine the overall battery performance.

On the other hand, a decreased pH level in the electrolyte can inhibit the formation of insoluble byproducts, which is expected to significantly enhance the Coulombic efficiency of Zn plating and stripping by eliminating surface contamination and improving the Zn²⁺ conductivity. However, this advantage is offset by a competing dynamic, namely, an increase in the thermodynamic HER potential. Under acidic conditions, a significant portion of the electrons intended for Zn deposition may instead be consumed by the HER, thereby diminishing the energy efficiency of the battery. Moreover, the hydrogen gas

bubbles and OH⁻ produced alongside the HER contribute to several detrimental effects. Some of these effects are listed below:

- (1) Safety risks, such as the generation of large amounts of highly flammable hydrogen gas, which can lead to explosion or fire hazards, negating the safety benefits of aqueous batteries.
- (2) Blocking of contact between the electrolyte and Zn-metal anode.
- (3) Triggering the formation of byproducts such as Zn(OH)₂.
- (4) Facilitation of battery short-circuiting through dendrite formation, ultimately decreasing the overall battery performance.

Additionally, in an acidic electrolyte, the intercalation of H⁺ into the cathode active materials might be favored over that of Zn²⁺. The smaller size and higher mobility of H⁺ allow them to migrate more readily within the electrolyte and intercalate into the lattice structure of cathode active materials, thus redirecting the energy storage mechanism of the battery toward H⁺-based



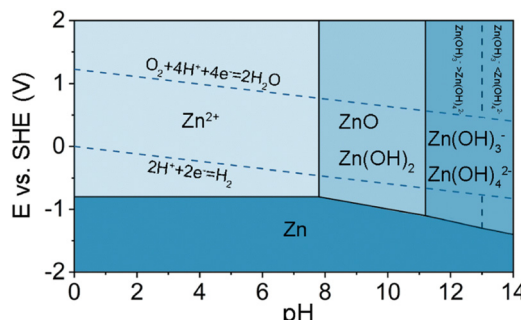


Fig. 47 Pourbaix diagram of Zn in aqueous electrolytes.^{577,580} Reprinted with permission from *Journal of Materials Chemistry A*.

reactions, and deviating from the expected Zn^{2+} -based redox reactions. Besides, acidic conditions accelerate the dissolution of transition metals from the cathode, thereby deteriorating the cycling stability of the battery. Note that H^+ can also originate from Brønsted weak acids (e.g. aquo metal ion complexes; $[\text{Zn}(\text{H}_2\text{O})_6]^{2+} \rightleftharpoons [\text{Zn}(\text{H}_2\text{O})_5(\text{OH})]^+ + \text{H}^+$, $\text{p}K_a \sim 9$), present in the electrolyte with strong Lewis acids (e.g. Zn^{2+}).^{563,564,581}

Overall, the pH of the electrolyte plays an essential role in determining the electrochemical and chemical dynamics, as well as the overall performance of aqueous Zn-metal batteries. Higher pH levels can facilitate the formation of insoluble byproducts with poor Zn^{2+} conductivity, thereby reducing the cycling efficiency and increasing the internal resistance of batteries. On the other hand, lower pH levels may accelerate the HER, trigger unexpected H^+ -based redox reactions, and cause severe side reactions, which degrade both the battery performance and safety. This intricate balance among pH levels, electrochemical reactions, and battery performance underscores the critical need for alternative methods to mitigate all side reactions, ensuring the efficiency and safety of Zn-metal batteries.

7.3. Limited options for Zn salts

The type of Zn salt used in the electrolyte significantly influences the electrochemical and chemical properties, thereby affecting the battery performance, and impacting practical aspects such as battery safety and cost. However, the limited variety of available Zn salts presents a significant challenge in addressing the broad range of issues faced by aqueous Zn-metal batteries. Table 12

outlines the properties of various Zn salts, providing insights into their potential advantages and disadvantages.

Zinc sulfate (ZnSO_4) is one of the most frequently used salts in aqueous Zn-metal batteries, as highlighted in Table 11. Its popularity stems from its moderate solubility in water, low cost, high ionic conductivity, and mildly acidic electrolyte pH (pH 4–6).^{582,583} These characteristics are favorable for achieving high Coulombic efficiency in Zn plating and stripping processes. However, the interactions among Zn metal, SO_4^{2-} , and OH^- can lead to the formation of insoluble zinc hydroxide compounds, such as $\text{Zn}_4(\text{OH})_6\text{SO}_4 \cdot n\text{H}_2\text{O}$, which obstruct effective Zn^{2+} transport and contribute to capacity fading over continuous cycles (Fig. 48). While *ex situ* coating on Zn metal can mitigate this issue, ensuring the stability of the coating materials during the extensive volume changes associated with Zn plating and stripping remains challenging. Details of this approach and its challenges will be further discussed in Section 7.5.

The high solubility and ionic conductivity of zinc chloride (ZnCl_2) render it a preferred choice in aqueous Zn-metal batteries.⁵⁸⁴ In 2020, Chen's group developed low-temperature aqueous Zn-metal batteries using a mildly salt-concentrated 7.5 m ZnCl_2 solution, which remained liquid even at extremely low temperatures (-114°C) (Fig. 49).⁵⁸⁵ They investigated the relationships among the ZnCl_2 concentration, solution structure, and phase-transition temperature of the electrolyte. MD simulations showed that the dissolution of 7.5 m ZnCl_2 in water was thermodynamically favorable compared to the separate existence of solid ZnCl_2 and liquid water at 300 K (27°C). When the temperature was lowered to 100 K (-173°C), the formation of crystallized ZnCl_2 and ice became more energetically favorable than the formation of a metastable amorphous glass. However, an energy barrier must be overcome to transition from the amorphous glass state to a crystalline structure, and this is hindered by the reduced thermal motion at such low temperatures (as demonstrated by the supercooling phenomenon discussed in Section 4.3). For instance, at 100 K (-173°C), the mobility of Zn^{2+} was significantly restricted, with the ions moving less than 0.5 Å from their original positions. This was in stark contrast to the distance traversed (8.3 Å) at 300 K (27°C). As for the stability of the liquid phase, low-temperature Raman spectroscopy confirmed that the water and ions remained interconnected, similar to the case in their liquid

Table 12 Properties of diverse salts for aqueous Zn electrolytes

Salts	Molecular weight (g mol ⁻¹)	Solubility (mol kg ⁻¹)	Cost	Advantages	Concerns
ZnSO_4	161.4	3.4	Low	Low cost, moderate Zn plating/stripping efficiency	Poor oxidation stability, byproduct formation
ZnCl_2	136.3	31	Low	Low cost, high solubility	Poor oxidation stability, corrosive
ZnF_2	103.4	<0.1	Low	Low cost	Low solubility
Zn(OAc)_2	183.4	1.6	Low	Low cost, pH control	Poor oxidation stability
$\text{Zn(ClO}_4)_2$	261.8	4.6	Low	Low cost	Explosive
$\text{Zn(NO}_3)_2$	189.3	6.2	Low	Low cost	An oxidizing agent
$\text{Zn(PF}_6)_2$	355.3	—	Moderate	High oxidation stability	Hydrolysis
$\text{Zn(BF}_4)_2$	239.0	—	Moderate	High oxidation stability	Hydrolysis
Zn(OTf)_2	363.5	4.2	High	High Zn plating/stripping efficiency	Cost, purity
Zn(TFSI)_2	625.7	3.7	High	High Zn plating/stripping efficiency	Cost, purity



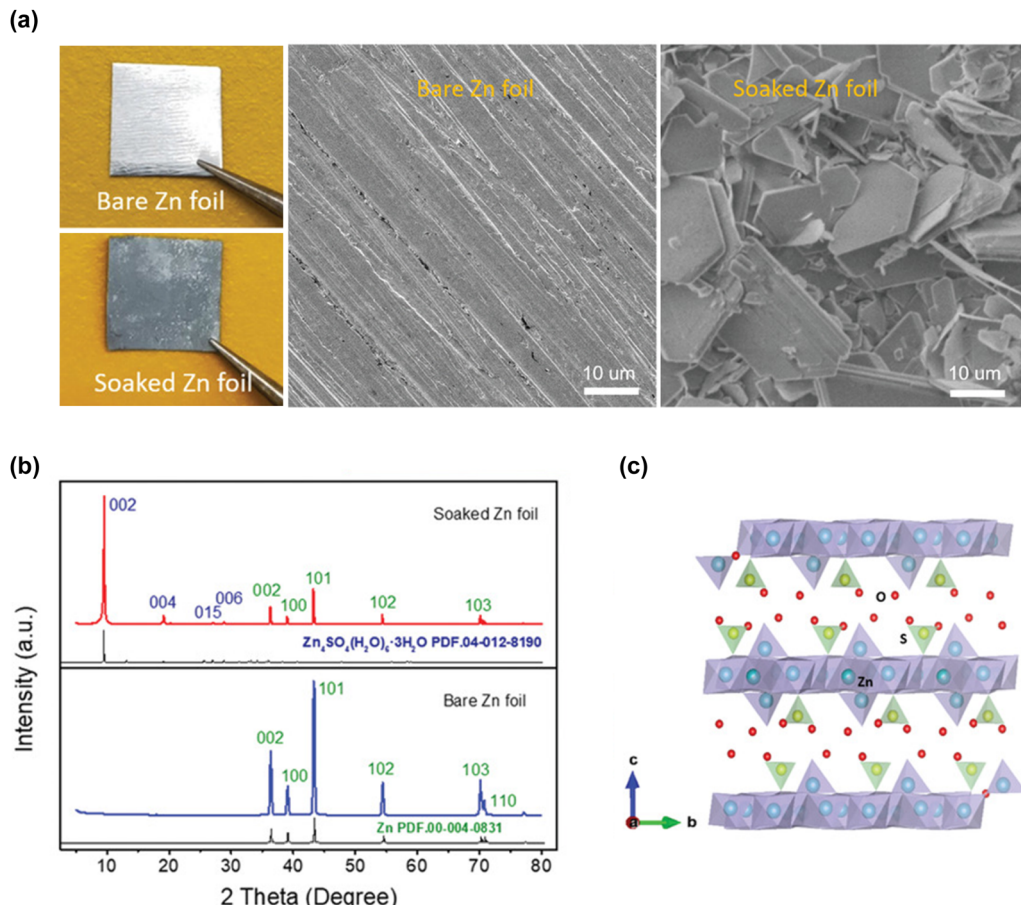


Fig. 48 (a) Photographs and SEM images and (b) XRD patterns before and after soaking Zn metal in a 1 M ZnSO₄ solution for several days. (c) Crystal structure of the byproduct, Zn₄SO₄(OH)₆·3H₂O.⁴⁴⁴ Reprinted with permission from *Advanced Functional Materials*.

state, preventing the crystallization of ZnCl₂ even at a temperature as low as -150 °C. The superior supercooling ability of the 7.5 M ZnCl₂/H₂O electrolyte allowed the stable cycling of aqueous polyaniline|Zn full cells over 2000 cycles, with nearly 100% capacity retention at a constant current of 200 mA g⁻¹ and temperature of -70 °C.

In 2023, Borodin *et al.* developed a high-entropy Li₂ZnCl₄·9H₂O electrolyte by adding LiCl as a supporting salt to the aqueous ZnCl₂ solution (Fig. 50).⁵⁸⁶ In this electrolyte, the pronounced acidity allowed ZnCl₂ to accept donated Cl⁻, leading to the formation of ZnCl₄²⁻ anions, while the water molecules either remained within the free solvent network or were coordinated with Li⁺. This contributed to enhancing the ionic conductivity of the electrolytes over a wide temperature range (-80 to $+80$ °C), resulting in these electrolytes outperforming conventional aqueous electrolytes. The assembled Zn-air battery sustained stable cycling for 800 h at a current density of 0.4 mA cm⁻² between -60 and $+80$ °C.

However, ZnCl₂-based electrolytes exhibit strong corrosiveness toward metals such as Al, Cu, and Ni, and also SUS, limiting the use of cost-effective materials for current collectors and other battery components.^{250,587,588} While Ti, which has high resistance to chloride solutions,⁵⁸⁹ can be used as an alternative, its high cost and low flexibility make it less desirable for battery

manufacturing, as demonstrated in Section 4.4. Additionally, the high acidity of ZnCl₂ electrolytes poses further challenges. For example, a highly concentrated ZnCl₂ aqueous electrolyte maintains a pH below 1, facilitating transition metal dissolution from the cathode and electrolyte reduction on the Zn anode surface with a substantially increased thermodynamic HER potential.

In 2021, Feng *et al.* developed an electrolyte incorporating a zinc fluoride (ZnF₂) additive.⁵⁹⁰ They showed that the addition of ZnF₂ could control the growth orientation of Zn crystals (details in Section 7.7) and help in forming a F-rich protective surface layer (details in Section 7.4), both of which mitigated byproduct formation and electrolyte reduction. As a result, high average Coulombic efficiencies of Zn plating and stripping in SUS|Zn cells (96.56% after 3000 cycles at 0.6 mA h cm⁻² and 1 mA cm⁻²; 99.58%, 99.53%, 99.87%, and 99.68% after 1000 cycles at 0.6 mA h cm⁻²; higher current densities of 10, 20, 30, and 40 mA cm⁻², respectively) were achieved in the 2.0 M ZnSO₄ + 0.08 M ZnF₂/H₂O electrolyte. However, the extremely low solubility of ZnF₂ restricts its use as the main salt in aqueous systems.

Zinc acetate (Zn(OAc)₂) is valued for its affordability, environmental friendliness, and its ability to act as a buffer, thereby stabilizing the pH levels of electrolytes. In 2023, Lu and co-workers utilized hydrotropic solubilization, a technique commonly used in the pharmaceutical industry, to increase the



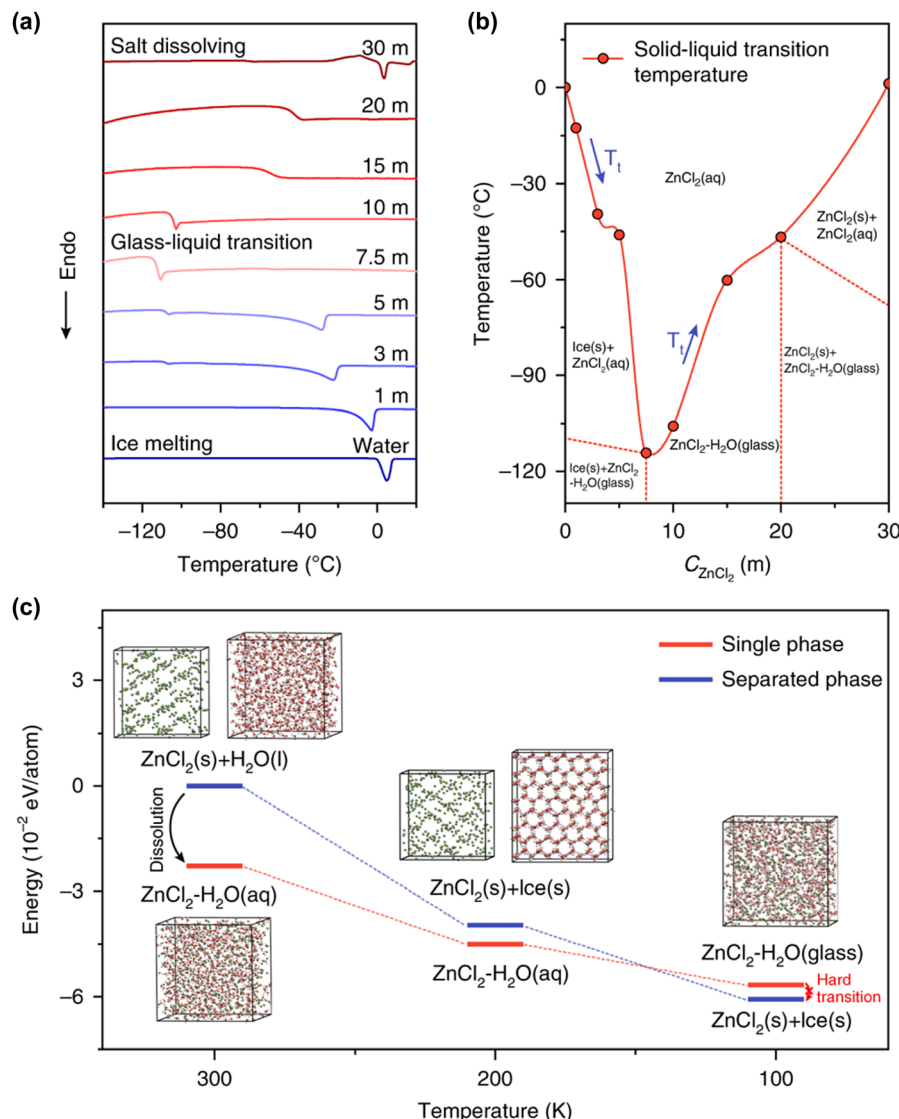


Fig. 49 (a) Differential scanning calorimetry curves and (b) obtained phase transition diagram of a ZnCl₂/water binary system. (c) Calculated transition state in the transformation from the glass state to the separated crystalline state of a 7.5 m ZnCl₂/H₂O solution.⁵⁸⁵ Reprinted with permission from *Nature Communications*.

solubility of water-insoluble drugs by enabling the formation of soluble complexes or associations with hydroscopic agents, to address the low-solubility issue of the Zn(OAc)₂ salt (≤ 1.6 m).⁵⁵⁸ By adding KOAc as a hydroscopic agent, they prepared various aqueous Zn electrolytes with total anion concentrations of ~ 35 m. In the tests conducted on Cu|Zn cells using a 25 m solution composed of 10 m Zn(OAc)₂ and 15 m KOAc, the cells achieved a Coulombic efficiency of 99.4% for the first 100 cycles, which improved to 99.6% after 150 cycles. This performance significantly surpassed that of the 1.6 m Zn(OAc)₂/H₂O electrolyte, which maintained a Coulombic efficiency of approximately 98.3% for approximately 50 cycles before experiencing a sudden failure due to a short circuit. However, the poor oxidation stability of the OAc⁻ anion restricts the use of Zn(OAc)₂ as a salt in developing high-voltage aqueous Zn-metal batteries.

Zinc perchlorate (Zn(ClO₄)₂) offers high ionic conductivity and reduction stability. Sun *et al.* reported that the average Coulombic efficiency of Zn plating and stripping in Cu|Zn cells using 1 m Zn(ClO₄)₂/H₂O reached 99.0% at 2 mA cm⁻² and 2 mA h cm⁻², which is higher than the Coulombic efficiencies of 98.0% and 98.2% achieved with 1 m ZnSO₄/H₂O and 1 m Zn(OAc)₂/H₂O, respectively.⁵⁹¹ However, although Zn(ClO₄)₂ salt contributes to highly reversible Zn utilization, its potentially explosive nature when concentrated or in contact with reactive metals or organic solvents necessitates cautious handling, rendering it less suitable for battery applications.

Kasiri *et al.* compared the stability of copper hexacyanoferate cathodes in a zinc nitrate (Zn(NO₃)₂)-based electrolyte with those in other Zn salts (ZnSO₄, ZnF₂, and Zn(ClO₄)₂), with salt concentrations ranging from 20 to 100 mM (Fig. 51).⁵⁹² The charge and discharge curves in the electrolyte with NO₃⁻ anions

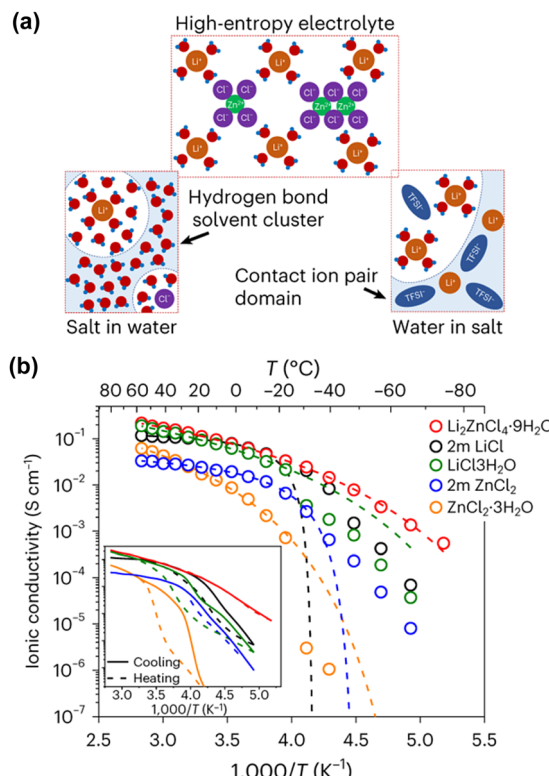


Fig. 50 (a) Illustration of solution structures in different electrolytes: salt-in-water, water-in-salt, and high-entropy electrolytes. (b) Ionic conductivity of the $\text{Li}_2\text{ZnCl}_4 \cdot 9\text{H}_2\text{O}$ electrolyte compared with those of different concentrated and diluted aqueous solutions.⁵⁸⁶ Reprinted with permission from *Nature Sustainability*.

displayed notable differences, which were attributed to their strong oxidizing properties. Rapid degradation of the battery performance, along with Zn metal oxidation and a local increase in the electrolyte pH, were observed using the $\text{Zn}(\text{NO}_3)_2$ -based electrolyte, suggesting that $\text{Zn}(\text{NO}_3)_2$ might not be an ideal salt for aqueous Zn-metal batteries.

Zinc hexafluorophosphate ($\text{Zn}(\text{PF}_6)_2$) and zinc tetrafluoroborate ($\text{Zn}(\text{BF}_4)_2$) enhance the oxidation stability of electrolytes. In 2016, a team led by Schubert fabricated an aqueous Zn-metal battery using redox-active polymer cathodes based on 9,10-di(1,3-dithiol-2-ylidene)-9,10-dihydroanthracene and a 1 M $\text{Zn}(\text{BF}_4)_2 \cdot n\text{H}_2\text{O}$ electrolyte.⁵⁴⁹ The battery, tested between 0.6 and 1.7 V at a constant current of 10C, maintained 86% of its initial capacity after 9400 cycles. The research team suggested that the slightly acidic pH of the electrolyte ($\sim \text{pH } 6$) helped prevent the oxidation of the Zn-metal anode and the formation of dendrites. However, the introduction of $\text{Zn}(\text{PF}_6)_2$ and $\text{Zn}(\text{BF}_4)_2$ salts into aqueous solutions poses challenges owing to the strong propensity of the PF_6^- and BF_4^- anions to hydrolyze, which lowers the electrolyte pH and leads to drastic capacity decay with severe corrosion of the battery electrodes and components. This issue becomes more pronounced under practical battery operating conditions, such as elevated temperatures.

Zinc triflate ($\text{Zn}(\text{OTf})_2$) and zinc bis(trifluoromethanesulfonyl)imide ($\text{Zn}(\text{TFSI})_2$) provide mildly acidic conditions

(pH 3–5),^{593,594} a high oxidation stability, and a high Coulombic efficiency in Zn plating and stripping reactions. Chen *et al.* compared ZnSO_4 and $\text{Zn}(\text{OTf})_2$ solutions at various concentrations (Fig. 52),⁵⁹⁵ demonstrating that $\text{Zn}(\text{OTf})_2/\text{H}_2\text{O}$ offered improved reversibility and reduced overpotentials for Zn plating and stripping compared to $\text{ZnSO}_4/\text{H}_2\text{O}$. This was attributed to the bulky OTf^- anions, which reduced the coordination number of water molecules around Zn^{2+} cations, thereby diminishing the solvation effect and facilitating Zn^{2+} transportation.^{595,596} Notably, the mildly salt-concentrated 3.0 M $\text{Zn}(\text{OTf})_2/\text{H}_2\text{O}$ solution (pH 3.6) provided a high electrochemical stability with reduced water-induced side reactions as well as high ionic conductivity, enabling the long-term cycling of an aqueous cation-defective $\text{ZnMn}_2\text{O}_4/\text{Zn}$ full cell over 500 cycles at 500 mA cm^{-2} .

$\text{Zn}(\text{OTf})_2$ and $\text{Zn}(\text{TFSI})_2$ are considerably more expensive than common inorganic Zn salts, such as $\text{Zn}(\text{OAc})_2$ (Fig. 53).^{597,598} Additionally, the purity of commercially available $\text{Zn}(\text{OTf})_2$ ranges from 98 to 99%, which falls short of the battery-grade requirement of over 99.9%. Table 13 illustrates the stability of Zn plating and stripping in $\text{Zn}(\text{OTf})_2$ -based aqueous electrolytes.

For instance, data from previous reports show that the cycle life of $\text{Zn}|\text{Zn}$ symmetric cells varies from 100 to 1226 h in 1 M $\text{Zn}(\text{OTf})_2/\text{H}_2\text{O}$ and from 97 to 900 h in 2 M $\text{Zn}(\text{OTf})_2/\text{H}_2\text{O}$ under conditions of 0.5 mA cm^{-2} to 1.0 mA cm^{-2} and 0.5 mA h cm^{-2} to 1.0 mA h cm^{-2} . This considerable variation can be attributed to differences in the measurement protocols and issues with the purity of the $\text{Zn}(\text{OTf})_2$ salt.

The exploration of innovative salt systems has extended beyond traditional options. In 2013, Zhang *et al.* introduced zinc phenolsulfonate ($\text{Zn}(\text{PS})_2$, $\text{Zn}(\text{C}_6\text{H}_4\text{OHSO}_3)_2$), a compound typically used in cosmetics, as an electrolyte salt.⁶¹⁴ This unique choice improved the Coulombic efficiency of Zn plating and stripping processes. A 1.0 M $\text{Zn}(\text{PS})_2/\text{H}_2\text{O}$ electrolyte exhibited a cycle life of 202 h in a $\text{Zn}|\text{Zn}$ cell under test conditions of 1 mA cm^{-2} and 1 mA h cm^{-1} , which surpassed the performance of a 1.0 M $\text{ZnSO}_4/\text{H}_2\text{O}$ solution that lasted 190 h. Similar to imide TFSI^- , the bulky PS^- anion, which is approximately two and a half times larger than the SO_4^{2-} anion, effectively reduces the coordination number of water molecules around Zn^{2+} , thus diminishing hydrogen evolution during Zn plating. Additionally, the inclusion of 0.2 mg mL^{-1} of tetrabutylammonium 4-toluenesulfonate, acting as a brightener (a leveling agent; details in Section 7.7), to 1.0 M $\text{Zn}(\text{PS})_2/\text{H}_2\text{O}$, significantly extended the cell cycle life to over 2000 h and helped prevent Zn dendrite formation.

In the same year, Li *et al.* developed a multifunctional fluorine-free Zn salt, zinc bis(benzenesulfonyl)benzenesulfonamide ($\text{Zn}(\text{BBI})_2$, $\text{Zn}[(\text{C}_6\text{H}_5)_2\text{N}(\text{SO}_2)_2]_2$) (Fig. 54).⁵⁹⁸ The hydrophilic sulfonamide group $\text{R}-\text{SO}_2-\text{N}-\text{SO}_2-\text{R}'$ of the BBI^- anion enhances salt solubility and strengthens $\text{H}_2\text{O}-\text{anion}$ interactions, while the hydrophobic and spacious phenyl group $-\text{C}_6\text{H}_5$ disrupts the long-range hydrogen bond network between water molecules, effectively reducing the water activity. Raman spectroscopy analyses confirmed these effects, showing lower peak intensities at 3000 – 3800 cm^{-1} , which is indicative of a weakened hydrogen bonding network, in 1.0 M $\text{Zn}(\text{BBI})_2/\text{H}_2\text{O}$



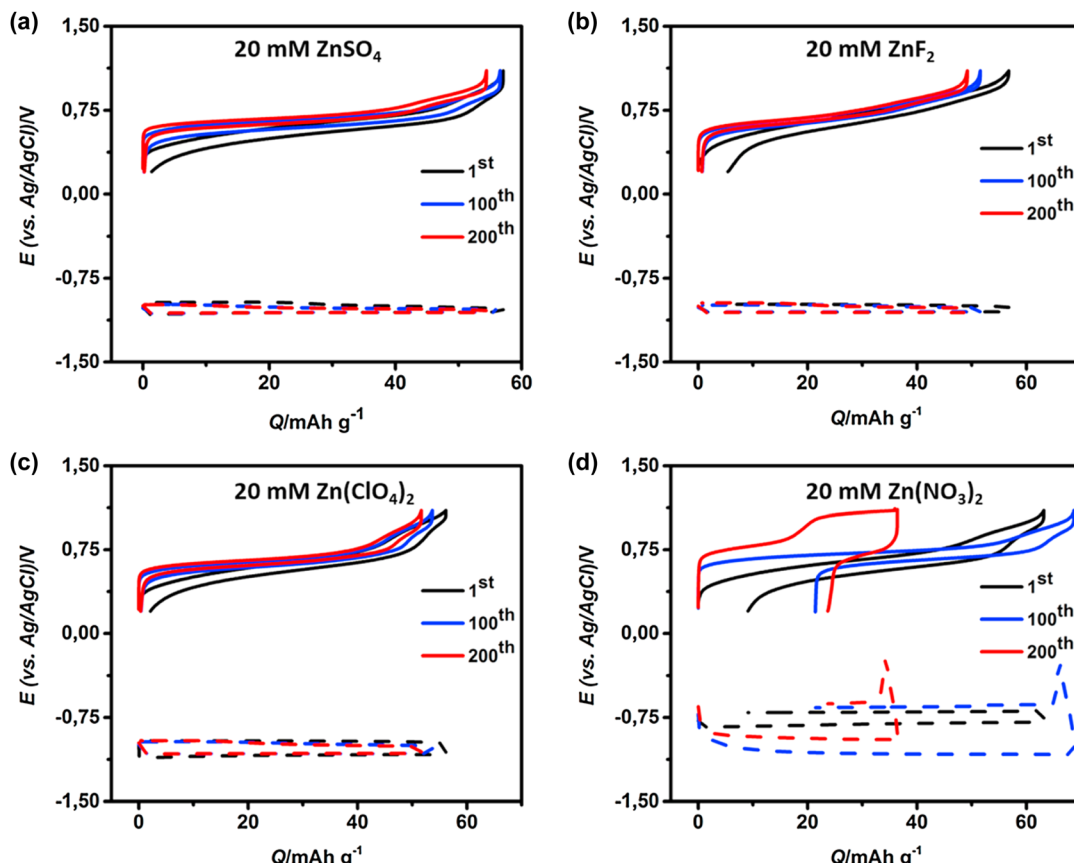


Fig. 51 Potential profiles of the copper hexacyanoferrate cathode (solid line) and Zn-metal anode (dashed line) in (a) 20 mM ZnSO_4 , (b) 20 mM ZnF_2 , (c) 20 mM $\text{Zn}(\text{ClO}_4)_2$, and (d) 20 mM $\text{Zn}(\text{NO}_3)_2$ solutions.⁵⁹² Reprinted with permission from *Electrochimica Acta*.

compared to solutions based on $\text{Zn}(\text{TFSI})_2$, $\text{Zn}(\text{OTf})_2$, and ZnSO_4 salts. Moreover, the water vapor pressure in $\text{Zn}(\text{BBI})_2$ solutions, an indicator of the water activity, was lower than in other compared electrolytes. As a result, the cycle life of $\text{Zn}|\text{Zn}$ cells tested at 2 mA cm^{-2} and 2 mA h cm^{-2} in 1.0 M $\text{Zn}(\text{BBI})_2/\text{H}_2\text{O}$ exceeded 2800 h, significantly outperforming those in 1.0 M $\text{Zn}(\text{TFSI})_2/\text{H}_2\text{O}$ (415 h), 1.0 M $\text{Zn}(\text{OTf})_2/\text{H}_2\text{O}$ (134 h), and 1.0 M $\text{ZnSO}_4/\text{H}_2\text{O}$ electrolytes (346 h).

Overall, a multidisciplinary approach that integrates materials science, organic/inorganic chemistry, and electrochemical engineering is essential to meet the increasingly demanding requirements of energy storage technologies. The development of new Zn salts and electrolyte systems is critical to effectively unlock the full potential of aqueous Zn-metal batteries. Continuous studies are needed to meet rigorous practical requirements, including a high Coulombic efficiency for Zn plating and stripping under various operating conditions, high oxidation stability, affordability, environmental sustainability, safety, low corrosivity, and high purity.

7.4. Uncertainty in SEI formation

Zn^{2+} tend to deposit in a manner that minimizes the surface energy, which complicates the prevention of dendrite formation during plating. Further, the uneven electron distribution during stripping can lead to the formation of “dead” Zn. Both factors

contribute to short circuits and significant capacity fading in batteries. Equally important is the control of non-faradaic (chemical) side reactions involving anions and water molecules, as well as faradaic (electrochemical) side reactions that continuously deplete Zn^{2+} resources and the electrolyte, accompanied by the generation of hydrogen gas. To address these issues, the concept of an SEI in nonaqueous Li-ion/Li-metal batteries has been applied to aqueous Zn-metal batteries. However, its applicability remains highly debatable.

It is essential to comprehensively understand the formation, maintenance, and functionalities of an SEI. In aqueous electrolytes, SEI formation largely relies on anion reduction. However, the reduction potentials of free TFSI^- and OTF^- anions, which are commonly used in aqueous Zn electrolytes, are significantly lower than the redox potential of Zn/Zn^{2+} , rendering the formation of the anion-derived SEI before Zn deposition challenging.^{615,616} As previously demonstrated in Section 4.1, intense interactions between strong Lewis acidic Zn^{2+} and anions can promote anion reduction at higher potentials. Computational calculations estimated the reduction potential of $\text{Zn}^{2+}(\text{TFSI}^-)_1$ and $\text{Zn}^{2+}(\text{TFSI}^-)_2$ ion pairs to be 0.2–0.4 V and 0.9 V vs. Zn/Zn^{2+} , respectively.⁶¹⁶ However, the solubility of $\text{Zn}(\text{TFSI})_2$ and $\text{Zn}(\text{OTf})_2$ was limited to less than 4 m, providing a negligible amount of $\text{Zn}(\text{anion})_n$ ion pairs.⁶¹⁷ Furthermore, considering the overpotential of the anion reduction reaction on Zn metal, the complete formation of the anion-derived SEI



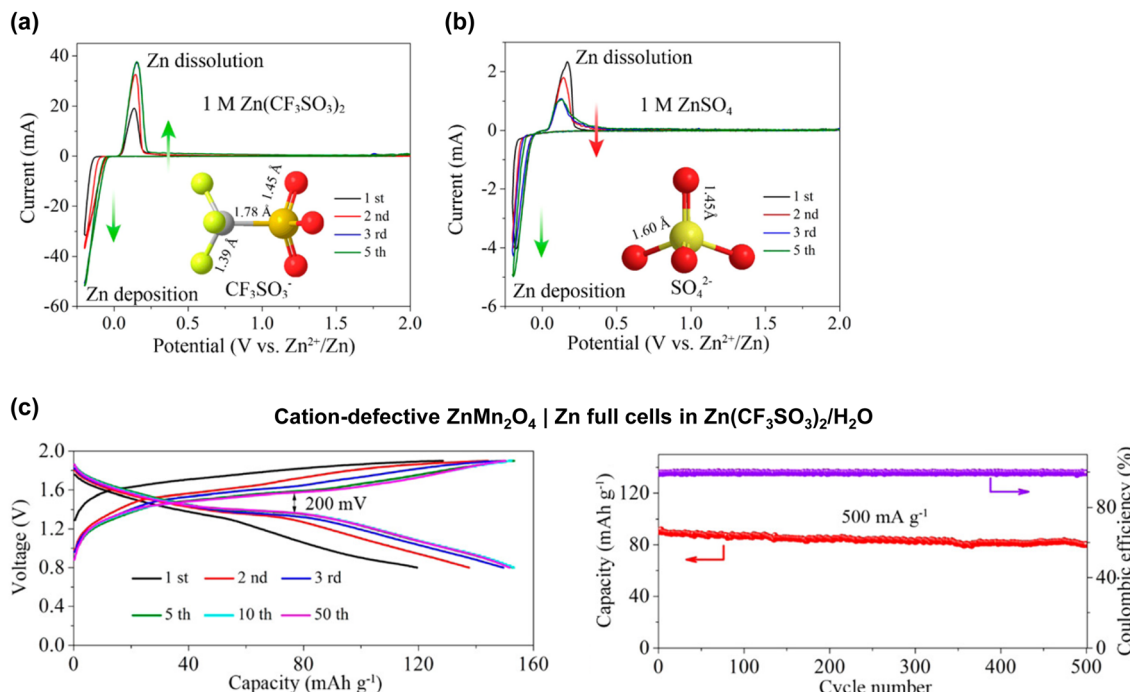


Fig. 52 Cyclic voltammograms of the Zn plating/stripping in (a) 1 M Zn(OTf)₂ and (b) 1 M ZnSO₄ solutions. (c) Galvanostatic charge and discharge curves at 50 mA g⁻¹ and (d) long-term cycling performance of carbon-coated cation-defective ZnMn₂O₄ | Zn full cells in 3 M Zn(OTf)₂/H₂O at 500 mA g⁻¹.⁵⁹⁵ Reprinted with permission from *Journal of the American Chemical Society*.

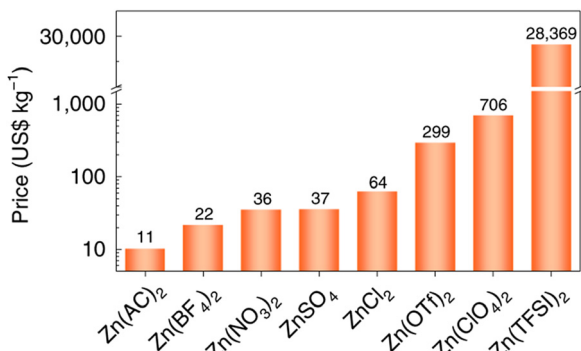


Fig. 53 Cost comparison of various Zn salts.^{597,598} Zn(AC)₂ and Zn(OAc)₂ refer to the same chemical compound, Zn(CH₃COO)₂. Reprinted with permission from *Nature Sustainability*.

should occur at lower potentials than the calculated values. For example, in case of Li systems, the calculated reduction potential of the Li⁺(TFSI⁻)_n ion pair was ~2.9 V vs. Li/Li⁺.¹⁸ However, even with multiple favorable conditions for the formation of an anion-derived SEI—such as using an Al electrode with a high HER overpotential and a highly salt-concentrated Li(PTFSI)_{0.6}(TFSI)_{0.4}·1H₂O hydrate melt, which involves large amounts of ion-pair aggregations and significantly reduced water activity owing to the breakage of hydrogen bonds between water molecules—the actual potential at which the SEI was completely formed was ~2.2 V vs. Li/Li⁺, much lower than the theoretically predicted reduction potential.⁸⁵ All these observations suggest that the formation of an SEI on Zn metal through

the electrochemical reduction of anions is challenging. This is also supported by transmission electron microscopy (TEM) images that confirm the absence of an SEI on Zn metal after the plating and stripping reactions in nearly saturated 4 M Zn(OTf)₂/H₂O and 4 M Zn(TFSI)₂/H₂O electrolytes (Fig. 55).^{618,619}

Maintaining the SEI might be more challenging than its formation. The SEI does not exist statically on the electrode surface, but undergoes dynamic changes involving deformation and regeneration. Components of the SEI diffuse into the bulk electrolyte, and the insertion of electrolyte solvents into the SEI causes it to swell. This dynamic change of the SEI hampers the complete blocking of electrolyte contact with the electrode surface, particularly in the case of metal electrodes, which undergo significant volume changes.

Cui *et al.* revealed that nonaqueous electrolytes, which ensure high Coulombic efficiency in Li plating and stripping (e.g., highly salt-concentrated electrolytes, locally salt-concentrated electrolytes, and weakly solvating electrolytes with ion pair-predominant solution structures), can suppress the swelling of the SEI and the diffusion of SEI components into the bulk electrolyte (Fig. 56).^{621,622} In these electrolytes, the ligand of Li⁺ is replaced by multiple anions rather than solvents, resulting in a high concentration of anions on the anode surface, which cannot dissolve or cause swelling of the SEI. Additionally, the use of bulky, nonpolar, or low-dielectric-constant solvents that have low solubility for SEI components and are difficult to diffuse into the SEI might be another reason for the suppressed changes in the SEI.

As mentioned before, maintaining the SEI in aqueous electrolytes is even more challenging than forming an SEI



Table 13 Reported stabilities of electrolytes and Zn metal in $\text{Zn}(\text{OTf})_2/\text{H}_2\text{O}$ solutions

Electrolytes	Cell configuration	Cycle conditions	Cycle life or average Coulombic efficiency (%)
1 m $\text{Zn}(\text{OTf})_2/\text{H}_2\text{O}$ ⁵⁹⁹	$\text{Zn} \text{Zn}$	0.5 mA cm^{-2} , 0.5 mA h cm^{-2}	1226 h
	$\text{Cu} \text{Zn}$	0.5 mA cm^{-2} , 0.5 mA h cm^{-2} 1.0 mA cm^{-2} , 1.0 mA h cm^{-2}	~90% over 500 cycles ~90% over 400 cycles
1 m $\text{Zn}(\text{OTf})_2/\text{H}_2\text{O}$ ⁶⁰⁰	$\text{Cu} \text{Zn}$	0.5 mA cm^{-2} , 0.5 mA h cm^{-2}	~91% over 500 cycles
	$\text{Zn} \text{Zn}$	0.5 mA cm^{-2} , 0.5 mA h cm^{-2}	105 h
1 M $\text{Zn}(\text{OTf})_2/\text{H}_2\text{O}$ ⁶⁰¹	$\text{Zn} \text{Zn}$	1.0 mA cm^{-2} , 1.0 mA h cm^{-2}	100 h
	$\text{Zn} \text{Zn}$	2.0 mA cm^{-2} , 2.0 mA h cm^{-2}	134 h
1 M $\text{Zn}(\text{OTf})_2/\text{H}_2\text{O}$ ⁶⁰²	$\text{Zn} \text{Zn}$	5.0 mA cm^{-2} , 5.0 mA h cm^{-2}	160 h
	$\text{Zn} \text{Zn}$	20 mA cm^{-2} , 1.0 mA h cm^{-2}	137 h
1 M $\text{Zn}(\text{OTf})_2/\text{H}_2\text{O}$ ⁵⁸³	$\text{Zn} \text{Zn}$	1.0 mA cm^{-2} , 1.0 mA h cm^{-2}	650 h
	$\text{Zn} \text{Zn}$	1.0 mA cm^{-2} , 0.5 mA h cm^{-2}	
1 M $\text{Zn}(\text{OTf})_2/\text{H}_2\text{O}$ ⁶⁰³	$\text{Zn} \text{Zn}$	1.0 mA cm^{-2} , 0.5 mA h cm^{-2}	
	$\text{Zn} \text{Zn}$	1.0 mA cm^{-2} , 1.0 mA h cm^{-2}	300 h
2 M $\text{Zn}(\text{OTf})_2/\text{H}_2\text{O}$ ⁶⁰⁴	$\text{Zn} \text{Zn}$	1.0 mA cm^{-2} , 1.0 mA h cm^{-2}	~75%, short circuit after 100 cycles
	$\text{Ti} \text{Zn}$	0.5 mA cm^{-2} , 0.5 mA h cm^{-2}	180 h
2 M $\text{Zn}(\text{OTf})_2/\text{H}_2\text{O}$ ⁶⁰⁵	$\text{Zn} \text{Zn}$	0.5 mA cm^{-2} , 0.5 mA h cm^{-2}	~60%, short circuit after 10 cycles
	$\text{Ti} \text{Zn}$	0.5 mA cm^{-2} , 0.5 mA h cm^{-2}	175 h
2 M $\text{Zn}(\text{OTf})_2/\text{H}_2\text{O}$ ³⁹⁵	$\text{Zn} \text{Zn}$	2.0 mA cm^{-2} , 1.0 mA h cm^{-2}	~80%, short circuit after 50 cycles
	$\text{Cu} \text{Zn}$	1.0 mA cm^{-2} , 1.0 mA h cm^{-2}	20 h
2 M $\text{Zn}(\text{OTf})_2/\text{H}_2\text{O}$ ⁴⁰⁸	$\text{Zn} \text{Zn}$	5.0 mA cm^{-2} , 1.5 mA h cm^{-2}	
	$\text{Ti} \text{Zn}$	1.0 mA cm^{-2} , 1.0 mA h cm^{-2}	Short circuit after 20 cycles
2 M $\text{Zn}(\text{OTf})_2/\text{H}_2\text{O}$ ⁶⁰⁶	$\text{Zn} \text{Zn}$	1.0 mA cm^{-2} , 1.0 mA h cm^{-2}	~200 h
	$\text{Zn} \text{Zn}$	5.0 mA cm^{-2} , 5.0 mA h cm^{-2}	54 h
2 M $\text{Zn}(\text{OTf})_2/\text{H}_2\text{O}$ ⁶⁰⁷	$\text{Zn} \text{Zn}$	10 mA cm^{-2} , 10 mA h cm^{-2}	~50 h
	$\text{Zn} \text{Zn}$	0.25 mA cm^{-2} , 0.25 mA h cm^{-2}	136 h
2 M $\text{Zn}(\text{OTf})_2/\text{H}_2\text{O}$ ⁶⁰⁸	$\text{Zn} \text{Zn}$	1.0 mA cm^{-2} , 1.0 mA h cm^{-2}	97 h
	$\text{Cu} \text{Zn}$	5.0 mA cm^{-2} , 5.0 mA h cm^{-2}	60 h
2 M $\text{Zn}(\text{OTf})_2/\text{H}_2\text{O}$ ⁶⁰⁸	$\text{Zn} \text{Zn}$	5.0 mA cm^{-2} , 1.0 mA h cm^{-2}	Short circuit after 310 cycles
	$\text{Zn} \text{Zn}$	0.25 mA cm^{-2} , 1.0 mA h cm^{-2}	600–800 h
3 m $\text{Zn}(\text{OTf})_2/\text{H}_2\text{O}$ ⁶⁰⁹	$\text{Cu} \text{Zn}$	1.0 mA cm^{-2} , 1.0 mA h cm^{-2}	400–900 h
	$\text{Zn} \text{Zn}$	0.5 mA cm^{-2} , 0.5 mA h cm^{-2}	120–600 h
3 M $\text{Zn}(\text{OTf})_2/\text{H}_2\text{O}$ ⁶¹⁰	$\text{Ti} \text{Zn}$	1.0 mA cm^{-2} , 0.5 mA h cm^{-2}	Short circuit after 300 cycles
	$\text{Zn} \text{Zn}$	1.0 mA cm^{-2} , 1.0 mA h cm^{-2}	~70%, short circuit after 40 cycles
3 M $\text{Zn}(\text{OTf})_2/\text{H}_2\text{O}$ ⁶¹¹	$\text{Zn} \text{Zn}$	1.0 mA cm^{-2} , 1.0 mA h cm^{-2}	490 h
	$\text{Zn} \text{Zn}$	0.5 mA cm^{-2} , 2.5 mA h cm^{-2}	~85%, short circuit after 25 cycles
3 M $\text{Zn}(\text{OTf})_2/\text{H}_2\text{O}$ ⁶¹²	$\text{Zn} \text{Zn}$	0.5 mA cm^{-2} , 2.5 mA h cm^{-2}	150 h
	$\text{Zn} \text{Zn}$		20 h
4 m $\text{Zn}(\text{OTf})_2/\text{H}_2\text{O}$ ⁵³⁵	$\text{Ti} \text{Zn}$	1.0 mA cm^{-2} , 1.0 mA h cm^{-2}	Short circuit after 3 cycles
	$\text{Zn} \text{Zn}$	0.2 mA cm^{-2} , 1.0 mA h cm^{-2}	1500 h
4 m $\text{Zn}(\text{OTf})_2/\text{H}_2\text{O}$ ⁶¹³	$\text{Ti} \text{Zn}$	1.0 mA cm^{-2} , 1.0 mA h cm^{-2}	500 h
	$\text{Zn} \text{Zn}$	1.0 mA cm^{-2} , 0.5 mA h cm^{-2}	~85%, short circuit after 200 cycles

(Fig. 57). Most SEI components easily dissolve in or are highly reactive in water. The high dielectric constant of water facilitates the rapid diffusion of SEI components into the bulk electrolyte. Moreover, the diameter of water molecules is 2.75 Å, almost similar to the diameter of hydrated alkali ions (Stokes radius in Table 2), indicating that water molecules can be easily inserted into the SEI. The thickness of the SEI formed in aqueous electrolytes is generally several ten to hundred times higher than that formed in nonaqueous electrolytes.²⁰ The generation of hydrogen gas due to the reduction of water molecules causes exfoliation of the SEI from the electrode surface. The difficulty in SEI formation and the maintenance of the SEI in aqueous systems can also be inferred from the poor initial Coulombic efficiency (70–80%) related to SEI formation in aqueous alkali-ion (Li^+ , Na^+ , and K^+) batteries.

The formation and maintenance of the SEI might be relatively easier in hybrid aqueous/nonaqueous electrolytes. However, introducing co-solvents with higher reduction potentials than water to force the formation of solvent-derived SEIs has rarely been attempted. In most cases, the addition of co-solvents aimed to reduce the water activity by decreasing the amount of

water in the system and through the realization of various hydrogen bond-related effects, as described in Section 6.3. This suggests that the higher HER overpotential on Zn metal might be a predominant cause for the improved Coulombic efficiency in hybrid aqueous/nonaqueous electrolytes rather than SEI formation.

Additionally, hybrid Zn electrolytes typically demonstrate high initial efficiencies of over 90%. This is similar to the initial Coulombic efficiency obtained in nonaqueous Li electrolytes with a graphite anode, which has a small surface area and undergoes a slight (10%) volume change during charging and discharging, thus forming a few-nanometer-thick SEI. However, TEM observations showed thick layers, with thicknesses ranging from tens to thousands of nanometers, on cycled Zn metal in hybrid aqueous/nonaqueous Zn electrolytes (Fig. 55). This indicates that the observed thick layers might not be part of the SEI but have originated as a result of irreversible chemical side reactions.

Moreover, as described in Section 7.1, the conductivity of divalent ions within solids is significantly lower than that of monovalent (alkali) ions because the higher charge density of



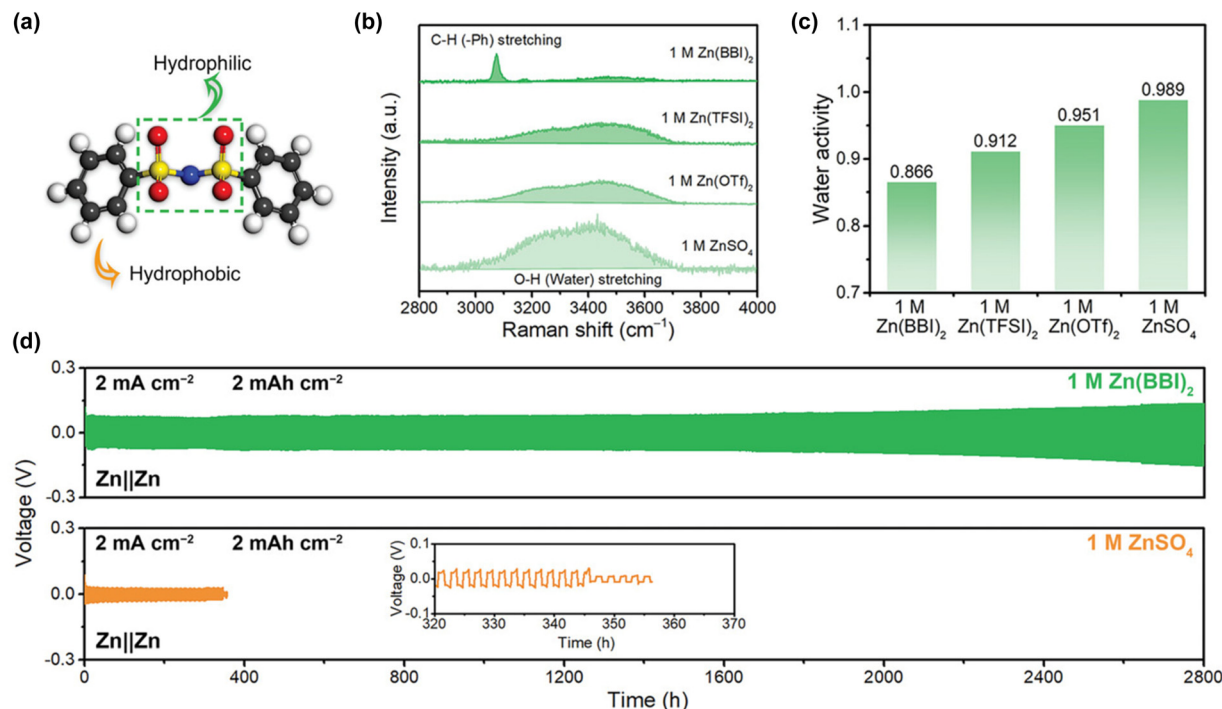


Fig. 54 (a) Atomic structure of the BBI⁻ anion, with C, H, O, N, and S atoms denoted in black, light-gray, red, blue, and yellow, respectively. (b) Raman spectra and (c) water activities of various Zn solutions. (d) Cycling performance of symmetric Zn|Zn cells in 1 M Zn(BBI)₂ and 1 M ZnSO₄ electrolytes under the given conditions.⁵⁹⁸ Reprinted with permission from *Advanced Materials*.

the former results in stronger Coulombic interactions with the surrounding ligands, hindering their movement.^{623–626} However, most studies have illustrated smooth Zn plating and stripping despite the presence of thick layers on Zn metal, which requires substantially high carrier ion conductivity. This directly or indirectly suggests that the electrolyte can still approach the electrode surface easily and that the formation of a genuine SEI—an interphase that blocks electrolyte contact while allowing ion transport—on Zn metal is not yet certain.

The formation and functionalities of ZnF₂-rich SEIs are also debatable. In many cases, X-ray photoelectron spectroscopy (XPS) has been used to confirm the presence of ZnF₂ within the SEI. However, the decomposition of residual salts and solvents and their reduced fragments on the electrode sample during XPS measurements can produce a strong Zn–F signal, especially under Ar⁺ sputtering conditions.^{19,627,628} The concept of a F-rich SEI, an extension of ideas proposed for nonaqueous Li-ion/Li-metal batteries, might not simply apply to aqueous Zn-metal batteries. For example, both experimental and theoretical analyses have highlighted the effect of LiF in compacting the SEI by trapping other SEI components owing to the high electronegativity of fluorine.^{629,630} LiF has low solubility in organic solvents, allowing it to stably exist on the electrode surface and serve as an anchor, connecting the anode and SEI.^{631,632} In the LiF-rich SEI, Li⁺ are expected to conduct not through LiF itself but rather through other SEI components or at the grain boundary between LiF and other SEI components because of the significantly high migration barrier for Li⁺ within the LiF crystals.^{358,359,633–637} Importantly, various SEI

components, which ensure a high Li⁺ conductivity, are present within the LiF-rich SEI, and the synergistic effect of these components with LiF contributes to the maintenance of the SEI and the improvement of the SEI functionalities.^{358,359,633–637}

The migration of Zn²⁺ within ZnF₂ encounters more resistance than the migration of Li⁺ within LiF, as multivalent ions typically exhibit higher migration resistance than alkali ions. Computational calculations of Zn²⁺ conduction on/within ZnF₂-rich layers have often assumed direct contact between ZnF₂ and Zn metal (details in Section 7.5).^{638–640} However, the layers formed on Zn metal are tens to thousands of nanometers thick, and most of the ZnF₂ exists within the layer without direct contact with the Zn metal. Additionally, studies in other multivalent-ion systems (such as Ca²⁺ and Mg²⁺) have demonstrated that the use of imide salt-based electrolytes, which form F-rich SEIs, results in a high migration resistance of the carrier ions, leading to inferior Coulombic efficiency in plating and stripping.^{641–643} There is no evidence that Zn²⁺ can migrate rapidly within F-rich layers, unlike other multivalent ions (Ca²⁺ and Mg²⁺). Moreover, as discussed in Section 6, fluorinated compounds cannot stably exist on metal surfaces even in highly salt-concentrated aqueous electrolytes (Fig. 32). Furthermore, a synergistic effect with ZnF₂ and other rapid Zn²⁺-conducting SEI components is hardly expected, as there have been limited reports of fast multivalent ion-conducting materials.^{623,625,644} Introducing borate salts into nonaqueous electrolytes provides high Coulombic efficiency in Ca and Mg plating/stripping reactions, forming the SEI with sufficient Ca²⁺ and Mg²⁺ transport.^{575,642–646} However, borate salts are prone to hydrolysis, rendering their use in aqueous systems challenging.



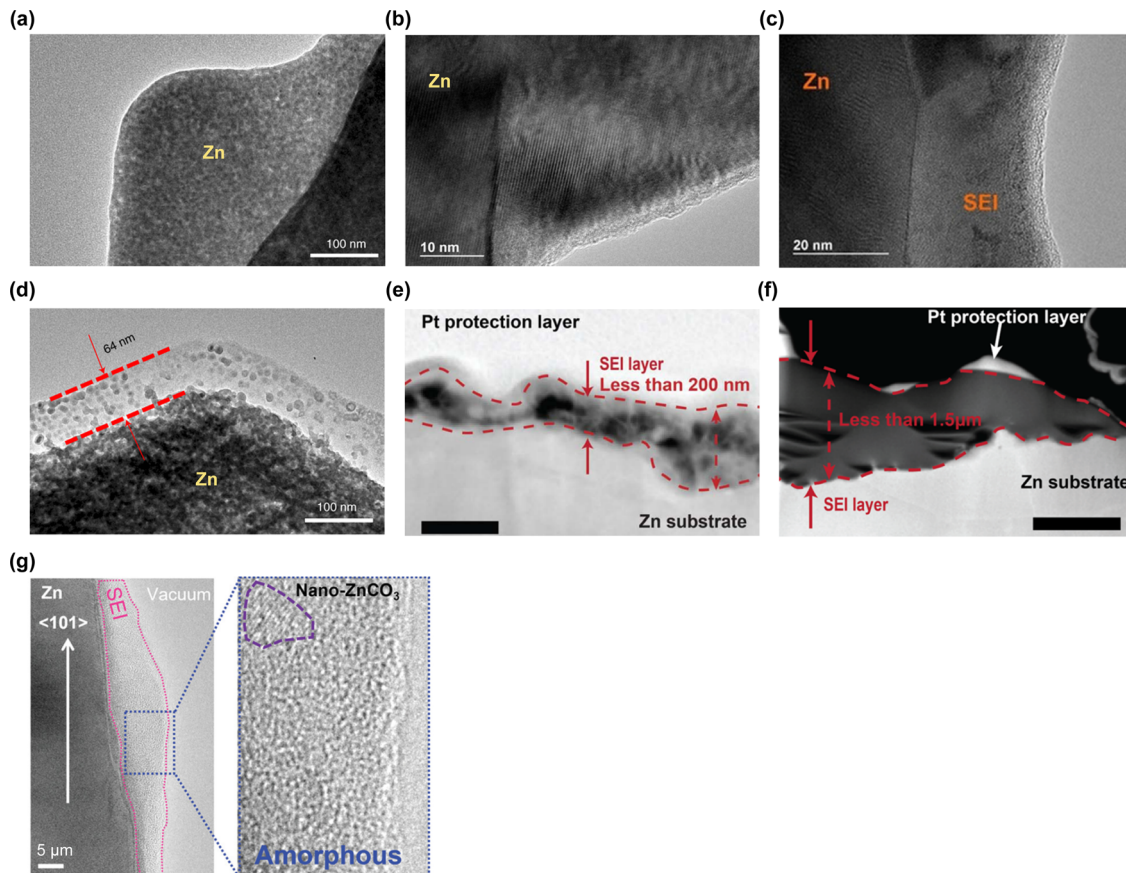


Fig. 55 TEM images of the cycled Zn metal in various electrolytes. No SEI was observed on the Zn-metal surface in aqueous (a) 4 m $\text{Zn}(\text{OTf})_2/\text{H}_2\text{O}$ ⁶¹⁸ and (b) 4 m $\text{Zn}(\text{TFSI})_2/\text{H}_2\text{O}$.⁶¹⁹ The presence of the SEI was confirmed only in the hybrid aqueous/nonaqueous Zn electrolytes, such as (c) 4 m $\text{Zn}(\text{TFSI})_2 + 4$ m tributyl (2-methoxyethyl)-TFSI/ H_2O ,⁶¹⁹ (d) 4 m $\text{Zn}(\text{OTf})_2 + 0.5$ m trimethylsilylaminium-OTf/ H_2O ,⁶¹⁸ (e) 30 m $\text{ZnCl}_2 + 5$ m $\text{LiCl} + 10$ m trimethylsilylaminium-Cl/dimethyl carbonate/ H_2O (1 : 5, $n : n$),⁵³⁷ (f) 30 m $\text{ZnCl}_2 + 5$ m $\text{LiCl} + 10$ m trimethylsilylaminium-Cl/diethyl carbonate/ H_2O (1 : 5, $n : n$),⁵³⁷ and (g) 1 M $\text{Zn}(\text{OTf})_2/\text{tetrahydrofuran}$ / H_2O (1 : 3, v : v).⁶²⁰ However, the observed SEI, with a thickness ranging from tens to thousands of nanometers, questions whether sufficient Zn^{2+} transport into the SEI is possible. Reprinted with permission from *Nature Nanotechnology* (a) and (c), *Angewandte Chemie International Edition* (b) and (d), *Nature Sustainability* (e) and (f), and *Advanced Materials* (g).

In summary, the presence and function of the SEI in aqueous Zn-metal batteries lack substantial supporting evidence. To summarize the rationale for this statement:

- (1) The high redox potential of Zn metal provides insufficient thermodynamic driving force for anion-derived SEI formation.
- (2) The high dielectric constant and small molecular size of water, along with hydrogen-gas generation from water reduction, critically hinder the maintenance of the SEI.
- (3) ZnF_2 has a high Zn^{2+} migration resistance and seldom interacts directly with the metal surface in thick SEI layers.
- (4) It is unclear whether specific compounds that provide sufficient Zn^{2+} conductivity are abundantly present within the SEI.

The increased HER overpotential on Zn metal, induced by a high salt concentration; the deposits of electrolyte reduction products; and interactions among water, anions, co-solvents, and their reduction species on Zn metal and in the electrolyte might contribute more to suppressing the side reactions than the SEI. Further research on the formation, maintenance, and functionalities of the SEI in aqueous Zn-metal batteries, with a comprehensive understanding and careful investigation is needed.

7.5. Limited evidence on the effects of *ex situ* artificial SEIs and scaffolds

The challenges associated with forming an *in situ* SEI through electrolyte modification have driven the development of *ex situ* artificial SEIs and scaffolds designed to facilitate smooth Zn plating and stripping while preventing various side reactions.^{647–650} Table 14 lists the types of *ex situ* artificial SEIs and scaffolds that have been introduced, along with their contributions to the Zn-metal stability. Although a considerable number of papers have been published on *ex situ* artificial SEIs and scaffolds, numerous questions about these technologies persist, some of which are listed below:

- (1) Among the commonly discussed mechanisms, which factor (e.g., hydrophobic binder, electrolyte wettability, nucleation overpotential, and distribution of Zn^{2+} and electrons) is the most crucial for stable Zn plating and stripping?
- (2) Why are there only a handful of studies conducted under practical conditions, where a substantial amount of Zn^{2+} is involved in plating and stripping with a high state of charge and depth of discharge?

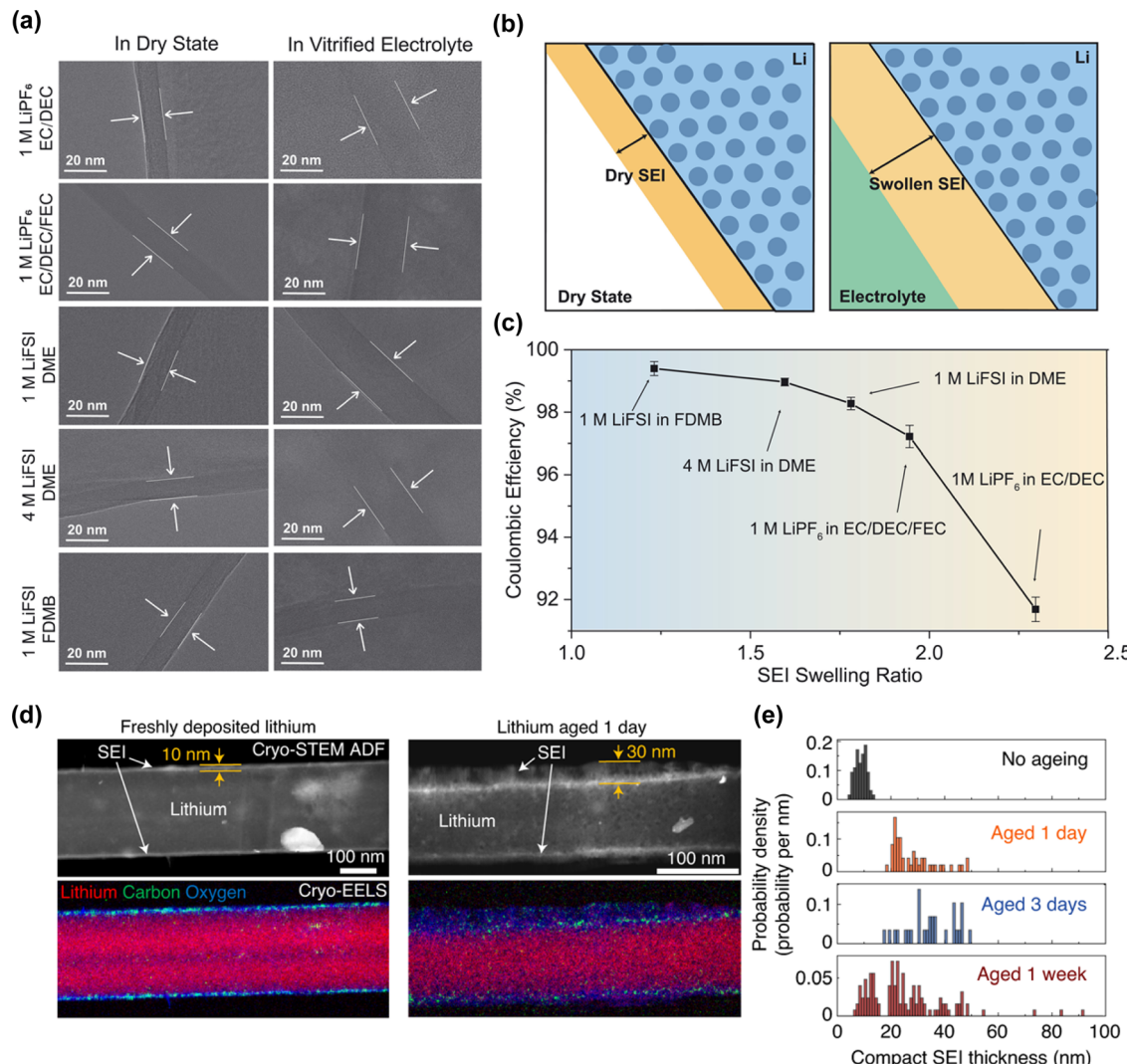


Fig. 56 (a) and (b) Comparison of the SEI thickness in the dry state and in a vitrified electrolyte.⁶²¹ (c) Correlation between the Coulombic efficiency of Li plating/stripping and the SEI swelling ratio in various electrolytes. Electrolytes providing high Coulombic efficiency in Li plating and stripping have a low SEI swelling ratio (SEI thickness in the dried state compared to that in the vitrified state in the electrolyte).⁶²¹ (d) SEI growth on Li metal before and after calendar aging in LiPF₆/ethylene carbonate:diethyl carbonate.⁶²² (e) Histogram of the time-dependent change in the SEI thickness.⁶²² An electrolyte design that suppresses changes in the SEI, such as swelling and dissolving, will ensure high Coulombic efficiency in batteries. Reprinted with permission from *Science* (a)–(c) and *Nature Energy* (d) and (e).

(3) Can *ex situ* artificial SEIs ensure sufficient Zn²⁺ conductivity?

(4) Is delaying a short circuit of the battery using three-dimensional scaffolds more important than their potential for accelerating electrolyte reduction due to the increased surface area of plated Zn?

All these questions highlight the persistent need for extensive research from both scientific and practical perspectives. Before delving into detailed discussions, an overview of the research conducted on *ex situ* artificial SEIs and scaffolds will be presented.

In 2018, Wang and Jiang's group were successful in enhancing the Zn-metal stability by coating it with a 90 µm-thick porous carbon film, which endowed high electrical conductivity and chemical stability (Fig. 58).⁶⁵¹ This treatment facilitated

homogeneous current distribution, enabling uniform Zn deposition without dendrite formation. In symmetric cell tests using a 0.4 M Zn(OTf)₂ + 8 M NaClO₄/H₂O electrolyte at 2.5 mA cm⁻² and 1.0 mA h cm⁻², the carbon-coated Zn metal demonstrated stable cycling over 300 h, in contrast to bare Zn, which short-circuited after just 20 h.

In 2019, Lu and co-workers adopted a three-dimensional carbon nanotube framework with a high surface area and electrical conductivity as a scaffold for Zn plating and stripping.⁶⁵³ This setup reduced the overpotential for Zn plating and minimized the tip effect by homogeneously distributing the electric field. Consequently, the symmetric cell in 2 M ZnSO₄/H₂O, operating at 2.0 mA cm⁻² and 2.0 mA h cm⁻², demonstrated stable performance over 200 h with suppressed side reactions and Zn dendrite growth.

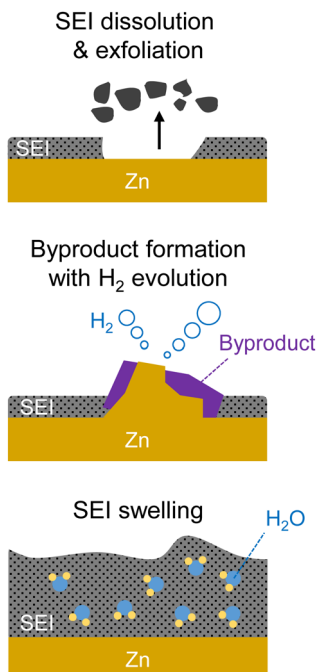


Fig. 57 Various SEI degradation modes in aqueous electrolytes.

In 2023, Zhang *et al.* fabricated 20 nm-thick carbon-coated Zn metal through magnetron sputtering.⁶⁶¹ The enhanced wettability of the electrolyte, evidenced by a decrease in the contact angle from 99° to 47°, promoted more uniform charge distribution on the Zn metal. The plated Zn on the carbon-coated surface was flatter, more compact, and uniform compared to the loosely and unevenly distributed nanosheet-like features on bare Zn, thus reducing electrolyte decomposition with a smaller reaction area. Remarkably, the cycling stability of symmetric cells in 2 M ZnSO₄/H₂O exceeded 3500 h under various conditions (0.5 mA cm⁻²/0.5 mA h cm⁻², 1.0 mA cm⁻²/1.0 mA h cm⁻², and 2.0 mA cm⁻²/2.0 mA h cm⁻²), with a notable suppression of byproduct formation.

The introduction of inorganic materials as artificial SEIs has been explored for its potential benefits. In 2018, Mai *et al.* applied a chemically and electrochemically stable amorphous TiO₂ layer to Zn metal *via* atomic layer deposition, resulting in an 8 nm-thick barrier that reduced the formation of less-conductive byproducts like Zn(OH)₂ and minimized electrolyte decomposition, as shown in Fig. 59.⁶¹¹ In symmetric cell tests with 3 M Zn(OTf)₂/H₂O at 1.0 mA cm⁻² and 1.0 mA h cm⁻², the TiO₂-coated Zn exhibited enhanced stability, lasting over 150 h. This was in contrast to the behavior of bare Zn, which failed just after 30 h.

Around the same time, Kang and co-workers engineered a porous, *ex situ* artificial SEI composed of nano CaCO₃ and polyvinylidene difluoride. The SEI was designed to mitigate dendrite growth and suppress electrolyte reduction by guiding the Zn plating and stripping processes beneath the artificial SEI.⁶⁶⁴ This modification enabled sustained Zn plating and stripping for over 840 h in a symmetric cell containing a 3 M ZnSO₄ + 0.1 M MnSO₄/H₂O electrolyte at 0.25 mA cm⁻² and 0.05 mA h cm⁻². To further

emphasize the role of metal affinity in the SEI performance, Wang *et al.* demonstrated that TiO₂ with a low metal affinity offered enhanced protective effects, inducing Zn plating and stripping beneath the layer, as depicted in Fig. 59.⁶⁷¹ Density functional theory calculations showed that the TiO₂ (001) facet exhibited lower Zn affinity than the TiO₂ (100) facet. TiO₂-coated Zn metal, which was strategically prepared to expose primarily the TiO₂ (001) facet, offered reduced dendrite growth and byproduct formation, thereby extending the cycle life of Zn plating and stripping in a symmetric cell using 1 M ZnSO₄/H₂O to over 460 h at 1.0 mA cm⁻² and 1.0 mA h cm⁻².

In 2021, Li *et al.* reported computational studies on the enhanced cycling performance with ZnF₂-coated Zn metal. Their analyses revealed that the ZnF₂ matrix on the Zn surface aided Zn²⁺ desolvation from the electrolyte and ensured a more uniform distribution, thus suppressing dendrite growth.⁶⁴⁰ Concurrently, using the climbing image nudged elastic band method, Ma *et al.* found that the diffusion energy barrier for a single Zn²⁺ ion was significantly lower on the ZnF₂ (002) facet (0.27 eV) compared to that on the bulk ZnF₂ surface (0.67 eV).⁶³⁹ This suggested that Zn²⁺ exhibited higher conductivity on the exposed ZnF₂ (002)/Zn metal surface, thereby kinetically facilitating their insertion into the ZnF₂-coated Zn metal with a reduced energy barrier (0.52 eV), compared to those on bulk ZnF₂ (4.08 eV) and bulk Zn (0.67 eV). Supporting this, Han and co-workers presented corroborative results, which showed that based on the defect formation energy calculations for ZnF₂, the formation of Zn²⁺ interstitials made them the most energetically favorable defect.⁶³⁸ This allowed interstitial Zn²⁺ to stably remain within the ZnF₂ matrix. Furthermore, the ZnF₂ structure contained channels along the *c*-axis, which spanned the entire structure, providing diffusion barriers of 0.25 eV for Zn²⁺ and 0.15 eV for Zn⁰, thereby facilitating the transport of Zn²⁺ to/from the Zn anode. However, note that the electrochemical properties of ZnF₂ are still under debate, as discussed in Section 7.4.

The cycling stability of aqueous Zn-metal batteries is significantly affected by uncontrollable morphological changes and the formation of numerous cracks and defects during the Zn plating and stripping processes. Thermodynamically, the formation of nuclei at dislocated sites is favored, leading to the creation of numerous protuberances that eventually grow into Zn dendrites, thereby shortening the lifespan of batteries. To address these challenges, Lang *et al.* introduced lamella-nanostructured eutectic zinc-aluminum (Zn₈₈Al₁₂) alloys (Fig. 60).⁶⁷² Zn and Al lamellas serve dual roles—they provide charge carriers for Zn²⁺ and offer a favorable skeleton for Zn plating. The formation of an Al₂O₃ layer on Al lamellas protects against the dissolution of Al, driven by the low thermodynamic potential of Al (Al/Al³⁺: -1.66 V vs. SHE) relative to that of Zn (Zn/Zn²⁺: -0.76 V vs. SHE), inhibits electron transfer from Al to Zn²⁺, and forms a positive electrostatic shield around the Al/Al₂O₃ lamellas. This shield prevents the direct reduction of Zn²⁺ on the Al lamellas and ensures uniform Zn deposition within their interlayer spacing at Zn precursor sites. A symmetric cell test performed in an O₂-free 2 M ZnSO₄/H₂O electrolyte at 0.5 mA cm⁻² and 0.5 mA h cm⁻² exhibited almost negligible voltage hysteresis over 2000 h, which



Table 14 Materials used for *ex situ* artificial SEIs and scaffolds and their electrochemical properties. The Zn-metal stability is represented by the cycle life, which corresponds to the amount of time for which Zn plating and stripping processes can be sustained in symmetric cells (modified Zn|modified Zn) until a short circuit occurs

Year	Materials	Electrolytes	Cycle conditions	Cycle life (h)
2018	Active carbon ⁶⁵¹	0.4 M Zn(OTf) ₂ + 8 M NaClO ₄ /H ₂ O	1.0 mA cm ⁻² , 1.0 mA h cm ⁻² 2.5 mA cm ⁻² , 1.0 mA h cm ⁻²	200 300
2018	Reduced graphene oxide ⁶⁵²	1 M ZnSO ₄ /H ₂ O	1.0 mA cm ⁻² , 2.0 mA h cm ⁻² 2.0 mA cm ⁻² , 2.0 mA h cm ⁻² 5.0 mA cm ⁻² , 2.0 mA h cm ⁻² 10 mA cm ⁻² , 2.0 mA h cm ⁻² 2.0 mA cm ⁻² , 2.0 mA h cm ⁻² 5.0 mA cm ⁻² , 2.5 mA h cm ⁻²	200 200 200 200 200 200
2019	Carbon nanotube ⁶⁵³	2 M ZnSO ₄ /H ₂ O	0.2 mA cm ⁻² , 0.2 mA h cm ⁻² 0.4 mA cm ⁻² , 0.4 mA h cm ⁻²	150 2000
2019	Reduced graphene oxide ⁶⁵⁴	0.5 M ZnSO ₄ /H ₂ O	1.0 mA cm ⁻² , 1.0 mA h cm ⁻² 1.0 mA cm ⁻² , 1.0 mA h cm ⁻² 2.0 mA cm ⁻² , 2.0 mA h cm ⁻² 5.0 mA cm ⁻² , 5.0 mA h cm ⁻² 10 mA cm ⁻² , 10 mA h cm ⁻²	1200 400 400 400 400
2020	ZIF-8 metal organic framework-derived carbon ⁶⁵⁵	1 M ZnSO ₄ /H ₂ O	0.1 mA cm ⁻² , 0.5 mA h cm ⁻² 0.1 mA cm ⁻² , 0.1 mA h cm ⁻² 0.25 mA cm ⁻² , 0.125 mA h cm ⁻² 1.0 mA cm ⁻² , 1.0 mA h cm ⁻² 5.0 mA cm ⁻² , 5.0 mA h cm ⁻² 0.25 mA cm ⁻² , 0.25 mA h cm ⁻² 2.0 mA cm ⁻² , 1.0 mA h cm ⁻²	1800 200 200 1200 300 3800 2000
2020	Carbon nanotube ⁶⁵⁶	2 M Zn(OTf) ₂ /H ₂ O	0.5 mA cm ⁻² , 0.5 mA h cm ⁻²	3500
2020	Graphite ⁶⁵⁷	2 M ZnSO ₄ /H ₂ O	1.0 mA cm ⁻² , 1.0 mA h cm ⁻²	3500
2021	Carbon fiber/carbon ⁶⁵⁸	3 M Zn(OTf) ₂ /H ₂ O	0.25 mA cm ⁻² , 0.125 mA h cm ⁻²	200
2021	N-Doped graphene oxide ⁶⁵⁹	2 M ZnSO ₄ /H ₂ O	1.0 mA cm ⁻² , 1.0 mA h cm ⁻² 5.0 mA cm ⁻² , 5.0 mA h cm ⁻²	1200 300
2023	Fullerene C ₆₀ ⁶⁶⁰	2 M ZnSO ₄ /H ₂ O	0.25 mA cm ⁻² , 0.25 mA h cm ⁻² 2.0 mA cm ⁻² , 1.0 mA h cm ⁻²	3800 2000
2023	20 nm carbon ⁶⁶¹	2 M ZnSO ₄ /H ₂ O	0.5 mA cm ⁻² , 0.5 mA h cm ⁻² 1.0 mA cm ⁻² , 1.0 mA h cm ⁻² 2.0 mA cm ⁻² , 2.0 mA h cm ⁻²	3500 3500 3500
2023	Hollow porous carbon nanospheres ⁶⁶²	2 M ZnSO ₄ /H ₂ O	1.0 mA cm ⁻² , 1.0 mA h cm ⁻² 5.0 mA cm ⁻² , 1.0 mA h cm ⁻² 10 mA cm ⁻² , 10 mA h cm ⁻²	2700 1515 280
2023	β-Cyclodextrin-carbon nanotube ⁶⁶³	1 M ZnSO ₄ /H ₂ O	5.0 mA cm ⁻² , 1.0 mA h cm ⁻² 10 mA cm ⁻² , 2.0 mA h cm ⁻²	1000 350
2018	TiO ₂ ⁶¹¹	3 M Zn(OTf) ₂ /H ₂ O	1.0 mA cm ⁻² , 1.0 mA h cm ⁻²	150
2018	CaCO ₃ ⁶⁶⁴	3 M ZnSO ₄ + 0.1 M MnSO ₄ /H ₂ O	0.25 mA cm ⁻² , 0.05 mA h cm ⁻²	836
	SiO ₂ ⁶⁶⁴		0.25 mA cm ⁻² , 0.05 mA h cm ⁻²	200–250
2019	Acetylene black ⁶⁶⁴		0.25 mA cm ⁻² , 0.05 mA h cm ⁻²	400
2019	Au ⁶⁶⁵	3 M ZnSO ₄ /H ₂ O	0.25 mA cm ⁻² , 0.05 mA h cm ⁻²	2000
2019	ZnO ⁶⁶⁶	2 M ZnSO ₄ + 0.1 M MnSO ₄ /H ₂ O	5.0 mA cm ⁻² , 1.25 mA h cm ⁻²	500
2020	In ⁶⁶⁷	2 M ZnSO ₄ /H ₂ O	0.2 mA cm ⁻² , 0.2 mA h cm ⁻²	1500
2020	In ⁶⁶⁸	2 M ZnSO ₄ /H ₂ O	1.0 mA cm ⁻² , 1.0 mA h cm ⁻² 0.25 mA cm ⁻² , 0.05 mA h cm ⁻² 1.0 mA cm ⁻² , 1.0 mA h cm ⁻²	500 1400 300
2020	Cu ⁶⁶⁹	3 M ZnSO ₄ /H ₂ O	4.0 mA cm ⁻² , 1.0 mA h cm ⁻²	400
2020	ZnS ⁶⁷⁰	1 M ZnSO ₄ /H ₂ O	1.0 mA cm ⁻² , 0.5 mA h cm ⁻²	1500
2020	TiO ₂ ⁶⁷¹	1 M ZnSO ₄ /H ₂ O	2.0 mA cm ⁻² , 2.0 mA h cm ⁻²	1100
2020	Zn ₈₈ Al ₁₂ ⁶⁷²	O ₂ free – 2 M ZnSO ₄ /H ₂ O	1.0 mA cm ⁻² , 1.0 mA h cm ⁻²	460
2020	ZnO ₂ ⁶⁷³	1 M Zn(OTf) ₂ /H ₂ O	2.0 mA cm ⁻² , 2.0 mA h cm ⁻² 0.5 mA cm ⁻² , 0.5 mA h cm ⁻² 0.2 mA cm ⁻² , 0.2 mA h cm ⁻² 1.0 mA cm ⁻² , 1.0 mA h cm ⁻² 5.0 mA cm ⁻² , 2.5 mA h cm ⁻²	280 2000 1000 400 100
2020	Al ₂ O ₃ ⁶⁷⁴	3 M Zn(OTf) ₂ /H ₂ O	1.0 mA cm ⁻² , 1.0 mA h cm ⁻²	500
2020	Kaolin (Al ₂ Si ₂ O ₅ (OH) ₄) ⁶⁷⁵	2 M ZnSO ₄ /H ₂ O	4.4 mA cm ⁻² , 1.1 mA h cm ⁻²	800
2020	ZrO ₂ ⁶⁷⁶	2 M ZnSO ₄ /H ₂ O	0.25 mA cm ⁻² , 0.125 mA h cm ⁻²	3800
2020	NaTi ₂ (PO ₄) ₃ ⁶⁷⁷	2 M ZnSO ₄ /H ₂ O	5.0 mA cm ⁻² , 1.0 mA h cm ⁻²	2100
2021	Cu ⁶⁷⁸	3 M ZnSO ₄ + 0.1 M MnSO ₄ /H ₂ O	1.0 mA cm ⁻² , 1.0 mA h cm ⁻² 1.0 mA cm ⁻² , 1.0 mA h cm ⁻² 5.0 mA cm ⁻² , 2.0 mA h cm ⁻²	250 5000 1500
2021	In ⁶⁷⁹	3 M ZnSO ₄ /H ₂ O	1.0 mA cm ⁻² , 0.5 mA h cm ⁻² 20 mA cm ⁻² , 20 mA h cm ⁻²	700 80
2021	Ag ⁶⁸⁰	3 M Zn(OTf) ₂ /H ₂ O	0.2 mA cm ⁻² , 0.2 mA h cm ⁻² 1.0 mA cm ⁻² , 1.0 mA h cm ⁻² 2.0 mA cm ⁻² , 2.0 mA h cm ⁻²	1450 350 150
2021	Sn ⁶⁸¹	1 M ZnSO ₄ /H ₂ O	0.5 mA cm ⁻² , 1.0 mA h cm ⁻²	500
2021	Sn ⁶⁸²	2 M ZnSO ₄ /H ₂ O	1.0 mA cm ⁻² , 0.5 mA h cm ⁻²	500
2021	Sn ⁶⁸³	1 M ZnSO ₄ /H ₂ O	1.0 mA cm ⁻² , 1.0 mA h cm ⁻²	800
2021	Zn ₃ Mn ⁶⁸⁴	2 M ZnSO ₄ /H ₂ O	80 mA cm ⁻² , 16 mA h cm ⁻²	750
2021	Ga-In ⁶⁸⁵	3 M ZnSO ₄ /H ₂ O	0.25 mA cm ⁻² , 0.05 mA h cm ⁻² 1.0 mA cm ⁻² , 0.1 mA h cm ⁻²	2100 1250



Table 14 (continued)

Year	Materials	Electrolytes	Cycle conditions	Cycle life (h)
2021	Ga-In-Zn ⁶⁸⁶	2 M ZnSO ₄ /H ₂ O	5.0 mA cm ⁻² , 0.1 mA h cm ⁻² 1.0 mA cm ⁻² , 0.5 mA h cm ⁻² 2.5 mA cm ⁻² , 2.5 mA h cm ⁻²	370 500 200
2021	ZnSe ⁶⁸⁷	2 M ZnSO ₄ /H ₂ O	0.5 mA cm ⁻² , 1.0 mA h cm ⁻² 1.0 mA cm ⁻² , 1.0 mA h cm ⁻² 10 mA cm ⁻² , 1.0 mA h cm ⁻² 10 mA cm ⁻² , 5.0 mA h cm ⁻²	450 1500 1500 160
2021	ZnSe ⁶⁸⁸	2 M ZnSO ₄ /H ₂ O	1.0 mA cm ⁻² , 1.0 mA h cm ⁻² 30 mA cm ⁻² , 10 mA h cm ⁻²	1530 170
2021	ZnSe ⁶⁸⁹	2 M ZnSO ₄ /H ₂ O	1.0 mA cm ⁻² , 0.5 mA h cm ⁻²	1700
2021	Cu ₃ N ⁶⁹⁰	2 M ZnSO ₄ /H ₂ O	0.5 mA cm ⁻² , 0.5 mA h cm ⁻²	800
2021	TiN ⁶⁹¹	2 M ZnSO ₄ /H ₂ O	1.0 mA cm ⁻² , 1.0 mA h cm ⁻² 2.0 mA cm ⁻² , 2.0 mA h cm ⁻²	2800 1000
2021	Si ₃ N ₄ /polyacrylonitrile ⁶⁹²	2 M ZnSO ₄ /H ₂ O	5.0 mA cm ⁻² , 0.5 mA h cm ⁻² 0.25 mA cm ⁻² , 0.25 mA h cm ⁻² 1.0 mA cm ⁻² , 1.0 mA h cm ⁻² 5.0 mA cm ⁻² , 5.0 mA h cm ⁻²	500 800 800 400
2021	ZnP ⁶⁹³	2 M ZnSO ₄ /H ₂ O	10 mA cm ⁻² , 10 mA h cm ⁻² 2.0 mA cm ⁻² , 0.5 mA h cm ⁻² 5.0 mA cm ⁻² , 1.25 mA h cm ⁻²	250 3300 3200
2021	γ-Al ₂ O ₃ ⁶⁹⁴	2 M ZnSO ₄ /H ₂ O	10 mA cm ⁻² , 2.5 mA h cm ⁻²	1900
2021	BaTiO ₃ ⁶⁹⁵	2 M ZnSO ₄ /H ₂ O	1.0 mA cm ⁻² , 0.5 mA h cm ⁻² 1.0 mA cm ⁻² , 1.0 mA h cm ⁻² 5.0 mA cm ⁻² , 2.5 mA h cm ⁻²	300 2000 1500
2021	BaTiO ₃ /polyvinylidene difluoride ⁶⁹⁶	1 M ZnSO ₄ + 0.1 M MnSO ₄ /H ₂ O	1.0 mA cm ⁻² , 1.0 mA h cm ⁻² 10 mA cm ⁻² , 2.0 mA h cm ⁻² 20 mA cm ⁻² , 2.0 mA h cm ⁻² 40 mA cm ⁻² , 2.0 mA h cm ⁻²	4100 1300 600 225
2021	Sc ₂ O ₃ ⁶⁹⁷	2 M ZnSO ₄ + 0.1 M MnSO ₄ /H ₂ O	0.5 mA cm ⁻² , 0.5 mA h cm ⁻² 1.0 mA cm ⁻² , 1.0 mA h cm ⁻²	275 200
2021	CeO ₂ ⁶⁹⁸	2 M ZnSO ₄ + 0.1 M MnSO ₄ /H ₂ O	2.0 mA cm ⁻² , 2.0 mA h cm ⁻²	250
2021	CeO ₂ ⁶⁹⁹	2 M ZnSO ₄ /H ₂ O	1.8 mA cm ⁻² , 0.45 mA h cm ⁻² 4.4 mA cm ⁻² , 1.1 mA h cm ⁻²	100 1200
2021	HfO ₂ ⁷⁰⁰	2 M ZnSO ₄ /H ₂ O	0.5 mA cm ⁻² , 0.25 mA h cm ⁻²	1300
2021	Zn _x V ₂ O ₅ ·nH ₂ O ⁷⁰¹	2 M ZnSO ₄ /H ₂ O	0.4 mA cm ⁻² , 0.1 mA h cm ⁻²	1300
2021	Mg _{0.667} Al _{0.333} (OH) ₂ ⁷⁰² (CO ₃) _{0.167} (H ₂ O) _{0.5}	2 M ZnSO ₄ /H ₂ O	0.25 mA cm ⁻² , 0.05 mA h cm ⁻² 0.5 mA cm ⁻² , 0.5 mA h cm ⁻² 1.0 mA cm ⁻² , 1.0 mA h cm ⁻² 2.0 mA cm ⁻² , 1.0 mA h cm ⁻² 5.0 mA cm ⁻² , 1.0 mA h cm ⁻²	570 1450 400 400 400
2021	ZnF ₂ ⁶⁴⁰	2 M ZnSO ₄ /H ₂ O	5.0 mA cm ⁻² , 1.0 mA h cm ⁻² 0.5 mA cm ⁻² , 1.0 mA h cm ⁻² 1.0 mA cm ⁻² , 1.0 mA h cm ⁻²	500 500 800
2021	ZnF ₂ ⁶³⁹	2 M ZnSO ₄ /H ₂ O	10 mA cm ⁻² , 1.0 mA h cm ⁻² 1.0 mA cm ⁻² , 1.0 mA h cm ⁻² 2.0 mA cm ⁻² , 1.0 mA h cm ⁻² 5.0 mA cm ⁻² , 1.0 mA h cm ⁻²	500 2500 2500 2500
2021	ZnF ₂ ⁶³⁸	2 M ZnSO ₄ /H ₂ O	0.5 mA cm ⁻² , 0.5 mA h cm ⁻²	700
2021	ZnF ₂ /Zn ₃ (PO ₄) ₂ /CF _x ⁷⁰³	2 M ZnSO ₄ /H ₂ O	1.0 mA cm ⁻² , 2.0 mA h cm ⁻²	500
2021	Zn-Sb ₃ P ₂ O ₁₄ ⁷⁰⁴	3 M ZnSO ₄ + 0.1 M MnSO ₄ /H ₂ O	14.2 mA cm ⁻² , 7.1 mA h cm ⁻² 1.0 mA cm ⁻² , 1.0 mA h cm ⁻² 10 mA cm ⁻² , 10 mA h cm ⁻²	187 1300 450
2022	ZnF ₂ /Ag ⁷⁰⁵	2 M ZnSO ₄ /H ₂ O	2.0 mA cm ⁻² , 2.0 mA h cm ⁻² 5.0 mA cm ⁻² , 10 mA h cm ⁻²	2200 140
2022	ZnF ₂ /Cu ⁷⁰⁶	1 M ZnSO ₄ /H ₂ O	0.25 mA cm ⁻² , 0.25 mA h cm ⁻² (−40 °C) 1.0 mA cm ⁻² , 1.0 mA h cm ⁻² 3.0 mA cm ⁻² , 3.0 mA h cm ⁻²	1600 2000 700
2022	MgF ₂ ⁷⁰⁷	1 M Zn(OTf) ₂ /H ₂ O	1.0 mA cm ⁻² , 1.0 mA h cm ⁻² 10 mA cm ⁻² , 1.0 mA h cm ⁻²	500 1600
2022	In ⁷⁰⁸	2 M ZnSO ₄ /H ₂ O	1.0 mA cm ⁻² , 0.5 mA h cm ⁻² 5.0 mA cm ⁻² , 0.5 mA h cm ⁻²	9400 8000
2022	Sn ⁷⁰⁹	2 M ZnSO ₄ /H ₂ O	0.5 mA cm ⁻² , 0.5 mA h cm ⁻²	1200
2022	Sb ⁷¹⁰	2 M ZnSO ₄ /H ₂ O	1.0 mA cm ⁻² , 1.0 mA h cm ⁻² 3.0 mA cm ⁻² , 1.0 mA h cm ⁻²	800 1000
2022	Zn ₇₃ Al ₂₇ ⁷¹¹	2 M ZnSO ₄ /H ₂ O	1.0 mA cm ⁻² , 1.0 mA h cm ⁻² 5.0 mA cm ⁻² , 1.0 mA h cm ⁻² 2.0 mA cm ⁻² , 0.5 mA h cm ⁻² 2.0 mA cm ⁻² , 2.0 mA h cm ⁻²	3000 480 400 500
2022	ZnMoO ₄ ⁷¹²	3 M ZnSO ₄ /H ₂ O	0.25 mA cm ⁻² , 0.125 mA h cm ⁻² 1.0 mA cm ⁻² , 1.0 mA h cm ⁻²	1000 2000



Table 14 (continued)

Year	Materials	Electrolytes	Cycle conditions	Cycle life (h)
2022	Zn ₃ (OH) ₂ V ₂ O ₇ ·2H ₂ O ⁷¹³	2 M ZnSO ₄ /H ₂ O	10 mA cm ⁻² , 1.0 mA h cm ⁻² 1.0 mA cm ⁻² , 0.5 mA h cm ⁻² 2.0 mA cm ⁻² , 1.0 mA h cm ⁻² 10 mA cm ⁻² , 1.0 mA h cm ⁻² 0.5 mA cm ⁻² , 0.25 mA h cm ⁻² 2.0 mA cm ⁻² , 1.0 mA h cm ⁻² 1.0 mA cm ⁻² , 1.0 mA h cm ⁻² 2.0 mA cm ⁻² , 1.0 mA h cm ⁻² 0.5 mA cm ⁻² , 1.0 mA h cm ⁻² 5.0 mA cm ⁻² , 1.0 mA h cm ⁻² 10 mA cm ⁻² , 1.0 mA h cm ⁻² 6.0 mA cm ⁻² , 1.0 mA h cm ⁻² 6.0 mA cm ⁻² , 3.0 mA h cm ⁻² 10 mA cm ⁻² , 10 mA h cm ⁻²	10 000 2000 1100 1000 2800 900 1200 800 780 780 350 3000 450 80
2022	Zn ₃ (PO ₄) ₂ /Nafion ⁷¹⁴	1 M ZnSO ₄ /H ₂ O	0.5 mA cm ⁻² , 0.25 mA h cm ⁻²	2800
2022	KTa _{0.54} Nb _{0.46} O ₃ ⁷¹⁵	1 M ZnSO ₄ /H ₂ O	2.0 mA cm ⁻² , 1.0 mA h cm ⁻² 1.0 mA cm ⁻² , 1.0 mA h cm ⁻² 2.0 mA cm ⁻² , 1.0 mA h cm ⁻² 0.5 mA cm ⁻² , 1.0 mA h cm ⁻² 5.0 mA cm ⁻² , 1.0 mA h cm ⁻²	900 1200 800 780 780
2022	ZrP ⁷¹⁶	2 M ZnSO ₄ /H ₂ O	10 mA cm ⁻² , 1.0 mA h cm ⁻² 5.0 mA cm ⁻² , 1.0 mA h cm ⁻²	350 780
2022	<i>n</i> -Butylamine intercalated α -ZrP ⁷¹⁷	2 M ZnSO ₄ /H ₂ O	10 mA cm ⁻² , 1.0 mA h cm ⁻² 6.0 mA cm ⁻² , 1.0 mA h cm ⁻² 6.0 mA cm ⁻² , 3.0 mA h cm ⁻² 10 mA cm ⁻² , 10 mA h cm ⁻²	3000 450 80
2022	MoS ₂ ⁷¹⁸	1 M ZnSO ₄ + 1 M MnSO ₄ /H ₂ O	2.5 mA cm ⁻² , 0.416 mA h cm ⁻²	170
2023	Fe ₆₄ Ni ₃₆ ⁷¹⁹	3 M ZnSO ₄ /H ₂ O	0.5 mA cm ⁻² , 0.5 mA h cm ⁻²	700
2023	Cu ⁷²⁰	2 M ZnSO ₄ /H ₂ O	0.2 mA cm ⁻² , 0.2 mA h cm ⁻² 1.0 mA cm ⁻² , 0.2 mA h cm ⁻²	1200 400
2023	Au ⁷²¹	1 M ZnSO ₄ /H ₂ O	5.0 mA cm ⁻² , 1.0 mA h cm ⁻² 10 mA cm ⁻² , 1.0 mA h cm ⁻² 20 mA cm ⁻² , 1.0 mA h cm ⁻² 50 mA cm ⁻² , 1.0 mA h cm ⁻² 5.0 mA cm ⁻² , 10 mA h cm ⁻² 20 mA cm ⁻² , 10 mA h cm ⁻²	1200 1200 1200 200 500 500
2023	Sn/Cu/reduced graphene oxide ⁷²²	2 M ZnSO ₄ /H ₂ O	0.5 mA cm ⁻² , 1.0 mA h cm ⁻² 2.0 mA cm ⁻² , 1.0 mA h cm ⁻² 10 mA cm ⁻² , 1.0 mA h cm ⁻² 10 mA cm ⁻² , 10 mA h cm ⁻²	3000 3500 1600 250
2023	Si/polyvinylidene fluoride ⁷²³	3 M ZnSO ₄ /H ₂ O	0.25 mA cm ⁻² , 0.05 mA h cm ⁻²	3800
2023	Cu-Zn/polyvinyl butyral ⁷²⁴	2 M ZnSO ₄ /H ₂ O	0.5 mA cm ⁻² , 0.5 mA h cm ⁻²	2750
2023	SnSb/Nafion ⁷²⁵	3 M ZnSO ₄ /H ₂ O	1.0 mA cm ⁻² , 1.0 mA h cm ⁻² 6.0 mA cm ⁻² , 1.0 mA h cm ⁻² 5.0 mA cm ⁻² , 5.0 mA h cm ⁻² 10 mA cm ⁻² , 10 mA h cm ⁻²	1500 650 350 180
2023	SiO ₂ -OH ⁷²⁶	2 M ZnSO ₄ /H ₂ O	1.0 mA cm ⁻² , 1.0 mA h cm ⁻² 10 mA cm ⁻² , 1.0 mA h cm ⁻²	3400 2500
2023	β'' -Al ₂ O ₃ ⁷²⁷	2 M ZnSO ₄ /H ₂ O	1.0 mA cm ⁻² , 1.0 mA h cm ⁻² 2.0 mA cm ⁻² , 1.0 mA h cm ⁻² 4.0 mA cm ⁻² , 1.0 mA h cm ⁻² 10 mA cm ⁻² , 1.0 mA h cm ⁻²	1600 1125 1200 750
2023	HfO _{2-x} ⁷²⁸	2 M ZnSO ₄ /H ₂ O	1.0 mA cm ⁻² , 1.0 mA h cm ⁻²	5000
2023	SrTiO ₃ ⁷²⁹	2 M ZnSO ₄ /H ₂ O	5.0 mA cm ⁻² , 1.0 mA h cm ⁻² 0.5 mA cm ⁻² , 0.5 mA h cm ⁻² 1.0 mA cm ⁻² , 1.0 mA h cm ⁻² 2.0 mA cm ⁻² , 2.0 mA h cm ⁻² 5.0 mA cm ⁻² , 5.0 mA h cm ⁻²	4000 3000 700 400
2023	ZnO ⁷³⁰	2 M ZnSO ₄ /H ₂ O	1.0 mA cm ⁻² , 1.0 mA h cm ⁻² 20 mA cm ⁻² , 10 mA h cm ⁻²	1500 600
2023	ZnP ⁷³¹	2 M ZnSO ₄ /H ₂ O	1.0 mA cm ⁻² , 1.0 mA h cm ⁻² 10 mA cm ⁻² , 5.0 mA h cm ⁻² 20 mA cm ⁻² , 10 mA h cm ⁻²	2000 1260 100
2024	ZnO/carbon fiber ⁷³²	2 M ZnSO ₄ /H ₂ O	0.2 mA cm ⁻² , 0.2 mA h cm ⁻² 1.0 mA cm ⁻² , 1.0 mA h cm ⁻² 5.0 mA cm ⁻² , 2.5 mA h cm ⁻² 20 mA cm ⁻² , 10 mA h cm ⁻² 30 mA cm ⁻² , 15 mA h cm ⁻² 10 mA cm ⁻² , 1.0 mA h cm ⁻²	4000 1000 950 1750 1800 430
2024	Fe-N-porous carbon ⁷³³	2 M ZnSO ₄ /H ₂ O	10 mA cm ⁻² , 1.0 mA h cm ⁻²	1000
2019	UiO-66 ⁷³⁴	3 M ZnSO ₄ + 0.1 M MnSO ₄ /H ₂ O	1.0 mA cm ⁻² , 0.5 mA h cm ⁻² 3.0 mA cm ⁻² , 0.5 mA h cm ⁻²	500 500
2020	ZIF-7 ⁷³⁵	2 M ZnSO ₄ /H ₂ O	0.5 mA cm ⁻² , 0.5 mA h cm ⁻²	3000
2020	Zeolite/Nafion ⁷³⁶	2 M ZnSO ₄ /H ₂ O	1.0 mA cm ⁻² , 0.5 mA h cm ⁻² 2.0 mA cm ⁻² , 0.5 mA h cm ⁻² 5.0 mA cm ⁻² , 0.5 mA h cm ⁻² 1.0 mA cm ⁻² , 10 mA h cm ⁻²	1000 1000 10 000 1000
2020	ZIF-8 ⁷³⁷	2 M ZnSO ₄ /H ₂ O	2.0 mA cm ⁻² , 1.0 mA h cm ⁻² 2.0 mA cm ⁻² , 2.0 mA h cm ⁻²	1300 700
2021	ZIF-8 ⁷³⁸	2 M ZnSO ₄ /H ₂ O	0.5 mA cm ⁻² , 0.5 mA h cm ⁻² 2.0 mA cm ⁻² , 1.0 mA h cm ⁻² 10 mA cm ⁻² , 1.0 mA h cm ⁻²	2000 320 5000



Table 14 (continued)

Year	Materials	Electrolytes	Cycle conditions	Cycle life (h)
2021	Zn(benzene tricarboxylate) ₃ ⁷³⁹	2 M ZnSO ₄ /H ₂ O	1.0 mA cm ⁻² , 1.0 mA h cm ⁻² 3.0 mA cm ⁻² , 0.5 mA h cm ⁻² 4.0 mA cm ⁻² , 1.0 mA h cm ⁻²	800 400 400
2021	Covalent organic framework ⁷⁴⁰	2 M ZnSO ₄ /H ₂ O	1.0 mA cm ⁻² , 1.0 mA h cm ⁻² 2.0 mA cm ⁻² , 1.0 mA h cm ⁻²	420 260
2021	Fluorinated covalent organic framework ⁷⁴¹	2 M ZnSO ₄ /H ₂ O	5.0 mA cm ⁻² , 1.0 mA h cm ⁻² 40 mA cm ⁻² , 1.0 mA h cm ⁻²	1700 750
2021	Montmorillonite ⁷⁴²	2 M ZnSO ₄ /H ₂ O	1.0 mA cm ⁻² , 0.25 mA h cm ⁻² 10 mA cm ⁻² , 45 mA h cm ⁻²	1000 1000
2021	Zn-montmorillonite ⁷⁴³	2 M ZnSO ₄ /H ₂ O	1.0 mA cm ⁻² , 0.5 mA h cm ⁻² 2.0 mA cm ⁻² , 0.5 mA h cm ⁻² 2.0 mA cm ⁻² , 1.0 mA h cm ⁻²	900 700 700
2022	ZIF-8 ⁷⁴⁴	2 M ZnSO ₄ /H ₂ O	0.5 mA cm ⁻² , 0.2 mA h cm ⁻²	680
2022	ZIF-8/graphene oxide ⁷⁴⁵	2 M ZnSO ₄ /H ₂ O	0.5 mA cm ⁻² , 0.5 mA h cm ⁻² 10 mA cm ⁻² , 0.5 mA h cm ⁻²	2200 2400
2022	MCM-41 mesoporous molecular sieves ⁷⁴⁶	3 M ZnSO ₄ /H ₂ O	1.0 mA cm ⁻² , 1.0 mA h cm ⁻² 2.0 mA cm ⁻² , 2.0 mA h cm ⁻² 5.0 mA cm ⁻² , 1.0 mA h cm ⁻²	1800 1500 2200
2022	Covalent organic framework (TpPa-SO ₃ H) ⁷⁴⁷	1 M ZnSO ₄ /H ₂ O	1.0 mA cm ⁻² , 5.0 mA h cm ⁻²	1000
2023	Sn-MCM-41/polyvinylidene fluoride ⁷⁴⁸	2 M ZnSO ₄ /H ₂ O	5.0 mA cm ⁻² , 5.0 mA h cm ⁻² 0.4 mA cm ⁻² , 0.2 mA h cm ⁻²	1000 1400
2023	UiO-66-(COOH) ₂ ⁷⁴⁹	2 M ZnSO ₄ /H ₂ O	2.0 mA cm ⁻² , 2.0 mA h cm ⁻² 5.0 mA cm ⁻² , 5.0 mA h cm ⁻²	2800 800
2023	ZIF-8 ⁷⁵⁰	2 M ZnSO ₄ /H ₂ O	10 mA cm ⁻² , 10 mA h cm ⁻² 1.0 mA cm ⁻² , 1.0 mA h cm ⁻² 5.0 mA cm ⁻² , 5.0 mA h cm ⁻²	400 1100 600
2023	UiO-66-(COOH) ₂ ⁷⁵¹	2 M ZnSO ₄ /H ₂ O	1.0 mA cm ⁻² , 1.0 mA h cm ⁻² 5.0 mA cm ⁻² , 5.0 mA h cm ⁻²	2700 1600
2019	Polyamide ⁷⁵²	2 M ZnSO ₄ /H ₂ O	0.5 mA cm ⁻² , 0.25 mA h cm ⁻²	8000
2020	Polyppyrrole ⁷⁵³	2 M ZnSO ₄ /H ₂ O	2.0 mA cm ⁻² , 1.0 mA h cm ⁻²	540
2020	Polyvinyl butyral ⁴⁴⁴	1 M ZnSO ₄ /H ₂ O	0.5 mA cm ⁻² , 0.5 mA h cm ⁻²	2200
2020	Polyacrylamide/polyvinylpyrrolidone ⁷⁵⁴	3 M Zn(OTf) ₂ /H ₂ O	0.2 mA cm ⁻² , 0.1 mA h cm ⁻²	2200
2021	(3-Aminopropyl)triethoxysilane ⁷⁵⁵	2 M ZnSO ₄ /H ₂ O	2.0 mA cm ⁻² , 0.5 mA h cm ⁻² 20 mA cm ⁻² , 5.0 mA h cm ⁻²	3500 600
2021	Lignin ⁷⁵⁶	2 M ZnSO ₄ /H ₂ O	2.0 mA cm ⁻² , 2.0 mA h cm ⁻² 5.0 mA cm ⁻² , 2.0 mA h cm ⁻²	650 400
2021	β -Polyvinylidene difluoride ⁷⁵⁷	2 M ZnSO ₄ /H ₂ O	0.25 mA cm ⁻² , 0.05 mA h cm ⁻² 1.5 mA cm ⁻² , 0.3 mA h cm ⁻² 0.25 mA cm ⁻² , 0.5 mA h cm ⁻²	2000 100 100
2021	Poly(vinylidene fluoride-trifluoroethylene) ⁷⁵⁸	2 M ZnSO ₄ /H ₂ O	0.2 mA cm ⁻² , 0.2 mA h cm ⁻²	2000
2021	Polyacrylonitrile ⁷⁵⁹	2 M Zn(OTf) ₂ /H ₂ O	1.0 mA cm ⁻² , 1.0 mA h cm ⁻²	1100
2021	Poly(2,5-dihydroxy-1,4-benzoquinonyl sulfide) ⁷⁶⁰	2 M ZnSO ₄ /H ₂ O	1.0 mA cm ⁻² , 1.0 mA h cm ⁻²	100
2021	Cross-linked polymer (self-healable ion regulator) ⁷⁶¹	2 M ZnSO ₄ /H ₂ O	2.0 mA cm ⁻² , 2.0 mA h cm ⁻² 5.0 mA cm ⁻² , 20 mA h cm ⁻² 10 mA cm ⁻² , 10 mA h cm ⁻²	3500 950 2000
2021	Cross-linked gelatin ⁶⁰³	1 M Zn(OTf) ₂ /H ₂ O	1.0 mA cm ⁻² , 1.0 mA h cm ⁻²	4000
2021	Bacterial cellulose ⁷⁶²	2 M ZnSO ₄ /H ₂ O	0.5 mA cm ⁻² , 0.25 mA h cm ⁻² 5.0 mA cm ⁻² , 2.5 mA h cm ⁻² 5.0 mA cm ⁻² , 5.0 mA h cm ⁻²	3000 570 300
2022	Alginate – thermoplastic polyurethane ⁷⁶³	2 M ZnSO ₄ /H ₂ O	5.0 mA cm ⁻² , 5.0 mA h cm ⁻² 10 mA cm ⁻² , 10 mA h cm ⁻²	1200 500
2022	Zinc alginate gel ⁷⁶⁴	2 M ZnSO ₄ /H ₂ O	1.0 mA cm ⁻² , 1.0 mA h cm ⁻²	500
2022	Polyvinyl alcohol ⁶⁰⁷	2 M Zn(OTf) ₂ /H ₂ O	0.25 mA cm ⁻² , 0.25 mA h cm ⁻² 1.0 mA cm ⁻² , 1.0 mA h cm ⁻² 0.25 mA cm ⁻² , 0.25 mA h cm ⁻²	5000 2200 2200
2023	Polyvinylidene difluoride ⁷⁶⁵	3 M ZnSO ₄ /H ₂ O	1.0 mA cm ⁻² , 1.0 mA h cm ⁻² 5.0 mA cm ⁻² , 5.0 mA h cm ⁻²	5000 970
2023	Chitosan/sodium alginate ⁷⁶⁶	2 M ZnSO ₄ /H ₂ O	10 mA cm ⁻² , 10 mA h cm ⁻² 1.0 mA cm ⁻² , 1.0 mA h cm ⁻² 5.0 mA cm ⁻² , 2.5 mA h cm ⁻²	350 6700 1750
2023	Proteins (silk fibroin/lysozyme) ⁷⁶⁷	2 M ZnSO ₄ /H ₂ O	10 mA cm ⁻² , 10 mA h cm ⁻² 1.0 mA cm ⁻² , 1.0 mA h cm ⁻² 5.0 mA cm ⁻² , 5.0 mA h cm ⁻²	250 7000 2000
2023	Carboxymethyl cellulose ⁷⁶⁸	1.5 M ZnSO ₄ /H ₂ O	10 mA cm ⁻² , 10 mA h cm ⁻² 1.0 mA cm ⁻² , 0.1 mA h cm ⁻²	1100 200



Table 14 (continued)

Year	Materials	Electrolytes	Cycle conditions	Cycle life (h)
2023	Poly(vinylidene fluoride-hexafluoro propylene) codoped with poly(ethylene oxide)/Zn-montmorillonite ⁶⁰⁸	2 M Zn(OTf) ₂ /H ₂ O	0.25 mA cm ⁻² , 0.25 mA h cm ⁻² 1.0 mA cm ⁻² , 1.0 mA h cm ⁻² 5.0 mA cm ⁻² , 1.0 mA h cm ⁻²	6000 3250 2000
2023	Polyglycidyl methacrylate/polyethylene glycol diamine/polyvinylidene fluoride ⁷⁶⁹	2 M ZnSO ₄ + 0.1 M MnSO ₄ /H ₂ O	0.5 mA cm ⁻² , 0.5 mA h cm ⁻² 1.0 mA cm ⁻² , 1.0 mA h cm ⁻² 5.0 mA cm ⁻² , 2.5 mA h cm ⁻²	2370 1280 160
2023	Polyvinyl-phosphonic acrylamide/Zn ⁷⁷⁰	2 M ZnSO ₄ /H ₂ O	0.5 mA cm ⁻² , 0.25 mA h cm ⁻² 5.0 mA cm ⁻² , 2.5 mA h cm ⁻²	6000 1092
2023	Cellulose/Al(OH) ₃ /polytetrafluoroethylene ⁶¹²	3 M Zn(OTf) ₂ /H ₂ O	1.0 mA cm ⁻² , 0.16 mA h cm ⁻² 2.5 mA cm ⁻² , 0.5 mA h cm ⁻²	1000 260
2023	Polymerized 2-methacryloyloxyethyl phosphorylcholine/carboxymethyl chitosan ⁷⁷¹	2 M ZnSO ₄ /H ₂ O	40 mA cm ⁻² , 1.0 mA h cm ⁻² 40 mA cm ⁻² , 10 mA h cm ⁻²	1000 325
2023	1,3,5,9-Tetrathiophenylpyrene ⁷⁷²	2 M ZnSO ₄ /H ₂ O	0.885 mA cm ⁻² , 0.885 mA h cm ⁻²	1000
2019	Ti ₃ C ₂ T _x ⁷⁷³	2 M ZnSO ₄ /H ₂ O	1.0 mA cm ⁻² , 1.0 mA h cm ⁻² 2.0 mA cm ⁻² , 4.0 mA h cm ⁻²	300 180
2020	Hydrogen-substituted graphdiyne ⁷⁷⁴	2 M ZnSO ₄ /H ₂ O	0.5 mA cm ⁻² , 0.1 mA h cm ⁻² 1.0 mA cm ⁻² , 0.1 mA h cm ⁻² 2.0 mA cm ⁻² , 0.1 mA h cm ⁻²	2400 2400 2400
2021	Ti ₃ C ₂ T _x /Sb ⁷⁷⁵	2 M ZnSO ₄ /H ₂ O	0.5 mA cm ⁻² , 0.5 mA h cm ⁻² 2.0 mA cm ⁻² , 2.0 mA h cm ⁻² 5.0 mA cm ⁻² , 5.0 mA h cm ⁻²	1000 550 550
2021	Ti ₃ C ₂ T _x /ZnS ⁷⁷⁶	2 M ZnSO ₄ /H ₂ O	0.5 mA cm ⁻² , 0.5 mA h cm ⁻² 1.0 mA cm ⁻² , 0.5 mA h cm ⁻² 1.0 mA cm ⁻² , 1.0 mA h cm ⁻² 5.0 mA cm ⁻² , 5.0 mA h cm ⁻² 10 mA cm ⁻² , 1.0 mA h cm ⁻²	4600 1100 1100 400 180
2021	Graphitic carbon nitride (g-C ₃ N ₄) ⁷⁷⁷	2 M ZnSO ₄ /H ₂ O	2.0 mA cm ⁻² , 2.0 mA h cm ⁻² 10 mA cm ⁻² , 5.0 mA h cm ⁻²	500 120
2021	Sulfonate group-modified boron nitride ⁷⁷⁸	2 M ZnSO ₄ /H ₂ O	2.0 mA cm ⁻² , 2.0 mA h cm ⁻² 5.0 mA cm ⁻² , 2.5 mA h cm ⁻² 10 mA cm ⁻² , 10 mA h cm ⁻²	2500 1000 350
2022	N/Se-Ti ₃ C ₂ T _x /ZnSe ⁷⁷⁹	2 M ZnSO ₄ /H ₂ O	1.0 mA cm ⁻² , 1.0 mA h cm ⁻² 2.0 mA cm ⁻² , 1.0 mA h cm ⁻² 5.0 mA cm ⁻² , 5.0 mA h cm ⁻² 10 mA cm ⁻² , 10 mA h cm ⁻²	2500 1500 700 800
2022	Ti ₃ C ₂ T _x /chitosan ⁷⁸⁰	2 M ZnSO ₄ /H ₂ O	0.5 mA cm ⁻² , 0.5 mA h cm ⁻² 1.0 mA cm ⁻² , 1.0 mA h cm ⁻² 5.0 mA cm ⁻² , 1.0 mA h cm ⁻² 0.2 mA cm ⁻² , 0.2 mA h cm ⁻²	1350 2100 270 2500
2022	Ti ₃ C ₂ T _x /polypyrrole ⁷⁸¹	2 M ZnSO ₄ /H ₂ O	1.0 mA cm ⁻² , 1.0 mA h cm ⁻²	1050
2022	Ti ₃ C ₂ T _x /reduced graphene oxide ⁷⁸²	2 M ZnSO ₄ /H ₂ O	10 mA cm ⁻² , 1.0 mA h cm ⁻²	1000
2022	Boron nitride ⁷⁸³	2 M ZnSO ₄ /H ₂ O	1.0 mA cm ⁻² , 1.0 mA h cm ⁻² 5.0 mA cm ⁻² , 2.5 mA h cm ⁻² 1.0 mA cm ⁻² , 1.0 mA h cm ⁻² (-10 °C)	3000 1600 300
2022	Boron nitride ⁷⁸⁴	2 M ZnSO ₄ /H ₂ O	1.0 mA cm ⁻² , 0.5 mA h cm ⁻² 2.0 mA cm ⁻² , 2.0 mA h cm ⁻² 5.0 mA cm ⁻² , 2.0 mA h cm ⁻² 10 mA cm ⁻² , 2.0 mA h cm ⁻² 0.1 mA cm ⁻² , 1.0 mA h cm ⁻²	1600 500 600 600 600
2023	Graphdiyne ⁷⁸⁵	2 M ZnSO ₄ /H ₂ O	2.0 mA cm ⁻² , 1.0 mA h cm ⁻² 5.0 mA cm ⁻² , 2.5 mA h cm ⁻² 8.0 mA cm ⁻² , 4.0 mA h cm ⁻²	1400 850 450
2022	Phytic acid ⁷⁸⁶	2 M ZnSO ₄ /H ₂ O	0.5 mA cm ⁻² , 0.25 mA h cm ⁻² 5.0 mA cm ⁻² , 2.5 mA h cm ⁻²	2000 1800
2022	Phytic acid ⁷⁸⁷	2 M ZnSO ₄ /H ₂ O	5.0 mA cm ⁻² , 1.0 mA h cm ⁻² 10 mA cm ⁻² , 1.0 mA h cm ⁻²	2400 1100
2022	Phosphoric acid ⁷⁸⁸	1 M ZnSO ₄ /H ₂ O	2.0 mA cm ⁻² , 1.0 mA h cm ⁻² 10 mA cm ⁻² , 1.0 mA h cm ⁻² 20 mA cm ⁻² , 1.0 mA h cm ⁻²	780 1100 1800
2023	Polyphosphoric acid ⁷⁸⁹	2 M ZnSO ₄ /H ₂ O	2.0 mA cm ⁻² , 1.0 mA h cm ⁻² 10 mA cm ⁻² , 1.0 mA h cm ⁻² 10 mA cm ⁻² , 5.0 mA h cm ⁻²	6500 800 300



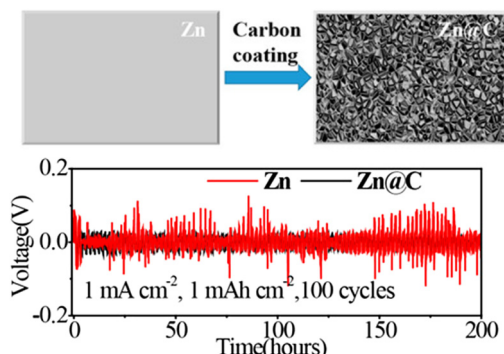


Fig. 58 Prevention of Zn dendrite formation by carbon coating.⁶⁵¹ Reprinted with permission from *ACS Applied Materials & Interfaces*.

is a marked improvement over the significant voltage hysteresis observed in a bare Zn-based cell after only 26 h.

Metal-organic frameworks (MOFs) offer a higher specific surface area than activated carbons or zeolites and feature a porous coordination network structure created through interactions between metal ions or cluster nodes and organic ligands. In 2019, Pan *et al.* demonstrated that UiO-66, a type of metal-organic framework, enhances electrolyte wetting capabilities owing to its high surface area. This characteristic contributes to stable and uniform Zn plating and stripping.⁷³⁴ This enabled stable Zn plating and stripping for over 500 h in a symmetric cell

test using a 3 M ZnSO₄ + 0.1 M MnSO₄/H₂O electrolyte at a constant current of 1.0 mA cm⁻² or 3.0 mA cm⁻² and an areal capacity of 0.5 mA h cm⁻². The following year, Zhou's group employed Raman spectroscopy to demonstrate that electrolytes became highly concentrated within the channels of MOFs.⁷³⁵ The small pores and channels in these frameworks posed challenges for inserting large solvated-ion complexes, leading to a solution structure dominated by ion pairs and reducing the presence of free water molecules. This distinct environment enabled smooth Zn plating and stripping while minimizing side reactions (Fig. 61).

In 2021, Park *et al.* developed covalent organic frameworks (COFs)-coated Zn-metal anodes, enabling stable Zn plating and stripping over 400 h with suppressed side reactions (Fig. 62).⁷⁴⁰ Later that year, Zhao *et al.* demonstrated that introducing fluorinated COFs significantly enhanced the stability of Zn metal and the electrolyte.⁷⁴¹ The strong interactions between electronegative fluorine atoms in these frameworks and zinc atoms in the Zn-metal anode directed the plating orientation to produce a densely packed Zn deposit, which helped suppress dendrite growth. As a result, they achieved stable cycling performance over 1700 h at 5.0 mA cm⁻² and 1.0 mA h cm⁻² in a 2 M ZnSO₄/H₂O electrolyte (Fig. 62).

In the field of Zn electroplating, brighteners, also known as levelers, are commonly used to enhance the surface gloss by increasing the Zn nucleation overpotential through strong

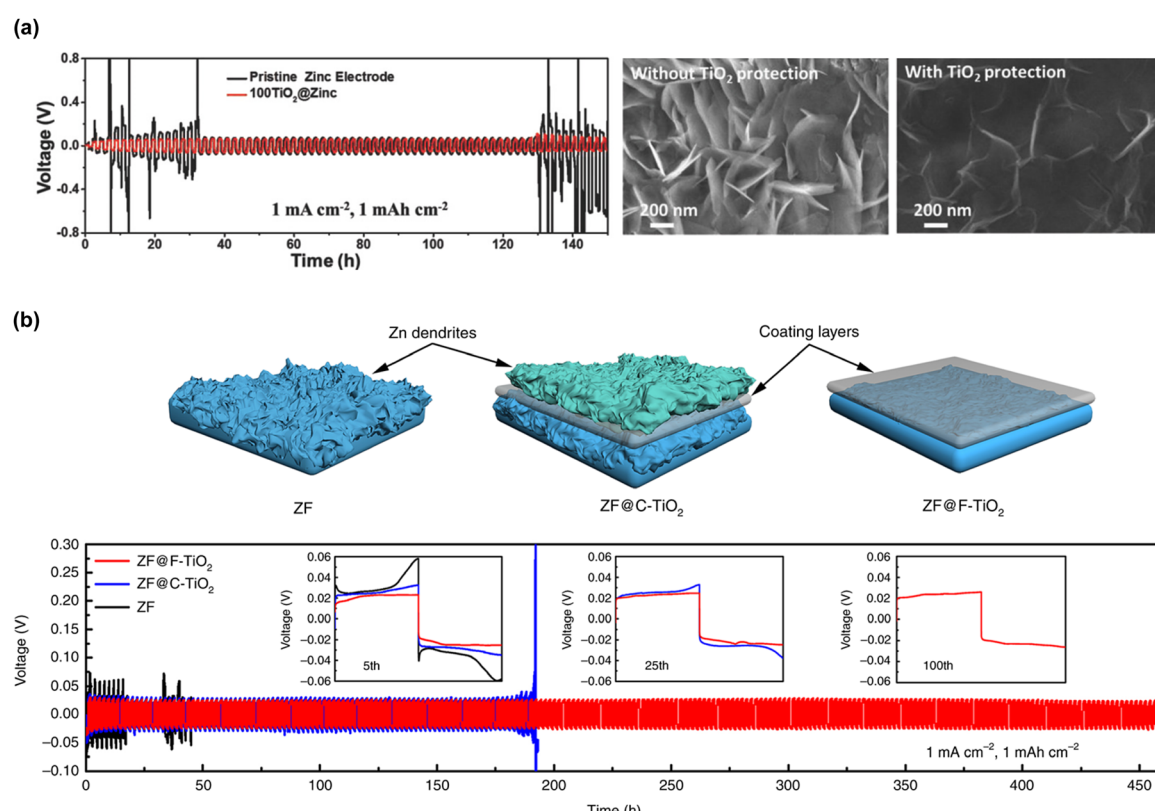


Fig. 59 (a) Performance of Zn|Zn symmetric cells with and without an 8 nm-thick TiO₂ coating on Zn metal.⁶¹¹ (b) Schematic of Zn plating and Zn|Zn symmetric cell results under different coating conditions. ZF, C-TiO₂, and F-TiO₂ correspond to Zn foil, commercial TiO₂, and highly (001) facet-exposed TiO₂, respectively.⁶⁷¹ Reprinted with permission from *Advanced Materials Interfaces* (a) and *Nature Communications* (b).



coordination with Zn^{2+} in the electrolyte, thereby promoting the growth of finer Zn nuclei. In 2019, Zhao and co-workers applied this principle to prevent dendrite formation in aqueous Zn-metal batteries (Fig. 63).⁷⁵² They engineered a polymeric interphase composed of polyamide and $Zn(OTf)_2$, which increased the nucleation overpotential during Zn plating. This polyamide-coated Zn metal contributed to long-term cycling stability, enduring over 8000 h in a symmetric cell test conducted in a 2 M $ZnSO_4/H_2O$ electrolyte at 0.5 $mA\ cm^{-2}$ and 0.25 $mA\ h\ cm^{-2}$. In 2020, Hao *et al.* developed a thin polyvinyl butyral coating on Zn metal using spin-coating techniques.⁴⁴⁴ The polyvinyl butyral served as an effective *ex situ* artificial SEI with distinct properties; it functioned as an electronic insulator with an electrical resistivity of $2.4 \times 10^5\ \Omega\ cm$. Its abundant oxygen functional groups ensured strong adhesion to the Zn metal and facilitated Zn^{2+} transport, while its high hydrophilicity improved the electrolyte wettability. As a result, the polyvinyl butyral-coated Zn metal displayed stable performance for over 2200 h in a symmetric cell that was tested at 0.5 $mA\ cm^{-2}$ and 0.5 $mA\ h\ cm^{-2}$ in a 1 M $ZnSO_4/H_2O$ electrolyte.

Research on two-dimensional materials, mainly focusing on $Ti_3C_2T_x$ MXene, graphdiyne, graphitic carbon nitride ($g\text{-}C_3N_4$), and boron nitride, has been conducted because of their remarkable flexibility, mechanical strength, chemical stability, and electrolyte wettability. For instance, in 2022, Qiu *et al.* applied sulfonate group-modified boron nitride nanosheets to Zn metal, achieving a substantial reduction in the Zn nucleation overpotential (26 mV at a current density of 1 $mA\ cm^{-2}$) and solvation/desolvation activation energy (57.2 $kJ\ mol^{-1}$), compared to those on bare Zn, for which the corresponding values were 112 mV and 76.9 $kJ\ mol^{-1}$, respectively (Fig. 64).⁷⁷⁸ The symmetrical cell utilizing this sulfonate group-modified boron nitride-coated Zn metal exhibited a prolonged cycling life, enduring up to 2500 h at 2.0 $mA\ cm^{-2}$ and 2.0 $mA\ h\ cm^{-2}$, 1000 h at 5.0 $mA\ cm^{-2}$ and 2.5 $mA\ h\ cm^{-2}$, and 350 h at 10 $mA\ cm^{-2}$ and 10 $mA\ h\ cm^{-2}$.

Recent studies have focused on simplifying the formation process of artificial SEIs by immersing Zn metal in acidic solutions like phytic acid and phosphoric acid. For example, Zn metal dipped in a 2 mM phytic acid solution for 1 min under ambient conditions forms a phytic acid–Zn complex layer with a lamellar structure due to the strong chelating action of the rich phosphate/carboxyl groups in phytic acid (Fig. 65).⁷⁸⁶ The anti-corrosion effectiveness of this layer was evident, as demonstrated by its substantially lower charge-transfer resistance compared to that of the untreated bulk Zn metal after resting for two days in a 2 M $ZnSO_4/H_2O$ electrolyte. In symmetric cell tests, the phytic acid-treated Zn metal exhibited high cycling stability, lasting for 1400, 850, and 450 h at 2.0 $mA\ cm^{-2}/1.0\ mA\ h\ cm^{-2}$, 5.0 $mA\ cm^{-2}/2.5\ mA\ h\ cm^{-2}$, and 8.0 $mA\ cm^{-2}/4.0\ mA\ h\ cm^{-2}$, respectively.

However, there is insufficient evidence to confirm that the materials commonly used in artificial SEIs and scaffolds provide adequate Zn^{2+} conductivity. Additionally, the electrolyte/electrode conditions that promote the growth of finer Zn nuclei with high Zn nucleation overpotentials may also increase the Zn growth overpotentials, thereby accelerating electrolyte reduction, generating hydrogen gas bubbles, and ultimately hindering uniform Zn

plating. Therefore, performance enhancement by modifying the nucleation overpotentials might only be effective under specific conditions where the operating potential window of the electrolyte and the battery operating parameters, such as the current density and temperature, are optimally aligned. Ideally, a protective film on Zn metal should simultaneously maintain substantially high HER overpotentials and low Zn plating/stripping overpotentials. However, the rapid ion conductivity of protons over Zn^{2+} , especially in acidic solutions, coupled with the facilitated Volmer step of the HER due to the strong Lewis acidity of Zn^{2+} , make the implementation of this strategy challenging.

Most importantly, the performance of aqueous Zn-metal batteries has rarely been evaluated practically. To increase the battery energy density, limiting the amounts of Zn metal and electrolyte is essential. Under these conditions, long-term cycling performance with sufficiently high Coulombic efficiency should be guaranteed. However, most studies on aqueous Zn-metal batteries, including those utilizing electrolyte modification and artificial SEIs/scaffolds, have overlooked this aspect.

The required metal thickness (T_M , in μm) to obtain a capacity of 1 $mA\ cm^{-2}$ can be estimated using the following equation:

$$\text{Required metal thickness } (T_M) = \frac{M_W \times 10\,000}{n \times F \times \rho} \quad (20)$$

Here, M_W , n , F , and ρ represent the molecular weight of the metal ($g\ mol^{-1}$), the number of electrons transferred (–), the Faraday constant ($96\,485\ C\ mol^{-1}$) which can be converted to $26\,801\ mA\ h\ mol^{-1}$, and the density of the metal ($g\ cm^{-3}$). Based on eqn (20), the thickness required to achieve 1 $mA\ h\ cm^{-2}$ for Zn metal is calculated to be 1.71 μm , with $M_W = 65.38\ g\ mol^{-1}$, $n = 2$, and $\rho = 7.14\ g\ cm^{-3}$. This thickness is lesser than that required for Li metal, which is 4.85–6.8 μm (with $M_W = 6.94\ g\ mol^{-1}$, $n = 1$, and $\rho = 0.53\ g\ cm^{-3}$).

To increase the energy density, batteries must be assembled with thin metal anodes; however, this configuration can limit the supply of carrier ion resources and potentially degrade the long-term cycling performance. This underscores the need to maintain a proper balance among metal thickness, battery energy density, and overall battery performance. For nonaqueous Li-metal batteries, extensive research is underway to apply limited amounts of Li metal. This involves using Li^+ resources, ranging from none ($\times 0$ excess; anode-free setup) to an amount equal to that provided by the cathode active materials ($\times 1$ excess). For instance, with a layered oxide $LiNi_{0.8}Mn_{0.1}Co_{0.1}O_2$ cathode active material having a specific capacity of $200\ mA\ h\ g^{-1}$ and a cathode loading of $20\ mg\ cm^{-2}$, thereby yielding a capacity of $4\ mA\ h\ cm^{-2}$, the Li metal should be 19.4 μm thick (a capacity of $4\ mA\ h\ cm^{-2}$ from Li metal) to be able to supply the same amount ($\times 1$ excess) of Li^+ resources provided from the cathode (Fig. 66).

The same standards can also be used for aqueous Zn-metal batteries, although most cathode active materials for aqueous Zn-metal batteries do not include Zn^{2+} carrier ion resources, unlike those for nonaqueous Li-metal batteries. Furthermore, as discussed in Section 7.1, the capacity of cathode active materials for aqueous Zn-metal batteries is primarily derived from the co-intercalation of proton and/or water, not pure



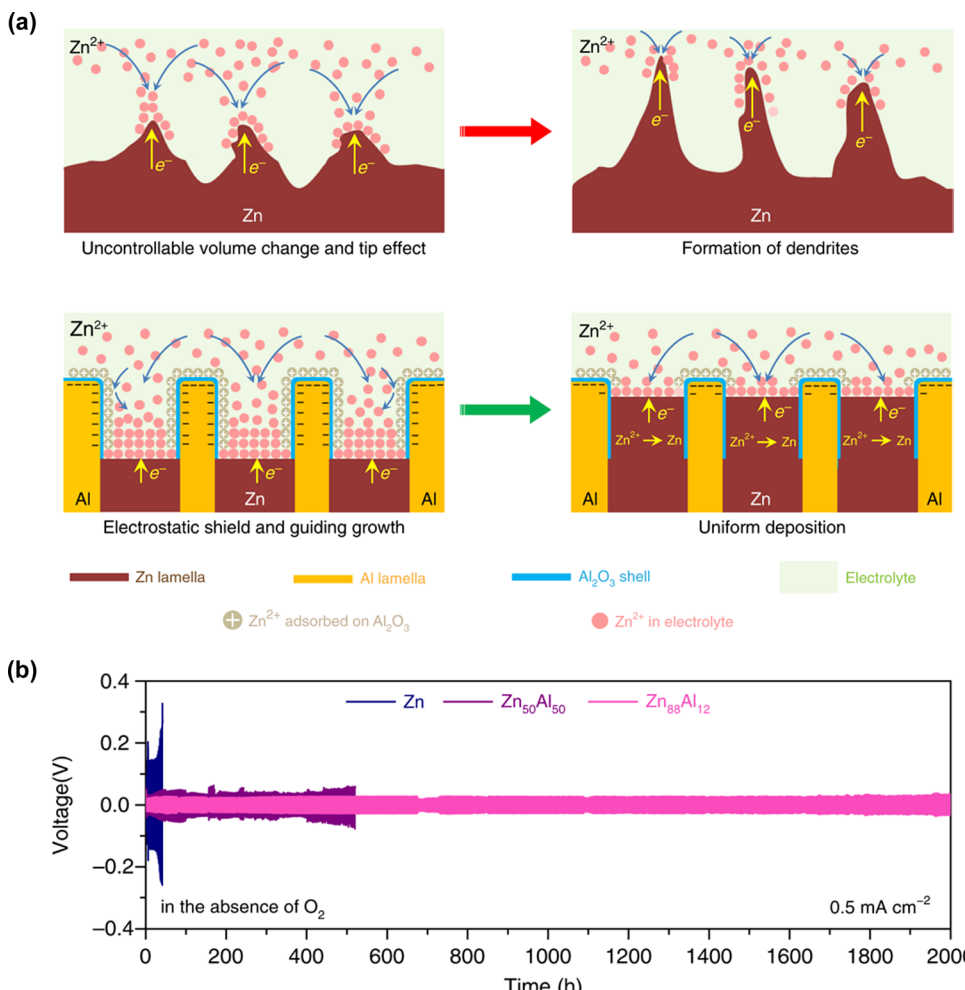


Fig. 60 (a) Schematic of suppressed Zn dendrite growth on lamella-nanostructured eutectic Zn₈₈Al₁₂ alloys. (b) Long-term cycling of symmetric batteries in an O₂-free aqueous ZnSO₄ solution.⁶⁷² Reprinted with permission from *Nature Communications*.

(desolvated) Zn²⁺ intercalation. If the electrode comprises 20 mg cm⁻² of a cathode active material that does not offer Zn²⁺ carrier ion resources initially and provides a capacity of 2 mA h cm⁻² with pure (desolvated) Zn²⁺ intercalation, a 6.84 μ m-thick Zn metal (a capacity of 4 mA h cm⁻² from Zn metal) would be required to fabricate $\times 1$ excess Zn-metal batteries (Fig. 66).

Additionally, assuming the use of a 12 mm-diameter electrode (1.13 cm²) in coin-cell fabrication for symmetric or asymmetric Zn-metal stability tests and considering an aqueous Zn electrolyte density of 1 mg mL⁻¹, the amount of electrolyte required under commercial standards (2–3 mg mA h⁻¹ in Li-ion and Li-metal batteries) with 2 mA h cm⁻² cathodes would be approximately 4.5 μ L.

However, many studies used substantially thicker Zn metal and larger amounts of electrolyte. For instance, data from approximately 90 papers referenced in Table 14 (excluding those where values are not mentioned) show an average Zn metal thickness of 120 μ m, with minimum and maximum values of 10 and 1000 μ m, respectively. The exact amount of electrolyte used is often unspecified; however, most aqueous batteries employed thick glass fiber separators that require at

least 30–100 μ L of the electrolyte to ensure complete saturation. These findings reveal that the Zn metal thickness and electrolyte volume used in an academic scenario significantly deviate from those used in commercial standards.

Additionally, side reactions between the electrolyte and Zn metal involve the formation of complexes such as Zn_x(OH)_y(anion)_z·nH₂O and the evolution of hydrogen gas (HER), which are highly dependent on the Arrhenius equation (eqn (16)). The overpotentials for HER are typically higher than those for Zn plating on the Zn-metal surface (details in Section 7.7). The high dielectric constant of water in aqueous Zn electrolytes ensures rapid ion conductivity even at low temperatures—a stark contrast to nonaqueous electrolytes used in conventional Li-ion batteries, which face conductivity issues at low temperatures (details in Section 7.7). These distinct properties, which help stabilize Zn metal and the electrolyte, thereby improving Coulombic efficiency with suppressed side reactions at low temperatures, can be disrupted by *ex situ* coating.⁷⁹⁰ On the other hand, at higher temperatures, Zn metal and electrolyte consumption increase due to accelerated side reactions, which can compromise the performance and lifespan of the

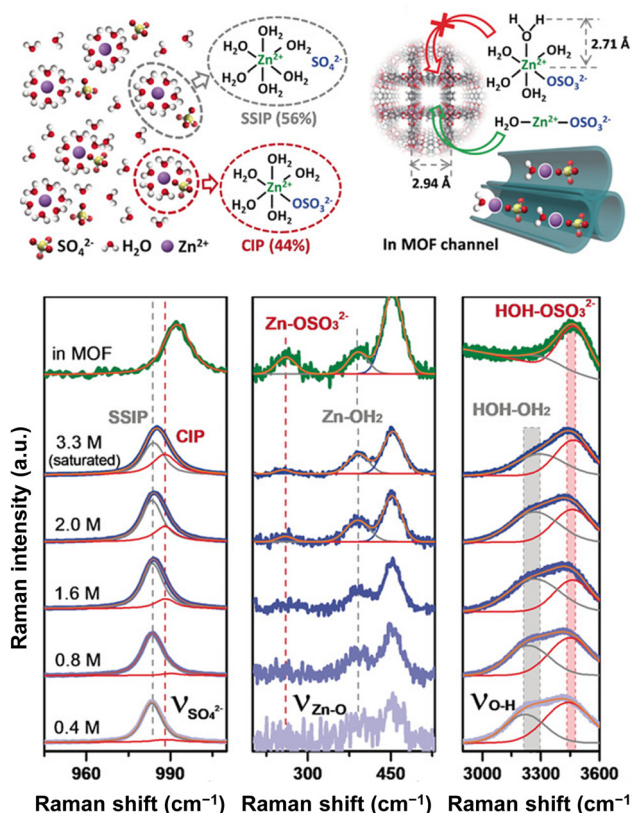


Fig. 61 Construction of a super-saturated ZnSO_4 electrolyte in metal-organic-framework channels, demonstrated by Raman spectroscopy.⁷³⁵ Reprinted with permission from *Angewandte Chemie International Edition*.

battery. However, most studies on *ex situ* artificial SEIs and scaffolds have been conducted at room temperature.

Importantly, under the required strict conditions, small and medium-scale devices like mobile phones and electric vehicles must ensure a minimum of 1000 cycles, while large-scale devices, including energy storage systems, are expected to last for at least 100 000 cycles under a relatively low current of ≤ 0.1 C. These discrepancies highlight the substantial challenges faced by aqueous Zn-metal batteries in meeting practical standards.

7.6. Non-standardized methods for estimating Coulombic efficiency

In all strategies, accurate measurement of the Coulombic efficiency is the first step for enhancing battery stability. In 2020, the research team at the US Army Research Laboratory underscored that studies on rechargeable Zn-metal batteries have employed different testing methods and conditions, rendering direct comparisons of their performance a complex process.^{791,792} Two electrochemical techniques are commonly used to measure the Coulombic efficiency of Zn plating and stripping reactions: the potentiostatic method (using cyclic voltammetry, which sweeps the potential at a constant rate) and galvanostatic cycling (which involves applying a constant current until specific cut-off conditions, such as voltage, capacity, or time, are achieved). Fig. 67 illustrates the normalized

cyclic voltammetry curves from previous papers, revealing unrealistic potential ranges for Zn plating and stripping.⁷⁹² These include an extremely low plating potential beyond -0.5 V vs. Zn/Zn^{2+} and a high cut-off stripping potential beyond the operating potentials of common Zn cathodes. The Zn-metal anode is maintained near the Zn/Zn^{2+} potential in real battery applications, and the Zn stripping potential is constrained by the full-cell discharge cut-off voltage, typically ≤ 1.5 V. Furthermore, cyclic voltammetry does not control important battery operation parameters such as the current density and areal capacity.

Compared to cyclic voltammetry, galvanostatic cycling, which closely replicates real battery operation, is more suitable for accurately measuring the Coulombic efficiency during Zn plating and stripping. However, considerable variability still exists in the galvanostatic test parameters and setups reported in the literature, and this has already been highlighted in previous papers on Li-metal batteries. In 2017, Adams *et al.* introduced an overview of the galvanostatic cycling conditions and illustrated how variations in these methods could lead to differences in the experimental results.⁷⁹³ The representative methods are described below.

Method 1. Since the 1970s (or even earlier), a cell comprising a Li|inert substrate (*e.g.*, such as Cu, Ni) has often been utilized to measure the Coulombic efficiency during the metal plating and stripping in nonaqueous electrolytes (Fig. 68).⁷⁹⁴ The inert substrate represents a substrate that has no excess metal. Thus, the average Coulombic efficiency from Method 1 is determined using the following equation:

$$(\text{Method 1}) \text{ Average coulombic efficiency} = \frac{1}{n} \sum \frac{Q_{\text{stripping}}}{Q_{\text{plating}}} \quad (21)$$

Here, n , is the number of cycles, and Q_{plating} and $Q_{\text{stripping}}$ correspond to the amount of charge passed during the plating and stripping processes, respectively. This method provides valuable insights into the development and study of anode-free rechargeable batteries.

Method 2. In 1990, Aurbach *et al.* introduced a protocol for measuring the Coulombic efficiency. The method involved the electrochemical plating of a certain amount of metal onto inert substrates, followed by periodic stripping and re-plating with 15–60% of the deposited metal in a systematic manner (Fig. 68).⁷⁹⁵ This method helps to reduce uncertainties related to the interactions among the substrate surface, electrolyte, and plated metal during initial plating and stripping processes (*e.g.* the reaction of surface oxides on Cu foil with Li to form Cu and Li_2O), thus allowing for a more accurate assessment of the Coulombic efficiency during the plating and stripping processes. The average Coulombic efficiency from Method 2 can be derived as follows (eqn (22)):

$$(\text{Method 2}) \text{ Average coulombic efficiency} \quad (22)$$

$$= \frac{nQ_{\text{stripping/re-plating}} + Q_{\text{final stripping}}}{nQ_{\text{stripping/re-plating}} + Q_{\text{pre-plating}}} \quad (22)$$

Here, $nQ_{\text{stripping/re-plating}}$, $Q_{\text{pre-plating}}$, and $nQ_{\text{final stripping}}$ represent the amount of charge used to cycling processes, the charge used for the



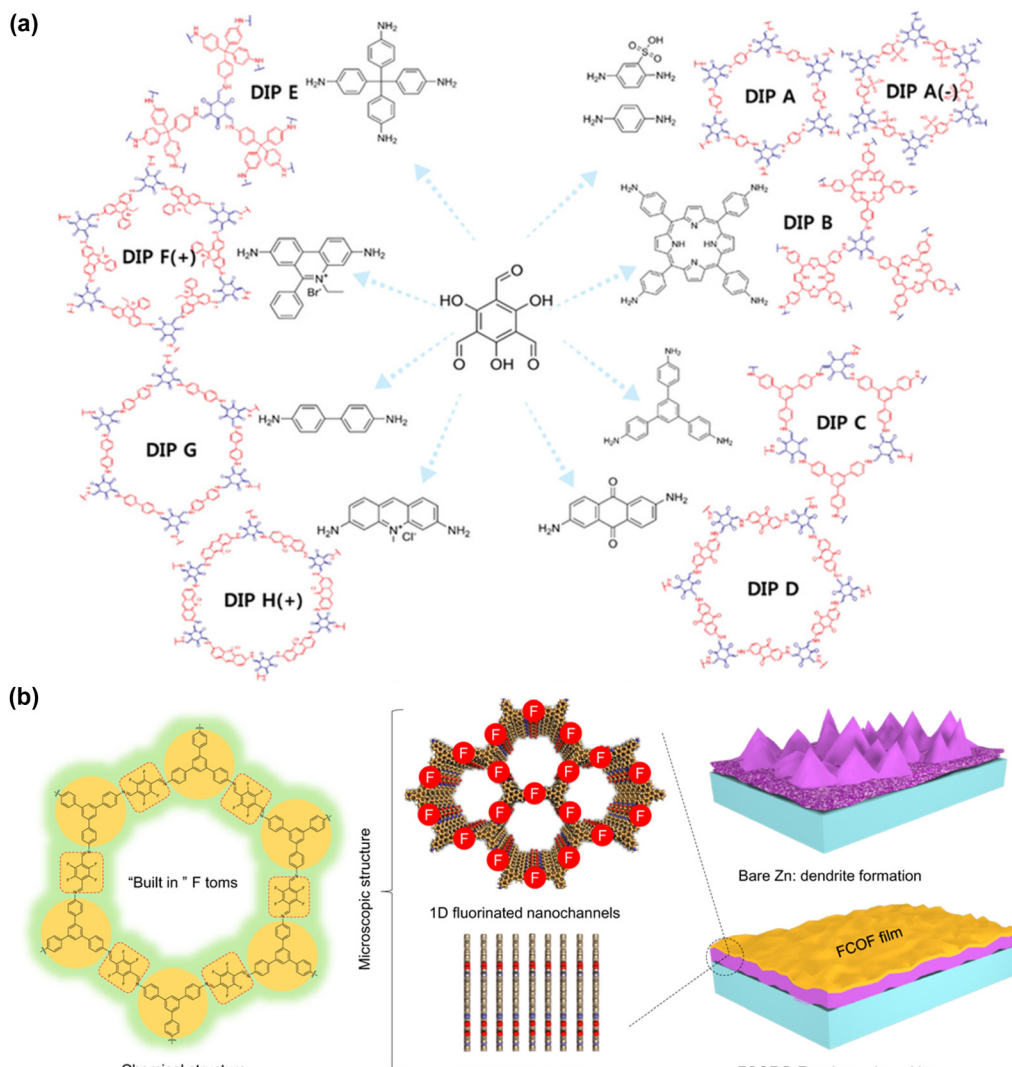


Fig. 62 (a) Structures of diverse covalent organic frameworks (COFs), formed from the 1,3,5-triformylphloroglucinol precursor and various aromatic amine linkers.⁷⁴⁰ (b) Suppression of Zn dendrite formation by a fluorinated COFs film.⁷⁴¹ Reprinted with permission from *Advanced Materials* (a) and *Nature Communications* (b).

initial pre-plating of metal onto the inert substrate to establish a metal reservoir, and the charge passed during the concluding stripping process, respectively. In the practical operation of rechargeable metal batteries, the metal is not entirely stripped from the substrate. Instead, metal plating and stripping occur on a metal surface rather than on an inert substrate, suggesting that this method provides critical perspectives for developing advanced rechargeable metal batteries.

Method 3. It is generally known that electrolyte reduction species cover both the metal and substrate surfaces during the initial plating and stripping cycles in the electrolyte. Therefore, the Pacific Northwest National Laboratory team introduced a modified protocol that involved pre-treatment or substrate conditioning steps before proceeding with Method 2 (Fig. 68).⁷⁹³ This method helped to eliminate the initial charge loss associated with conditioning the metal and substrate surfaces, thus providing a more accurate measure of the intrinsic stability of the metal in the electrolyte.

Method 4. Employing a metal|metal symmetric cell to measure the Coulombic efficiency has been explored but presents several challenges, including the absence of a voltage change, which complicates assessing the cycling status or detecting short circuits in the cell. Additionally, cycling a metal|metal symmetric cell until the metal is fully depleted, using an electrolyte that ensures high Coulombic efficiency, is impractical and time-consuming.

Under the assumption that the redox potential of the cathodes is located within the operating potential window of the electrolyte, thereby minimizing electrolyte oxidation on the cathode surface, the Coulombic efficiency of aqueous Zn-metal batteries is expected to primarily originate from electrolyte reduction on the Zn-metal surface. In this case, Method 3 would be most suitable for comparing the electrolyte stability on the Zn-metal surface. The Coulombic efficiency also largely depends on the current density, areal capacity, and cut-off

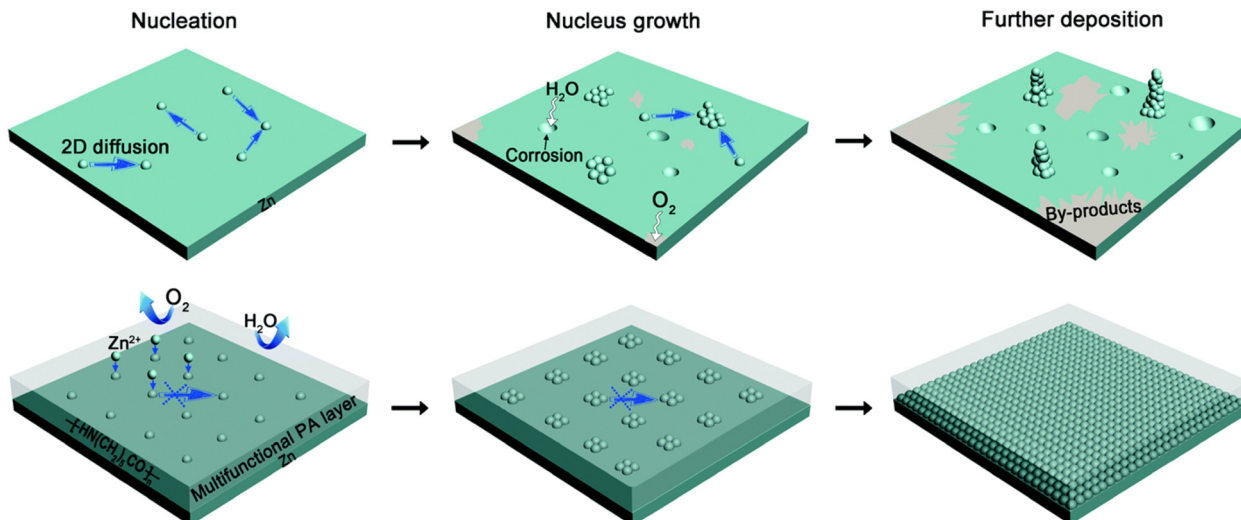


Fig. 63 Mechanism of suppressed Zn dendrite growth with a multifunctional polymeric interphase composed of polyamide and $Zn(OTf)_2$. Initial Zn nucleation was delocalized by the introduced polymeric interphase.⁷⁵² Reprinted with permission from *Energy & Environmental Science*.

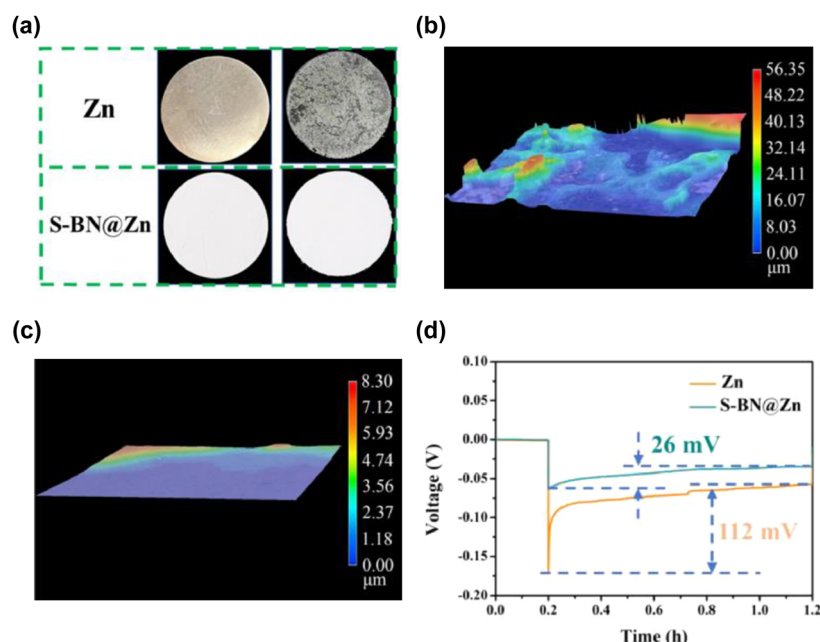


Fig. 64 (a)–(c) Photographs and three-dimensional distribution images of bare Zn and sulfonate group-modified boron nitride-coated Zn(S-BN@Zn) before and after 50 cycles in symmetric cells. (d) Decreased initial Zn nucleation overpotential on S-BN@Zn.⁷⁷⁸ Reprinted with permission from *Energy Storage Materials*.

voltage.^{792,796} The US Army Research Laboratory team recommended the following protocols: a current density of 0.5 mA cm^{-2} , areal capacity of 1 mA h cm^{-2} , an upper cut-off voltage of 0.5 V with a modest cycling number (*e.g.*, ten cycles to avoid interference from dendrite formation or excessive impedance growth), and a $Q_{\text{stripping/re-plating}}/Q_{\text{pre-plating}}$ ratio of 1/5 using a $100\text{ }\mu\text{m}$ -thick Zn foil counter electrode.⁷⁹²

Note that Method 1, which utilizes protocols similar to those of Method 3, proves advantageous for monitoring electrolyte stability and consumption over prolonged battery cycling. Moreover, it would benefit the future development of anode-

free batteries, contingent upon a rise in Zn-metal prices. Given the dual functionality of Zn metal as both a carrier ion provider and a current collector, selecting a substrate for Method 1 is debatable. Considering the drawbacks of alternative substrates, such as accelerated electrolyte reduction with a low HER overpotential on SUS,⁷⁹⁷ prohibitive costs and limited adaptability of Ti across various battery configurations, and low adhesion of Zn deposits due to the fast formation of an Al_2O_3 film on Al in aqueous solutions,⁷⁹⁸ Cu foil stands out as an ideal substrate choice in Method 1 owing to its affordability, flexibility, and adequate HER overpotential.



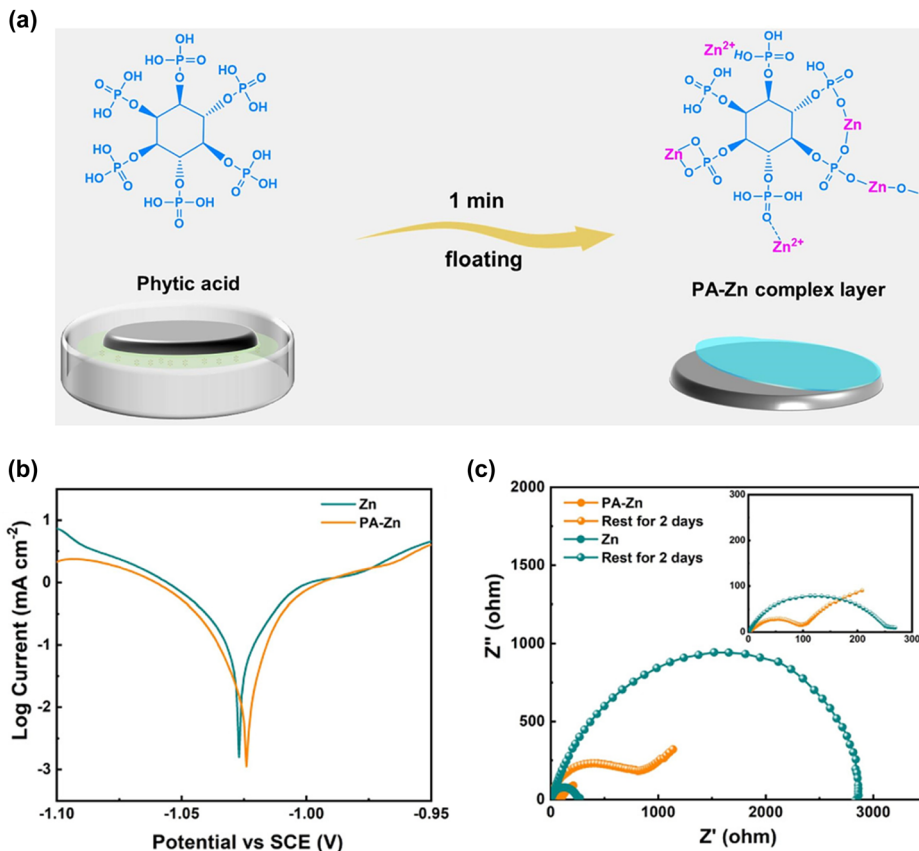


Fig. 65 (a) Preparation of phytic acid-treated Zn metal (PA-Zn). (b) Tafel curves showing increased corrosion potential in PA-Zn. (c) Nyquist plots demonstrating a significant difference in the surface charge-transfer resistance between bare Zn and PA-Zn before and after immersion in the 2 M ZnSO₄ solution for two days.⁷⁸⁶ Reprinted with permission from ACS Applied Materials & Interfaces.

Method 5. A modified “deposition-rest-dissolution” protocol, initially suggested by Yoo *et al.*, would be a practical method for estimating the stability between electrolytes and Zn metal under these varying temperature conditions (Fig. 69).⁷⁹⁹ Specifically, after completing a conditioning protocol (*e.g.*, initial conditioning cycling in Method 3), a specific amount of Zn is plated onto a substrate at room temperature. It is then maintained in the electrolyte at a set temperature for various rest periods. During these periods, side reactions occur between the plated Zn metal and the electrolyte, consuming both. Thereafter, the remaining Zn metal is stripped at room temperature. As indicated in eqn (23), the ratio of the mass of the stripped Zn after resting ($m_{\text{stripping after resting}}$) and initially plated Zn (m_{plating}) quantifies the stability of the electrolyte and Zn metal at specific temperatures based on Faraday’s law, whereby the change in the mass of Zn is proportional to the change in charge.

$$\begin{aligned}
 \text{(Method 5) Coulombic efficiency} &= \frac{m_{\text{plating}} - m_{\text{corrosion}}}{m_{\text{plating}}} \\
 &= \frac{m_{\text{stripping after resting}}}{m_{\text{plating}}} \quad (23) \\
 &= \frac{Q_{\text{stripping after resting}}}{Q_{\text{plating}}}
 \end{aligned}$$

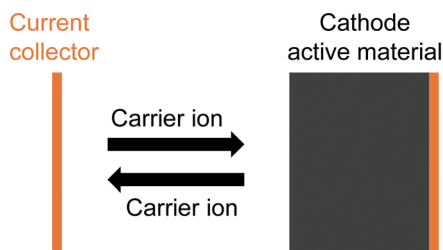
For instance, if 1 mA h cm⁻² of Zn is plated onto Cu foils at a constant current of 0.5 mA cm⁻² in two electrolytes, A and B, and

then maintained at 60 °C for a week, values of 0.1 mA h cm⁻² and 0.6 mA h cm⁻² are obtained for electrolytes A and B, respectively, through a stripping process at 0.5 mA cm⁻² and an upper cut-off voltage of 0.5 V. The test results demonstrate that electrolyte B offers superior stability with Zn metal, enhancing the battery performance at higher temperatures.

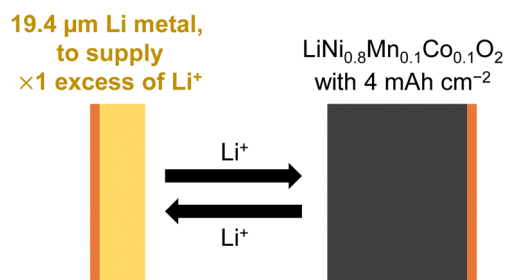
Method 6. Previous methods have primarily focused on measuring the efficiency of plating and stripping between Zn metals or between Zn metal and various metal-based substrates. However, these methods still cannot exclude the possibility of significantly different results based on test conditions, including parameters of the coin-cell components and the size of the Zn metal and substrate. Furthermore, avoiding the “edge effect,” which leads to the preferential formation of “dead” Zn at the edge zones and thus leads to significant differences in the Coulombic efficiency, is challenging in coin-cell tests.⁸⁰⁰

A more ideal approach is to evaluate the cycling performance and Coulombic efficiency within a full-cell configuration, which includes host cathodes capable of carrier ion intercalation and deintercalation, along with Zn-metal anodes, resembling the setup of Li-metal batteries. In this regard, aqueous Zn-metal batteries fabricated with Chevrel phase-Mo₆S₈ cathodes and Zn-metal anodes represent a standard system for evaluating the stability of the electrolyte and Zn metal (Fig. 70). Mo₆S₈, known for its ease of synthesis, high stability in the electrolyte,

(a) Anode-free batteries



(b) An example of practical Li-metal batteries



(c) An example of practical Zn-metal batteries

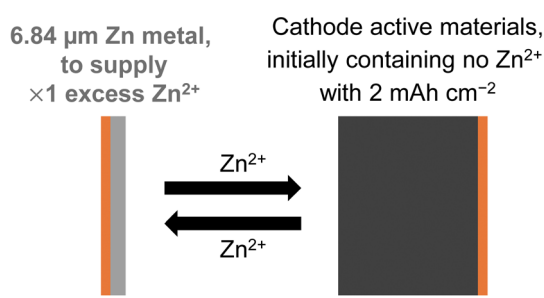


Fig. 66 Practical configuration of (a) anode-free, (b) and (c) metal-based batteries.

and moderate capacity ($\sim 100 \text{ mA h g}^{-1}$), along with its high density and electrical and ionic conductivities, allows for the preparation of high-loading-level cathodes exceeding 20 mg cm^{-2} . This setup is beneficial for the extensive testing of Zn plating and stripping processes, typically involving more than 2 mA h cm^{-2} ,^{545,801} offering a robust platform for assessing the battery stability.

Moreover, unlike many cathode materials for aqueous Zn-metal batteries that exhibit different charge and discharge curves in aqueous and nonaqueous electrolytes owing to complex co-intercalation reactions, Mo_6S_8 exhibits identical curves in both types of electrolytes, with negligible co-intercalation of protons and/or water, thus simplifying the evaluation of Zn^{2+} carrier ion consumption. Furthermore, the intercalation and deintercalation of Zn^{2+} into Mo_6S_8 occur within a potential range of $0.2\text{--}1.0 \text{ V}$ vs. Zn/Zn^{2+} , where neither the HER nor OER occurs on the electrode surfaces, respectively, in most aqueous electrolytes. These advantageous conditions indicate that the stability of the electrolyte

and Zn metal can both be effectively quantified by analyzing the cycling performance and Coulombic efficiency of a $\text{Mo}_6\text{S}_8/\text{Zn}$ full cell, constructed with limited amounts of Zn and the electrolyte.

7.7. Challenges with controlling the morphology and orientation of Zn plating

One straightforward method to prevent Zn dendrite formation is by controlling the morphology of Zn plating by using an increased operating current density. This technique has been proposed since the early twentieth century.^{802,803} Kundu *et al.* reported significant improvements in the cycle life of Ti/Zn cells in a $3 \text{ M ZnSO}_4/\text{H}_2\text{O}$ electrolyte when the current density was increased from a low value of 1 mA cm^{-2} to a high value of 20 mA cm^{-2} . The cycle life extended from 244 h to over 8000 h, affording uniform and dense plated Zn (Fig. 71).⁸⁰⁴ Further supporting this approach, Liu *et al.* studied the Zn plating morphology under various current densities and areal capacities in SUS/Zn cells, depicted in Fig. 72.⁸⁰⁵ Their findings indicated that Zn dendrite formation was effectively suppressed at high current densities such as 20 mA cm^{-2} . Similarly, Yang and Zhou *et al.* observed a densely packed morphology of Zn plated on Cu foil at a high current density (30 mA cm^{-2}) without the flake-like shapes prevalent at lower current densities (0.3 mA cm^{-2}).⁸⁰⁶ Additionally, the amount of hydrogen evolved during Zn plating decreased drastically from 60.04% to 2.11% when the current density was increased from 0.05 to 10 mA cm^{-2} .

Recent studies have questioned and sought to explain deviations from the traditional theory, which posits that non-uniform and dendritic metal deposition occurs at a high current density owing to a rapid decrease in the ion concentration at the electrode-electrolyte interface.⁸⁰⁷

Indeed, the concept of “high current density” and its effects vary significantly across different battery systems, particularly due to differences in the physicochemical properties and behavior of the electrolytes and metals used. The issues associated with high current densities often involve imbalanced plating caused by mass transport limitations. The crucial factor here is not the current density but the mass transport limitations resulting from reduced carrier ion concentration at the electrode-electrolyte interface. Understanding the distinction between “interface” and “interphase” is also essential.⁸⁰⁸

Nonaqueous Li electrolytes for Li-metal batteries typically exhibit ionic conductivities below 10 mS cm^{-1} . With its low redox potential of -3.0 V vs. SHE, Li metal promptly reduces these electrolytes. This reduction leads to the formation of an interphase (SEI)—a complex mixture of organic and inorganic species that can lower Li^+ transport compared to that in bulk electrolytes.

Conversely, aqueous Zn electrolytes, such as 1 M and $2 \text{ M ZnSO}_4/\text{H}_2\text{O}$, show higher ionic conductivities (47 mS cm^{-1} and 56 mS cm^{-1} , respectively) than typical nonaqueous solutions due to the small molecule size and high dielectric constant of water.⁸⁰⁹ Furthermore, as discussed in Section 7.4, the relatively high redox potential of Zn metal (-0.76 V vs. SHE) makes it less likely to be fully covered by an SEI, allowing the Zn-metal surface to function more as an interface—where the electrolyte



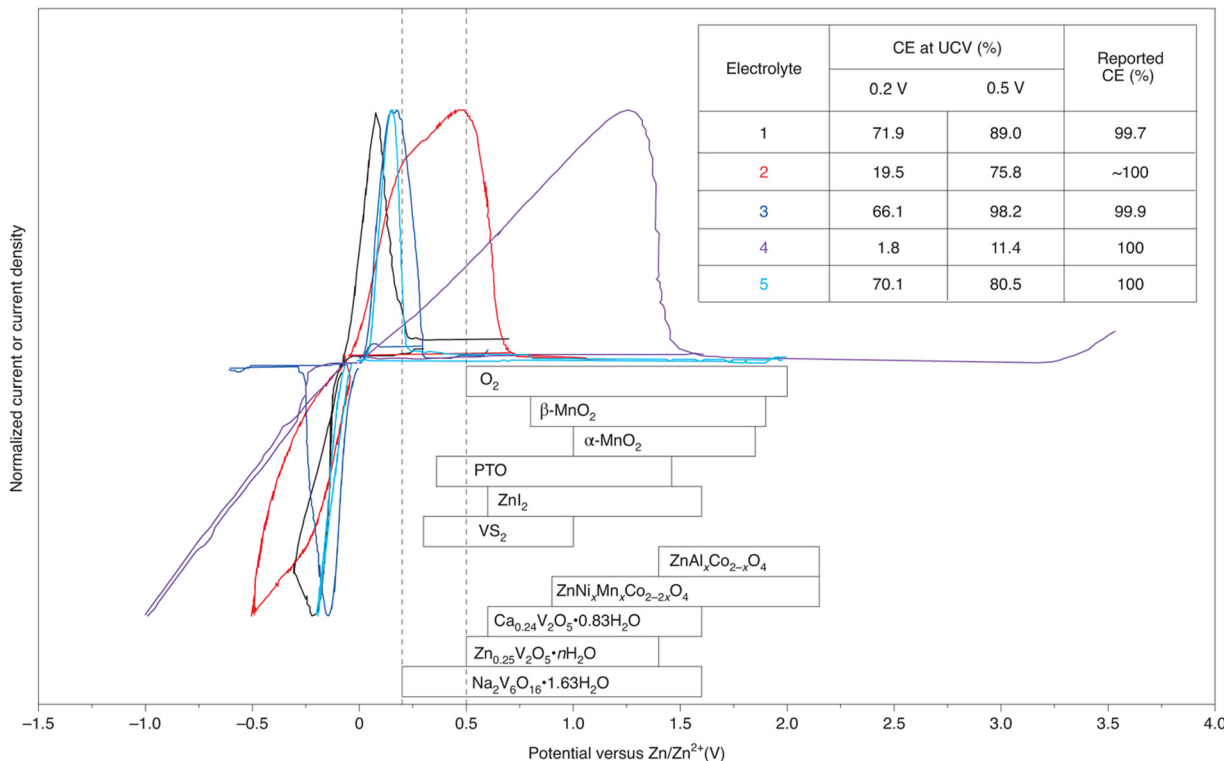


Fig. 67 Summary of cyclic voltammetry curves reported for determining the Coulombic efficiency in various Zn electrolytes: (1) $Zn(OTf)_2/LiTFSI/$ acetamide (1/2/7, $n/n/n$), (2) $Zn(TFSI)_2/$ acetamide (1/7, n/n), (3) 1 m $Zn(TFSI)_2 + 20$ m LiTFSI/ H_2O , (4) 0.5 M $Zn(TFSI)_2/$ propylene carbonate, and (5) 1 M $Zn(OTf)_2/H_2O$. The inset floating bars represent the operating potential ranges of various Zn cathodes. The current or current density is normalized to compare scan windows. The table in the top right displays the reported Coulombic efficiency values alongside those calculated via integration with more realistic upper cut-off voltages (UCVs; cut-off stripping potential in the manuscript) of 0.2 and 0.5 V.⁷⁹² Reprinted with permission from *Nature Energy*.



Fig. 68 (a)-(c) Protocols to estimate the Coulombic efficiency of metal plating and stripping.⁷⁹³ Reprinted with permission from *Advanced Energy Materials*.



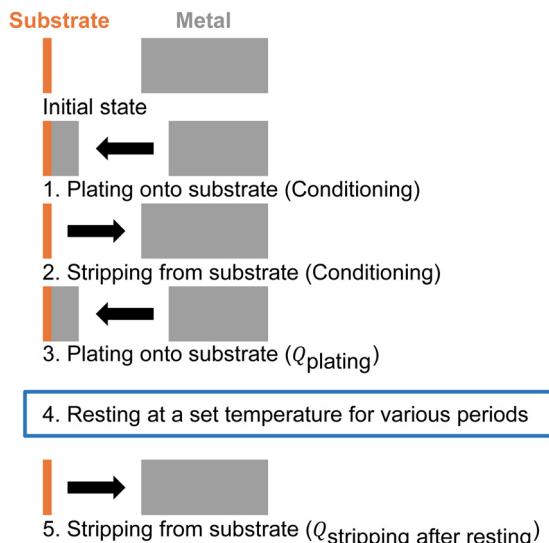
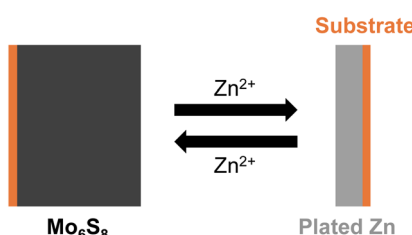


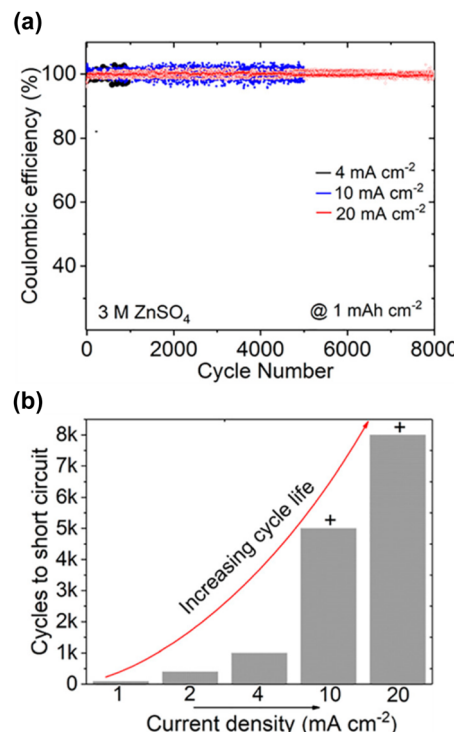
Fig. 69 Schematic of Method 5.

High-loading-level Mo_6S_8 | Limited amount of Zn with controlled electrolyte amount

Fig. 70 Schematic of Method 6. Utilization of a Mo_6S_8 /Zn full cell is one of the ideal methods to determine the Coulombic efficiency of Zn plating and stripping reactions.

directly contacts the electrode surface—rather than as an interphase.

Consequently, Zn plating in aqueous Zn electrolytes is likely to proceed with fast carrier ion transport, compared to Li plating in nonaqueous Li electrolytes, indicating that the threshold for the “high current density,” which triggers dendrite growth owing to mass transport limitations, is significantly higher in aqueous Zn than in nonaqueous Li systems. Sun *et al.* demonstrated that in 1–3 M $\text{ZnSO}_4/\text{H}_2\text{O}$, Sand’s time (Sand’s limiting current density; the current density at which the carrier ion concentration at the electrode surface decreases to zero, leading to unstable metal plating)⁸¹⁰ was estimated to be from 20 to 60 mA cm^{-2} based on areal capacities of 2.0 to 8.3 mA h cm^{-2} (Fig. 73),⁸¹¹ which was considerably higher compared to that for Li plating in nonaqueous Li electrolytes ($\leq 2 \text{ mA cm}^{-2}$) (Fig. 73).⁸¹² Additionally, Zn metal has a higher HER overpotential than other metals (Fig. 74).⁸¹³ As the current density increases, the HER overpotential also increases rapidly, helping to suppress the formation of hydrogen gas bubbles and the generation of OH^- . Moreover, computational calculations by Liu, Zhu, Huang, *et al.* illustrated that with an increase in the current density:⁸¹⁴ (i) the

Fig. 71 (a) Coulombic efficiencies of Zn plating and stripping in $\text{Ti}|\text{3 M ZnSO}_4/\text{H}_2\text{O}|\text{Zn}$ cells at various current densities. (b) Chart representation showing a drastic increase in the Coulombic efficiency with increasing current density.⁸⁰⁴ Reprinted with permission from ACS Applied Materials & Interfaces.

concentration of Zn^{2+} increased while that of anions decreased to compensate for the negative charge on the electrode surface, and (ii) the reaction kinetics for Zn plating were enhanced owing to the decreased thickness of the electrical double layer, as described by the Gouy–Chapman–Stern model,⁸¹⁵ thereby facilitating Zn^{2+} transport with a shortened diffusion distance.⁸¹⁴

Overall, the definition of “high current density,” which promotes dendrite growth through mass transport limitations, significantly varies between nonaqueous Li and aqueous Zn systems. In Li plating, a current density of 20 to 30 mA cm^{-2} is considered “high” and is likely to induce dendrite growth due to the low ionic conductivity of nonaqueous Li electrolytes and the presence of an “interphase” on the Li-metal surface. However, under the same conditions, Zn plating may not be subject to diffusion-controlled limitations, and both the HER and the accompanying generation of hydrogen gas bubbles and OH^- ions are suppressed. Simultaneously, the Zn^{2+} concentration increases while the anion concentration decreases at the electrode–electrolyte “interface,” collectively reducing side reactions, including byproduct formation. These points are further evidenced by the current density of conventional Zn electrowinning, which has been optimized since the early twentieth century and is generally controlled at 40 to 50 mA cm^{-2} .⁸⁰³

However, the “high current density” strategy poses practical limitations, especially in large-scale energy storage systems. Increasing the current density necessitates heavier wiring and chargers and leads to substantial heat generation, which can



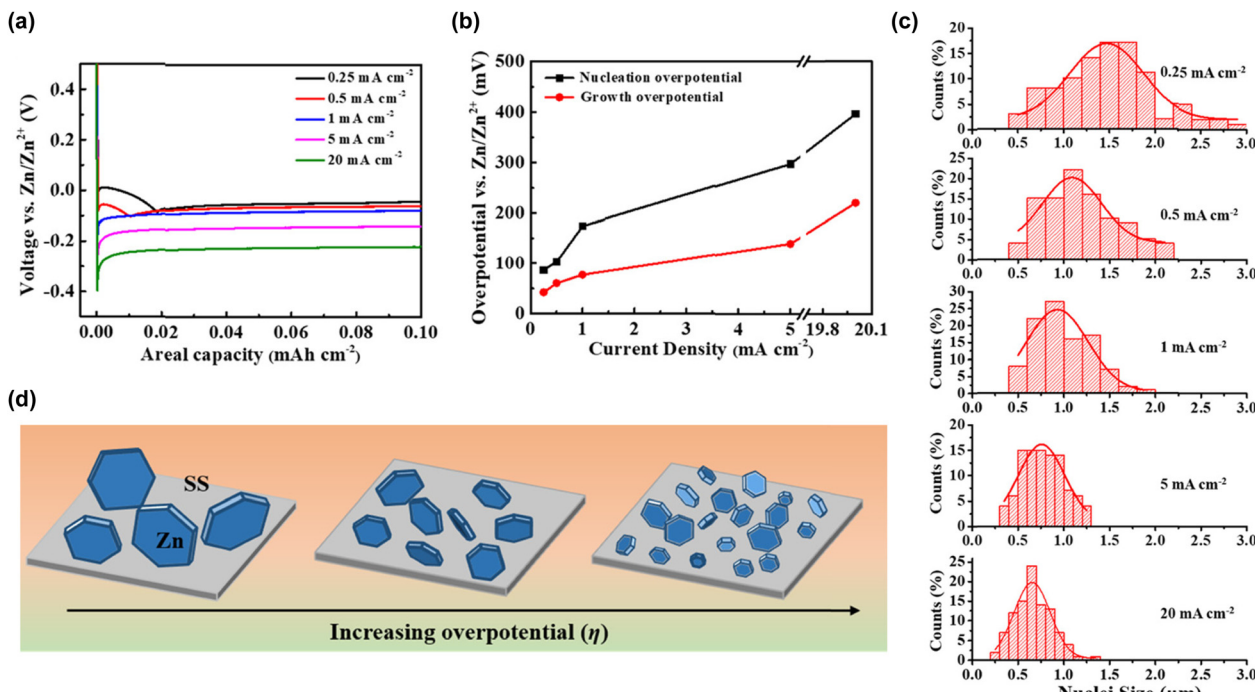


Fig. 72 (a) Voltage profiles of galvanostatic Zn plating on SUS. (b) Variation in nucleation and growth overpotentials with respect to the current density. (c) Histograms of Zn particle sizes after plating with a capacity of 0.1 mA h cm^{-2} . (d) Schematic of Zn growth at different overpotentials.⁸⁰⁵ Reprinted with permission from ACS Applied Materials & Interfaces.

trigger severe side reactions, degrade the battery performance, and in some cases, even cause fire accidents. This is particularly concerning in closed battery systems where the generated hydrogen gas cannot be immediately ventilated, unlike in conventional Zn electrowinning, which uses an open system. Therefore, developing aqueous Zn-metal batteries that guarantee stable Zn plating and stripping at sufficiently low current conditions (such as $\leq 0.1\text{C}$) is crucial for their practical utilization and for ensuring high safety.

On the other hand, numerous studies have been conducted on controlling the morphology of plated Zn through electrolyte modification. According to some studies by Haataja *et al.*,^{816,817} dendrite growth is largely inhibited by the adsorption and accumulation of electrolyte additives on the surface of the protrusions formed during metal plating. This mechanism involves the use of brighteners (levelers) in the electroplating field, which increase the nucleation overpotential during metal plating to form smaller and denser nuclei, a concept that has been well-documented for decades.⁸¹⁸

Further historical examples include the work of Sato in 1959, who reported significant changes in the morphology and orientation of Zn deposits upon adding small amounts of natural polymers like glue, gelatin, albumin, or carbohydrates such as gum arabic, dextrin, starch, and saponin to acidic ZnSO_4 solutions.⁸¹⁹ In later studies, Robinson *et al.* demonstrated the effective inhibition of dendrites by incorporating small amounts of antimony and animal glue.⁸²⁰ Additionally, the use of quaternary ammonium salts with varying alkyl groups to suppress Zn dendrite formation was explored by Diggle and Damjanovic in 1972⁸²¹ and further by Mackinnon

et al. in 1979.⁸²² Other substances, such as polyethylene glycol,⁸²³ perfluorocarboxylic acids,⁸²⁴ nonyl-phenyl-oxyethylene surfactant,⁸²⁵ lignin sulfonate,⁸²⁶ and ionic liquids^{827–829} have also proven effective in controlling the Zn morphology.

Guiding the orientation of metal plating to achieve densely packed layers with reduced interelectrode space is a key strategy for preventing Zn dendrite formation and “dead” Zn, which can compromise the battery stability and safety by increasing the risk of short circuits. The structure of the Zn plating, typically occurring in platelet shapes, is influenced by the thermodynamically low surface energy of the $(001)_{\text{Zn}}$ crystal plane in hexagonal close-packed Zn metal. Therefore, promoting the $[001]_{\text{Zn}}$ orientation during plating is expected to enhance the Coulombic efficiency and promote stable cycling.

In 2019, a team led by Archer explored this approach by leveraging substrates with crystallographic facets with a low lattice mismatch to the plated Zn, enabling epitaxial Zn plating with densely packed structures (Fig. 75).⁸³⁰ They prepared a graphene coated SUS substrate, which shares a similar atomic arrangement with the $(001)_{\text{Zn}}$ plane. This arrangement exhibits a lattice misfit of only 7%, significantly below the 25% threshold typically considered necessary for coherent or semicoherent interfaces. Such a low misfit facilitates successful epitaxial Zn plating. In graphene-coated SUS|Zn coin cells using a 2 M ZnSO_4 solution, the Coulombic efficiency exceeded 99% during 1000 cycles at 4.0 mA cm^{-2} and 0.8 mA h cm^{-2} . When tested under higher current densities of 16 and 40 mA cm^{-2} , the cells maintained nearly 99.9% of the Coulombic efficiency over 10 000 cycles. This was in sharp contrast to the performance



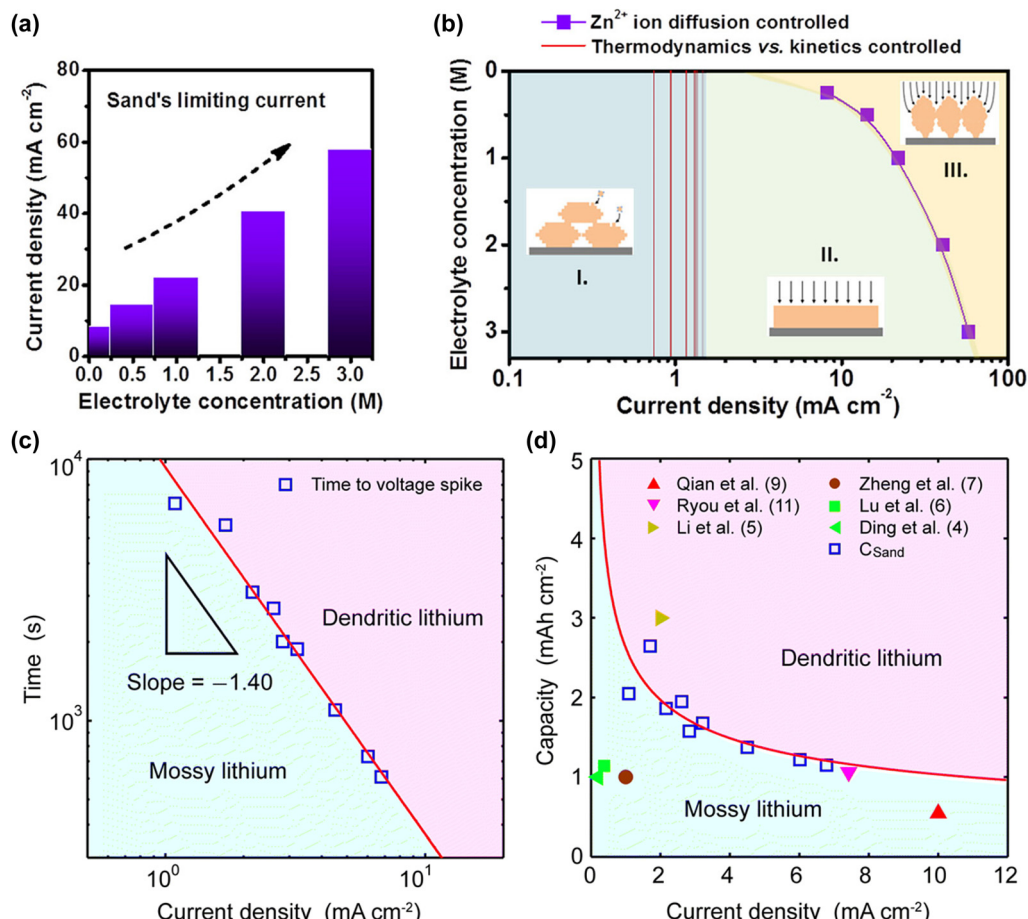


Fig. 73 (a) and (b) Sand's limiting current densities for Zn plating in aqueous ZnSO_4 electrolytes with different concentrations. The inset, model III, represents Zn dendrite growth.⁸¹¹ (c) and (d) Sand's time and capacity for Li plating in nonaqueous Li electrolytes at various current densities.⁸¹² Reprinted with permission from *Angewandte Chemie International Edition* (a) and (b) and *Energy & Environmental Science* (c) and (d).

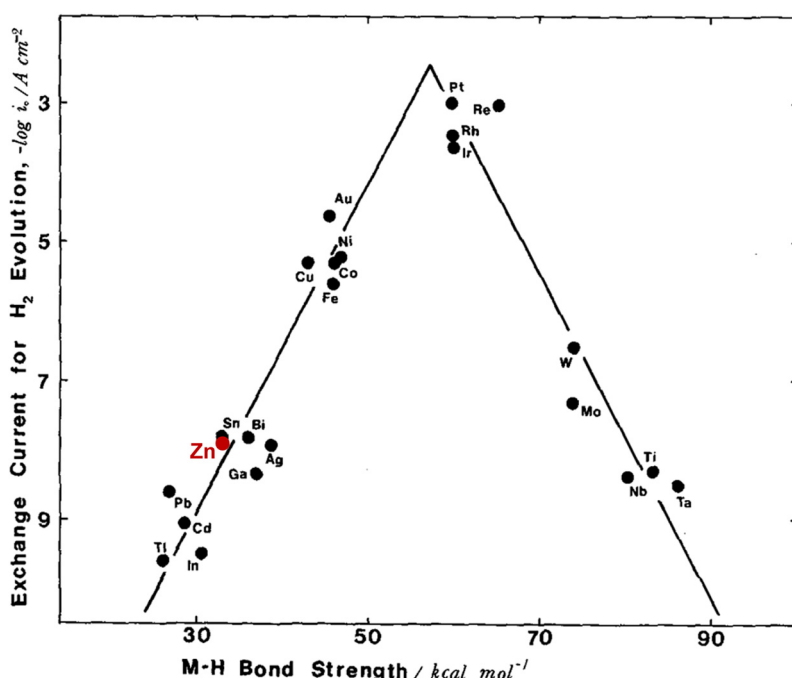


Fig. 74 Volcano plot for the HER. The intermediate Zn metal–hydrogen bond formed during the electrochemical reaction is weak, resulting in a high overpotential (low exchange current) for the HER.⁸¹³ Reprinted with permission from *Journal of Electroanalytical Chemistry and Interfacial Electrochemistry*.



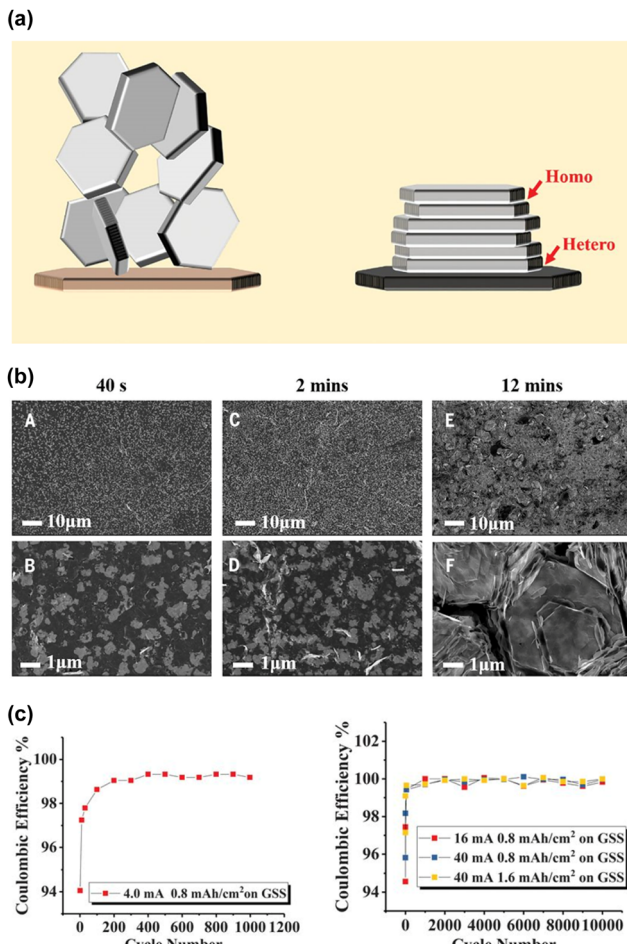


Fig. 75 (a) Design principle of epitaxial metal electrodeposition. (b) SEM images of Zn deposits on graphene-coated stainless steel (GSS). The epitaxial electrodeposition process is divided into two stages: stage I involves heteroepitaxy between Zn and graphene (A)–(D), and stage II involves the homoepitaxy of Zn after the graphene surface is fully covered (E) and (F). (c) Coulombic efficiency at different current densities on GSS.⁸³⁰ Reprinted with permission from *Science*.

of a bare SUS|Zn cell at 40 mA cm^{-2} and 0.8 mAh cm^{-2} , which was characterized by a poor Coulombic efficiency below 90% and short-circuit of the cell within just 10 cycles.

Achieving densely packed Zn plating is difficult when commercially available Zn plates, characterized by random orientations, are used as substrates. In 2021, Zhou *et al.* produced Zn plates that enabled Zn growth in a direction perpendicular to the Zn plane.⁶⁹⁷ In a symmetric cell setup with $2 \text{ M ZnSO}_4 + 0.1 \text{ M MnSO}_4/\text{H}_2\text{O}$ at 1 mA cm^{-2} and 1 mA h cm^{-2} , the developed Zn plates maintained stable cycling for over 500 h, unlike commercial Zn plates, which often short-circuited before reaching 50 cycles.

It is essential to clarify the distinction between “plane” and “orientation” in crystallography, as these terms have often been used interchangeably but inaccurately in the literature on aqueous Zn-metal batteries. For example, $(001)_{\text{Zn}}$ denotes a crystal “plane” as defined by the Miller indices, while $[001]$ represents the direction perpendicular to this plane. Often,

there is confusion where $(002)_{\text{Zn}}$ is referenced, but the actual exposed “plane” during the plating process is typically $(001)_{\text{Zn}}$. This discrepancy arises from the misapplication of the “systematic extinction rule” related to structure factor calculations. Even though certain crystal symmetries may result in specific structure factors being exactly zero, this does not negate the existence of the crystal “plane” or “orientation.” Furthermore, identifying these planes and orientations typically requires more than standard XRD techniques; a combination of SEM and electron back-scatter diffraction is necessary for precise determination.

In most aqueous Zn electrolytes, Zn is plated in hexagonal platelet shapes, with the $(001)_{\text{Zn}}$ plane exposed to minimize the thermodynamic surface energy. Fortunately, the $(001)_{\text{Zn}}$ plane offers a high HER overpotential, providing high reversibility for Zn plating and stripping despite the thermodynamic potential of Zn/Zn^{2+} being lower than that of the HER in the electrolytes. Therefore, controlling the “plane” is typically not the primary focus in aqueous Zn-metal battery development.

However, when it is expressed that Zn grows in the direction perpendicular to the $(001)_{\text{Zn}}$ plane, this implies that the plated Zn is oriented in the $[001]$ direction (where $[001]$ refers to the directional vector). Confirming the “orientation” of plated Zn requires detailed XRD analysis and comprehensive scanning of the reciprocal space, such as through pole-figure measurements, to analyze the crystal orientation distribution. The crystal growth “orientation” largely depends on the type of substrate, and also on factors such as the type of electrolyte and plating/stripping conditions (e.g., current density, temperature, and areal capacity). Interactions among the electrolyte, electrolyte reduction species, and the plated Zn can modify the growth “orientation” in various ways, even on substrates suitable for epitaxial growth. Thus, achieving densely packed Zn with a reduced interelectrode space—thereby enhancing the cycling stability of aqueous Zn-metal batteries and preventing the formation of Zn dendrites and “dead” Zn—requires the careful development of substrates and electrolytes, along with optimized plating and stripping conditions.

7.8. Electrolyte-decoupled batteries with conversion reaction-based cathodes

The electrolyte-decoupling concept has typically been utilized in redox flow batteries. Recent advancements in ion-exchange membranes, designed to prevent chemical crossover between the anolyte and catholyte while facilitating charge carrier-ion transport, have opened opportunities to apply this concept in conventional non-flow aqueous batteries.⁸³¹

Attention has also shifted toward cathode materials that align well with electrolyte-decoupling systems. A notable example is halogen|Zn batteries, proposed over 150 years ago, which utilize reversible conversion reactions between X^- and X_2/X_3^- ($\text{X} = \text{Cl}, \text{Br}, \text{and I}$). It is worth noting that F^-/F_2 is excluded from this review due to its extreme corrosiveness and toxicity, making battery fabrication highly challenging.

7.8.1. Cl_2/Zn batteries. Cl_2/Zn batteries provide a high theoretical energy density (300 W h kg^{-1}) and output voltage (2.1 V). The prototype, initially developed by Charles Renard in 1884, later evolved into a large-scale 2 kW h battery tested in

1976.⁸³² However, Cl_2 gas (boiling point -34°C) is heavier than air and reacts with moisture to form hydrochloric acid, which severely damages human tissues. This hazard was even exploited as a biochemical weapon during World War I, underscoring its extreme danger. To mitigate the risks, several approaches have been explored, including; adsorbing Cl_2 onto high-surface-area porous carbons,^{833,834} intercalating Cl^- between graphene layers in graphite,^{835–837} and fixing Cl_2 as solid-state chlorine complexes with coordinating agents.^{584,838–840} However, despite these efforts, the complete suppression of Cl_2 gas formation remains an unresolved issue.

7.8.2. $\text{Br}_2|\text{Zn}$ and $\text{I}_2|\text{Zn}$ batteries. Br_2 and I_2 , with boiling points of 59°C and 184°C respectively, exist as liquid and solid under room-temperature operation, making them relatively safer alternatives. $\text{Br}_2|\text{Zn}$ batteries (theoretically 150 W h kg^{-1} , 1.8 V) were patented in 1885, and kW h to MW h-scale hybrid flow systems were developed during the 1970s and 1990s.^{841–845} $\text{I}_2|\text{Zn}$ batteries (theoretically 80 W h kg^{-1} , 1.3 V) were first demonstrated by Martin in 1949, using a potassium iodide solution as the active cathode material.⁸⁴⁶ Recently, Xiao Liang *et al.* proposed a four-electron $\text{I}^-/\text{I}_2/\text{I}^+$ conversion reaction-based battery, enhancing the battery output voltage from 1.3 V to 1.8 V ($2\text{I}^- \rightleftharpoons \text{I}_2 + 2\text{e}^-$: 1.3 V vs. Zn/Zn^{2+} and consequent $\text{I}_2 + 2\text{Cl}^- \rightleftharpoons 2\text{ICl} + 2\text{e}^-$: 1.8 V vs. Zn/Zn^{2+}) in a highly salt-concentrated hybrid aqueous/nonaqueous ($\text{ZnCl}_2 + \text{LiCl} + \text{acetonitrile}/\text{H}_2\text{O}$) electrolyte (Fig. 76).⁸⁴⁷

However, inhalation of highly volatile Br_2 vapors can severely damage the lungs and stomach. Moreover, oxidized halogen ions form polyhalides, which maintain equilibrium with dissociated X_{2n-1}^- and X_2 ($\text{X} = \text{Br}$ or I) in solution.^{848,849} The small molecular size and hydrophobic nature of halogen molecules (*e.g.* Br_2 , I_2), combined with the limited solubility of polyhalides in aqueous electrolytes, drive phase separation and crossover to the anode, substantially diminishing the battery's efficiency and stability. To address these issues, battery charging is often limited to two-thirds of the state of charge. Functional electrolyte additives such as quaternary ammonium, imidazolium, nitriles, pyridinium, and soft cation/hard anion-based zwitterionic trappers have also been studied to enhance the solubility of polyhalides and enable high states of charge *via* various stabilizing mechanisms, including electrostatic, dipole-dipole, and hydrogen-bonding interactions (Fig. 77).^{850–858}

While these advances show potential for improved Coulombic efficiency and charge/discharge depth, considerable obstacles persist. The addition of large amounts of electrolyte additives reduces energy efficiency with increased cell resistance. Furthermore, ensuring long-term safety and reliability in large-scale batteries over multi-year operations under practical conditions, including a wide temperature range, varying cycling rates, and alternating depths of charge and discharge remains a critical, unresolved challenge.

7.8.3. Transition metal oxides|Zn batteries. The limited exploration of cathode active materials, offering smooth Zn^{2+}

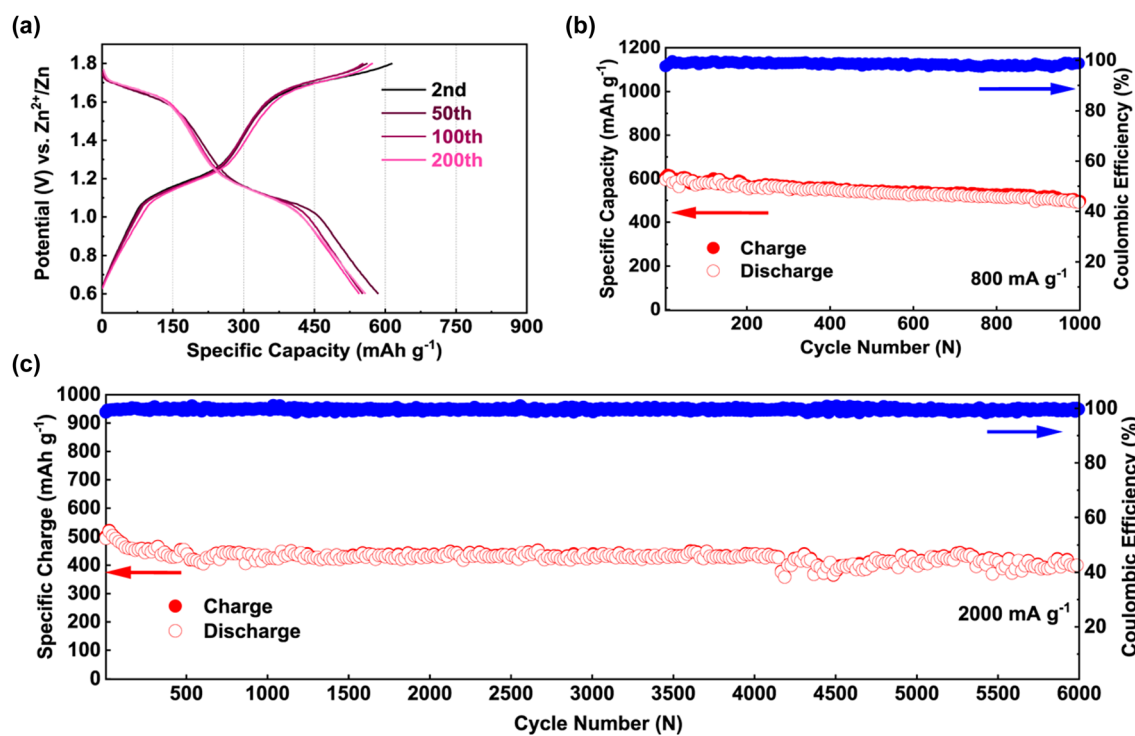


Fig. 76 High-voltage aqueous Zn-metal batteries based on $\text{I}^-/\text{I}_2/\text{I}^+$ conversion reactions in a highly salt-concentrated hybrid aqueous/nonaqueous ($\text{ZnCl}_2 + \text{LiCl} + \text{acetonitrile}/\text{H}_2\text{O}$) electrolyte. (a) Voltage profiles at 400 mA g^{-1} , demonstrating an increased upper cut-off voltage from 1.3 V (I^-/I_2) to 1.8 V ($\text{I}^-/\text{I}_2/\text{I}^+$). Note that while the theoretical capacity of the $\text{I}^-/\text{I}_2/\text{I}^+$ conversion reaction is 422 mA h g^{-1} , a use of a carbon cathode host provides additional capacitance, increasing the total capacity to 594 mA h g^{-1} . (b) and (c) Long-term cycling performance of the battery at 800 mA g^{-1} and 2000 mA g^{-1} , respectively.⁸⁴⁷ Reprinted with permission from *Nature Communications*.



intercalation/deintercalation, has revived interest in transition metal oxides (*e.g.* MnO_2 , PbO_2 , Co_3O_4 , NiCo_2O_4 , NiO)-based on conversion reactions.^{859–861} Fig. 78 shows one representative example of electrolyte-decoupled $\text{MnO}_2\text{||Zn}$ batteries.^{862–864} Theoretically, using electrolytes with different pH values for the anode and cathode (anolyte at pH 14 and catholyte at pH 0) can expand the operating potential window to 2.06 V (Fig. 10). Additionally, the Zn redox potential in an alkaline environment ($\text{Zn}(\text{OH})_4^{2-}/\text{Zn}$: -1.20 V *vs.* SHE) is 0.44 V lower than in acidic or neutral conditions (Zn/Zn^{2+} : -0.76 V *vs.* SHE), further contributing to an increase in battery voltage. While alkaline $\text{MnO}_2\text{||Zn}$ batteries have long been commercialized, as reviewed in Section 1, their performance deteriorates at high states of charge (high upper cut-off voltage) due to the formation of irreversible intermediate products such as $\text{Mn}(\text{OH})_2$, Mn_2O_3 , and Mn_3O_4 .^{865,866} To ensure high-voltage cycling with suppressed byproduct formation, Cheng Zhong, Wenbin Hu, and colleagues proposed a electrolyte-

decoupled battery system, MnO_2 with an acidic catholyte|cation-exchange membrane| K_2SO_4 solution|anion-exchange membrane|Zn metal with an alkaline anolyte ($\text{MnO}_2/\text{Mn}^{2+}$: 2.44 V *vs.* $\text{Zn}(\text{OH})_4^{2-}/\text{Zn}$), maintaining a capacity retention rate of over 98% after 200 hours (Fig. 78).⁸⁶² Similarly, Zhenhai Wen *et al.* developed a 3 V-class battery, consisting of PbO_2 with an acidic catholyte|cation-exchange membrane| K_2SO_4 solution|anion-exchange membrane|Zn metal with an alkaline anolyte ($\text{PbO}_2/\text{Pb}^{2+}$: 2.88 V *vs.* $\text{Zn}(\text{OH})_4^{2-}/\text{Zn}$) (Fig. 79).⁸⁶⁷

However, electrolyte-decoupling systems face a fundamental limitation in their energy storage and release mechanisms, which are heavily dependent on electrolyte volume. Additionally, achieving reversible conversion reactions in transition metal oxides involves nano-engineering, inherently lowering Coulombic efficiency with accelerated electrolyte oxidation due to the increased surface area. This, in turn, necessitates a large amount of electrolyte to sustain long-term cycling, significantly

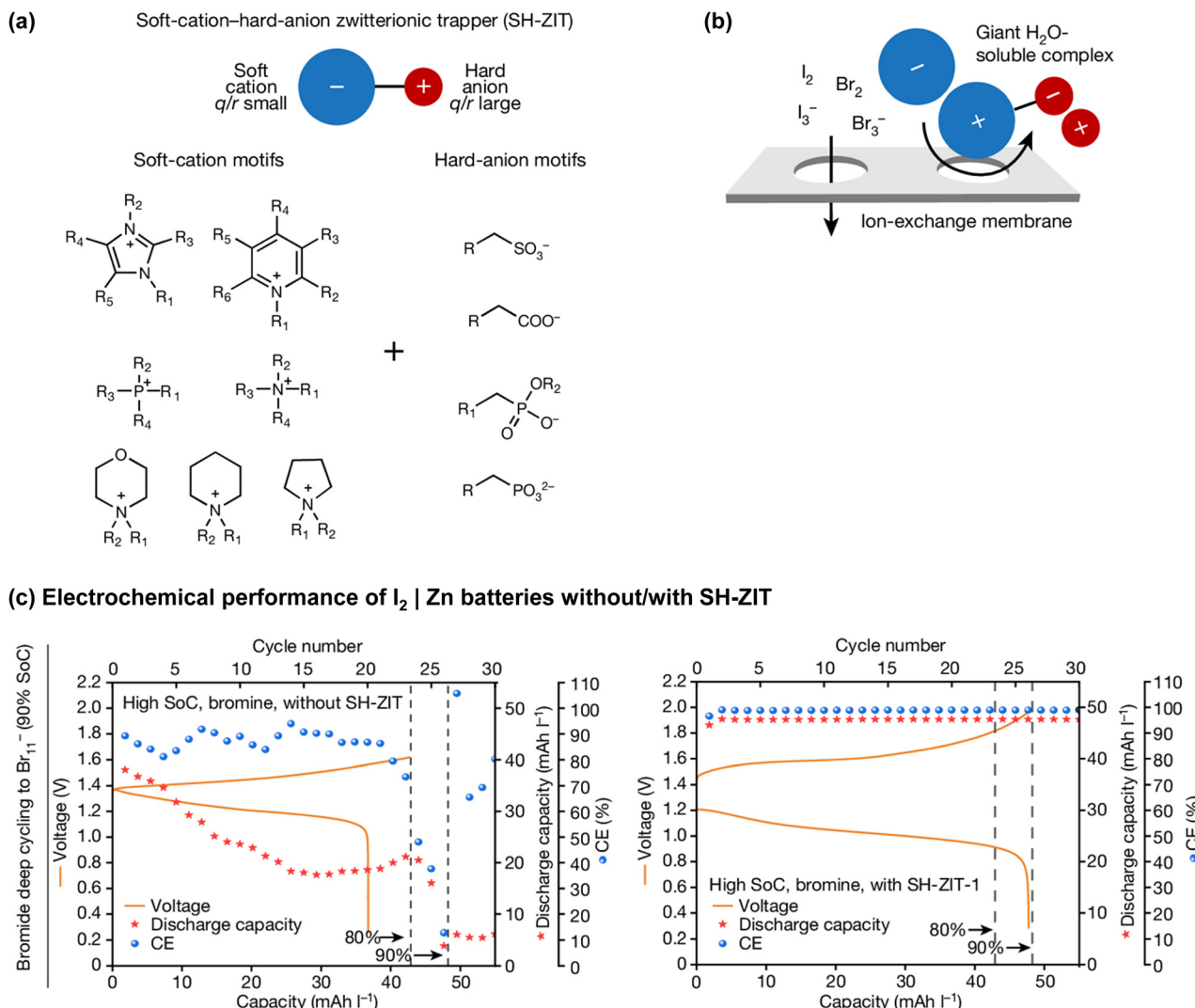


Fig. 77 (a) Design principle and (b) proposed reaction mechanism of soft-hard zwitterionic trappers (SH-ZITs) with polyhalides, leading to the formation of soluble phases and reduced permeability. (c) Electrochemical performance of 2 M KBr catholyte charged to 80–90% state of charge without/with 2 M SH-ZIT. Excess 1,1'-bis[3-sulfonatopropyl]-4,4'-bipyridinium and 2 M KBr anolyte were utilized with cation-exchange membranes.⁸⁵⁸ Reprinted with permission from *Nature*.

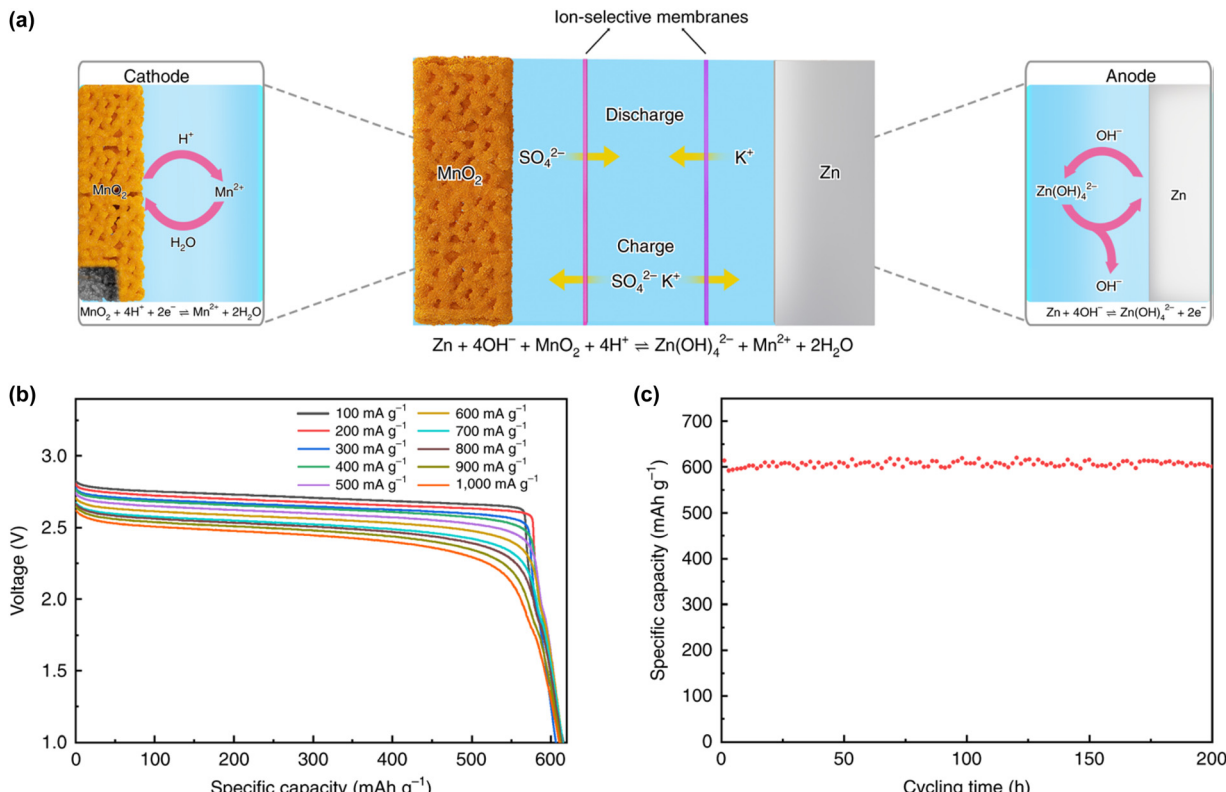


Fig. 78 (a) The working mechanism of an electrolyte-decoupled $\text{MnO}_2|\text{Zn}$ battery. (b) and (c) Discharge voltage profiles and long-term cycling stability of the cell.⁸⁶² Reprinted with permission from *Nature Energy*.

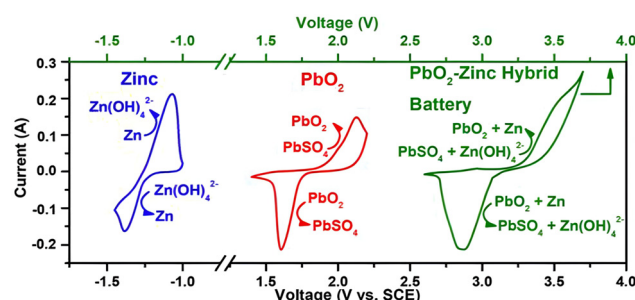


Fig. 79 Cyclic voltammetry curves of Zn in an alkaline electrolyte (blue), PbO_2 in an acidic electrolyte (red), and a $\text{PbO}_2|\text{Zn}$ battery with an electrolyte decoupling system (alkaline anolyte and acidic catholyte) (green) under a scan rate of 10 mV s^{-1} .⁸⁶⁷ Reprinted with permission from *Angewandte Chemie International Edition*.

diminishing energy density. The differing Coulombic efficiencies of anode and cathode redox reactions require varying electrolyte volumes within the system, adding complexity and further reducing practicality. This stands in stark contrast to intercalation/deintercalation-based batteries—a success story recognized by the Nobel Prize—that largely enhance energy density by drastically reducing electrolyte volume with a high Coulombic efficiency exceeding 99.95% in a single electrolyte system. Also, batteries containing Pb pose significant environmental risks, and Zn plating/stripping reactions in alkaline environments often suffer from insufficient reversibility, as demonstrated in Section 7.2.

Another challenge lies in ion-exchange membranes, which are typically composed of a hydrophobic polymer matrix, fixed ionic functional groups, and mobile counter-ions, with their ability to select/transport ions governed by Donnan equilibrium.⁸³¹ The small size and high mobility of protons (H^+) and hydroxide ions (OH^-) make it particularly difficult to prevent their crossover during long-term battery operation. Once H^+ and OH^- cross the membrane, they undergo a neutralization reaction (H_2O formation), disrupting the local ionic balance and equilibrium. Although advanced configurations, such as dual-membranes (cation-exchange membrane|buffer electrolyte|anion-exchange membrane) or bipolar membranes (cation-exchange membrane|intermediate catalyst layer|anion-exchange membrane), have been explored to address these issues, increasing the number of membranes raises diffusion resistance, overpotential, and system complexity, ultimately reducing the battery operation efficiency. Furthermore, separating the anolyte and catholyte in traditional electrode designs (*e.g.* jelly roll) and manufacturing processes is infeasible without specialized methods such as semi-solid electrode techniques, which are still in developmental stages (Fig. 80).

8. Conclusions and perspectives

The advancements and challenges associated with rechargeable aqueous Li-, Na-, K-, and Zn-ion batteries have been thoroughly discussed in this review. These batteries are promising because



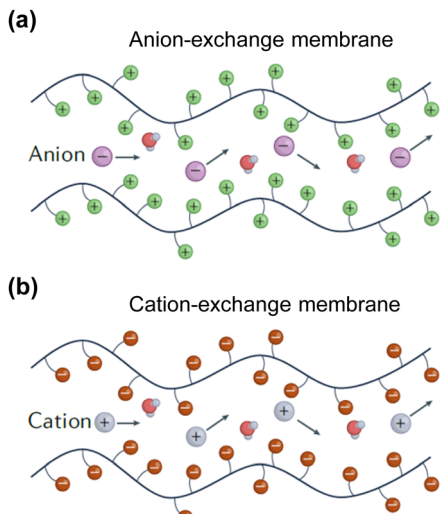


Fig. 80 Schematic representation of ion transport mechanisms in (a) anion- and (b) cation-exchange membranes.⁸³¹ Reprinted with permission from *Nature Review Chemistry*.

of their low production costs, high safety, and environmental benefits, rendering them ideal for various energy storage applications, particularly in large-scale systems. However, realizing their full potential, *i.e.*, offering high energy and power densities while maintaining long-term cycling stability under practical operating conditions, requires addressing several complex challenges related to (1) the narrow operating potential windows of aqueous electrolytes, (2) unstable SEI, (3) insufficient exploration and optimization of active materials, and (4) electrode/cell designs to mitigate side reactions, lower manufacturing costs, and ensure ease of production. These points are summarized below:

(1) The thermodynamically narrow potential window of water (1.23 V) limits the output voltage of aqueous batteries. Although highly salt-concentrated aqueous electrolytes, which provide substantially reduced water activity, help to widen the electrolyte potential window both thermodynamically and kinetically, they introduce additional issues such as increased viscosity, decreased ionic conductivity, high costs, and poor wide-temperature-range functionalities, all of which impact the battery performance and manufacturability.

(2) Forming and maintaining an SEI in aqueous environments are more challenging than in nonaqueous systems. The HER consumes the electrons needed for SEI formation, leading to SEI exfoliation by the generation of hydrogen gas bubbles. Additionally, the small molecular size and high dielectric constant of water destabilize the SEI by expanding it and accelerating the diffusion of SEI components into the bulk electrolyte. These issues are more pronounced in Na, K, and Zn systems than in aqueous Li electrolytes owing to the weak Lewis acidity of Na^+ and K^+ and the high redox potential of Zn/Zn^{2+} , which do not provide sufficient driving force to lower the water activity and facilitate anion reduction, respectively. Although *ex situ* SEI formation has been explored as a solution, its effectiveness remains under debate because of its low ionic conductivity, poor stability, and limited functionality under practical operating conditions.

(3) The active materials introduced in aqueous systems are often merely an extension of those developed for nonaqueous batteries. There has been insufficient consideration of the unique requirements of aqueous environments, such as high chemical stability, minimal proton and/or water co-intercalation, low catalytic effect on water electrolysis, and high resistance to dissolution in water. Furthermore, the limited exploration of suitable active materials for K^+ and Zn^{2+} presents challenges akin to those encountered in nonaqueous systems. In some instances, research and development efforts have been misguided owing to misunderstood intercalation chemistry.

(4) The compatibility of various battery components, such as separators and current collectors with aqueous electrolytes, presents significant challenges. Traditional separators designed for nonaqueous batteries exhibit poor wettability in aqueous electrolytes. Consequently, most studies on rechargeable aqueous batteries have relied heavily on thick glass fiber-based separators that necessitate the use of a large volume of electrolyte, thus reducing the energy density of the battery. Moreover, using Ti, which offers high deformation resistance and limited ductility, as the exclusive current collector in aqueous systems, further complicates manufacturing and escalates production costs. Research on binders and carbon additives suitable for aqueous batteries is scant, as are studies on the optimization of electrode compositions incorporating these materials.

Addressing the aforementioned challenges requires prioritizing a profound and clear understanding of practical issues, the mechanisms behind proposed solutions, and the validity of evaluation and analysis methods. Multidisciplinary approaches that integrate materials science, organic/inorganic chemistry, and electrochemical engineering are essential for material development. Innovative electrolyte formulations based on novel salts, co-solvents, additives, and advanced SEI formation protocols or mechanisms, such as pulse charging/discharging, need exploration.

Optimizing the potential diagram of full cells (potential-shift strategy) can be one of the promising directions. Particularly crucial is addressing the significant issue of electrolyte reduction at the anode through a collective understanding of how the electrostatic potential (liquid Madelung potential) of carrier ions in the electrolyte is destabilized. Factors influencing the electrode potential, such as the dielectric properties and entropy of the electrolyte, should also be studied quantitatively and systematically. Research dedicated to tailoring active materials for aqueous electrolytes, coupled with an intensive exploration of structures that facilitate smooth intercalation and deintercalation of large and/or divalent ions, as well as doping/coating of active materials and the use of electrode additives, will enhance the battery energy density and long-term cycling stability. Furthermore, the development of new separators and current collectors that are thin, flexible, strong, and highly compatible with aqueous electrolytes will enhance battery safety. The use of electrolyte additives that allow for the employment of Al and Cu current collectors and the optimization of overall electrode and battery designs, including binders, carbon additives, and other components, is advantageous in this research direction.

Overcoming these barriers through strategic and innovative methods will pave the way for the future expansion of high-energy-density rechargeable aqueous batteries. Such advancements will play a pivotal role in promoting a green power network and realizing an energy-efficient and sustainable society.

Author contributions

A. Y. conceived and guided the manuscript direction and thoroughly reviewed the manuscript. S. K. wrote the first draft. S. N., N. T., A. K. contributed to editing Sections 5 and 7.7, 6.1 and 7.4, 1 and 4.3, respectively.

Data availability

This review article does not contain any primary data. All data discussed in this manuscript are available within the cited literature and publicly accessible sources.

Conflicts of interest

There are no conflicts to declare.

Acknowledgements

This study was supported by the Japan Science and Technology Agency (JST) CREST Program (grant no. JP 21467943), a JST Program on Open Innovation Platform for Industry-Academia Co-Creation (grant no. JPMJPF2016), a Japan Society for the Promotion of Science (JSPS) Grant-in Aid for Scientific Research (S) (grant no. 20H05673), a JSPS Grant-in-Aid for Specially Promoted Research (no. 15H05701), a JST FOREST Program (grant no. JPMJFR223L), and JSPS KAKENHI (grant no. 21K20480, 22K05284, 23K04906, 23K13817).

References

- 1 The Nobel Prize in Chemistry 2019, <https://www.nobelprize.org/prizes/chemistry/2019/popular-information>, 2024.12.29.
- 2 P. V. Kamat, *ACS Energy Lett.*, 2019, **4**, 2757–2759.
- 3 A. K. Stephan, *Joule*, 2019, **3**, 2583–2584.
- 4 J. Xie and Y.-C. Lu, *Nat. Commun.*, 2020, **11**, 2499.
- 5 A. Yoshino, *Angew. Chem., Int. Ed.*, 2012, **51**, 5798–5800.
- 6 P. F. Mottelay, *Bibliographical History of Electricity and Magnetism, chronologically arranged*, Charles Griffin and Company Limited, London, 2008, p. 247.
- 7 A. Kozawa, Primary Batteries—Leclanché Systems, *Comprehensive Treatise of Electrochemistry*, Springer US, Boston, 1981, pp. 207–218.
- 8 K. Kordes, Primary Batteries—Alkaline Manganese Dioxide-Zinc Batteries, *Comprehensive Treatise of Electrochemistry*, Springer US, Boston, 1981, pp. 219–232.
- 9 S. Ruben, Primary Batteries—Sealed Mercurial Cathode Dry Cells, *Comprehensive Treatise of Electrochemistry*, Springer US, Boston, 1981, pp. 233–245.
- 10 G. G. Yadav, X. Wei and M. Meeus, Primary zinc-air batteries, *Electrochemical Power Sources: Fundamentals Systems and Applications*, Elsevier, 2021, pp. 23–45.
- 11 D. Berndt, Secondary Batteries—Lead-Acid Batteries, *Comprehensive Treatise of Electrochemistry*, Springer US, Boston, 1981, pp. 371–384.
- 12 F. von Sturm, Secondary Batteries—Nickel-Cadmium Battery, *Comprehensive Treatise of Electrochemistry*, Springer US, Boston, 1981, pp. 385–405.
- 13 P. Ruetschi, F. Meli and J. Desilvestro, *J. Power Sources*, 1995, **57**, 85–91.
- 14 F. von Sturm, Secondary Batteries—Silver-Zinc Battery, *Comprehensive Treatise of Electrochemistry*, Springer US, Boston, 1981, pp. 407–419.
- 15 M. L. Kronenberg and G. E. Blomgren, Primary Batteries—Lithium Batteries, *Comprehensive Treatise of Electrochemistry*, Springer US, Boston, 1981, pp. 247–278.
- 16 G. V. Zhuang, K. Xu, H. Yang, T. R. Jow and P. N. Ross, *J. Phys. Chem. B*, 2005, **109**, 17567–17573.
- 17 W. Li, J. R. Dahn and D. S. Wainwright, *Science*, 1994, **264**, 1115–1118.
- 18 L. Suo, O. Borodin, T. Gao, M. Olguin, J. Ho, X. Fan, C. Luo, C. Wang and K. Xu, *Science*, 2015, **350**, 938–943.
- 19 Y. Yamada, K. Usui, K. Sodeyama, S. Ko, Y. Tateyama and A. Yamada, *Nat. Energy*, 2016, **1**, 16129.
- 20 L. Suo, D. Oh, Y. Lin, Z. Zhuo, O. Borodin, T. Gao, F. Wang, A. Kushima, Z. Wang, H.-C. Kim, Y. Qi, W. Yang, F. Pan, J. Li, K. Xu and C. Wang, *J. Am. Chem. Soc.*, 2017, **139**, 18670–18680.
- 21 S. Ko, Y. Yamada and A. Yamada, *ACS Appl. Mater. Interfaces*, 2019, **11**, 45554–45560.
- 22 H. Kim, J. Hong, K.-Y. Park, H. Kim, S.-W. Kim and K. Kang, *Chem. Rev.*, 2014, **114**, 11788–11827.
- 23 D. Bin, F. Wang, A. G. Tamirat, L. Suo, Y. Wang, C. Wang and Y. Xia, *Adv. Energy Mater.*, 2018, **8**(17), 1703008.
- 24 D. Pahari and S. Puravankara, *ACS Sustainable Chem. Eng.*, 2020, **8**(29), 10613–10625.
- 25 X. Zhang, T. Xiong, B. He, S. Feng, X. Wang, L. Wei and L. Mai, *Energy Environ. Sci.*, 2022, **15**, 3750–3774.
- 26 B. Tang, L. Shan, S. Liang and J. Zhou, *Energy Environ. Sci.*, 2019, **12**, 3288–3304.
- 27 X. Li, L. Wang, Y. Fu, H. Dang, D. Wang and F. Ran, *Nano Energy*, 2023, **116**, 108858.
- 28 K. Adachi, A. Kitada, K. Fukami and K. Murase, *Electrochim. Acta*, 2020, **338**, 135873.
- 29 J. Liu, J. Hu, Q. Deng, J. Mo, H. Xie, Z. Liu, Y. Xiong, X. Wu and Y. Wu, *Isr. J. Chem.*, 2015, **55**, 521–536.
- 30 D. Chao, W. Zhou, F. Xie, C. Ye, H. Li, M. Jaroniec and S.-Z. Qiao, *Sci. Adv.*, 2020, **6**, eaba4098.
- 31 Y. Liu, X. Lu, F. Lai, T. Liu, P. R. Shearing, I. P. Parkin, G. He and D. J. L. Brett, *Joule*, 2021, **5**, 2845–2903.
- 32 H. Ahn, D. Kim, M. Lee and K. W. Nam, *Commun. Mater.*, 2023, **4**, 37.
- 33 W. Li and J. R. Dahn, *J. Electrochem. Soc.*, 1995, **142**, 1742–1746.
- 34 G. N. Lewis and F. G. Keyes, *J. Am. Chem. Soc.*, 1913, **35**, 340–344.



35 R. G. Selim, K. R. Hill and M. L. B. Rao, National Aeronautics and Space Administration, Fourth Quarterly Report - Research and Development of a High Capacity Nonaqueous Secondary Battery, NAS CR-54874, 1965.

36 M. S. Whittingham, *Science*, 1976, **192**, 1126–1127.

37 S. Megahed and B. Scrosati, *J. Power Sources*, 1994, **51**, 79–104.

38 J. B. Goodenough, *Acc. Chem. Res.*, 2013, **46**, 1053–1061.

39 M. Li, J. Lu, Z. Chen and K. Amine, *Adv. Mater.*, 2018, **30**(13), 1800561.

40 Y. Nishi, *J. Power Sources*, 2001, **100**, 101–106.

41 M. M. Thackeray, C. Wolverton and E. D. Isaacs, *Energy Environ. Sci.*, 2012, **5**, 7854.

42 J. W. Choi and D. Aurbach, *Nat. Rev. Mater.*, 2016, **1**, 16013.

43 T. Placke, R. Kloepsch, S. Dühnen and M. Winter, *J. Solid State Electrochem.*, 2017, **21**, 1939–1964.

44 M. Winter, B. Barnett and K. Xu, *Chem. Rev.*, 2018, **118**, 11433–11456.

45 P. Albertus, S. Babinec, S. Litzelman and A. Newman, *Nat. Energy*, 2017, **3**, 16–21.

46 S. Ko, Y. Yamada and A. Yamada, *Joule*, 2021, **5**, 998–1009.

47 S. Ko, Y. Yamada and A. Yamada, *Batteries Supercaps*, 2020, 1–8.

48 S. Ko, X. Han, T. Shimada, N. Takenaka, Y. Yamada and A. Yamada, *Nat. Sustainability*, 2023, **6**, 1705–1714.

49 C.-Y. Wang, G. Zhang, S. Ge, T. Xu, Y. Ji, X.-G. Yang and Y. Leng, *Nature*, 2016, **529**, 515–518.

50 M.-T. F. Rodrigues, G. Babu, H. Gullapalli, K. Kalaga, F. N. Sayed, K. Kato, J. Joyner and P. M. Ajayan, *Nat. Energy*, 2017, **2**, 17108.

51 J. Hou, M. Yang, D. Wang and J. Zhang, *Adv. Energy Mater.*, 2020, **10**(18), 1904152.

52 J. Holoubek, H. Liu, Z. Wu, Y. Yin, X. Xing, G. Cai, S. Yu, H. Zhou, T. A. Pascal, Z. Chen and P. Liu, *Nat. Energy*, 2021, **6**, 303–313.

53 G. X. Wang, S. Zhong, D. H. Bradhurst, S. X. Dou and H. K. Liu, *J. Power Sources*, 1998, **74**, 198–201.

54 J. Köhler, H. Makihara, H. Uegaito, H. Inoue and M. Toki, *Electrochim. Acta*, 2000, **46**, 59–65.

55 H. Wang, K. Huang, Y. Zeng, S. Yang and L. Chen, *Electrochim. Acta*, 2007, **52**, 3280–3285.

56 H. Wang, K. Huang, Y. Zeng, F. Zhao and L. Chen, *Electrochim. Solid-State Lett.*, 2007, **10**, A199.

57 G. J. Wang, H. P. Zhang, L. J. Fu, B. Wang and Y. P. Wu, *Electrochim. Commun.*, 2007, **9**, 1873–1876.

58 G. J. Wang, N. H. Zhao, L. C. Yang, Y. P. Wu, H. Q. Wu and R. Holze, *Electrochim. Acta*, 2007, **52**, 4911–4915.

59 G. Wang, L. Fu, N. Zhao, L. Yang, Y. Wu and H. Wu, *Angew. Chem., Int. Ed.*, 2007, **46**, 295–297.

60 J.-Y. Luo and Y.-Y. Xia, *Adv. Funct. Mater.*, 2007, **17**, 3877–3884.

61 H. Wang, Y. Zeng, K. Huang, S. Liu and L. Chen, *Electrochim. Acta*, 2007, **52**, 5102–5107.

62 G. Wang, Q. Qu, B. Wang, Y. Shi, S. Tian and Y. Wu, *ChemPhysChem*, 2008, **9**, 2299–2301.

63 G. J. Wang, L. J. Fu, B. Wang, N. H. Zhao, Y. P. Wu and R. Holze, *J. Appl. Electrochem.*, 2008, **38**, 579–581.

64 X.-H. Liu, T. Saito, T. Doi, S. Okada and J. Yamaki, *J. Power Sources*, 2009, **189**, 706–710.

65 J.-Y. Luo, W.-J. Cui, P. He and Y.-Y. Xia, *Nat. Chem.*, 2010, **2**, 760–765.

66 G. J. Wang, L. C. Yang, Q. T. Qu, B. Wang, Y. P. Wu and R. Holze, *J. Solid State Electrochem.*, 2010, **14**, 865–869.

67 M. Zhao, Q. Zheng, F. Wang, W. Dai and X. Song, *Electrochim. Acta*, 2011, **56**, 3781–3784.

68 W. Tang, L. Liu, Y. Zhu, H. Sun, Y. Wu and K. Zhu, *Energy Environ. Sci.*, 2012, **5**, 6909.

69 R. B. Shivashankaraiah, H. Manjunatha, K. C. Mahesh, G. S. Suresh and T. V. Venkatesha, *J. Solid State Electrochem.*, 2012, **16**, 1279–1290.

70 L. Liu, F. Tian, M. Zhou, H. Guo and X. Wang, *Electrochim. Acta*, 2012, **70**, 360–364.

71 C. Li, X. Sun, Q. Du and H. Zhang, *Solid State Ionics*, 2013, **249**–**250**, 72–77.

72 M. Zhao, B. Zhang, G. Huang, H. Zhang and X. Song, *J. Power Sources*, 2013, **232**, 181–186.

73 M. Vujković, I. Stojković, N. Cvjetićanin and S. Mentus, *Electrochim. Acta*, 2013, **92**, 248–256.

74 H. Qin, Z. P. Song, H. Zhan and Y. H. Zhou, *J. Power Sources*, 2014, **249**, 367–372.

75 Y. Wang, X. Cui, Y. Zhang, L. Zhang, X. Gong and G. Zheng, *Adv. Mater.*, 2016, **28**, 7626–7632.

76 L. Suo, O. Borodin, W. Sun, X. Fan, C. Yang, F. Wang, T. Gao, Z. Ma, M. Schroeder, A. von Cresce, S. M. Russell, M. Armand, A. Angell, K. Xu and C. Wang, *Angew. Chem., Int. Ed.*, 2016, **55**, 7136–7141.

77 Z. Zhou, W. Luo, H. Huang, S. Huang, Y. Xia, N. Zhou and Z. He, *Ceram. Int.*, 2017, **43**, 99–105.

78 H. Wang, H. Zhang, Y. Cheng, K. Feng, X. Li and H. Zhang, *J. Mater. Chem. A*, 2017, **5**, 593–599.

79 L. Chen, W. Li, Z. Guo, Y. Wang, C. Wang, Y. Che and Y. Xia, *J. Electrochem. Soc.*, 2015, **162**, A1972–A1977.

80 X. Dong, H. Yu, Y. Ma, J. L. Bao, D. G. Truhlar, Y. Wang and Y. Xia, *Chem. – Eur. J.*, 2017, **23**, 2560–2565.

81 W. Sun, L. Suo, F. Wang, N. Eidson, C. Yang, F. Han, Z. Ma, T. Gao, M. Zhu and C. Wang, *Electrochim. Commun.*, 2017, **82**, 71–74.

82 Y. Liang, Y. Jing, S. Gheytani, K.-Y. Lee, P. Liu, A. Facchetti and Y. Yao, *Nat. Mater.*, 2017, **16**, 841–848.

83 F. Wang, L. Suo, Y. Liang, C. Yang, F. Han, T. Gao, W. Sun and C. Wang, *Adv. Energy Mater.*, 2017, **7**(8), 1600922.

84 H. Wang, H. Zhang, Y. Cheng, K. Feng, X. Li and H. Zhang, *Electrochim. Acta*, 2018, **278**, 279–289.

85 S. Ko, Y. Yamada, K. Miyazaki, T. Shimada, E. Watanabe, Y. Tateyama, T. Kamiya, T. Honda, J. Akikusa and A. Yamada, *Electrochim. Commun.*, 2019, **104**, 106488.

86 A. S. Lakhnot, T. Gupta, Y. Singh, P. Hundekar, R. Jain, F. Han and N. Koratkar, *Energy Storage Mater.*, 2020, **27**, 506–513.

87 H. Umeno, K. Kawai, D. Asakura, M. Okubo and A. Yamada, *Adv. Sci.*, 2022, **9**(12), 2104907.

88 K. Xu and C. Wang, *Nat. Energy*, 2016, **1**, 16161.

89 D. Reber, R.-S. Kühnel and C. Battaglia, *ACS Mater. Lett.*, 2019, **1**, 44–51.



90 Q. Zheng, S. Miura, K. Miyazaki, S. Ko, E. Watanabe, M. Okoshi, C. Chou, Y. Nishimura, H. Nakai, T. Kamiya, T. Honda, J. Akikusa, Y. Yamada and A. Yamada, *Angew. Chem., Int. Ed.*, 2019, **58**, 14202–14207.

91 D. Reber, N. Takenaka, R.-S. Kühnel, A. Yamada and C. Battaglia, *J. Phys. Chem. Lett.*, 2020, **11**, 4720–4725.

92 R. S. Carmichael, Mineral Composition of Rocks, *Practical Handbook of Physical Properties of Rocks and Minerals*, CRC Press, Boca Raton, 2017, p. 3.

93 J.-M. Tarascon, *Nat. Chem.*, 2010, **2**, 510.

94 E. A. Olivetti, G. Ceder, G. G. Gaustad and X. Fu, *Joule*, 2017, **1**, 229–243.

95 T. C. Wanger, *Conserv. Lett.*, 2011, **4**, 202–206.

96 Y. Li, Y. Lu, C. Zhao, Y.-S. Hu, M.-M. Titirici, H. Li, X. Huang and L. Chen, *Energy Storage Mater.*, 2017, **7**, 130–151.

97 Tradingeconomics, <https://tradingeconomics.com>, 2024.12.29.

98 K. Knehr, J. Kubal and S. Ahmed, Argonne National Laboratory, Report – Estimated cost of EV batteries 2019–2024, 2024.

99 D. Wu, X. Li, X. Liu, J. Yi, P. Acevedo-Peña, E. Reguera, K. Zhu, D. Bin, N. Melzack, R. G. A. Wills, J. Huang, X. Wang, X. Lin, D. Yu and J. Ma, *J. Phys.: Energy*, 2022, **4**, 041501.

100 E. R. Nightingale, *J. Phys. Chem.*, 1959, **63**, 1381–1387.

101 J. Mähler and I. Persson, *Inorg. Chem.*, 2012, **51**, 425–438.

102 R. D. Shannon, *Acta Crystallogr., Sect. A*, 1976, **32**, 751–767.

103 N. Yabuuchi, K. Kubota, M. Dahbi and S. Komaba, *Chem. Rev.*, 2014, **114**, 11636–11682.

104 T. Hosaka, K. Kubota, A. S. Hameed and S. Komaba, *Chem. Rev.*, 2020, **120**, 6358–6466.

105 N. Ohtomo and K. Arakawa, *Bull. Chem. Soc. Jpn.*, 1979, **52**, 2755–2759.

106 G. Pálinkás, T. Radnai and F. Hajdu, *Z. Naturforsch.*, 1980, **35**, 107–114.

107 S. Bouazizi and S. Nasr, *J. Mol. Struct.*, 2007, **837**, 206–213.

108 M. Maeda and H. Ohtaki, *Bull. Chem. Soc. Jpn.*, 1975, **48**, 3755–3756.

109 N. Ohtomo and K. Arakawa, *Bull. Chem. Soc. Jpn.*, 1980, **53**, 1789–1794.

110 H. Ohtaki and N. Fukushima, *J. Solution Chem.*, 1992, **21**, 23–38.

111 R. Mancinelli, A. Botti, F. Bruni, M. A. Ricci and A. K. Soper, *J. Phys. Chem. B*, 2007, **111**, 13570–13577.

112 A. K. Soper and K. Weckström, *Biophys. Chem.*, 2006, **124**, 180–191.

113 H. H. Loeffler and B. M. Rode, *J. Chem. Phys.*, 2002, **117**, 110–117.

114 W. Rudolph, M. H. Brooker and C. C. Pye, *J. Phys. Chem.*, 1995, **99**, 3793–3797.

115 H. Du, J. C. Rasaiah and J. D. Miller, *J. Phys. Chem. B*, 2007, **111**, 209–217.

116 S. S. Azam, T. S. Hofer, B. R. Randolph and B. M. Rode, *J. Phys. Chem. A*, 2009, **113**, 1827–1834.

117 S. Liu, R. Zhang, J. Mao, J. Yuwono, C. Wang, K. Davey and Z. Guo, *Appl. Phys. Rev.*, 2023, **10**, 021304.

118 T. Hosaka, A. Noda, K. Kubota, K. Chiguchi, Y. Matsuda, K. Ida, S. Yasuno and S. Komaba, *ACS Appl. Mater. Interfaces*, 2022, **14**, 23507–23517.

119 X. Wu, Y. Cao, X. Ai, J. Qian and H. Yang, *Electrochem. Commun.*, 2013, **31**, 145–148.

120 K. Nakamoto, R. Sakamoto, Y. Sawada, M. Ito and S. Okada, *Small Methods*, 2019, **3**, 1800220.

121 L. Jiang, L. Liu, J. Yue, Q. Zhang, A. Zhou, O. Borodin, L. Suo, H. Li, L. Chen, K. Xu and Y. Hu, *Adv. Mater.*, 2020, **32**(2), 1904427.

122 L. Jiang, Y. Lu, C. Zhao, L. Liu, J. Zhang, Q. Zhang, X. Shen, J. Zhao, X. Yu, H. Li, X. Huang, L. Chen and Y.-S. Hu, *Nat. Energy*, 2019, **4**, 495–503.

123 X. Wu, Y. Cao, X. Ai, J. Qian and H. Yang, *Electrochem. Commun.*, 2013, **31**, 145–148.

124 C. Deng, S. Zhang, Z. Dong and Y. Shang, *Nano Energy*, 2014, **4**, 49–55.

125 Y. Liu, B. H. Zhang, S. Y. Xiao, L. L. Liu, Z. B. Wen and Y. P. Wu, *Electrochim. Acta*, 2014, **116**, 512–517.

126 Y. Liu, Y. Qiao, W. Zhang, H. Xu, Z. Li, Y. Shen, L. Yuan, X. Hu, X. Dai and Y. Huang, *Nano Energy*, 2014, **5**, 97–104.

127 M. Pasta, C. D. Wessells, N. Liu, J. Nelson, M. T. McDowell, R. A. Huggins, M. F. Toney and Y. Cui, *Nat. Commun.*, 2014, **5**, 3007.

128 D. J. Kim, Y. H. Jung, K. K. Bharathi, S. H. Je, D. K. Kim, A. Coskun and J. W. Choi, *Adv. Energy Mater.*, 2014, **4**(12), 1400133.

129 Y. Liu, Y. Qiao, W. Zhang, H. Wang, K. Chen, H. Zhu, Z. Li and Y. Huang, *J. Mater. Chem. A*, 2015, **3**, 7780–7785.

130 Y. Wang, L. Mu, J. Liu, Z. Yang, X. Yu, L. Gu, Y. Hu, H. Li, X. Yang, L. Chen and X. Huang, *Adv. Energy Mater.*, 2015, **5**(22), 1501005.

131 A. J. Fernández-Ropero, D. Saurel, B. Acebedo, T. Rojo and M. Casas-Cabanas, *J. Power Sources*, 2015, **291**, 40–45.

132 X. Wu, M. Sun, S. Guo, J. Qian, Y. Liu, Y. Cao, X. Ai and H. Yang, *ChemNanoMat*, 2015, **1**, 188–193.

133 Y. Liu, Y. Qiao, X. Lou, X. Zhang, W. Zhang and Y. Huang, *ACS Appl. Mater. Interfaces*, 2016, **8**, 14564–14571.

134 Q. Zhang, C. Liao, T. Zhai and H. Li, *Electrochim. Acta*, 2016, **196**, 470–478.

135 H. Gao and J. B. Goodenough, *Angew. Chem., Int. Ed.*, 2016, **55**, 12768–12772.

136 L. Suo, O. Borodin, Y. Wang, X. Rong, W. Sun, X. Fan, S. Xu, M. A. Schroeder, A. V. Cresce, F. Wang, C. Yang, Y. Hu, K. Xu and C. Wang, *Adv. Energy Mater.*, 2017, **7**(21), 1701189.

137 K. Nakamoto, R. Sakamoto, M. Ito, A. Kitajou and S. Okada, *Electrochemistry*, 2017, **85**, 179–185.

138 J. Zhang, D. Zhang, F. Niu, X. Li, C. Wang and J. Yang, *ChemPlusChem*, 2017, **82**, 1170–1173.

139 Y. Wang, Z. Feng, D. Laul, W. Zhu, M. Provencher, M. L. Trudeau, A. Guerfi and K. Zaghib, *J. Power Sources*, 2018, **374**, 211–216.

140 H. Wang, T. Zhang, C. Chen, M. Ling, Z. Lin, S. Zhang, F. Pan and C. Liang, *Nano Res.*, 2018, **11**, 490–498.

141 X. Cao, L. Wang, J. Chen and J. Zheng, *J. Mater. Chem. A*, 2018, **6**, 15762–15770.

142 J. Han, H. Zhang, A. Varzi and S. Passerini, *ChemSusChem*, 2018, **11**, 3704–3707.



143 H. Zhang, S. Jeong, B. Qin, D. Vieira Carvalho, D. Buchholz and S. Passerini, *ChemSusChem*, 2018, **11**, 1382–1389.

144 L. Fu, X. Xue, Y. Tang, D. Sun, H. Xie and H. Wang, *Electrochim. Acta*, 2018, **289**, 21–28.

145 K. Nakamoto, R. Sakamoto, Y. Sawada, M. Ito and S. Okada, *Small Methods*, 2019, **3**(4), 1800220.

146 X. Shan, F. Guo, D. S. Charles, Z. Lebens-Higgins, S. Abdel Razek, J. Wu, W. Xu, W. Yang, K. L. Page, J. C. Neufeld, M. Feygenson, L. F. J. Piper and X. Teng, *Nat. Commun.*, 2019, **10**, 4975.

147 Z. Liu, G. Pang, S. Dong, Y. Zhang, C. Mi and X. Zhang, *Electrochim. Acta*, 2019, **311**, 1–7.

148 Y. Qiu, Y. Yu, J. Xu, Y. Liu, M. Ou, S. Sun, P. Wei, Z. Deng, Y. Xu, C. Fang, Q. Li, J. Han and Y. Huang, *J. Mater. Chem. A*, 2019, **7**, 24953–24963.

149 S. Liu, L. Wang, J. Liu, M. Zhou, Q. Nian, Y. Feng, Z. Tao and L. Shao, *J. Mater. Chem. A*, 2019, **7**, 248–256.

150 S. Sevinc, B. Tekin, A. Ata, M. Morcrette, H. Perrot, O. Sel and R. Demir-Cakan, *J. Power Sources*, 2019, **412**, 55–62.

151 L. Sharma, K. Nakamoto, R. Sakamoto, S. Okada and P. Barpanda, *ChemElectroChem*, 2019, **6**, 444–449.

152 Q. Nian, S. Liu, J. Liu, Q. Zhang, J. Shi, C. Liu, R. Wang, Z. Tao and J. Chen, *ACS Appl. Energy Mater.*, 2019, **2**, 4370–4378.

153 S. Qiu, X. Wu, M. Wang, M. Lucero, Y. Wang, J. Wang, Z. Yang, W. Xu, Q. Wang, M. Gu, J. Wen, Y. Huang, Z. J. Xu and Z. Feng, *Nano Energy*, 2019, **64**, 103941.

154 B. Wang, X. Wang, C. Liang, M. Yan and Y. Jiang, *Chem-ElectroChem*, 2019, **6**, 4848–4853.

155 Z. Hou, X. Zhang, H. Ao, M. Liu, Y. Zhu and Y. Qian, *Mater. Today Energy*, 2019, **14**, 100337.

156 T. Jin, X. Ji, P. Wang, K. Zhu, J. Zhang, L. Cao, L. Chen, C. Cui, T. Deng, S. Liu, N. Piao, Y. Liu, C. Shen, K. Xie, L. Jiao and C. Wang, *Angew. Chem., Int. Ed.*, 2021, **60**, 11943–11948.

157 K. Nakamoto, R. Sakamoto, Y. Nishimura, J. Xia, M. Ito and S. Okada, *Electrochemistry*, 2021, **89**, 21–00056.

158 D. Reber, R. Grissa, M. Becker, R. Kühnel and C. Battaglia, *Adv. Energy Mater.*, 2021, **11**(5), 2002913.

159 W. Yang, X. Wang, S. Lu, Y. Gao, T. Gao, T. Guo, Q. Xie and Y. Ruan, *ChemSusChem*, 2023, **16**(8), e202202257.

160 D. S. Charles, M. Feygenson, K. Page, J. Neufeld, W. Xu and X. Teng, *Nat. Commun.*, 2017, **8**, 15520.

161 M. Xia, X. Zhang, T. Liu, H. Yu, S. Chen, N. Peng, R. Zheng, J. Zhang and J. Shu, *Chem. Eng. J.*, 2020, **394**, 124923.

162 M. Wang, H. Wang, H. Zhang and X. Li, *J. Energy Chem.*, 2020, **48**, 14–20.

163 Y. Li, W. Deng, Z. Zhou, C. Li, M. Zhang, X. Yuan, J. Hu, H. Chen and R. Li, *J. Mater. Chem. A*, 2021, **9**, 2822–2829.

164 J. Ge, X. Yi, L. Fan and B. Lu, *J. Energy Chem.*, 2021, **57**, 28–33.

165 H. Chen, Z. Zhang, Z. Wei, G. Chen, X. Yang, C. Wang and F. Du, *Sustainable Energy Fuels*, 2020, **4**, 128–131.

166 G. Liang, Z. Gan, X. Wang, X. Jin, B. Xiong, X. Zhang, S. Chen, Y. Wang, H. He and C. Zhi, *ACS Nano*, 2021, **15**, 17717–17728.

167 T. Hosaka, R. Takahashi, K. Kubota, R. Tatara, Y. Matsuda, K. Ida, K. Kuba and S. Komaba, *J. Power Sources*, 2022, **548**, 232096.

168 J. Ge, L. Fan, A. M. Rao, J. Zhou and B. Lu, *Nat. Sustainability*, 2021, **5**, 225–234.

169 D. Reber, R. Figi, R.-S. Kühnel and C. Battaglia, *Electrochim. Acta*, 2019, **321**, 134644.

170 S. Ko, Y. Yamada and A. Yamada, *Electrochem. Commun.*, 2020, **116**, 106764.

171 R.-S. Kühnel, D. Reber and C. Battaglia, *J. Electrochem. Soc.*, 2020, **167**, 070544.

172 S. Kondou, E. Nozaki, S. Terada, M. L. Thomas, K. Ueno, Y. Umebayashi, K. Dokko and M. Watanabe, *J. Phys. Chem. C*, 2018, **122**, 20167–20175.

173 R.-S. Kühnel, D. Reber, A. Remhof, R. Figi, D. Bleiner and C. Battaglia, *Chem. Commun.*, 2016, **52**, 10435–10438.

174 Y. Yokoyama, T. Fukutsuka, K. Miyazaki and T. Abe, *J. Electrochem. Soc.*, 2018, **165**, A3299–A3303.

175 M. Becker, D. Rentsch, D. Reber, A. Aribia, C. Battaglia and R. Kühnel, *Angew. Chem., Int. Ed.*, 2021, **60**, 14100–14108.

176 P. Jaumaux, X. Yang, B. Zhang, J. Safaei, X. Tang, D. Zhou, C. Wang and G. Wang, *Angew. Chem., Int. Ed.*, 2021, **60**, 19965–19973.

177 J. Zheng, G. Tan, P. Shan, T. Liu, J. Hu, Y. Feng, L. Yang, M. Zhang, Z. Chen, Y. Lin, J. Lu, J. C. Neufeld, Y. Ren, K. Amine, L.-W. Wang, K. Xu and F. Pan, *Chem*, 2018, **4**, 2872–2882.

178 S. Kondou, E. Nozaki, S. Terada, M. L. Thomas, K. Ueno, Y. Umebayashi, K. Dokko and M. Watanabe, *J. Phys. Chem. C*, 2018, **122**, 20167–20175.

179 M. R. Lukatskaya, J. I. Feldblyum, D. G. Mackanic, F. Lissel, D. L. Michels, Y. Cui and Z. Bao, *Energy Environ. Sci.*, 2018, **11**, 2876–2883.

180 D. Reber, R.-S. Kühnel and C. Battaglia, *Sustainable Energy Fuels*, 2017, **1**, 2155–2161.

181 M. H. Lee, S. J. Kim, D. Chang, J. Kim, S. Moon, K. Oh, K.-Y. Park, W. M. Seong, H. Park, G. Kwon, B. Lee and K. Kang, *Mater. Today*, 2019, **29**, 26–36.

182 X. Bu, L. Su, Q. Dou, S. Lei and X. Yan, *J. Mater. Chem. A*, 2019, **7**, 7541–7547.

183 R. Sakamoto, M. Yamashita, K. Nakamoto, Y. Zhou, N. Yoshimoto, K. Fujii, T. Yamaguchi, A. Kitajou and S. Okada, *Phys. Chem. Chem. Phys.*, 2020, **22**, 26452–26458.

184 R.-S. Kühnel, D. Reber and C. Battaglia, *ACS Energy Lett.*, 2017, **2**, 2005–2006.

185 A. Kitada, S. Ko, R. Ikeya, Y. Yamada and A. Yamada, *J. Phys. Chem. C*, 2023, **127**, 3432–3436.

186 P. L. Stigliano, N. Pianta, S. Bonizzoni, M. Mauri, R. Simonutti, R. Lorenzi, B. Vigani, V. Berbenni, S. Rossi, P. Mustarelli and R. Ruffo, *Phys. Chem. Chem. Phys.*, 2021, **23**, 1139–1145.

187 J. Han, A. Mariani, H. Zhang, M. Zarzabeitia, X. Gao, D. V. Carvalho, A. Varzi and S. Passerini, *Energy Storage Mater.*, 2020, **30**, 196–205.

188 D. P. Leonard, Z. Wei, G. Chen, F. Du and X. Ji, *ACS Energy Lett.*, 2018, **3**, 373–374.



189 T. Liu, L. Tang, H. Luo, S. Cheng and M. Liu, *Chem. Commun.*, 2019, **55**, 12817–12820.

190 W. Deng, X. Wang, C. Liu, C. Li, J. Chen, N. Zhu, R. Li and M. Xue, *Energy Storage Mater.*, 2019, **20**, 373–379.

191 L. Coustan, G. Shul and D. Bélanger, *Electrochem. Commun.*, 2017, **77**, 89–92.

192 D. Degou lange, N. Dubouis and A. Grimaud, *J. Chem. Phys.*, 2021, **155**, 064701.

193 N. Dubouis, A. Serva, R. Berthoin, G. Jeanmairet, B. Porcheron, E. Salager, M. Salanne and A. Grimaud, *Nat. Catal.*, 2020, **3**, 656–663.

194 A. von Wald Cresce and K. Xu, *Carbon Energy*, 2021, **3**, 721–751.

195 D. Çirmi, R. Aydin and F. Köleli, *J. Electroanal. Chem.*, 2015, **736**, 101–106.

196 F. Habashi, S. A. Mikhail and K. V. Van, *Can. J. Chem.*, 1976, **54**, 3646–3650.

197 L. Suo, D. Oh, Y. Lin, Z. Zhuo, O. Borodin, T. Gao, F. Wang, A. Kushima, Z. Wang, H. C. Kim, Y. Qi, W. Yang, F. Pan, J. Li, K. Xu and C. Wang, *J. Am. Chem. Soc.*, 2017, **139**, 18670–18680.

198 K. Miyazaki, N. Takenaka, E. Watanabe, Y. Yamada, Y. Tateyama and A. Yamada, *ACS Appl. Mater. Interfaces*, 2020, **12**, 42734–42738.

199 K. Miyazaki, N. Takenaka, E. Watanabe, S. Iizuka, Y. Yamada, Y. Tateyama and A. Yamada, *J. Phys. Chem. Lett.*, 2019, **10**, 6301–6305.

200 Y. Yamada, J. Wang, S. Ko, E. Watanabe and A. Yamada, *Nat. Energy*, 2019, **4**, 269–280.

201 K. Sodeyama, Y. Yamada, K. Aikawa, A. Yamada and Y. Tateyama, *J. Phys. Chem. C*, 2014, **118**, 14091–14097.

202 Y. Yamada, K. Furukawa, K. Sodeyama, K. Kikuchi, M. Yaegashi, Y. Tateyama and A. Yamada, *J. Am. Chem. Soc.*, 2014, **136**, 5039–5046.

203 C. Xu, B. Sun, T. Gustafsson, K. Edström, D. Brandell and M. Hahlin, *J. Mater. Chem. A*, 2014, **2**, 7256–7264.

204 D. Aurbach, I. Weissman, A. Schechter and H. Cohen, *Langmuir*, 1996, **12**, 3991–4007.

205 B. S. Parimalam and B. L. Lucht, *J. Electrochem. Soc.*, 2018, **165**, A251–A255.

206 D. L. Wood, J. Li and C. Daniel, *J. Power Sources*, 2015, **275**, 234–242.

207 D. H. Jeon, *Energy Storage Mater.*, 2019, **18**, 139–147.

208 L. Zhao, Y. Li, M. Yu, Y. Peng and F. Ran, *Adv. Sci.*, 2023, **10**(17), 2300283.

209 Z. Li, R. Bouchal, T. Mendez-Morales, A.-L. Rollet, C. Rizzi, S. Le Vot, F. Favier, B. Rotenberg, O. Borodin, O. Fontaine and M. Salanne, *J. Phys. Chem. B*, 2019, **123**, 10514–10521.

210 Z. Yu, L. A. Curtiss, R. E. Winans, Y. Zhang, T. Li and L. Cheng, *J. Phys. Chem. Lett.*, 2020, **11**, 1276–1281.

211 J. Kim, B. Koo, J. Lim, J. Jeon, C. Lim, H. Lee, K. Kwak and M. Cho, *ACS Energy Lett.*, 2022, **7**, 189–196.

212 J. Lim, K. Park, H. Lee, J. Kim, K. Kwak and M. Cho, *J. Am. Chem. Soc.*, 2018, **140**, 15661–15667.

213 O. Borodin, L. Suo, M. Gobet, X. Ren, F. Wang, A. Faraone, J. Peng, M. Olguin, M. Schroeder, M. S. Ding, E. Gobrogge, A. von Wald Cresce, S. Munoz, J. A. Dura, S. Greenbaum, C. Wang and K. Xu, *ACS Nano*, 2017, **11**, 10462–10471.

214 K. Goloviznina, A. Serva and M. Salanne, *J. Am. Chem. Soc.*, 2024, **146**, 8142–8148.

215 M. McEldrew, Z. A. H. Goodwin, S. Bi, A. A. Kornyshev and M. Z. Bazant, *J. Electrochem. Soc.*, 2021, **168**, 050514.

216 T. R. Kartha, D. N. Reddy and B. S. Mallik, *Mater. Adv.*, 2021, **2**, 7691–7700.

217 M. A. González, H. Akiba, O. Borodin, G. J. Cuello, L. Hennet, S. Kohara, E. J. Maginn, L. Mangin-Thro, O. Yamamuro, Y. Zhang, D. L. Price and M.-L. Saboungi, *Phys. Chem. Chem. Phys.*, 2022, **24**, 10727–10736.

218 T. Shimada, N. Takenaka, E. Watanabe, Y. Yamada, Y.-T. Cui, Y. Harada, M. Okubo and A. Yamada, *J. Phys. Chem. B*, 2021, **125**, 11534–11539.

219 X. Liu, S.-C. Lee, S. Seifert, L. He, C. Do, R. E. Winans, G. Kwon and T. Li, *Chem. Mater.*, 2023, **35**, 2088–2094.

220 Y. Zhang and E. J. Maginn, *J. Phys. Chem. B*, 2021, **125**, 13246–13254.

221 L. Ma and J. Jiang, *J. Phys. Chem. Lett.*, 2024, **15**, 4531–4537.

222 N. H. C. Lewis, B. Dereka, Y. Zhang, E. J. Maginn and A. Tokmakoff, *J. Phys. Chem. B*, 2022, **126**, 5305–5319.

223 A. Einstein, *Ann. Phys.*, 1905, **322**, 549–560.

224 W. Sutherland, *London, Edinburgh Dublin Philos. Mag. J. Sci.*, 1905, **9**, 781–785.

225 G. G. Stokes, *On the Effect of the Internal Friction of Fluids on the Motion of Pendulums*, Mathematical and Physical Papers, Cambridge University Press, England Cambridge, 2009, pp. 1–10.

226 J. Han, A. Mariani, S. Passerini and A. Varzi, *Energy Environ. Sci.*, 2023, **16**, 1480–1501.

227 L. Jiang, D. Dong and Y.-C. Lu, *Nano Res. Energy*, 2022, **1**, e9120003.

228 D. Turnbull and J. C. Fisher, *J. Chem. Phys.*, 1949, **17**, 71–73.

229 W. H. Wang, C. Dong and C. H. Shek, *Mater. Sci. Eng., R*, 2004, **44**, 45–89.

230 O. Schumacher, C. J. Marvel, M. N. Kelly, P. R. Cantwell, R. P. Vinci, J. M. Rickman, G. S. Rohrer and M. P. Harmer, *Curr. Opin. Solid State Mater. Sci.*, 2016, **20**, 316–323.

231 D. Li, D. Zeng, X. Yin, H. Han, L. Guo and Y. Yao, *Calphad*, 2016, **53**, 78–89.

232 S. Arrhenius, *Z. Phys. Chem.*, 1889, **4**, 96–116.

233 S. Arrhenius, *Z. Phys. Chem.*, 1889, **4**, 226–248.

234 K. Tasaki, K. Kanda, S. Nakamura and M. Ue, *J. Electrochem. Soc.*, 2003, **150**, A1628.

235 M. E. Jacox, K. K. Irikura and W. E. Thompson, *J. Chem. Phys.*, 2000, **113**, 5705–5715.

236 S. Di Muzio, O. Palumbo, S. Brutti and A. Paolone, *J. Electrochem. Soc.*, 2022, **169**, 070523.

237 C. G. Barlowz, *Electrochem. Solid-State Lett.*, 1999, **2**, 362.

238 K. Xu, *Chem. Rev.*, 2004, **104**, 4303–4418.

239 L. Terborg, S. Nowak, S. Passerini, M. Winter, U. Karst, P. R. Haddad and P. N. Nesterenko, *Anal. Chim. Acta*, 2012, **714**, 121–126.

240 L. J. Krause, W. Lamanna, J. Summerfield, M. Engle, G. Korba, R. Loch and R. Atanasoski, *J. Power Sources*, 1997, **68**, 320–325.



241 X. Wang, E. Yasukawa and S. Mori, *J. Electrochem. Soc.*, 1999, **146**, 3992–3998.

242 B. Liu, T. Lv, A. Zhou, X. Zhu, Z. Lin, T. Lin and L. Suo, *Nat. Commun.*, 2024, **15**, 2922.

243 C. Behling, J. Lüchtfeld, S. J. Wachs, K. J. J. Mayrhofer and B. B. Berkes, *Electrochim. Acta*, 2024, **473**, 143480.

244 M. Aziz-Kerrzo, K. G. Conroy, A. M. Fenlon, S. T. Farrell and C. B. Breslin, *Biomaterials*, 2001, **22**, 1531–1539.

245 Y. Ohko, S. Saitoh, T. Tatsuma and A. Fujishima, *J. Electrochem. Soc.*, 2001, **148**, B24.

246 A. S. Malik and L. A. Fredin, *J. Phys. Chem. C*, 2023, **127**, 3444–3451.

247 J. Li, J. Fleetwood, W. B. Hawley and W. Kays, *Chem. Rev.*, 2022, **122**, 903–956.

248 R. Choudhury, J. Wild and Y. Yang, *Joule*, 2021, **5**, 1301–1305.

249 H. Jeong, J. Jang and C. Jo, *Chem. Eng. J.*, 2022, **446**, 136860.

250 X. Ji, *eScience*, 2021, **1**, 99–107.

251 J. Warner, *Handbook of Lithium-Ion Battery Pack Design: Chemistry, Components, Types and Terminology*, Elsevier, 2015.

252 L. H. Saw, Y. Ye and A. A. O. Tay, *J. Clean Prod.*, 2016, **113**, 1032–1045.

253 K. Wang, L. Wang, K. Zheng, Z. He, D. J. Politis, G. Liu and S. Yuan, *Int. J. Extreme Manuf.*, 2020, **2**, 032001.

254 MSE supplies, <https://www.msesupplies.com>, 2024.12.29.

255 MTI corporation, <https://www.mtixtl.com>, 2024.12.29.

256 Sigma-Aldrich, <https://www.sigmaldrich.com>, 2024.12.29.

257 F. C. Walsh, *Trans. IMF*, 1991, **69**, 107–110.

258 E. Lizundia, C. M. Costa, R. Alves and S. Lanceros-Méndez, *Carbohydr. Polym. Technol. Appl.*, 2020, **1**, 100001.

259 S. Li, W. Zhu, Q. Tang, Z. Huang, P. Yu, X. Gui, S. Lin, J. Hu and Y. Tu, *Energy Fuels*, 2021, **35**, 12938–12947.

260 H. Kim, J. Hong, K.-Y. Park, H. Kim, S.-W. Kim and K. Kang, *Chem. Rev.*, 2014, **114**, 11788–11827.

261 X. Zhang, T. Xiong, B. He, S. Feng, X. Wang, L. Wei and L. Mai, *Energy Environ. Sci.*, 2022, **15**, 3750–3774.

262 R. Benedek, M. M. Thackeray and A. van de Walle, *Chem. Mater.*, 2008, **20**, 5485–5490.

263 N. Makivć, J.-Y. Cho, K. D. Harris, J.-M. Tarascon, B. Limoges and V. Balland, *Chem. Mater.*, 2021, **33**, 3436–3448.

264 T. Ohzuku, M. Kitagawa and T. Hirai, *J. Electrochem. Soc.*, 1990, **137**, 769–775.

265 M. M. Thackeray, P. J. Johnson, L. A. de Picciotto, P. G. Bruce and J. B. Goodenough, *Mater. Res. Bull.*, 1984, **19**, 179–187.

266 N. Nakayama, T. Nozawa, Y. Iriyama, T. Abe, Z. Ogumi and K. Kikuchi, *J. Power Sources*, 2007, **174**, 695–700.

267 L. Tian and A. Yuan, *J. Power Sources*, 2009, **192**, 693–697.

268 T. Zhang, D. Li, Z. Tao and J. Chen, *Prog. Nat. Sci.*, 2013, **23**, 256–272.

269 K. Amine, H. Tukamoto, H. Yasuda and Y. Fujita, *J. Power Sources*, 1997, **68**, 604–608.

270 R. Ruffo, C. Wessells, R. A. Huggins and Y. Cui, *Electrochem. Commun.*, 2009, **11**, 247–249.

271 K. Mizushima, P. C. Jones, P. J. Wiseman and J. B. Goodenough, *Mater. Res. Bull.*, 1980, **15**, 783–789.

272 C. Delmas, C. Fouassier and P. Hagenmuller, *Eur. Phys. J. B*, 1980, **99**, 81–85.

273 A. Ramanujapuram, D. Gordon, A. Magasinski, B. Ward, N. Nitta, C. Huang and G. Yushin, *Energy Environ. Sci.*, 2016, **9**, 1841–1848.

274 C. Lee, Y. Yokoyama, Y. Kondo, Y. Miyahara, T. Abe and K. Miyazaki, *ACS Appl. Mater. Interfaces*, 2020, **12**, 56076–56085.

275 H. Umeno, K. Kawai, D. Asakura, M. Okubo and A. Yamada, *Adv. Sci.*, 2022, **9**(12), 2104907.

276 C. Lee, Y. Yokoyama, Y. Kondo, Y. Miyahara, K. Miyazaki and T. Abe, *Chem. Lett.*, 2021, **50**, 1071–1074.

277 C. Lee, Y. Yokoyama, Y. Kondo, Y. Miyahara, K. Miyazaki and T. Abe, *J. Power Sources*, 2020, **477**, 229036.

278 C. Lee, Y. Yokoyama, Y. Kondo, Y. Miyahara, T. Abe and K. Miyazaki, *Adv. Energy Mater.*, 2021, **11**(25), 2100756.

279 C. Lee, Y. Yokoyama, Y. Kondo, Y. Miyahara, T. Abe and K. Miyazaki, *ACS Appl. Mater. Interfaces*, 2021, **13**, 44284–44293.

280 C. Lee, J.-M. Choi, Y. Miyahara, I. Jeon, K. Miyazaki and T. Abe, *Chem. Mater.*, 2024, **36**, 860–869.

281 A. K. Padhi, K. S. Nanjundaswamy and J. B. Goodenough, *J. Electrochem. Soc.*, 1997, **144**, 1188–1194.

282 A. K. Padhi, K. S. Nanjundaswamy, C. Masquelier, S. Okada and J. B. Goodenough, *J. Electrochem. Soc.*, 1997, **144**, 1609–1613.

283 A. Yamada, S. C. Chung and K. Hinokuma, *J. Electrochem. Soc.*, 2001, **148**, A224.

284 A. Yamada, H. Koizumi, N. Sonoyama and R. Kanno, *Electrochem. Solid-State Lett.*, 2005, **8**, A409.

285 P. He, X. Zhang, Y.-G. Wang, L. Cheng and Y.-Y. Xia, *J. Electrochem. Soc.*, 2008, **155**, A144.

286 P. He, J.-L. Liu, W.-J. Cui, J.-Y. Luo and Y.-Y. Xia, *Electrochim. Acta*, 2011, **56**, 2351–2357.

287 R. Malik, D. Burch, M. Bazant and G. Ceder, *Nano Lett.*, 2010, **10**, 4123–4127.

288 M. Minakshi, P. Singh, S. Thurgate and K. Prince, *Electrochem. Solid-State Lett.*, 2006, **9**, A471.

289 M. D. Johannes, K. Hoang, J. L. Allen and K. Gaskell, *Phys. Rev. B: Condens. Matter Mater. Phys.*, 2012, **85**, 115106.

290 J. R. Dahn, T. V. Buuren and U. Vonsacken, *US Pat.*, 4965150, 1990.

291 A. Kannan, *Solid State Ionics*, 2003, **159**, 265–271.

292 H. Li, P. He, Y. Wang, E. Hosono and H. Zhou, *J. Mater. Chem.*, 2011, **21**, 10999.

293 M. Zhang and J. R. Dahn, *J. Electrochem. Soc.*, 1996, **143**, 2730–2735.

294 S. Lee, I. N. Ivanov, J. K. Keum and H. N. Lee, *Sci. Rep.*, 2016, **6**, 19621.

295 T. Partheeban and M. Sasidharan, *J. Mater. Sci.*, 2020, **55**, 2155–2165.

296 M. Zhao, B. Zhang, G. Huang, H. Zhang and X. Song, *J. Power Sources*, 2013, **232**, 181–186.

297 J. M. Tarascon, F. J. Disalvo, D. W. Murphy, G. W. Hull, E. A. Rietman and J. V. Waszczak, *J. Solid State Chem.*, 1984, **54**, 204–212.

298 P. J. Mulhern and R. R. Haering, *Can. J. Phys.*, 1984, **62**, 527–531.

299 E. Levi, G. Gershinsky, D. Aurbach and O. Isnard, *Inorg. Chem.*, 2009, **48**, 8751–8758.



300 G. X. Wang, D. H. Bradhurst, S. X. Dou and H. K. Liu, *J. Power Sources*, 2003, **124**, 231–236.

301 B. Zhang, R. Tan, L. Yang, J. Zheng, K. Zhang, S. Mo, Z. Lin and F. Pan, *Energy Storage Mater.*, 2018, **10**, 139–159.

302 R. Li, C. Lin, N. Wang, L. Luo, Y. Chen, J. Li and Z. Guo, *Adv. Compos. Hybrid Mater.*, 2018, **1**, 440–459.

303 T. Ohzuku, A. Ueda and N. Yamamoto, *J. Electrochem. Soc.*, 1995, **142**, 1431–1435.

304 T. Ohzuku and T. Ohzuku, *7th International Meeting on Lithium Batteries*, Boston, 1994.

305 E. Ferg, R. J. Gummow, A. de Kock and M. M. Thackeray, *J. Electrochem. Soc.*, 1994, **141**, L147–L150.

306 A. Deschanvres, B. Raveau and Z. Sekkal, *Mater. Res. Bull.*, 1971, **6**, 699–704.

307 K. M. Colbow, J. R. Dahn and R. R. Haering, *J. Power Sources*, 1989, **26**, 397–402.

308 H. Yan, D. Zhang Qilu, X. Duo and X. Sheng, *Ceram. Int.*, 2021, **47**, 5870–5895.

309 J. Gao, B. Gong, Q. Zhang, G. Wang, Y. Dai and W. Fan, *Ionics*, 2015, **21**, 2409–2416.

310 H. Liu, Z. Zhu, J. Huang, X. He, Y. Chen, R. Zhang, R. Lin, Y. Li, S. Yu, X. Xing, Q. Yan, X. Li, M. J. Frost, K. An, J. Feng, R. Kostecki, H. Xin, S. P. Ong and P. Liu, *ACS Mater. Lett.*, 2019, **1**, 96–102.

311 F. Sauvage, E. Baudrin and J.-M. Tarascon, *Sens. Actuators, B*, 2007, **120**, 638–644.

312 J. F. Whitacre, T. Wiley, S. Shanbhag, Y. Wenzhuo, A. Mohamed, S. E. Chun, E. Weber, D. Blackwood, E. Lynch-Bell, J. Gulakowski, C. Smith and D. Humphreys, *J. Power Sources*, 2012, **213**, 255–264.

313 W. Song, X. Ji, Y. Zhu, H. Zhu, F. Li, J. Chen, F. Lu, Y. Yao and C. E. Banks, *ChemElectroChem*, 2014, **1**, 871–876.

314 L. H. B. Nguyen, T. Broux, P. S. Camacho, D. Denux, L. Bourgeois, S. Belin, A. Iadecola, F. Fauth, D. Carlier, J. Olchowka, C. Masquelier and L. Croguennec, *Energy Storage Mater.*, 2019, **20**, 324–334.

315 W. Ji, H. Huang, X. Zhang, D. Zheng, T. Ding, T. H. Lambert and D. Qu, *Nano Energy*, 2020, **72**, 104705.

316 Y. Ishado, A. Inoishi and S. Okada, *Electrochemistry*, 2020, **88**, 457–462.

317 Y. Qi, Z. Tong, J. Zhao, L. Ma, T. Wu, H. Liu, C. Yang, J. Lu and Y.-S. Hu, *Joule*, 2018, **2**, 2348–2363.

318 S. I. Park, I. Gocheva, S. Okada and J. Yamaki, *J. Electrochem. Soc.*, 2011, **158**, A1067.

319 M. Wu, W. Ni, J. Hu and J. Ma, *Nano-Micro Lett.*, 2019, **11**, 44.

320 Q. T. Qu, L. L. Liu, Y. P. Wu and R. Holze, *Electrochim. Acta*, 2013, **96**, 8–12.

321 A. A. Karyakin, *Electroanalysis*, 2001, **13**, 813–819.

322 P. Poizot, J. Gaubicher, S. Renault, L. Dubois, Y. Liang and Y. Yao, *Chem. Rev.*, 2020, **120**, 6490–6557.

323 S. Xu, Y. Chen and C. Wang, *J. Mater. Chem. A*, 2020, **8**, 15547–15574.

324 K. Hurlbutt, S. Wheeler, I. Capone and M. Pasta, *Joule*, 2018, **2**, 1950–1960.

325 V. D. Neff, *J. Electrochem. Soc.*, 1978, **125**, 886–887.

326 C. Ma, C. Lin, N. Li, Y. Chen, Y. Yang, L. Tan, Z. Wang, Q. Zhang and Y. Zhu, *Small*, 2024, **20**(23), 2310184.

327 M. A. Lumley, D.-H. Nam and K.-S. Choi, *ACS Appl. Mater. Interfaces*, 2020, **12**, 36014–36025.

328 W. Deng, Y. Shen, J. Qian, Y. Cao and H. Yang, *ACS Appl. Mater. Interfaces*, 2015, **7**, 21095–21099.

329 X. Wu, Y. Qi, J. J. Hong, Z. Li, A. S. Hernandez and X. Ji, *Angew. Chem., Int. Ed.*, 2017, **56**, 13026–13030.

330 J. Han, Y. Niu, S. Bao, Y.-N. Yu, S.-Y. Lu and M. Xu, *PhysChemComm*, 2016, **52**, 11661–11664.

331 N. Voronina, J. H. Jo, A. Konarov, J. Kim and S. Myung, *Small*, 2020, **16**(20), 2001090.

332 S. Komaba, T. Hasegawa, M. Dahbi and K. Kubota, *Electrochim. Commun.*, 2015, **60**, 172–175.

333 L. Droguet, G. M. Hobold, M. F. Lagadec, R. Guo, C. Lethien, M. Hallot, O. Fontaine, J.-M. Tarascon, B. M. Gallant and A. Grimaud, *ACS Energy Lett.*, 2021, **6**, 2575–2583.

334 S. J. Visco, V. Nimon, A. Petrov, K. Pridatko, N. Goncharenko, E. Nimon, L. De Jonghe, M. Hendrickson and E. Plichta, *Lithium Air Batteries Based on Protected Lithium Electrodes*, Springer New York, New York, 2014, pp. 179–200.

335 S. Visco, U.S. DOE Advanced Manufacturing Office Peer Review Meeting, Manufacturing of Protected Lithium Electrodes for Advanced Lithium-Air, Lithium-Water & Lithium-Sulfur Batteries, May, 2015.

336 X. Wang, Y. Hou, Y. Zhu, Y. Wu and R. Holze, *Sci. Rep.*, 2013, **3**, 1401.

337 C. Yang, J. Chen, T. Qing, X. Fan, W. Sun, A. von Cresce, M. S. Ding, O. Borodin, J. Vatamanu, M. A. Schroeder, N. Eidson, C. Wang and K. Xu, *Joule*, 2017, **1**, 122–132.

338 H. Moon, R. Tatara, T. Mandai, K. Ueno, K. Yoshida, N. Tachikawa, T. Yasuda, K. Dokko and M. Watanabe, *J. Phys. Chem. C*, 2014, **118**, 20246–20256.

339 P. K. R. Kottam, D. Kalkan, M. Wohlfahrt-Mehrens and M. Marinaro, *J. Electrochem. Soc.*, 2019, **166**, A1574–A1579.

340 S. Ko, T. Obukata, T. Shimada, N. Takenaka, M. Nakayama, A. Yamada and Y. Yamada, *Nat. Energy*, 2022, **7**, 1217–1224.

341 E. Hückel, *Ergebnisse der Exakten Naturwissenschaften*, Springer Berlin Heidelberg, Berlin, Heidelberg, 1924, pp. 199–276.

342 S. Ko, N. Takenaka, A. Kitada and A. Yamada, *Next Energy*, 2023, **1**, 100014.

343 N. Takenaka, S. Ko, A. Kitada and A. Yamada, *Nat. Commun.*, 2024, **15**, 1319.

344 E. A. Guggenheim and J. C. Turgeon, *Trans. Faraday Soc.*, 1955, **51**, 747.

345 K. S. Pitzer, *J. Phys. Chem.*, 1973, **77**, 268–277.

346 D. Reber, R. Grissa, M. Becker, R. Kühnel and C. Battaglia, *Adv. Energy Mater.*, 2021, **11**(5), 2002913.

347 W. A. Henderson, F. McKenna, M. A. Khan, N. R. Brooks, V. G. Young and R. Frech, *Chem. Mater.*, 2005, **17**, 2284–2289.

348 M. McEldrew, Z. A. H. Goodwin, A. A. Kornyshev and M. Z. Bazant, *J. Phys. Chem. Lett.*, 2018, **9**, 5840–5846.

349 J. Vatamanu and O. Borodin, *J. Phys. Chem. Lett.*, 2017, **8**, 4362–4367.



350 M. Amereller, M. Multerer, C. Schreiner, J. Lodermeyer, A. Schmid, J. Barthel and H. J. Gores, *J. Chem. Eng. Data*, 2009, **54**, 468–471.

351 R. Von Burg, *J. Appl. Toxicol.*, 1995, **15**, 237–241.

352 D. G. Churchill, *J. Chem. Educ.*, 2006, **83**, 1798.

353 M. R. Lukatskaya, J. I. Feldblyum, D. G. Mackanic, F. Lissel, D. L. Michels, Y. Cui and Z. Bao, *Energy Environ. Sci.*, 2018, **11**, 2876–2883.

354 T. Fujie, N. Takenaka and M. Nagaoka, *J. Comput. Chem.*, 2019, **18**, 29–37.

355 D. Aurbach, A. Zaban, A. Schechter, Y. Ein-Eli, E. Zinigrad and B. Markovsky, *J. Electrochem. Soc.*, 1995, **142**, 2873–2882.

356 I. A. Shkrob, Y. Zhu, T. W. Marin and D. Abraham, *J. Phys. Chem. C*, 2013, **117**, 19270–19279.

357 Y. Yamada and A. Yamada, *J. Electrochem. Soc.*, 2015, **162**, A2406–A2423.

358 D. Aurbach, *J. Electrochem. Soc.*, 1995, **142**, 2873–2882.

359 D. Aurbach, Y. Ein-Eli and A. Zaban, *J. Electrochem. Soc.*, 1994, **141**, L1–L3.

360 E. Markevich, G. Salitra and D. Aurbach, *ACS Energy Lett.*, 2017, **2**, 1337–1345.

361 E. Peled and S. Menkin, *J. Electrochem. Soc.*, 2017, **164**, A1703–A1719.

362 C. Zhang, Z. Cai, R. Huang and H. Pan, *Batteries Supercaps*, 2023, **6**(6), e202300053.

363 I. Stojković, N. Cvjetićanin, I. Pašti, M. Mitić and S. Mentus, *Electrochem. Commun.*, 2009, **11**, 1512–1514.

364 F. Wang, O. Borodin, M. S. Ding, M. Gobet, J. Vatamanu, X. Fan, T. Gao, N. Eidson, Y. Liang, W. Sun, S. Greenbaum, K. Xu and C. Wang, *Joule*, 2018, **2**, 927–937.

365 F. Wang, Y. Lin, L. Suo, X. Fan, T. Gao, C. Yang, F. Han, Y. Qi, K. Xu and C. Wang, *Energy Environ. Sci.*, 2016, **9**, 3666–3673.

366 C. Yang, L. Suo, O. Borodin, F. Wang, W. Sun, T. Gao, X. Fan, S. Hou, Z. Ma, K. Amine, K. Xu and C. Wang, *Proc. Natl. Acad. Sci. U. S. A.*, 2017, **114**, 6197–6202.

367 P. Jiang, L. Chen, H. Shao, S. Huang, Q. Wang, Y. Su, X. Yan, X. Liang, J. Zhang, J. Feng and Z. Liu, *ACS Energy Lett.*, 2019, **4**, 1419–1426.

368 J. Xie, Z. Liang and Y.-C. Lu, *Nat. Mater.*, 2020, **19**, 1006–1011.

369 L. Chen, J. Zhang, Q. Li, J. Vatamanu, X. Ji, T. P. Pollard, C. Cui, S. Hou, J. Chen, C. Yang, L. Ma, M. S. Ding, M. Garaga, S. Greenbaum, H.-S. Lee, O. Borodin, K. Xu and C. Wang, *ACS Energy Lett.*, 2020, **5**, 968–974.

370 Y. Shang, N. Chen, Y. Li, S. Chen, J. Lai, Y. Huang, W. Qu, F. Wu and R. Chen, *Adv. Mater.*, 2020, **32**(40), 2004017.

371 J. M. Wrogemann, S. Künne, A. Heckmann, I. A. Rodríguez-Pérez, V. Siozios, B. Yan, J. Li, M. Winter, K. Beltrop and T. Placke, *Adv. Energy Mater.*, 2020, **10**(8), 1902709.

372 J. Chen, J. Vatamanu, L. Xing, O. Borodin, H. Chen, X. Guan, X. Liu, K. Xu and W. Li, *Adv. Energy Mater.*, 2020, **10**(3), 1902654.

373 Z. Hou, M. Dong, Y. Xiong, X. Zhang, Y. Zhu and Y. Qian, *Adv. Energy Mater.*, 2020, **10**(15), 1903665.

374 Y. Wang, T. Wang, D. Dong, J. Xie, Y. Guan, Y. Huang, J. Fan and Y.-C. Lu, *Matter*, 2022, **5**, 162–179.

375 S. Chen, P. Sun, B. Sun, J. Humphreys, P. Zou, K. Xie and S. Tao, *Energy Storage Mater.*, 2021, **37**, 598–608.

376 Q. Nian, W. Zhu, S. Zheng, S. Chen, B.-Q. Xiong, Z. Wang, X. Wu, Z. Tao and X. Ren, *ACS Appl. Mater. Interfaces*, 2021, **13**, 51048–51056.

377 D. Dong, J. Xie, Z. Liang and Y.-C. Lu, *ACS Energy Lett.*, 2022, **7**, 123–130.

378 X. Hou, T. P. Pollard, W. Zhao, X. He, X. Ju, J. Wang, L. Du, E. Paillard, H. Lin, K. Xu, O. Borodin, M. Winter and J. Li, *Small*, 2022, **18**(5), 2104986.

379 Z. Ma, J. Chen, J. Vatamanu, O. Borodin, D. Bedrov, X. Zhou, W. Zhang, W. Li, K. Xu and L. Xing, *Energy Storage Mater.*, 2022, **45**, 903–910.

380 X. Zhang, J. Chen, Z. Xu, Q. Dong, H. Ao, Z. Hou and Y. Qian, *Energy Storage Mater.*, 2022, **46**, 147–154.

381 J. Xu, X. Ji, J. Zhang, C. Yang, P. Wang, S. Liu, K. Ludwig, F. Chen, P. Kofinas and C. Wang, *Nat. Energy*, 2022, **7**, 186–193.

382 R. Lin, C. Ke, J. Chen, S. Liu and J. Wang, *Joule*, 2022, **6**, 399–417.

383 C. Zhang, B. Chen, Z. Cai, F. Zhang, R. Huang, M. Yan, Y. Liu and H. Pan, *J. Mater. Chem. A*, 2022, **10**, 20545–20551.

384 P. R. Kumar, Y. H. Jung, J. E. Wang and D. K. Kim, *J. Power Sources*, 2016, **324**, 421–427.

385 P. Ramesh Kumar, A. Kheireddine, U. Nisar, R. A. Shakoor, R. Essehli, R. Amin and I. Belharouak, *J. Power Sources*, 2019, **429**, 149–155.

386 H. Ao, C. Chen, Z. Hou, W. Cai, M. Liu, Y. Jin, X. Zhang, Y. Zhu and Y. Qian, *J. Mater. Chem. A*, 2020, **8**, 14190–14197.

387 Q. Nian, X. Zhang, Y. Feng, S. Liu, T. Sun, S. Zheng, X. Ren, Z. Tao, D. Zhang and J. Chen, *ACS Energy Lett.*, 2021, **6**, 2174–2180.

388 Z. Liang, F. Tian, G. Yang and C. Wang, *Nat. Commun.*, 2023, **14**, 3591.

389 Y. Li, Z. Zhou, W. Deng, C. Li, X. Yuan, J. Hu, M. Zhang, H. Chen and R. Li, *ChemElectroChem*, 2021, **8**, 1451–1454.

390 X. Yuan, Y. Li, Y. Zhu, W. Deng, C. Li, Z. Zhou, J. Hu, M. Zhang, H. Chen and R. Li, *ACS Appl. Mater. Interfaces*, 2021, **13**, 38248–38255.

391 J. Chen, S. Lei, S. Zhang, C. Zhu, Q. Liu, C. Wang, Z. Zhang, S. Wang, Y. Shi, L. Yin and R. Wang, *Adv. Funct. Mater.*, 2023, **33**(19), 2215027.

392 M. Xia, H. Fu, K. Lin, A. M. Rao, L. Cha, H. Liu, J. Zhou, C. Wang and B. Lu, *Energy Environ. Sci.*, 2024, **17**, 1255–1265.

393 L. Miao, R. Wang, W. Xin, L. Zhang, Y. Geng, H. Peng, Z. Yan, D. Jiang, Z. Qian and Z. Zhu, *Energy Storage Mater.*, 2022, **49**, 445–453.

394 D. Yang, M. Watanabe and T. Ishihara, *Small Methods*, 2023, **7**(9), 2300249.

395 G. Ma, L. Miao, Y. Dong, W. Yuan, X. Nie, S. Di, Y. Wang, L. Wang and N. Zhang, *Energy Storage Mater.*, 2022, **47**, 203–210.

396 S. Hosseini, A. Abbasi, L.-O. Uginet, N. Haustraete, S. Prasertthdam, T. Yonezawa and S. Kheawhom, *Sci. Rep.*, 2019, **9**, 14958.



397 L. Cao, D. Li, E. Hu, J. Xu, T. Deng, L. Ma, Y. Wang, X.-Q. Yang and C. Wang, *J. Am. Chem. Soc.*, 2020, **142**, 21404–21409.

398 Y. Zhang, H. Huang, X. Ning, C. Li, Z. Fan and L. Pan, *Energy Storage Mater.*, 2023, **56**, 542–550.

399 Y. Liu, C. Yu, X. Song, S. Hou, S. Lan, J. Yu, Y. Xie and J. Qiu, *J. Energy Chem.*, 2024, **93**, 361–367.

400 R. Feng, X. Chi, Q. Qiu, J. Wu, J. Huang, J. Liu and Y. Liu, *ACS Appl. Mater. Interfaces*, 2021, **13**, 40638–40647.

401 F. Ming, Y. Zhu, G. Huang, A.-H. Emwas, H. Liang, Y. Cui and H. N. Alshareef, *J. Am. Chem. Soc.*, 2022, **144**, 7160–7170.

402 J. Liu, C. Yang, X. Chi, B. Wen, W. Wang and Y. Liu, *Adv. Funct. Mater.*, 2022, **32**(1), 2106811.

403 A. Naveed, H. Yang, J. Yang, Y. Nuli and J. Wang, *Angew. Chem., Int. Ed.*, 2019, **58**, 2760–2764.

404 S. Wu, B. Su, M. Sun, S. Gu, Z. Lu, K. Zhang, D. Y. W. Yu, B. Huang, P. Wang, C. Lee and W. Zhang, *Adv. Mater.*, 2021, **33**(41), 2102390.

405 B. Qiu, L. Xie, G. Zhang, K. Cheng, Z. Lin, W. Liu, C. He, P. Zhang and H. Mi, *Chem. Eng. J.*, 2022, **449**, 137843.

406 Y. Wang, Z. Wang, W. K. Pang, W. Lie, J. A. Yuwono, G. Liang, S. Liu, A. M. D. Angelo, J. Deng, Y. Fan, K. Davey, B. Li and Z. Guo, *Nat. Commun.*, 2023, **14**, 2720.

407 G. Ni, M. Sun, Z. Hao, G. Zou, F. Cao, L. Qin, W. Chen and C. Zhou, *Mater Today Energy*, 2023, **31**, 101204.

408 W. Wang, S. Chen, X. Liao, R. Huang, F. Wang, J. Chen, Y. Wang, F. Wang and H. Wang, *Nat. Commun.*, 2023, **14**, 5443.

409 S. Chen, P. Sun, J. Humphreys, P. Zou, M. Zhang, G. Jeerh, B. Sun and S. Tao, *ACS Appl. Mater. Interfaces*, 2021, **13**, 46634–46643.

410 W. Deng, Z. Xu and X. Wang, *Energy Storage Mater.*, 2022, **52**, 52–60.

411 F. Wu, Y. Chen, Y. Chen, R. Yin, Y. Feng, D. Zheng, X. Xu, W. Shi, W. Liu and X. Cao, *Small*, 2022, **18**(27), 2202363.

412 Q. Jian, T. Wang, J. Sun, B. Liu and T. Zhao, *Chem. Eng. J.*, 2023, **466**, 143189.

413 M.-K. Huang, K. S. Anuratha, Y. Xiao, Y.-P. Chen and J.-Y. Lin, *Electrochim. Acta*, 2022, **424**, 140612.

414 X. Feng, P. Li, J. Yin, Z. Gan, Y. Gao, M. Li, Y. Cheng, X. Xu, Y. Su and S. Ding, *ACS Energy Lett.*, 2023, **8**, 1192–1200.

415 Y. Deng, Y. Wu, K. Zhang, M. Fan, L. Wang, Y. He and L. Yan, *J. Mater. Chem. A*, 2023, **11**, 8368–8379.

416 C. Lu, Z. Wang, Y. Zhang, G. Tang, Y. Wang, X. Guo, J. Li and L. Wei, *Nano Energy*, 2024, **120**, 109158.

417 W. Xiong, T. K. A. Hoang, D. Yang, Y. Liu, M. Ahmed, J. Xu, X. Qiu and P. Chen, *J. Energy Storage*, 2019, **26**, 100920.

418 J. Kong, H. Guo, Y. Li, M. Gong, X. Lin, L. Zhang and D. Wang, *Sustainable Energy Fuels*, 2024, **8**, 826–836.

419 H. Yan, X. Zhang, Z. Yang, M. Xia, C. Xu, Y. Liu, H. Yu, L. Zhang and J. Shu, *Coord. Chem. Rev.*, 2022, **452**, 214297.

420 J. Yue, J. Zhang, Y. Tong, M. Chen, L. Liu, L. Jiang, T. Lv, Y. Hu, H. Li, X. Huang, L. Gu, G. Feng, K. Xu, L. Suo and L. Chen, *Nat. Chem.*, 2021, **13**, 1061–1069.

421 S.-D. Han, O. Borodin, D. M. Seo, Z.-B. Zhou and W. A. Henderson, *J. Electrochem. Soc.*, 2014, **161**, A2042–A2053.

422 S.-D. Han, R. D. Sommer, P. D. Boyle, Z.-B. Zhou, V. G. Young, O. Borodin and W. A. Henderson, *J. Electrochem. Soc.*, 2022, **169**, 110544.

423 D. M. Seo, O. Borodin, S.-D. Han, P. D. Boyle and W. A. Henderson, *J. Electrochem. Soc.*, 2012, **159**, A1489–A1500.

424 G. R. Pastel, Y. Chen, T. P. Pollard, M. A. Schroeder, M. E. Bowden, A. Zheng, N. T. Hahn, L. Ma, V. Murugesan, J. Ho, M. Garaga, O. Borodin, K. Mueller, S. Greenbaum and K. Xu, *Energy Environ. Sci.*, 2022, **15**, 2460–2469.

425 W. A. Henderson, M. L. Helm, D. M. Seo, P. C. Trulove, H. C. De Long and O. Borodin, *J. Electrochem. Soc.*, 2022, **169**, 060515.

426 G. A. Vidulich and R. L. Kay, *J. Phys. Chem.*, 1962, **66**, 383.

427 V. Staemmler, *Angew. Chem., Int. Ed. Engl.*, 1979, **91**, 595.

428 M. Rabinovitz, Solute-Solute and Solute-Solvent Interactions: NMR Studies, *Jerusalem Symposia on Quantum Chemistry and Biochemistry*, Springer, Dordrecht, 1976, pp. 229–238.

429 W. Liu, L. Dong, B. Jiang, Y. Huang, X. Wang, C. Xu, Z. Kang, J. Mou and F. Kang, *Electrochim. Acta*, 2019, **320**, 134565.

430 X. Ji and L. F. Nazar, *Nat. Sustainability*, 2024, **7**, 98–99.

431 M. J. Park, H. Yaghoobnejad Asl and A. Manthiram, *ACS Energy Lett.*, 2020, **5**, 2367–2375.

432 J. Yang, R. Zhao, Y. Wang, Z. Hu, Y. Wang, A. Zhang, C. Wu and Y. Bai, *Adv. Funct. Mater.*, 2023, **33**(14), 2213510.

433 R. D. Shannon, *Acta Crystallogr., Sect. A*, 1976, **32**, 751–767.

434 J. Muldoon, C. B. Bucur and T. Gregory, *Chem. Rev.*, 2014, **114**, 11683–11720.

435 Z. Rong, R. Malik, P. Canepa, G. Sai Gautam, M. Liu, A. Jain, K. Persson and G. Ceder, *Chem. Mater.*, 2015, **27**, 6016–6021.

436 P. Canepa, G. Sai Gautam, D. C. Hannah, R. Malik, M. Liu, K. G. Gallagher, K. A. Persson and G. Ceder, *Chem. Rev.*, 2017, **117**, 4287–4341.

437 M. Liu, Z. Rong, R. Malik, P. Canepa, A. Jain, G. Ceder and K. A. Persson, *Energy Environ. Sci.*, 2015, **8**, 964–974.

438 D. Kundu, B. D. Adams, V. Duffort, S. H. Vajargah and L. F. Nazar, *Nat. Energy*, 2016, **1**, 16119.

439 W. Sun, F. Wang, S. Hou, C. Yang, X. Fan, Z. Ma, T. Gao, F. Han, R. Hu, M. Zhu and C. Wang, *J. Am. Chem. Soc.*, 2017, **139**, 9775–9778.

440 D. Kundu, S. Hosseini Vajargah, L. Wan, B. Adams, D. Prendergast and L. F. Nazar, *Energy Environ. Sci.*, 2018, **11**, 881–892.

441 L. E. Blanc, D. Kundu and L. F. Nazar, *Joule*, 2020, **4**, 771–799.

442 H. Yaghoobnejad Asl, S. Sharma and A. Manthiram, *J. Mater. Chem. A*, 2020, **8**, 8262–8267.

443 M. Yan, P. He, Y. Chen, S. Wang, Q. Wei, K. Zhao, X. Xu, Q. An, Y. Shuang, Y. Shao, K. T. Mueller, L. Mai, J. Liu and J. Yang, *Adv. Mater.*, 2018, **30**(1), 1703725.

444 J. Hao, X. Li, S. Zhang, F. Yang, X. Zeng, S. Zhang, G. Bo, C. Wang and Z. Guo, *Adv. Funct. Mater.*, 2020, **30**(30), 2001263.

445 C. Xu, B. Li, H. Du and F. Kang, *Angew. Chem., Int. Ed.*, 2012, **51**, 933–935.

446 J. Lee, J. B. Ju, W. Il Cho, B. W. Cho and S. H. Oh, *Electrochim. Acta*, 2013, **112**, 138–143.

447 B. Lee, C. S. Yoon, H. R. Lee, K. Y. Chung, B. W. Cho and S. H. Oh, *Sci. Rep.*, 2014, **4**, 6066.



448 B. Zhang, Y. Liu, X. Wu, Y. Yang, Z. Chang, Z. Wen and Y. Wu, *Chem. Commun.*, 2014, **50**, 1209–1211.

449 J. Hao, J. Mou, J. Zhang, L. Dong, W. Liu, C. Xu and F. Kang, *Electrochim. Acta*, 2018, **259**, 170–178.

450 M. H. Alfaruqi, V. Mathew, J. Gim, S. Kim, J. Song, J. P. Baboo, S. H. Choi and J. Kim, *Chem. Mater.*, 2015, **27**, 3609–3620.

451 H. Pan, Y. Shao, P. Yan, Y. Cheng, K. S. Han, Z. Nie, C. Wang, J. Yang, X. Li, P. Bhattacharya, K. T. Mueller and J. Liu, *Nat. Energy*, 2016, **1**, 16039.

452 N. Zhang, F. Cheng, Y. Liu, Q. Zhao, K. Lei, C. Chen, X. Liu and J. Chen, *J. Am. Chem. Soc.*, 2016, **138**, 12894–12901.

453 B. Jiang, C. Xu, C. Wu, L. Dong, J. Li and F. Kang, *Electrochim. Acta*, 2017, **229**, 422–428.

454 Y. Zeng, X. Zhang, Y. Meng, M. Yu, J. Yi, Y. Wu, X. Lu and Y. Tong, *Adv. Mater.*, 2017, **29**(26), 1700274.

455 W. Sun, F. Wang, S. Hou, C. Yang, X. Fan, Z. Ma, T. Gao, F. Han, R. Hu, M. Zhu and C. Wang, *J. Am. Chem. Soc.*, 2017, **139**, 9775–9778.

456 N. Zhang, F. Cheng, J. Liu, L. Wang, X. Long, X. Liu, F. Li and J. Chen, *Nat. Commun.*, 2017, **8**, 405.

457 H. Li, Z. Liu, G. Liang, Y. Huang, Y. Huang, M. Zhu, Z. Pei, Q. Xue, Z. Tang, Y. Wang, B. Li and C. Zhi, *ACS Nano*, 2018, **12**, 3140–3148.

458 B. Wu, G. Zhang, M. Yan, T. Xiong, P. He, L. He, X. Xu and L. Mai, *Small*, 2018, **14**(13), 1703850.

459 V. Soundharajan, B. Sambandam, S. Kim, V. Mathew, J. Jo, S. Kim, J. Lee, S. Islam, K. Kim, Y.-K. Sun and J. Kim, *ACS Energy Lett.*, 2018, **3**, 1998–2004.

460 C. Zhu, G. Fang, J. Zhou, J. Guo, Z. Wang, C. Wang, J. Li, Y. Tang and S. Liang, *J. Mater. Chem. A*, 2018, **6**, 9677–9683.

461 M. H. Alfaruqi, V. Mathew, J. Song, S. Kim, S. Islam, D. T. Pham, J. Jo, S. Kim, J. P. Baboo, Z. Xiu, K.-S. Lee, Y.-K. Sun and J. Kim, *Chem. Mater.*, 2017, **29**, 1684–1694.

462 P. Hu, M. Yan, T. Zhu, X. Wang, X. Wei, J. Li, L. Zhou, Z. Li, L. Chen and L. Mai, *ACS Appl. Mater. Interfaces*, 2017, **9**, 42717–42722.

463 N. Zhang, Y. Dong, M. Jia, X. Bian, Y. Wang, M. Qiu, J. Xu, Y. Liu, L. Jiao and F. Cheng, *ACS Energy Lett.*, 2018, **3**, 1366–1372.

464 J. Zhou, L. Shan, Z. Wu, X. Guo, G. Fang and S. Liang, *Chem. Commun.*, 2018, **54**, 4457–4460.

465 T. Wei, Q. Li, G. Yang and C. Wang, *Electrochim. Acta*, 2018, **287**, 60–67.

466 Y. Yang, Y. Tang, G. Fang, L. Shan, J. Guo, W. Zhang, C. Wang, L. Wang, J. Zhou and S. Liang, *Energy Environ. Sci.*, 2018, **11**, 3157–3162.

467 P. He, G. Zhang, X. Liao, M. Yan, X. Xu, Q. An, J. Liu and L. Mai, *Adv. Energy Mater.*, 2018, **8**(10), 1702463.

468 V. Soundharajan, B. Sambandam, S. Kim, M. H. Alfaruqi, D. Y. Putro, J. Jo, S. Kim, V. Mathew, Y.-K. Sun and J. Kim, *Nano Lett.*, 2018, **18**, 2402–2410.

469 F. Ming, H. Liang, Y. Lei, S. Kandambeth, M. Eddaoudi and H. N. Alshareef, *ACS Energy Lett.*, 2018, **3**, 2602–2609.

470 G. Yang, T. Wei and C. Wang, *ACS Appl. Mater. Interfaces*, 2018, **10**, 35079–35089.

471 T. Wei, Q. Li, G. Yang and C. Wang, *J. Mater. Chem. A*, 2018, **6**, 20402–20410.

472 L. Chen, Y. Ruan, G. Zhang, Q. Wei, Y. Jiang, T. Xiong, P. He, W. Yang, M. Yan, Q. An and L. Mai, *Chem. Mater.*, 2019, **31**, 699–706.

473 Z. Li, S. Ganapathy, Y. Xu, Z. Zhou, M. Sarilar and M. Wagemaker, *Adv. Energy Mater.*, 2019, **9**(22), 1900237.

474 L. Chen, Z. Yang and Y. Huang, *Nanoscale*, 2019, **11**, 13032–13039.

475 Y. Ding, Y. Peng, S. Chen, X. Zhang, Z. Li, L. Zhu, L.-E. Mo and L. Hu, *ACS Appl. Mater. Interfaces*, 2019, **11**, 44109–44117.

476 Y. Li, Z. Huang, P. K. Kalambate, Y. Zhong, Z. Huang, M. Xie, Y. Shen and Y. Huang, *Nano Energy*, 2019, **60**, 752–759.

477 X. Chen, L. Wang, H. Li, F. Cheng and J. Chen, *J. Energy Chem.*, 2019, **38**, 20–25.

478 J. Lai, H. Zhu, X. Zhu, H. Koritala and Y. Wang, *ACS Appl. Energy Mater.*, 2019, **2**, 1988–1996.

479 Q. Li, T. Wei, K. Ma, G. Yang and C. Wang, *ACS Appl. Mater. Interfaces*, 2019, **11**, 20888–20894.

480 Z. Cao, H. Chu, H. Zhang, Y. Ge, R. Clemente, P. Dong, L. Wang, J. Shen, M. Ye and P. M. Ajayan, *J. Mater. Chem. A*, 2019, **7**, 25262–25267.

481 X. Li, L. Ma, Y. Zhao, Q. Yang, D. Wang, Z. Huang, G. Liang, F. Mo, Z. Liu and C. Zhi, *Mater Today Energy*, 2019, **14**, 100361.

482 N. Zhang, M. Jia, Y. Dong, Y. Wang, J. Xu, Y. Liu, L. Jiao and F. Cheng, *Adv. Funct. Mater.*, 2019, **29**(10), 1807331.

483 T. Wei, Q. Li, G. Yang and C. Wang, *Adv. Energy Mater.*, 2019, **9**(34), 1901480.

484 J. Shin, D. S. Choi, H. J. Lee, Y. Jung and J. W. Choi, *Adv. Energy Mater.*, 2019, **9**(14), 1900083.

485 L. Shan, J. Zhou, W. Zhang, C. Xia, S. Guo, X. Ma, G. Fang, X. Wu and S. Liang, *Energy Technol.*, 2019, **7**(6), 1900022.

486 F. Hu, D. Xie, D. Zhao, G. Song and K. Zhu, *J. Energy Chem.*, 2019, **38**, 185–191.

487 K. Zhu, T. Wu and K. Huang, *ACS Nano*, 2019, **13**, 14447–14458.

488 L. Shan, Y. Yang, W. Zhang, H. Chen, G. Fang, J. Zhou and S. Liang, *Energy Storage Mater.*, 2019, **18**, 10–14.

489 L. Ma, N. Li, C. Long, B. Dong, D. Fang, Z. Liu, Y. Zhao, X. Li, J. Fan, S. Chen, S. Zhang and C. Zhi, *Adv. Funct. Mater.*, 2019, **29**(46), 1906142.

490 S. Islam, M. H. Alfaruqi, D. Y. Putro, V. Soundharajan, B. Sambandam, J. Jo, S. Park, S. Lee, V. Mathew and J. Kim, *J. Mater. Chem. A*, 2019, **7**, 20335–20347.

491 Y. Liu, Q. Li, K. Ma, G. Yang and C. Wang, *ACS Nano*, 2019, **13**, 12081–12089.

492 X. Wang, B. Xi, Z. Feng, W. Chen, H. Li, Y. Jia, J. Feng, Y. Qian and S. Xiong, *J. Mater. Chem. A*, 2019, **7**, 19130–19139.

493 S. Chen, Y. Zhang, H. Geng, Y. Yang, X. Rui and C. C. Li, *J. Power Sources*, 2019, **441**, 227192.

494 K. Zhu, T. Wu and K. Huang, *Adv. Energy Mater.*, 2019, **9**(38), 1901968.

495 Y. Liu, P. Hu, H. Liu, X. Wu and C. Zhi, *Mater Today Energy*, 2020, **17**, 100431.



496 F. Cui, J. Zhao, D. Zhang, Y. Fang, F. Hu and K. Zhu, *Chem. Eng. J.*, 2020, **390**, 124118.

497 H. Luo, B. Wang, F. Wang, J. Yang, F. Wu, Y. Ning, Y. Zhou, D. Wang, H. Liu and S. Dou, *ACS Nano*, 2020, **14**, 7328–7337.

498 P. He, J. Liu, X. Zhao, Z. Ding, P. Gao and L.-Z. Fan, *J. Mater. Chem. A*, 2020, **8**, 10370–10376.

499 M. Liao, J. Wang, L. Ye, H. Sun, Y. Wen, C. Wang, X. Sun, B. Wang and H. Peng, *Angew. Chem., Int. Ed.*, 2020, **59**, 2273–2278.

500 W. Zhang, C. Tang, B. Lan, L. Chen, W. Tang, C. Zuo, S. Dong, Q. An and P. Luo, *J. Alloys Compd.*, 2020, **819**, 152971.

501 W. Tang, B. Lan, C. Tang, Q. An, L. Chen, W. Zhang, C. Zuo, S. Dong and P. Luo, *ACS Sustainable Chem. Eng.*, 2020, **8**, 3681–3688.

502 D. Bin, W. Huo, Y. Yuan, J. Huang, Y. Liu, Y. Zhang, F. Dong, Y. Wang and Y. Xia, *Chem*, 2020, **6**, 968–984.

503 H. Jiang, Y. Zhang, L. Xu, Z. Gao, J. Zheng, Q. Wang, C. Meng and J. Wang, *Chem. Eng. J.*, 2020, **382**, 122844.

504 J. Li, K. McColl, X. Lu, S. Sathasivam, H. Dong, L. Kang, Z. Li, S. Zhao, A. G. Kafizas, R. Wang, D. J. L. Brett, P. R. Shearing, F. Corà, G. He, C. J. Carmalt and I. P. Parkin, *Adv. Energy Mater.*, 2020, **10**(15), 2000058.

505 Y.-Y. Liu, T.-T. Lv, H. Wang, X.-T. Guo, C.-S. Liu and H. Pang, *Chem. Eng. J.*, 2021, **417**, 128408.

506 Z. Zhang, B. Xi, X. Wang, X. Ma, W. Chen, J. Feng and S. Xiong, *Adv. Funct. Mater.*, 2021, **31**(34), 2103070.

507 H. Zhang, Z. Yao, D. Lan, Y. Liu, L. Ma and J. Cui, *J. Alloys Compd.*, 2021, **861**, 158560.

508 Z. Qi, T. Xiong, T. Chen, W. Shi, M. Zhang, Z. W. J. Ang, H. Fan, H. Xiao, W. S. V. Lee and J. Xue, *J. Alloys Compd.*, 2021, **870**, 159403.

509 J. Cao, D. Zhang, Y. Yue, T. Pakornchote, T. Bovornratanarak, M. Sawangphruk, X. Zhang and J. Qin, *Mater. Today Energy*, 2021, **21**, 100824.

510 C. Liu, R. Li, W. Liu, G. Shen and D. Chen, *ACS Appl. Mater. Interfaces*, 2021, **13**, 37194–37200.

511 S. Wu, S. Liu, L. Hu and S. Chen, *J. Alloys Compd.*, 2021, **878**, 160324.

512 Y. Shao, J. Zeng, J. Li, H. Ren, Z. Zhang, J. Liu, C. Mao, X. Guo and G. Li, *ChemElectroChem*, 2021, **8**, 1784–1791.

513 D. Chen, M. Lu, B. Wang, H. Cheng, H. Yang, D. Cai, W. Han and H. J. Fan, *Nano Energy*, 2021, **83**, 105835.

514 M. Liao, J. Wang, L. Ye, H. Sun, P. Li, C. Wang, C. Tang, X. Cheng, B. Wang and H. Peng, *J. Mater. Chem. A*, 2021, **9**, 6811–6818.

515 W. Shi, B. Yin, Y. Yang, M. B. Sullivan, J. Wang, Y.-W. Zhang, Z. G. Yu, W. S. V. Lee and J. Xue, *ACS Nano*, 2021, **15**, 1273–1281.

516 L. Shan, Y. Wang, S. Liang, B. Tang, Y. Yang, Z. Wang, B. Lu and J. Zhou, *InfoMat*, 2021, **3**, 1028–1036.

517 L. Yu, J. Huang, S. Wang, L. Qi, S. Wang and C. Chen, *Adv. Mater.*, 2023, **35**(21), 2210789.

518 Y. Wang, B. Liang, J. Zhu, G. Li, Q. Li, R. Ye, J. Fan and C. Zhi, *Angew. Chem., Int. Ed.*, 2023, **62**(23), e202302583.

519 G. Li, Z. Yang, Y. Jiang, C. Jin, W. Huang, X. Ding and Y. Huang, *Nano Energy*, 2016, **25**, 211–217.

520 G. Li, Z. Yang, Y. Jiang, W. Zhang and Y. Huang, *J. Power Sources*, 2016, **308**, 52–57.

521 H. B. Zhao, C. J. Hu, H. W. Cheng, J. H. Fang, Y. P. Xie, W. Y. Fang, T. N. L. Doan, T. K. A. Hoang, J. Q. Xu and P. Chen, *Sci. Rep.*, 2016, **6**, 25809.

522 J. Zhao, Y. Li, X. Peng, S. Dong, J. Ma, G. Cui and L. Chen, *Electrochem. Commun.*, 2016, **69**, 6–10.

523 W. Li, K. Wang, S. Cheng and K. Jiang, *Energy Storage Mater.*, 2018, **15**, 14–21.

524 F. Wan, Y. Zhang, L. Zhang, D. Liu, C. Wang, L. Song, Z. Niu and J. Chen, *Angew. Chem., Int. Ed.*, 2019, **58**, 7062–7067.

525 H. Shi, Y. Song, Z. Qin, C. Li, D. Guo, X. Liu and X. Sun, *Angew. Chem., Int. Ed.*, 2019, **58**, 16057–16061.

526 V. Verma, S. Kumar, W. Manalastas, J. Zhao, R. Chua, S. Meng, P. Kidkhunthod and M. Srinivasan, *ACS Appl. Energy Mater.*, 2019, **2**, 8667–8674.

527 P. Hu, T. Zhu, X. Wang, X. Zhou, X. Wei, X. Yao, W. Luo, C. Shi, K. A. Owusu, L. Zhou and L. Mai, *Nano Energy*, 2019, **58**, 492–498.

528 Z. Wu, Y. Wang, L. Zhang, L. Jiang, W. Tian, C. Cai, J. Price, Q. Gu and L. Hu, *ACS Appl. Energy Mater.*, 2020, **3**, 3919–3927.

529 J. S. Ko, P. P. Paul, G. Wan, N. Seitzman, R. H. DeBlock, B. S. Dunn, M. F. Toney and J. Nelson Weker, *Chem. Mater.*, 2020, **32**, 3028–3035.

530 Q. Ni, H. Jiang, S. Sandstrom, Y. Bai, H. Ren, X. Wu, Q. Guo, D. Yu, C. Wu and X. Ji, *Adv. Funct. Mater.*, 2020, **30**(36), 2003511.

531 Z. Wu, C. Lu, F. Ye, L. Zhang, L. Jiang, Q. Liu, H. Dong, Z. Sun and L. Hu, *Adv. Funct. Mater.*, 2021, **31**(45), 2106816.

532 L. Hu, Z. Wu, C. Lu, F. Ye, Q. Liu and Z. Sun, *Energy Environ. Sci.*, 2021, **14**, 4095–4106.

533 C. Li, W. Wu, H.-Y. Shi, Z. Qin, D. Yang, X. Yang, Y. Song, D. Guo, X.-X. Liu and X. Sun, *Chem. Commun.*, 2021, **57**, 6253–6256.

534 C. Li, W. Yuan, C. Li, H. Wang, L. Wang, Y. Liu and N. Zhang, *Chem. Commun.*, 2021, **57**, 4319–4322.

535 C. Li, R. Kingsbury, L. Zhou, A. Shyamsunder, K. A. Persson and L. F. Nazar, *ACS Energy Lett.*, 2022, **7**, 533–540.

536 G. Guo, X. Tan, K. Wang and H. Zhang, *ChemSusChem*, 2022, **15**(11), e202200313.

537 H. Jiang, L. Tang, Y. Fu, S. Wang, S. K. Sandstrom, A. M. Scida, G. Li, D. Hoang, J. J. Hong, N.-C. Chiu, K. C. Stylianou, W. F. Stickle, D. Wang, J. Li, P. A. Greaney, C. Fang and X. Ji, *Nat. Sustainability*, 2023, **6**, 806–815.

538 D. Hoang, Y. Li, M. S. Jung, S. K. Sandstrom, A. M. Scida, H. Jiang, T. C. Gallagher, B. A. Pollard, R. Jensen, N. Chiu, K. Stylianou, W. F. Stickle, P. A. Greaney and X. Ji, *Adv. Energy Mater.*, 2023, **13**(42), 2301712.

539 R. Trócoli and F. La Mantia, *ChemSusChem*, 2015, **8**, 481–485.

540 L. Zhang, L. Chen, X. Zhou and Z. Liu, *Adv. Energy Mater.*, 2015, **5**(2), 1400930.

541 Z. Liu, G. Pulletikurthi and F. Endres, *ACS Appl. Mater. Interfaces*, 2016, **8**, 12158–12164.

542 T. Gupta, A. Kim, S. Phadke, S. Biswas, T. Luong, B. J. Hertzberg, M. Chamoun, K. Evans-Lutterodt and D. A. Steingart, *J. Power Sources*, 2016, **305**, 22–29.



543 Z. Hou, X. Zhang, X. Li, Y. Zhu, J. Liang and Y. Qian, *J. Mater. Chem. A*, 2017, **5**, 730–738.

544 L. Qian, H. Zhu, T. Qin, R. Yao, J. Zhao, F. Kang and C. Yang, *Adv. Funct. Mater.*, 2023, **33**(23), 2301118.

545 Y. Cheng, L. Luo, L. Zhong, J. Chen, B. Li, W. Wang, S. X. Mao, C. Wang, V. L. Sprenkle, G. Li and J. Liu, *ACS Appl. Mater. Interfaces*, 2016, **8**, 13673–13677.

546 K. Koshika, N. Sano, K. Oyaizu and H. Nishide, *Macromol. Chem. Phys.*, 2009, **210**, 1989–1995.

547 C. Zhijiang and H. Chengwei, *J. Power Sources*, 2011, **196**, 10731–10736.

548 Z. Cai, J. Guo, H. Yang and Y. Xu, *J. Power Sources*, 2015, **279**, 114–122.

549 B. Häupler, C. Rössel, A. M. Schwenke, J. Winsberg, D. Schmidt, A. Wild and U. S. Schubert, *NPG Asia Mater.*, 2016, **8**, e283–e283.

550 F. Wan, L. Zhang, X. Wang, S. Bi, Z. Niu and J. Chen, *Adv. Funct. Mater.*, 2018, **28**(45), 1804975.

551 C. Kim, B. Y. Ahn, T.-S. Wei, Y. Jo, S. Jeong, Y. Choi, I.-D. Kim and J. A. Lewis, *ACS Nano*, 2018, **12**, 11838–11846.

552 H. Shi, Y. Ye, K. Liu, Y. Song and X. Sun, *Angew. Chem., Int. Ed.*, 2018, **57**, 16359–16363.

553 Q. Zhao, W. Huang, Z. Luo, L. Liu, Y. Lu, Y. Li, L. Li, J. Hu, H. Ma and J. Chen, *Sci. Adv.*, 2018, **4**, eaao1761.

554 G. Dawut, Y. Lu, L. Miao and J. Chen, *Inorg. Chem. Front.*, 2018, **5**, 1391–1396.

555 Z. Guo, Y. Ma, X. Dong, J. Huang, Y. Wang and Y. Xia, *Angew. Chem., Int. Ed.*, 2018, **57**, 11737–11741.

556 D. Kundu, P. Oberholzer, C. Glaros, A. Bouzid, E. Tervoort, A. Pasquarello and M. Niederberger, *Chem. Mater.*, 2018, **30**, 3874–3881.

557 Y. Wang, C. Wang, Z. Ni, Y. Gu, B. Wang, Z. Guo, Z. Wang, D. Bin, J. Ma and Y. Wang, *Adv. Mater.*, 2020, **32**(16), 2000338.

558 D. Dong, T. Wang, Y. Sun, J. Fan and Y.-C. Lu, *Nat. Sustainability*, 2023, **6**, 1474–1484.

559 F. Cheng, J. Zhao, W. Song, C. Li, H. Ma, J. Chen and P. Shen, *Inorg. Chem.*, 2006, **45**, 2038–2044.

560 C. Xu, S. W. Chiang, J. Ma and F. Kang, *J. Electrochem. Soc.*, 2013, **160**, A93–A97.

561 D. Wang, L. Wang, G. Liang, H. Li, Z. Liu, Z. Tang, J. Liang and C. Zhi, *ACS Nano*, 2019, **13**, 10643–10652.

562 A. Kozawa, T. Kalnoki-Kis and J. F. Yeager, *J. Electrochem. Soc.*, 1966, **113**, 405.

563 A. Singh, C. Laberty-Robert, V. Balland and B. Limoges, *Adv. Energy Mater.*, 2023, **13**(46), 2301745.

564 M. Mateos, N. Makivic, Y. Kim, B. Limoges and V. Balland, *Adv. Energy Mater.*, 2020, **10**(23), 2000332.

565 J. Ding, Z. Du, L. Gu, B. Li, L. Wang, S. Wang, Y. Gong and S. Yang, *Adv. Mater.*, 2018, **30**(26), 1800762.

566 P. Hu, P. Hu, T. D. Vu, M. Li, S. Wang, Y. Ke, X. Zeng, L. Mai and Y. Long, *Chem. Rev.*, 2023, **123**, 4353–4415.

567 S. Park, S. Nishimura, A. Kitada and A. Yamada, *ACS Appl. Energy Mater.*, 2024, **7**, 4347–4352.

568 R. Schöllhorn, M. Kümpers and J. O. Besenhard, *Mater. Res. Bull.*, 1977, **12**, 781–788.

569 E. Gocke, W. Schramm, P. Dolscheid and R. Schöllhorn, *J. Solid State Chem.*, 1987, **70**, 71–81.

570 M. S. Chae, J. W. Heo, S.-C. Lim and S.-T. Hong, *Inorg. Chem.*, 2016, **55**, 3294–3301.

571 L. Wang, M. Jiang, F. Liu, Q. Huang, L. Liu, L. Fu and Y. Wu, *Energy Fuels*, 2020, **34**, 11590–11596.

572 P. He, M. Yan, G. Zhang, R. Sun, L. Chen, Q. An and L. Mai, *Adv. Energy Mater.*, 2017, **7**(11), 1601920.

573 H. Liang, Z. Cao, F. Ming, W. Zhang, D. H. Anjum, Y. Cui, L. Cavallo and H. N. Alshareef, *Nano Lett.*, 2019, **19**, 3199–3206.

574 L. Geng, G. Lv, X. Xing and J. Guo, *Chem. Mater.*, 2015, **27**, 4926–4929.

575 D. Aurbach, Z. Lu, A. Schechter, Y. Gofer, H. Gizbar, R. Turgeman, Y. Cohen, M. Moshkovich and E. Levi, *Nature*, 2000, **407**, 724–727.

576 A. Paolella, C. Faure, V. Timoshevskii, S. Marras, G. Bertoni, A. Guerfi, A. Vijh, M. Armand and K. Zaghib, *J. Mater. Chem. A*, 2017, **5**, 18919–18932.

577 B. Beverskog and I. Puigdomenech, *Corros. Sci.*, 1997, **39**, 107–114.

578 B. Lee, H. R. Seo, H. R. Lee, C. S. Yoon, J. H. Kim, K. Y. Chung, B. W. Cho and S. H. Oh, *ChemSusChem*, 2016, **9**, 2948–2956.

579 L. Zhang, I. A. Rodríguez-Pérez, H. Jiang, C. Zhang, D. P. Leonard, Q. Guo, W. Wang, S. Han, L. Wang and X. Ji, *Adv. Funct. Mater.*, 2019, **29**(30), 1902653.

580 X. Guo and G. He, *J. Mater. Chem. A*, 2023, **11**, 11987–12001.

581 Y.-S. Kim, K. D. Harris, B. Limoges and V. Balland, *Chem. Sci.*, 2019, **10**, 8752–8763.

582 C. F. Bischoff, O. S. Fitz, J. Burns, M. Bauer, H. Gentischer, K. P. Birke, H.-M. Henning and D. Biro, *J. Electrochem. Soc.*, 2020, **167**, 020545.

583 H. Du, Y. Dong, Q. Li, R. Zhao, X. Qi, W. Kan, L. Suo, L. Qie, J. Li and Y. Huang, *Adv. Mater.*, 2023, **35**(25), 2210055.

584 G. Liang, B. Liang, A. Chen, J. Zhu, Q. Li, Z. Huang, X. Li, Y. Wang, X. Wang, B. Xiong, X. Jin, S. Bai, J. Fan and C. Zhi, *Nat. Commun.*, 2023, **14**, 1856.

585 Q. Zhang, Y. Ma, Y. Lu, L. Li, F. Wan, K. Zhang and J. Chen, *Nat. Commun.*, 2020, **11**, 4463.

586 C. Yang, J. Xia, C. Cui, T. P. Pollard, J. Vatamanu, A. Faraone, J. A. Dura, M. Tyagi, A. Kattan, E. Thimsen, J. Xu, W. Song, E. Hu, X. Ji, S. Hou, X. Zhang, M. S. Ding, S. Hwang, D. Su, Y. Ren, X.-Q. Yang, H. Wang, O. Borodin and C. Wang, *Nat. Sustainability*, 2023, **6**, 325–335.

587 G. Kear, B. D. Barker and F. C. Walsh, *Corros. Sci.*, 2004, **46**, 109–135.

588 R. T. Foley, *Corrosion*, 1970, **26**, 58–70.

589 D. Prando, A. Brenna, M. V. Diamanti, S. Beretta, F. Bolzoni, M. Ormellese and M. Pedeferrri, *J. Appl. Biomater. Funct. Mater.*, 2017, **15**, e291–e302.

590 Y. An, Y. Tian, K. Zhang, Y. Liu, C. Liu, S. Xiong, J. Feng and Y. Qian, *Adv. Funct. Mater.*, 2021, **31**(26), 2101886.

591 L. Wang, Y. Zhang, H. Hu, H.-Y. Shi, Y. Song, D. Guo, X.-X. Liu and X. Sun, *ACS Appl. Mater. Interfaces*, 2019, **11**, 42000–42005.

592 G. Kasiri, R. Trócoli, A. Bani Hashemi and F. La Mantia, *Electrochim. Acta*, 2016, **222**, 74–83.



593 X. Liu, H. Euchner, M. Zarrabeitia, X. Gao, G. A. Elia, A. Groß and S. Passerini, *ACS Energy Lett.*, 2020, **5**, 2979–2986.

594 L. Ma, T. P. Pollard, Y. Zhang, M. A. Schroeder, X. Ren, K. S. Han, M. S. Ding, A. V. Cresce, T. B. Atwater, J. Mars, L. Cao, H.-G. Steinrück, K. T. Mueller, M. F. Toney, M. Hourwitz, J. T. Fourkas, E. J. Maginn, C. Wang, O. Borodin and K. Xu, *One Earth*, 2022, **5**, 413–421.

595 N. Zhang, F. Cheng, Y. Liu, Q. Zhao, K. Lei, C. Chen, X. Liu and J. Chen, *J. Am. Chem. Soc.*, 2016, **138**, 12894–12901.

596 Z. Xu, Y. Zhang, W. Gou, M. Liu, Y. Sun, X. Han, W. Sun and C. Li, *Chem. Commun.*, 2022, **58**, 8145–8148.

597 D. Han, C. Cui, K. Zhang, Z. Wang, J. Gao, Y. Guo, Z. Zhang, S. Wu, L. Yin, Z. Weng, F. Kang and Q.-H. Yang, *Nat. Sustainability*, 2021, **5**, 205–213.

598 H. Du, Y. Dong, Q. Li, R. Zhao, X. Qi, W. Kan, L. Suo, L. Qie, J. Li and Y. Huang, *Adv. Mater.*, 2023, **35**(25), 2210055.

599 M. Peng, L. Li, L. Wang, X. Tang, K. Xiao, X. J. Gao, T. Hu, K. Yuan and Y. Chen, *Fundam. Res.*, 2024, **4**(6), 1488–1497.

600 X. Zeng, J. Mao, J. Hao, J. Liu, S. Liu, Z. Wang, Y. Wang, S. Zhang, T. Zheng, J. Liu, P. Rao and Z. Guo, *Adv. Mater.*, 2021, **33**(11), 2007416.

601 H. Meng, Q. Ran, T.-Y. Dai, H. Shi, S.-P. Zeng, Y.-F. Zhu, Z. Wen, W. Zhang, X.-Y. Lang, W.-T. Zheng and Q. Jiang, *Nano-Micro Lett.*, 2022, **14**, 128.

602 J. Shi, K. Xia, L. Liu, C. Liu, Q. Zhang, L. Li, X. Zhou, J. Liang and Z. Tao, *Electrochim. Acta*, 2020, **358**, 136937.

603 J. Shin, J. Lee, Y. Kim, Y. Park, M. Kim and J. W. Choi, *Adv. Energy Mater.*, 2021, **11**(39), 2100676.

604 Y. Dong, L. Miao, G. Ma, S. Di, Y. Wang, L. Wang, J. Xu and N. Zhang, *Chem. Sci.*, 2021, **12**, 5843–5852.

605 L. Zhang, G. Wang, J. Feng, Q. Ma, Z. Liu and X. Yan, *ChemElectroChem*, 2021, **8**, 1289–1297.

606 X. Chen, P. Gao, W. Li, N. A. Thieu, Z. M. Grady, N. G. Akhmedov, K. A. Sierros, M. Velayutham, V. V. Khramtsov, D. M. Reed, X. Li and X. Liu, *ACS Energy Lett.*, 2024, **9**, 1654–1665.

607 X. Chen, W. Li, S. Hu, N. G. Akhmedov, D. Reed, X. Li and X. Liu, *Nano Energy*, 2022, **98**, 107269.

608 X. Liu, Q. Ma, M. Shi, Q. Han and C. Liu, *Chem. Eng. J.*, 2023, **456**, 141016.

609 X. Zhao, X. Zhang, N. Dong, M. Yan, F. Zhang, K. Mochizuki and H. Pan, *Small*, 2022, **18**(21), 2200742.

610 D. Li, L. Cao, T. Deng, S. Liu and C. Wang, *Angew. Chem., Int. Ed.*, 2021, **60**, 13035–13041.

611 K. Zhao, C. Wang, Y. Yu, M. Yan, Q. Wei, P. He, Y. Dong, Z. Zhang, X. Wang and L. Mai, *Adv. Mater. Interfaces*, 2018, **5**(16), 1800848.

612 M. Shayan, R. Abouzeid, W. Xu, T. Wu and Q. Wu, *J. Mater. Chem. A*, 2024, **12**, 2820–2829.

613 J. Zhu, M. Yang, Y. Hu, M. Yao, J. Chen and Z. Niu, *Adv. Mater.*, 2024, **36**(3), 2304426.

614 S. Chen, D. Ji, Q. Chen, J. Ma, S. Hou and J. Zhang, *Nat. Commun.*, 2023, **14**, 3526.

615 N. R. Pitawela and S. K. Shaw, *ACS Meas. Sci. Au.*, 2021, **1**, 117–130.

616 H. Qiu, X. Du, J. Zhao, Y. Wang, J. Ju, Z. Chen, Z. Hu, D. Yan, X. Zhou and G. Cui, *Nat. Commun.*, 2019, **10**, 5374.

617 F. Wang, O. Borodin, T. Gao, X. Fan, W. Sun, F. Han, A. Faraone, J. A. Dura, K. Xu and C. Wang, *Nat. Mater.*, 2018, **17**, 543–549.

618 L. Cao, D. Li, T. Pollard, T. Deng, B. Zhang, C. Yang, L. Chen, J. Vatamanu, E. Hu, M. J. Hourwitz, L. Ma, M. Ding, Q. Li, S. Hou, K. Gaskell, J. T. Fourkas, X.-Q. Yang, K. Xu, O. Borodin and C. Wang, *Nat. Nanotechnol.*, 2021, **16**, 902–910.

619 L. Ma, T. P. Pollard, Y. Zhang, M. A. Schroeder, M. S. Ding, A. V. Cresce, R. Sun, D. R. Baker, B. A. Helms, E. J. Maginn, C. Wang, O. Borodin and K. Xu, *Angew. Chem., Int. Ed.*, 2021, **60**, 12438–12445.

620 G. Liang, Z. Tang, B. Han, J. Zhu, A. Chen, Q. Li, Z. Chen, Z. Huang, X. Li, Q. Yang and C. Zhi, *Adv. Mater.*, 2023, **35**(20), 2210051.

621 Z. Zhang, Y. Li, R. Xu, W. Zhou, Y. Li, S. T. Oyakhire, Y. Wu, J. Xu, H. Wang, Z. Yu, D. T. Boyle, W. Huang, Y. Ye, H. Chen, J. Wan, Z. Bao, W. Chiu and Y. Cui, *Science*, 2022, **375**, 66–70.

622 D. T. Boyle, W. Huang, H. Wang, Y. Li, H. Chen, Z. Yu, W. Zhang, Z. Bao and Y. Cui, *Nat. Energy*, 2021, **6**, 487–494.

623 J. Zhi, S. Zhao, M. Zhou, R. Wang and F. Huang, *Sci. Adv.*, 2023, **9**, eade2217.

624 Z. Xue, D. He and X. Xie, *J. Mater. Chem. A*, 2015, **3**, 19218–19253.

625 N. S. Schauser, R. Seshadri and R. A. Segalman, *Mol. Syst. Des. Eng.*, 2019, **4**, 263–279.

626 Z. W. B. Iton and K. A. See, *Chem. Mater.*, 2022, **34**, 881–898.

627 H. Steinrück, C. Cao, M. R. Lukatskaya, C. J. Takacs, G. Wan, D. G. Mackanic, Y. Tsao, J. Zhao, B. A. Helms, K. Xu, O. Borodin, J. F. Wishart and M. F. Toney, *Angew. Chem., Int. Ed.*, 2020, **59**, 23180–23187.

628 W. Yu, Z. Yu, Y. Cui and Z. Bao, *ACS Energy Lett.*, 2022, **7**, 3270–3275.

629 J. Tan, J. Matz, P. Dong, J. Shen and M. Ye, *Adv. Energy Mater.*, 2021, **11**(16), 2100046.

630 M. He, R. Guo, G. M. Hobold, H. Gao and B. M. Gallant, *Proc. Natl. Acad. Sci. U. S. A.*, 2020, **117**, 73–79.

631 J. Jones, M. Anouti, M. Caillon-Caravanier, P. Willmann and D. Lemordant, *Fluid Phase Equilib.*, 2009, **285**, 62–68.

632 D. Wynn, *Talanta*, 1984, **31**, 1036–1040.

633 H. Adenusi, G. A. Chass, S. Passerini, K. V. Tian and G. Chen, *Adv. Energy Mater.*, 2023, **13**(10), 2203307.

634 R. A. Vilá, D. T. Boyle, A. Dai, W. Zhang, P. Sayavong, Y. Ye, Y. Yang, J. A. Dionne and Y. Cui, *Sci. Adv.*, 2023, **9**, eadf3609.

635 Z. Shadike, H. Lee, O. Borodin, X. Cao, X. Fan, X. Wang, R. Lin, S.-M. Bak, S. Ghose, K. Xu, C. Wang, J. Liu, J. Xiao, X.-Q. Yang and E. Hu, *Nat. Nanotechnol.*, 2021, **16**, 549–554.

636 S. Zhang, R. Li, N. Hu, T. Deng, S. Weng, Z. Wu, D. Lu, H. Zhang, J. Zhang, X. Wang, L. Chen, L. Fan and X. Fan, *Nat. Commun.*, 2022, **13**, 5431.

637 D. Aurbach and I. Weissman, *Electrochim. Commun.*, 1999, **1**, 324–331.



638 J. Han, H. Euchner, M. Kuenzel, S. M. Hosseini, A. Groß, A. Varzi and S. Passerini, *ACS Energy Lett.*, 2021, **6**, 3063–3071.

639 L. Ma, Q. Li, Y. Ying, F. Ma, S. Chen, Y. Li, H. Huang and C. Zhi, *Adv. Mater.*, 2021, **33**(12), 2007406.

640 Y. Yang, C. Liu, Z. Lv, H. Yang, Y. Zhang, M. Ye, L. Chen, J. Zhao and C. C. Li, *Adv. Mater.*, 2021, **33**(11), 2007388.

641 R. Jay, A. W. Tomich, J. Zhang, Y. Zhao, A. De Gorostiza, V. Lavallo and J. Guo, *ACS Appl. Mater. Interfaces*, 2019, **11**, 11414–11420.

642 J. Forero-Saboya, C. Bodin and A. Ponrouch, *Electrochem. Commun.*, 2021, **124**, 106936.

643 A. Ponrouch, C. Frontera, F. Bardé and M. R. Palacín, *Nat. Mater.*, 2016, **15**, 169–172.

644 A. Shyamsunder, L. E. Blanc, A. Assoud and L. F. Nazar, *ACS Energy Lett.*, 2019, **4**, 2271–2276.

645 J. Forero-Saboya, C. Davoisne, R. Dedryvère, I. Yousef, P. Canepa and A. Ponrouch, *Energy Environ. Sci.*, 2020, **13**, 3423–3431.

646 D. Wang, X. Gao, Y. Chen, L. Jin, C. Kuss and P. G. Bruce, *Nat. Mater.*, 2018, **17**, 16–20.

647 P. Xiong, Y. Zhang, J. Zhang, S. H. Baek, L. Zeng, Y. Yao and H. S. Park, *EnergyChem*, 2022, **4**, 100076.

648 R. Qin, Y. Wang, L. Yao, L. Yang, Q. Zhao, S. Ding, L. Liu and F. Pan, *Nano Energy*, 2022, **98**, 107333.

649 J. Zheng, Z. Huang, F. Ming, Y. Zeng, B. Wei, Q. Jiang, Z. Qi, Z. Wang and H. Liang, *Small*, 2022, **18**(21), 2200006.

650 F. Wan, X. Zhou, Y. Lu, Z. Niu and J. Chen, *ACS Energy Lett.*, 2020, **5**, 3569–3590.

651 W. Li, K. Wang, M. Zhou, H. Zhan, S. Cheng and K. Jiang, *ACS Appl. Mater. Interfaces*, 2018, **10**, 22059–22066.

652 C. Shen, X. Li, N. Li, K. Xie, J. Wang, X. Liu and B. Wei, *ACS Appl. Mater. Interfaces*, 2018, **10**, 25446–25453.

653 Y. Zeng, X. Zhang, R. Qin, X. Liu, P. Fang, D. Zheng, Y. Tong and X. Lu, *Adv. Mater.*, 2019, **31**(36), 1903675.

654 A. Xia, X. Pu, Y. Tao, H. Liu and Y. Wang, *Appl. Surf. Sci.*, 2019, **481**, 852–859.

655 R. Yuksel, O. Buyukcakir, W. K. Seong and R. S. Ruoff, *Adv. Energy Mater.*, 2020, **10**(16), 1904215.

656 L. Dong, W. Yang, W. Yang, H. Tian, Y. Huang, X. Wang, C. Xu, C. Wang, F. Kang and G. Wang, *Chem. Eng. J.*, 2020, **384**, 123355.

657 Z. Li, L. Wu, S. Dong, T. Xu, S. Li, Y. An, J. Jiang and X. Zhang, *Adv. Funct. Mater.*, 2021, **31**(4), 2006495.

658 S. Zhai, N. Wang, X. Tan, K. Jiang, Z. Quan, Y. Li and Z. Li, *Adv. Funct. Mater.*, 2021, **31**(13), 2008894.

659 J. Zhou, M. Xie, F. Wu, Y. Mei, Y. Hao, R. Huang, G. Wei, A. Liu, L. Li and R. Chen, *Adv. Mater.*, 2021, **33**(33), 2101649.

660 Z. Ge, H. Zhang, J. Tian, J. Wu, Y. Xu, W. Deng, G. Zou, D. He, H. Hou, C. Wang and X. Ji, *Chem. Eng. J.*, 2023, **466**, 143054.

661 X. Zhang, Q. Ruan, L. Liu, D. Li, Y. Xu, Y. Wang, J. Liu, C. Huang, F. Xiong, B. Wang and P. K. Chu, *J. Electroanal. Chem.*, 2023, **936**, 117357.

662 Z. H. Xie, Y. F. Yuan, Z. J. Yao, M. Zhu, S. Y. Guo and P. F. Du, *Chem. Eng. J.*, 2024, **484**, 149601.

663 L. Kang, K. Yue, C. Ma, H. Yuan, J. Luo, Y. Wang, Y. Liu, J. Nai and X. Tao, *Nano Lett.*, 2024, **24**, 4150–4157.

664 L. Kang, M. Cui, F. Jiang, Y. Gao, H. Luo, J. Liu, W. Liang and C. Zhi, *Adv. Energy Mater.*, 2018, **8**(25), 1801090.

665 M. Cui, Y. Xiao, L. Kang, W. Du, Y. Gao, X. Sun, Y. Zhou, X. Li, H. Li, F. Jiang and C. Zhi, *ACS Appl. Energy Mater.*, 2019, **2**, 6490–6496.

666 X. Xie, S. Liang, J. Gao, S. Guo, J. Guo, C. Wang, G. Xu, X. Wu, G. Chen and J. Zhou, *Energy Environ. Sci.*, 2020, **13**, 503–510.

667 D. Han, S. Wu, S. Zhang, Y. Deng, C. Cui, L. Zhang, Y. Long, H. Li, Y. Tao, Z. Weng, Q. Yang and F. Kang, *Small*, 2020, **16**(29), 2001736.

668 K. Hu, X. Guan, R. Lv, G. Li, Z. Hu, L. Ren, A. Wang, X. Liu and J. Luo, *Chem. Eng. J.*, 2020, **396**, 125363.

669 Z. Cai, Y. Ou, J. Wang, R. Xiao, L. Fu, Z. Yuan, R. Zhan and Y. Sun, *Energy Storage Mater.*, 2020, **27**, 205–211.

670 J. Hao, B. Li, X. Li, X. Zeng, S. Zhang, F. Yang, S. Liu, D. Li, C. Wu and Z. Guo, *Adv. Mater.*, 2020, **32**(34), 2003021.

671 Q. Zhang, J. Luan, X. Huang, Q. Wang, D. Sun, Y. Tang, X. Ji and H. Wang, *Nat. Commun.*, 2020, **11**, 3961.

672 S.-B. Wang, Q. Ran, R.-Q. Yao, H. Shi, Z. Wen, M. Zhao, X.-Y. Lang and Q. Jiang, *Nat. Commun.*, 2020, **11**, 1634.

673 J. Y. Kim, G. Liu, G. Y. Shim, H. Kim and J. K. Lee, *Adv. Funct. Mater.*, 2020, **30**(36), 2004210.

674 H. He, H. Tong, X. Song, X. Song and J. Liu, *J. Mater. Chem. A*, 2020, **8**, 7836–7846.

675 C. Deng, X. Xie, J. Han, Y. Tang, J. Gao, C. Liu, X. Shi, J. Zhou and S. Liang, *Adv. Funct. Mater.*, 2020, **30**(21), 2000599.

676 P. Liang, J. Yi, X. Liu, K. Wu, Z. Wang, J. Cui, Y. Liu, Y. Wang, Y. Xia and J. Zhang, *Adv. Funct. Mater.*, 2020, **30**(13), 1908528.

677 M. Liu, J. Cai, H. Ao, Z. Hou, Y. Zhu and Y. Qian, *Adv. Funct. Mater.*, 2020, **30**(50), 2004885.

678 Y. Zhang, G. Wang, F. Yu, G. Xu, Z. Li, M. Zhu, Z. Yue, M. Wu, H.-K. Liu, S.-X. Dou and C. Wu, *Chem. Eng. J.*, 2021, **416**, 128062.

679 Z. Cai, Y. Ou, B. Zhang, J. Wang, L. Fu, M. Wan, G. Li, W. Wang, L. Wang, J. Jiang, Z. W. Seh, E. Hu, X.-Q. Yang, Y. Cui and Y. Sun, *J. Am. Chem. Soc.*, 2021, **143**, 3143–3152.

680 Q. Lu, C. Liu, Y. Du, X. Wang, L. Ding, A. Omar and D. Mikhailova, *ACS Appl. Mater. Interfaces*, 2021, **13**, 16869–16875.

681 S. Li, J. Fu, G. Miao, S. Wang, W. Zhao, Z. Wu, Y. Zhang and X. Yang, *Adv. Mater.*, 2021, **33**(21), 2008424.

682 W. Guo, Y. Zhang, X. Tong, X. Wang, L. Zhang, X. Xia and J. Tu, *Mater Today Energy*, 2021, **20**, 100675.

683 Z. Miao, M. Du, H. Li, F. Zhang, H. Jiang, Y. Sang, Q. Li, H. Liu and S. Wang, *EcoMat*, 2021, **3**(4), e12125.

684 H. Tian, Z. Li, G. Feng, Z. Yang, D. Fox, M. Wang, H. Zhou, L. Zhai, A. Kushima, Y. Du, Z. Feng, X. Shan and Y. Yang, *Nat. Commun.*, 2021, **12**, 237.

685 C. Liu, Z. Luo, W. Deng, W. Wei, L. Chen, A. Pan, J. Ma, C. Wang, L. Zhu, L. Xie, X.-Y. Cao, J. Hu, G. Zou, H. Hou and X. Ji, *ACS Energy Lett.*, 2021, **6**, 675–683.

686 H. Jia, Z. Wang, M. Dirican, S. Qiu, C. Y. Chan, S. Fu, B. Fei and X. Zhang, *J. Mater. Chem. A*, 2021, **9**, 5597–5605.



687 L. Zhang, B. Zhang, T. Zhang, T. Li, T. Shi, W. Li, T. Shen, X. Huang, J. Xu, X. Zhang, Z. Wang and Y. Hou, *Adv. Funct. Mater.*, 2021, **31**(26), 2100186.

688 X. Yang, C. Li, Z. Sun, S. Yang, Z. Shi, R. Huang, B. Liu, S. Li, Y. Wu, M. Wang, Y. Su, S. Dou and J. Sun, *Adv. Mater.*, 2021, **33**(52), 2105951.

689 T. C. Li, Y. Von Lim, X. Xie, X. L. Li, G. Li, D. Fang, Y. Li, Y. S. Ang, L. K. Ang and H. Y. Yang, *Small*, 2021, **17**(35), 2101728.

690 Z. Yang, C. Lv, W. Li, T. Wu, Q. Zhang, Y. Tang, M. Shao and H. Wang, *Small*, 2022, **18**(43), 2104148.

691 J. Zheng, Z. Cao, F. Ming, H. Liang, Z. Qi, W. Liu, C. Xia, C. Chen, L. Cavallo, Z. Wang and H. N. Alshareef, *ACS Energy Lett.*, 2022, **7**, 197–203.

692 S. Zhou, Y. Wang, H. Lu, Y. Zhang, C. Fu, I. Usman, Z. Liu, M. Feng, G. Fang, X. Cao, S. Liang and A. Pan, *Adv. Funct. Mater.*, 2021, **31**(46), 2104361.

693 P. Cao, X. Zhou, A. Wei, Q. Meng, H. Ye, W. Liu, J. Tang and J. Yang, *Adv. Funct. Mater.*, 2021, **31**(20), 2100398.

694 L. Dai, T. Wang, B. Jin, N. Liu, Y. Niu, W. Meng, Z. Gao, X. Wu, L. Wang and Z. He, *Surf. Coat. Technol.*, 2021, **42**, 127813.

695 K. Wu, J. Yi, X. Liu, Y. Sun, J. Cui, Y. Xie, Y. Liu, Y. Xia and J. Zhang, *Nano-Micro Lett.*, 2021, **13**, 79.

696 P. Zou, R. Zhang, L. Yao, J. Qin, K. Kisslinger, H. Zhuang and H. L. Xin, *Adv. Energy Mater.*, 2021, **11**(31), 2100982.

697 M. Zhou, S. Guo, G. Fang, H. Sun, X. Cao, J. Zhou, A. Pan and S. Liang, *J. Energy Chem.*, 2021, **55**, 549–556.

698 C. Deng, X. Xie, J. Han, B. Lu, S. Liang and J. Zhou, *Adv. Funct. Mater.*, 2021, **31**(51), 2103227.

699 H. Liu, J. Wang, W. Hua, H. Sun, Y. Huyan, S. Tian, Z. Hou, J. Yang, C. Wei and F. Kang, *Adv. Sci.*, 2021, **8**(23), 2102612.

700 B. Li, J. Xue, C. Han, N. Liu, K. Ma, R. Zhang, X. Wu, L. Dai, L. Wang and Z. He, *J. Colloid Interface Sci.*, 2021, **599**, 467–475.

701 P. Xiao, L. Xue, Y. Guo, L. Hu, C. Cui, H. Li and T. Zhai, *Sci. Bull.*, 2021, **66**, 545–552.

702 Y. Yang, C. Liu, Z. Lv, H. Yang, X. Cheng, S. Zhang, M. Ye, Y. Zhang, L. Chen, J. Zhao and C. C. Li, *Energy Storage Mater.*, 2021, **41**, 230–239.

703 S. Wu, S. Zhang, Y. Chu, Z. Hu and J. Luo, *Adv. Funct. Mater.*, 2021, **31**(49), 2107397.

704 Y. Zhang, M. Zhu, G. Wang, F. Du, F. Yu, K. Wu, M. Wu, S. Dou, H. Liu and C. Wu, *Small Methods*, 2021, **5**(10), 2100650.

705 D. Wang, D. Lv, H. Peng, N. Wang, H. Liu, J. Yang and Y. Qian, *Nano Lett.*, 2022, **22**, 1750–1758.

706 G. Liang, J. Zhu, B. Yan, Q. Li, A. Chen, Z. Chen, X. Wang, B. Xiong, J. Fan, J. Xu and C. Zhi, *Energy Environ. Sci.*, 2022, **15**, 1086–1096.

707 J. Y. Kim, G. Liu, R. E. A. Ardhi, J. Park, H. Kim and J. K. Lee, *Nano-Micro Lett.*, 2022, **14**, 46.

708 P. Xiao, H. Li, J. Fu, C. Zeng, Y. Zhao, T. Zhai and H. Li, *Energy Environ. Sci.*, 2022, **15**, 1638–1646.

709 S. Zhai, X. Shi, K. Jiang, X. Tan, W. Zhang, J. Zhang, H. Zhang and Z. Li, *Chem. Eng. J.*, 2022, **437**, 135246.

710 L. Hong, L. Wang, Y. Wang, X. Wu, W. Huang, Y. Zhou, K. Wang and J. Chen, *Adv. Sci.*, 2022, **9**(6), 2104866.

711 J. Zheng, Z. Huang, Y. Zeng, W. Liu, B. Wei, Z. Qi, Z. Wang, C. Xia and H. Liang, *Nano Lett.*, 2022, **22**, 1017–1023.

712 A. Chen, C. Zhao, Z. Guo, X. Lu, N. Liu, Y. Zhang, L. Fan and N. Zhang, *Energy Storage Mater.*, 2022, **44**, 353–359.

713 Y. Zhou, G. Li, S. Feng, H. Qin, Q. Wang, F. Shen, P. Liu, Y. Huang and H. He, *Adv. Sci.*, 2023, **10**(6), 2205874.

714 S. Wang, Z. Yang, B. Chen, H. Zhou, S. Wan, L. Hu, M. Qiu, L. Qie and Y. Yu, *Energy Storage Mater.*, 2022, **47**, 491–499.

715 T. Chen, F. Huang, Y. Wang, Y. Yang, H. Tian and J. M. Xue, *Adv. Sci.*, 2022, **9**(14), 2105980.

716 J. Yan, M. Ye, Y. Zhang, Y. Tang and C. Chao Li, *Chem. Eng. J.*, 2022, **432**, 134227.

717 H. Peng, C. Liu, N. Wang, C. Wang, D. Wang, Y. Li, B. Chen, J. Yang and Y. Qian, *Energy Environ. Sci.*, 2022, **15**, 1682–1693.

718 S. Bhoyate, S. Mhin, J. Jeon, K. Park, J. Kim and W. Choi, *ACS Appl. Mater. Interfaces*, 2020, **12**, 27249–27257.

719 Y. Xiong, F. Zhou, D. Zhu, X. Jing, H. Shi, W. Li and D. Wang, *J. Electrochem. Soc.*, 2023, **170**, 010516.

720 Z. Gong, Z. Li, P. Wang, K. Jiang, Z. Bai, K. Zhu, J. Yan, K. Ye, G. Wang, D. Cao and G. Chen, *Energy Mater. Adv.*, 2023, **4**, 0035.

721 H. J. Kim, S. Kim, S. Kim, S. Kim, K. Heo, J. Lim, H. Yashiro, H. Shin, H. Jung, Y. M. Lee and S. Myung, *Adv. Mater.*, 2024, **36**(1), 2308592.

722 H. Zhao, Z. Chi, Q. Zhang, D. Kong, L. Li, Z. Guo and L. Wang, *Appl. Surf. Sci.*, 2023, **613**, 156129.

723 C.-Y. Tian, W.-W. Li, X.-W. Liu, D.-T. Zhang, Y.-Y. Wang, C.-Y. Li, Y.-Q. Wang, B. Zhao, M.-F. Wang, M.-P. Li, H. Chen and M.-C. Liu, *ACS Sustainable Chem. Eng.*, 2023, **11**, 3576–3584.

724 Q. Zhang, J. Liang, M. Li, J. Qin, Y. Zhao, L. Ren, W. Liu, C. Yang and X. Sun, *Chem. Eng. J.*, 2023, **474**, 145981.

725 J. Duan, J. Dong, R. Cao, H. Yang, K. Fang, Y. Liu, Z. Shen, F. Li, R. Liu, H. Li and C. Chen, *Adv. Sci.*, 2023, **10**(29), 2303343.

726 H. Gan, J. Wu, F. Zhang, R. Li and H. Liu, *Energy Storage Mater.*, 2023, **55**, 264–271.

727 F. Zhang, H. Tao, Y. Li and X. Yang, *Mater. Today Commun.*, 2024, **39**, 108606.

728 K. Zhang, C. Li, J. Liu, S. Zhang, M. Wang and L. Wang, *Small*, 2024, **20**(14), 2306406.

729 J. Ko, S. So, M. Kim, I. Tae Kim, Y. Nam Ahn and J. Hur, *Chem. Eng. J.*, 2023, **462**, 142308.

730 C. Choi, J. B. Park, J. H. Park, S. Yu and D.-W. Kim, *Chem. Eng. J.*, 2023, **456**, 141015.

731 X. Lei, Z. Ma, L. Bai, L. Wang, Y. Ding, S. Song, A. Song, H. Dong, H. Tian, H. Tian, X. Meng, H. Liu, B. Sun, G. Shao and G. Wang, *Battery Energy*, 2023, **2**(6), 20230024.

732 H. Lu, W. Hua, Z. Zhang, X. An, J. Feng, B. Xi and S. Xiong, *Small*, 2024, **20**(30), 2312187.

733 P. Jiang, Y. Wang, Y. Li, L. Dai, N. Xu, J. Qiao and D. Ruan, *Sep. Purif. Technol.*, 2024, **341**, 126813.

734 M. Liu, L. Yang, H. Liu, A. Amine, Q. Zhao, Y. Song, J. Yang, K. Wang and F. Pan, *ACS Appl. Mater. Interfaces*, 2019, **11**, 32046–32051.



735 H. Yang, Z. Chang, Y. Qiao, H. Deng, X. Mu, P. He and H. Zhou, *Angew. Chem., Int. Ed.*, 2020, **59**, 9377–9381.

736 Y. Cui, Q. Zhao, X. Wu, X. Chen, J. Yang, Y. Wang, R. Qin, S. Ding, Y. Song, J. Wu, K. Yang, Z. Wang, Z. Mei, Z. Song, H. Wu, Z. Jiang, G. Qian, L. Yang and F. Pan, *Angew. Chem., Int. Ed.*, 2020, **59**, 16594–16601.

737 X. Liu, F. Yang, W. Xu, Y. Zeng, J. He and X. Lu, *Adv. Sci.*, 2020, **7**(21), 2002173.

738 X. Zeng, J. Zhao, Z. Wan, W. Jiang, M. Ling, L. Yan and C. Liang, *J. Phys. Chem. Lett.*, 2021, **12**, 9055–9059.

739 Y. Wang, Y. Liu, H. Wang, S. Dou, W. Gan, L. Ci, Y. Huang and Q. Yuan, *J. Mater. Chem. A*, 2022, **10**, 4366–4375.

740 J. H. Park, M. Kwak, C. Hwang, K. Kang, N. Liu, J. Jang and B. A. Grzybowski, *Adv. Mater.*, 2021, **33**(34), 2101726.

741 Z. Zhao, R. Wang, C. Peng, W. Chen, T. Wu, B. Hu, W. Weng, Y. Yao, J. Zeng, Z. Chen, P. Liu, Y. Liu, G. Li, J. Guo, H. Lu and Z. Guo, *Nat. Commun.*, 2021, **12**, 6606.

742 H. Yan, S. Li, Y. Nan, S. Yang and B. Li, *Adv. Energy Mater.*, 2021, **11**(18), 2100186.

743 L. Hong, X. Wu, C. Ma, W. Huang, Y. Zhou, K.-X. Wang and J.-S. Chen, *J. Mater. Chem. A*, 2021, **9**, 16814–16823.

744 M. Cui, B. Yan, F. Mo, X. Wang, Y. Huang, J. Fan, C. Zhi and H. Li, *Chem. Eng. J.*, 2022, **434**, 134688.

745 H. Gan, J. Wu, R. Li, B. Huang and H. Liu, *Energy Storage Mater.*, 2022, **47**, 602–610.

746 Z. Miao, F. Zhang, H. Zhao, M. Du, H. Li, H. Jiang, W. Li, Y. Sang, H. Liu and S. Wang, *Adv. Funct. Mater.*, 2022, **32**(20), 2111635.

747 J. Zhao, Y. Ying, G. Wang, K. Hu, Y. Di Yuan, H. Ye, Z. Liu, J. Y. Lee and D. Zhao, *Energy Storage Mater.*, 2022, **48**, 82–89.

748 L. Yuan, Y. Song, Y. Wan, J. Zhang and X. Liu, *Appl. Surf. Sci.*, 2023, **637**, 157936.

749 W. Xin, J. Xiao, J. Li, L. Zhang, H. Peng, Z. Yan and Z. Zhu, *Energy Storage Mater.*, 2023, **56**, 76–86.

750 Y. Xiang, Y. Zhong, P. Tan, L. Zhou, G. Yin, H. Pan, X. Li, Y. Jiang, M. Xu and X. Zhang, *Small*, 2023, **19**(43), 2302161.

751 D. Li, Y. Ouyang, H. Lu, Y. Xie, S. Guo, Q. Zeng, Y. Xiao, Q. Zhang and S. Huang, *Mater. Today Chem.*, 2023, **32**, 101629.

752 Z. Zhao, J. Zhao, Z. Hu, J. Li, J. Li, Y. Zhang, C. Wang and G. Cui, *Energy Environ. Sci.*, 2019, **12**, 1938–1949.

753 F. Zhang, C. Wang, J. Pan, F. Tian, S. Zeng, J. Yang and Y. Qian, *Mater Today Energy*, 2020, **17**, 100443.

754 Z. Li, W. Deng, C. Li, W. Wang, Z. Zhou, Y. Li, X. Yuan, J. Hu, M. Zhang, J. Zhu, W. Tang, X. Wang and R. Li, *J. Mater. Chem. A*, 2020, **8**, 17725–17731.

755 S. H. Park, S. Y. Byeon, J.-H. Park and C. Kim, *ACS Energy Lett.*, 2021, **6**, 3078–3085.

756 K. Wang, J.-B. Le, S.-J. Zhang, W.-F. Ren, J.-M. Yuan, T.-T. Su, B.-Y. Chi, C.-Y. Shao and R.-C. Sun, *J. Mater. Chem. A*, 2022, **10**, 4845–4857.

757 L. T. Hieu, S. So, I. T. Kim and J. Hur, *Chem. Eng. J.*, 2021, **411**, 128584.

758 Y. Wang, T. Guo, J. Yin, Z. Tian, Y. Ma, Z. Liu, Y. Zhu and H. N. Alshareef, *Adv. Mater.*, 2022, **34**(4), 2106937.

759 P. Chen, X. Yuan, Y. Xia, Y. Zhang, L. Fu, L. Liu, N. Yu, Q. Huang, B. Wang, X. Hu, Y. Wu and T. van Ree, *Adv. Sci.*, 2021, **8**(11), 2100309.

760 T. Sun, Z. Li, Y. Zhi, Y. Huang, H. J. Fan and Q. Zhang, *Adv. Funct. Mater.*, 2021, **31**(16), 2010049.

761 H. Du, R. Zhao, Y. Yang, Z. Liu, L. Qie and Y. Huang, *Angew. Chem., Int. Ed.*, 2022, **61**(10), e202114789.

762 S. Jiao, J. Fu, M. Wu, T. Hua and H. Hu, *ACS Nano*, 2022, **16**, 1013–1024.

763 Q. Liu, Y. Wang, X. Hong, R. Zhou, Z. Hou and B. Zhang, *Adv. Energy Mater.*, 2022, **12**(20), 2200318.

764 W. Fan, Z. Sun, Y. Yuan, X. Yuan, C. You, Q. Huang, J. Ye, L. Fu, V. Kondratiev and Y. Wu, *J. Mater. Chem. A*, 2022, **10**, 7645–7652.

765 G. Li, X. Wang, S. Lv, J. Wang, W. Yu, X. Dong and D. Liu, *Adv. Funct. Mater.*, 2023, **33**(4), 2208288.

766 X. Cai, X. Wang, Z. Bie, Z. Jiao, Y. Li, W. Yan, H. J. Fan and W. Song, *Adv. Mater.*, 2024, **36**(3), 2306734.

767 B. Zhou, B. Miao, Y. Gao, A. Yu and Z. Shao, *Small*, 2023, **19**(35), 2300895.

768 P. Tangthuam, W. Kao-ian, J. Sangsawang, C. Rojviriya, P. Chirawatkul, J. Kasemchainan, F. Mahlendorf, M. T. Nguyen, T. Yonezawa and S. Kheawhom, *Mater. Sci. Energy Technol.*, 2023, **6**, 417–428.

769 P. Ye, X. Li, K. He, A. Dou, X. Wang, A. Naveed, Y. Zhou, M. Su, P. Zhang and Y. Liu, *J. Power Sources*, 2023, **558**, 232622.

770 L. Xiong, H. Fu, K. Yang, J. Y. Kim, R. Ren, J. K. Lee, W. Yang and G. Liu, *Carbon Energy*, 2023, **5**(6), e370.

771 Z. Meng, Y. Jiao and P. Wu, *Angew. Chem., Int. Ed.*, 2023, **62**(31), e202307271.

772 X. Qi, F. Xie, Y.-T. Xu, H. Xu, C.-L. Sun, S.-H. Wang, J.-Y. Hu and X.-F. Wang, *Chem. Eng. J.*, 2023, **453**, 139963.

773 Y. Tian, Y. An, C. Wei, B. Xi, S. Xiong, J. Feng and Y. Qian, *ACS Nano*, 2019, **13**, 11676–11685.

774 Q. Yang, Y. Guo, B. Yan, C. Wang, Z. Liu, Z. Huang, Y. Wang, Y. Li, H. Li, L. Song, J. Fan and C. Zhi, *Adv. Mater.*, 2020, **32**(25), 2001755.

775 Y. Tian, Y. An, C. Liu, S. Xiong, J. Feng and Y. Qian, *Energy Storage Mater.*, 2021, **41**, 343–353.

776 Y. An, Y. Tian, C. Liu, S. Xiong, J. Feng and Y. Qian, *ACS Nano*, 2021, **15**, 15259–15273.

777 P. Liu, Z. Zhang, R. Hao, Y. Huang, W. Liu, Y. Tan, P. Li, J. Yan and K. Liu, *Chem. Eng. J.*, 2021, **403**, 126425.

778 M. Qiu, H. Jia, C. Lan, H. Liu and S. Fu, *Energy Storage Mater.*, 2022, **45**, 1175–1182.

779 Y. Tian, Y. An, Y. Yang and B. Xu, *Energy Storage Mater.*, 2022, **49**, 122–134.

780 L. Tan, C. Wei, Y. Zhang, Y. An, S. Xiong and J. Feng, *Chem. Eng. J.*, 2022, **431**, 134277.

781 Y. Zhang, Z. Cao, S. Liu, Z. Du, Y. Cui, J. Gu, Y. Shi, B. Li and S. Yang, *Adv. Energy Mater.*, 2022, **12**(13), 2103979.

782 J. Zhou, M. Xie, F. Wu, Y. Mei, Y. Hao, L. Li and R. Chen, *Adv. Mater.*, 2022, **34**(1), 2106897.

783 H. Jia, M. Qiu, C. Tang, H. Liu, S. Fu and X. Zhang, *EcoMat*, 2022, **4**(3), e12190.



784 Q. Song, J. Liang, S. Liu, Y. Zhang, J. Zhu and C. Zhu, *Nano Res.*, 2023, **16**, 403–410.

785 X. Liu, K. Wang, Y. Liu, F. Zhao, J. He, H. Wu, J. Wu, H. Liang and C. Huang, *Carbon Energy*, 2023, **5**(11), e343.

786 Y. Zhang, C. Peng, Z. Zeng, X. Zhang, L. Zhang, Y. Ma and Z. Wang, *ACS Appl. Mater. Interfaces*, 2022, **14**, 10419–10427.

787 H. Liu, J.-G. Wang, W. Hua, L. Ren, H. Sun, Z. Hou, Y. Huyan, Y. Cao, C. Wei and F. Kang, *Energy Environ. Sci.*, 2022, **15**, 1872–1881.

788 H. J. Kim, S. Kim, K. Heo, J. Lim, H. Yashiro and S. Myung, *Adv. Energy Mater.*, 2023, **13**(2), 2203189.

789 J. Li, Z. Zheng, Z. Yu, F. She, L. Lai, J. Prabowo, W. Lv, L. Wei and Y. Chen, *J. Mater. Chem. A*, 2023, **11**, 3051–3059.

790 H. He, H. Qin, F. Shen, N. Hu and J. Liu, *Chem. Commun.*, 2021, **57**, 11477–11480.

791 L. Ma, M. A. Schroeder, T. P. Pollard, O. Borodin, M. S. Ding, R. Sun, L. Cao, J. Ho, D. R. Baker, C. Wang and K. Xu, *Energy Environ. Mater.*, 2020, **3**, 516–521.

792 L. Ma, M. A. Schroeder, O. Borodin, T. P. Pollard, M. S. Ding, C. Wang and K. Xu, *Nat. Energy*, 2020, **5**, 743–749.

793 B. D. Adams, J. Zheng, X. Ren, W. Xu and J. Zhang, *Adv. Energy Mater.*, 2018, **8**(7), 1702097.

794 R. D. Rauh and S. B. Brummer, *Electrochim. Acta*, 1977, **22**, 75–83.

795 D. Aurbach, O. Youngman, Y. Gofer and A. Meitav, *Electrochim. Acta*, 1990, **35**, 625–638.

796 Z. Wu, Y. Li and J. Liu, *Small Methods*, 2024, **8**(1), 2300660.

797 G. Wu, Y. Yang, R. Zhu, W. Yang, H. Yang and H. Zhou, *Energy Environ. Sci.*, 2023, **16**, 4320–4325.

798 T. Xue, W. C. Cooper, R. Pascual and S. Saimoto, *J. Appl. Electrochem.*, 1991, **21**, 231–237.

799 K. Y. Kwon, T. H. Jo, J. S. Kim, F. Hasan and H. D. Yoo, *ACS Appl. Mater. Interfaces*, 2020, **12**, 42612–42621.

800 H. Lee, S. Chen, X. Ren, A. Martinez, V. Shutthanandan, M. Vijayakumar, K. S. Han, Q. Li, J. Liu, W. Xu and J. Zhang, *ChemSusChem*, 2018, **11**, 3821–3828.

801 M. S. Chae, J. W. Heo, S. C. Lim and S. T. Hong, *Inorg. Chem.*, 2016, **55**, 3294–3301.

802 B. K. Thomas and D. J. Fray, *J. Appl. Electrochem.*, 1981, **11**, 677–683.

803 C. Jiang, H. Huang, Q. Ji, J. Li, B. Chen, Y. He and Z. Guo, *J. Solid State Electrochem.*, 2022, **26**, 1455–1467.

804 H. Glatz, E. Tervoort and D. Kundu, *ACS Appl. Mater. Interfaces*, 2020, **12**, 3522–3530.

805 H. Liu, Y. Zhang, C. Wang, J. N. Glazer, Z. Shan and N. Liu, *ACS Appl. Mater. Interfaces*, 2021, **13**, 32930–32936.

806 H. Yang, Y. Yang, W. Yang, G. Wu and R. Zhu, *Energy Environ. Sci.*, 2024, **17**, 1975–1983.

807 Y. Yang, H. Yang, R. Zhu and H. Zhou, *Energy Environ. Sci.*, 2023, **16**, 2723–2731.

808 K. Xu, *J. Power Sources*, 2023, **559**, 232652.

809 J. T. Hinatsu, V. D. Tran and F. R. Foulkes, *J. Appl. Electrochem.*, 1992, **22**, 215–223.

810 H. J. S. Sand, *London, Edinburgh Dublin Philos. Mag. J. Sci.*, 1901, **1**, 45–79.

811 Z. Cai, J. Wang, Z. Lu, R. Zhan, Y. Ou, L. Wang, M. Dahbi, J. Alami, J. Lu, K. Amine and Y. Sun, *Angew. Chem., Int. Ed.*, 2022, **61**(14), e202116560.

812 P. Bai, J. Li, F. R. Brushett and M. Z. Bazant, *Energy Environ. Sci.*, 2016, **9**, 3221–3229.

813 S. Trasatti, *J. Electroanal. Chem. Interfacial Electrochem.*, 1972, **39**, 163–184.

814 Y. Cui, R. Cao, J. Du, Z. Zhuang, Z. Xie, Q. Wang, D. Bao, W. Liu, Y. Zhu and G. Huang, *Chem. Commun.*, 2023, **59**, 2437–2440.

815 H. Saboorian-Jooybari and Z. Chen, *Results Phys.*, 2019, **15**, 102501.

816 M. Haataja, D. J. Srolovitz and A. B. Bocarsly, *J. Electrochem. Soc.*, 2003, **150**, C708.

817 M. Haataja and D. J. Srolovitz, *Phys. Rev. Lett.*, 2002, **89**, 215509.

818 N. Sorour, W. Zhang, E. Ghali and G. Houlachi, *Hydrometallurgy*, 2017, **171**, 320–332.

819 R. Sato, *J. Electrochem. Soc.*, 1959, **106**, 206.

820 D. J. Robinson and T. J. O'keefe, *J. Appl. Electrochem.*, 1976, **6**, 1–7.

821 J. W. Diggle and A. Damjanovic, *J. Electrochem. Soc.*, 1972, **119**, 1649.

822 D. J. Mackinnon, J. M. Brannen and R. C. Kerby, *J. Appl. Electrochem.*, 1979, **9**, 55–70.

823 M. Karavasteva, *Hydrometallurgy*, 1994, **35**, 391–396.

824 B. C. Tripathy, S. C. Das, P. Singh, G. T. Hefta and V. N. Misra, *J. Electroanal. Chem.*, 2004, **565**, 49–56.

825 A. Y. Hosny, *Hydrometallurgy*, 1993, **32**, 261–269.

826 L. Oniciu and L. Mureşan, *J. Appl. Electrochem.*, 1991, **21**, 565–574.

827 Q. B. Zhang, Y. X. Hua, T. G. Dong and D. G. Zhou, *J. Appl. Electrochem.*, 2009, **39**, 1207–1216.

828 Q. Zhang and Y. Hua, *J. Appl. Electrochem.*, 2009, **39**, 1185–1192.

829 N. Sorour, W. Zhang, G. Gabra, E. Ghali and G. Houlachi, *Hydrometallurgy*, 2015, **157**, 261–269.

830 J. Zheng, Q. Zhao, T. Tang, J. Yin, C. D. Quilty, G. D. Renderos, X. Liu, Y. Deng, L. Wang, D. C. Bock, C. Jaye, D. Zhang, E. S. Takeuchi, K. J. Takeuchi, A. C. Marschilok and L. A. Archer, *Science*, 2019, **366**, 645–648.

831 Y. Zhu, Y. Cui, Z. Xie, Z. Zhuang, G. Huang and X. Zhang, *Nat. Rev. Chem.*, 2022, **6**, 505–517.

832 C. M. Blevins, *J. Power Sources*, 1981, **7**, 121–132.

833 G. L. Holleck, *J. Electrochem. Soc.*, 1972, **119**, 1158.

834 J. T. Kim and J. Jorné, *J. Electrochem. Soc.*, 1977, **124**, 1473–1477.

835 J. G. Hooley, *Carbon*, 1970, **8**, 333–339.

836 H. Selig and L. B. Ebert, *Adv. Inorg. Chem. Radiochem.*, 1980, **23**, 281–327.

837 M. Armand and P. Touzain, *Mater. Sci. Eng.*, 1977, **31**, 319–329.

838 I. Harris, *Nature*, 1943, **151**, 309.

839 L. Pauling and R. E. Marsh, *Proc. Natl. Acad. Sci. U. S. A.*, 1952, **38**, 112–118.

840 A. T. Bozzo, C. Hsiao-Sheng, J. R. Kass and A. J. Barduhn, *Desalination*, 1975, **16**, 303–320.



841 Y. V. Tolmachev, *J. Electrochem. Soc.*, 2023, **170**, 030505.

842 A. Khor, P. Leung, M. R. Mohamed, C. Flox, Q. Xu, L. An, R. G. A. Wills, J. R. Morante and A. A. Shah, *Mater. Today Energy*, 2018, **8**, 80–108.

843 A. Mahmood, Z. Zheng and Y. Chen, *Adv. Sci.*, 2024, **11**(3), 2305561.

844 H. Chen, T. N. Cong, W. Yang, C. Tan, Y. Li and Y. Ding, *Prog. Nat. Sci.*, 2009, **19**, 291–312.

845 H. S. Lim, A. M. Lackner and R. C. Knechtli, *J. Electrochem. Soc.*, 1977, **124**, 1154–1157.

846 D. R. Martin, *J. Chem. Educ.*, 1948, **25**, 495.

847 Y. Zou, T. Liu, Q. Du, Y. Li, H. Yi, X. Zhou, Z. Li, L. Gao, L. Zhang and X. Liang, *Nat. Commun.*, 2021, **12**, 170.

848 P. H. Svensson and L. Kloo, *Chem. Rev.*, 2003, **103**, 1649–1684.

849 H. A. Liebhafsky, *J. Am. Chem. Soc.*, 1934, **56**, 1500–1505.

850 J. Noack, N. Roznyatovskaya, T. Herr and P. Fischer, *Angew. Chem., Int. Ed.*, 2015, **54**, 9776–9809.

851 K. J. Cathro, K. Cedzynska, D. C. Constable and P. M. Hoobin, *J. Power Sources*, 1986, **18**, 349–370.

852 P. Singh, K. White and A. J. Parker, *J. Power Sources*, 1983, **10**, 309–318.

853 K. J. Cathro, *J. Power Sources*, 1988, **23**, 365–383.

854 M. Mastragostino and S. Valcher, *Electrochim. Acta*, 1983, **28**, 501–505.

855 P. M. Hoobin, K. J. Cathro and J. O. Niere, *J. Appl. Electrochem.*, 1989, **19**, 943–945.

856 D. Zhang, Q. Liu, X. Shi and Y. Li, *J. Power Sources*, 2012, **203**, 201–205.

857 D. Bryans, B. G. McMillan, M. Spicer, A. Wark and L. Berlouis, *J. Electrochem. Soc.*, 2017, **164**, A3342–A3348.

858 G. Choi, P. Sullivan, X.-L. Lv, W. Li, K. Lee, H. Kong, S. Gessler, J. R. Schmidt and D. Feng, *Nature*, 2024, **635**, 89–95.

859 Y. Zeng, Z. Lai, Y. Han, H. Zhang, S. Xie and X. Lu, *Adv. Mater.*, 2018, **30**(33), 1802396.

860 L. Ma, S. Chen, H. Li, Z. Ruan, Z. Tang, Z. Liu, Z. Wang, Y. Huang, Z. Pei, J. A. Zapien and C. Zhi, *Energy Environ. Sci.*, 2018, **11**, 2521–2530.

861 Z. Zhao, B. Liu, Y. Shen, T. Wu, X. Zang, Y. Zhao, C. Zhong, F. Ma and W. Hu, *J. Power Sources*, 2021, **510**, 230393.

862 C. Zhong, B. Liu, J. Ding, X. Liu, Y. Zhong, Y. Li, C. Sun, X. Han, Y. Deng, N. Zhao and W. Hu, *Nat. Energy*, 2020, **5**, 440–449.

863 D. Chao, C. Ye, F. Xie, W. Zhou, Q. Zhang, Q. Gu, K. Davey, L. Gu and S. Qiao, *Adv. Mater.*, 2020, **32**(25), 2001894.

864 Y. Yu, J. Xie, H. Zhang, R. Qin, X. Liu and X. Lu, *Small Science*, 2021, **1**(4), 2000066.

865 D. Boden, C. J. Venuto, D. Wisler and R. B. Wylie, *J. Electrochem. Soc.*, 1967, **114**, 415.

866 H. Y. Kang and C. C. Liang, *J. Electrochem. Soc.*, 1968, **115**, 6.

867 Y. Xu, P. Cai, K. Chen, Y. Ding, L. Chen, W. Chen and Z. Wen, *Angew. Chem., Int. Ed.*, 2020, **59**, 23593–23597.

